

https://dspace.org/

Dynamic shock wave reflection phenomena.

Naidoo, Kavendra.

2011-10-11
http://hdl.handle.net/10539/10527

Downloaded from a DSpace repository. https://dspace.org/

Dynamic Shock Wave Reflection Phenomena

Kavendra Naidoo

A thesis submitted to the Faculty of Engineering and the Built Environment, University of the Witwatersrand, Johannesburg, in the fulfilment of the requirements for the Degree of Doctor of Philosophy.

Johannesburg, May 2011

Declaration

I declare that this thesis is my own, unaided work, except where otherwise acknowledged. It is being submitted for the degree of Doctor of Philosophy at the University of the Witwatersrand, Johannesburg. It has not been submitted before for any degree or examination at any other university.

Signed this 16th day of May 2011

Kavendra Naidoo

To my baby girl, Kiara Prashanthi, my wife, Reshenthi, my parents, Loganathan and Pathmavathie and my brother, Mahendra

Acknowledgements

Sincere thanks go to my supervisor, Professor B.W Skews, for providing guidance on this new topic and especially for exercising extreme patience over the years. It is indeed fulfilling and exciting to make a contribution to the fascinating field of supersonic gas dynamics.

Thanks are extended to South Africa's CSIR for funding most of the work associated with this thesis and for having the vision to support the development of research professionals. Thanks are also extended to the Department of Science and Technology for their Research Professional Development Programme, administered at the CSIR by Shavanee Maduray, Joseph Tshikomba and Dan Pillay.

There are many people that contributed to the achievement of this work at the Defence, Peace Safety and Security Operating Unit of the CSIR , viz. Andre Nepgen, Johan Strydom, Monique Woodborne and Marlene Padavattan. There are many that supported this process at the Aeronautic Systems Competency, viz. Dr Igle Gledhill, Glen Snedden, Thomas Roos, Peter Lake, the late Brian Cannoo and Major General Desmond Barker. Special thanks are expressed to Dr Gledhill for her encouragement and support, especially in the early stages of this work. Sincere gratitude is extended to Beeuwen Gerryts for supporting the allocation of funds for most of this work. His patience and encouragement are gratefully acknowledged. Special thanks are extended to Mauro Morelli for providing the environment and the expertise without which this work would not have been completed. Expert technical assistance was provided on various aspects of this project by Bhavya Vallabh, Ndumiso Zwane, Kimal Hiralall, Alesha Saligram, Kaveshan Nayager, Martins Selepe, Robert Mokwebo, David Reinecke, Piet Ramaloko, Jimmy Hannan, Martin Mwila and Marius Olivier. Their assistance was critical to the completion of this work. Expert maintenance services, provided by Eugene and Deon Lemmer on the CSIR supersonic facility, are gratefully acknowledged. The expert machine services provided by Louis du Plessis were critical in the achievement of good experimental data. Sincere thanks are extended to Mike Woodhead for machine services on the earlier versions of the experimental rig.

Thanks are extended to various members of university staff for their expert assistance, advice and encouragement, viz. Dr Craig Law, Dr Luke Felthun, Dr Nandkishore Menon, Randall Paton, Gavin Li, Anton Meiring, David Maclucas, Dimi, Botie and Mr Cooper.

My wife deserves special praise for her love, support and patience during this work, especially in the early years of our marriage. I am grateful for the constant reminder that there is more to life than the laboratory. I am extremely grateful to my baby girl, Kiara Prashanthi, for being such a joyful and welcome distraction to this work. Sincere gratitude is expressed to my loving parents for their undying, unconditional support, without which this undertaking would not have been possible. A final word of gratitude is expressed to my dear friend and brother, Mahendra, for encouraging me to preserve my fondest and dearest aspirations, especially during very difficult times.

Table of Contents

Declaration . . . . . **i**

Acknowledgements . . . . . **iii**

Abstract . . . . . **xvi**

Published Works . . . . . **xviii**

Chapter 1 Introduction **1**
1.1 Background 1
1.2 Ideal, Steady, Two-Dimensional Shock Wave Reflection Transition 1
1.3 Problem Statement 4
1.4 Objectives 5
1.5 Chapter Overviews 6

Chapter 2 Literature Survey **7**
2.1 Introduction 7
2.2 Steady, Two-Dimensional, Theory 7
2.3 Ideal, Steady, Two-dimensional RR $\leftrightarrow$ MR Transition Criteria 13
2.3.1 RR to MR Transition in the Strong-Reflection Range 14
2.3.2 MR to RR Transition in the Strong-Reflection Range 15
2.3.3 Summary of Transition Conditions 15
2.4 The Persistence of Steady RR with a Length Scale Present at the Reflection Point 16
2.5 MR Configurations in a Steady Supersonic Free Stream 17
2.6 Early Origins of Rapid Wedge Rotation 18
2.7 Computational Simulation of Wedge Vibration and Impulsive Wedge Rotation 20
2.8 Dynamic Mach Stem Development for a Stationery Wedge 25
2.9 Research Gap 26

Chapter 3 Experimental Method **28**
3.1 Introduction 28
3.2 Background 28
3.2.1 Simulation of the Ground Plane 28
3.2.2 Evaluation of Free Stream Turbulence Levels in the Supersonic Facility 29
3.2.3 Three-Dimensional Wedge Edge Effects 29
3.3 Supersonic Wind Tunnel 30
3.3.1 Mach Number Measurement 32
3.3.2 Stagnation Temperature Measurement 33
3.4 Flow Visualisation 35
3.5 Image Calibration Technique 35
3.6 High-Speed Image Acquisition 38
3.7 Summary of Measurement Uncertainties 40

3.8 Dynamic Shock Wave Interaction Rig . . . 41
3.8.1 System Requirements Specification . . . 41
3.8.2 Design Description . . . 43
3.8.3 Actuator for Steady State Experiments . . . 44
3.8.4 Actuator for Dynamic Experiments . . . 47
3.9 Sample Image and Data Reduction . . . 54
3.10 Rig Development History . . . 57
3.11 Conclusion . . . 61

Chapter 4 Computational Method . . . 62
4.1 Introduction . . . 62
4.2 Code Description : Euler Code . . . 62
4.3 Code Description : Fluent V 12.0 . . . 63
4.4 Computational Model . . . 64
4.5 Dynamic Solution Procedure . . . 67
4.6 Grid Sensitivity Studies . . . 67
4.7 Fluent Benchmarking . . . 70
4.8 The Incidence-Induced Hysteresis Test . . . 70
4.9 Compensation for Boundary Layer Deflection . . . 71
4.10 Conclusion . . . 72

Chapter 5 Steady State RR $\leftrightarrow$ MR Transition . . . 74
5.1 Introduction . . . 74
5.2 A Brief Summary: The Three-Dimensional Nature of Wave Systems in an Experiment . . . 74
5.3 Steady State Experiment in the Weak-Reflection Region . . . 76
5.3.1 Three-dimensional Wave Structure . . . 76
5.3.2 Weak Surface Waves . . . 78
5.3.3 Experimental Results . . . 78
5.4 Steady State Experiment in the Strong-Reflection Region . . . 80
5.4.1 Theoretical Transition . . . 80
5.4.2 Three-dimensional Wave Structure . . . 82
5.4.3 Experimental Results . . . 82
5.5 Results . . . 84
5.6 Conclusion . . . 85

Chapter 6 Dynamic Two-Dimensional Regular to Mach Reflection Transition in an Ideal Steady Supersonic Free Stream . . . 88
6.1 Introduction . . . 88
6.2 Experimental Results for Dynamic RR to MR Transition . . . 89
6.2.1 Weak-Reflection Range . . . 94
6.2.2 Strong-Reflection Range . . . 94
6.3 Computational Simulation of Impulsive Rotation at $M = 2.98$ . . . 95
6.3.1 Steady Pressure-Deflection Shock Polars . . . 98
6.3.2 Dynamic Flow Solution . . . 99
6.3.3 Transient Pressure Rise through the Reflection/Triple Point . . . 101
6.4 Transition Criteria and Mechanism for Dynamic RR to MR Transition . . . 102
6.5 Parameter investigation for dynamic RR to MR transition . . . 107
6.5.1 $M = 1.93$ . . . 108
6.5.2 $M = 2.98$ . . . 108
6.5.3 Dynamic Mach Stem Development . . . 112
6.6 Conclusion . . . 113
6.7 Recommendations for Future Work . . . 115

Chapter 7 Dynamic Two-Dimensional Mach to Regular Reflection Transition in an Ideal Steady Supersonic Free Stream . . . 116
7.1 Introduction . . . 116
7.2 Experimental Results . . . 117
7.2.1 Weak-Reflection Range . . . 117
7.2.2 Strong-Reflection Range . . . 117
7.3 Parameter Investigation for Dynamic MR to RR Transition . . . 123
7.3.1 Impulsive Rotation About the Wedge Leading Edge at $M = 1.93$ . . . 124
7.3.2 Impulsive Rotation About the Wedge Trailing Edge at $M = 1.93$ . . . 125
7.3.3 Parameter Investigation for Dynamic MR to RR Transition at $M = 1.93$ . . . 128
7.3.4 Parameter Investigation for Dynamic MR to RR Transition at $M = 2.98$ . . . 132
7.4 Thoughts on Three-dimensional Effects . . . 134
7.5 Conclusion . . . 139
7.6 Recommendations for Future Work . . . 141

Chapter 8 Conclusions and Recommendations for Future Work . . . 153
8.1 Conclusions . . . 153
8.1.1 Summary of Results for Dynamic RR to MR Transition . . . 154
8.1.2 Summary of Results for Dynamic MR to RR Transition . . . 155
8.2 Recommendations for Future Work . . . 156
8.2.1 Dynamic RR to MR Transition . . . 156
8.2.2 Dynamic MR to RR Transition . . . 157

Appendix A Data Acquisition of Freestream Conditions . . . 158
A.1 Mach Number Measurement . . . 158
A.1.1 Pressure Transducer Calibration . . . 158
A.1.2 Pressure Transducer Specfication and Calibration Results . . . 160
A.1.3 Mach Number Calculation and Uncertainty Analysis . . . 162
A.2 Test Section Acoustic Speed Measurement . . . 168
A.2.1 Stagnation Temperature Probe and Transducer Specification . . . 168
A.2.2 Acoustic Speed Calculation and Uncertainty Analysis . . . 169
A.3 National Instruments Data Acquisition System . . . 171

Appendix B Schlieren System, High-Speed Imaging and Optics . . . 173
B.1 Schlieren System Specification . . . 173
B.1.1 Optical Alignment . . . 173
B.2 Technical Specifications of High Speed Camera . . . 174
B.3 Inclinometer Specification and Calibration . . . 174
B.4 Routine for co-ordination calculation in GNU Octave . . . 177

Appendix C Rig Design Calculations . . . 179
C.1 Maximum Rig Cross Sectional Area . . . 179
C.2 Motor Sizing for Servo-driven Actuator for Steady State Experiments . . . 179
C.3 Component Sizing for Spring-Based Actuator for Dynamic Tests . . . 184
C.4 Finite Element Analysis for Latch Design . . . 187
C.5 Description of the Rig Operator Interface . . . 188
C.6 Photographs of Rig . . . 188

References . . . 197

List of Figures

1.1 Simplified schematic of (a) steady shock wave reflection with the flight vehicle in steady, level flight and (b) dynamic shock wave reflection when the vehicle increases its pitch orientation rapidly . . . 2
1.2 Simplified schematics of regular and Mach reflection generated by a wedge in a steady supersonic free stream . . . 3
1.3 Typical curvature observed in flow computations by Felthun & Skews [12] for rapid increasing wedge incidence . . . 5

2.1 Simplified schematic of idealised regular reflection and flow conditions in the vicinity of the reflection point . . . 9
2.2 Simplified schematic of idealised Mach reflection and flow conditions in the vicinity of the triple point . . . 9
2.3 Locus of flow conditions that can be achieved through an oblique shock wave in a $M = 3.0$ free stream . . . 10
2.4 Sample pressure-deflection polars for regular and Mach reflection at $M = 3.0$ . . . 11
2.5 Pressure-deflection at the detachment and von Neumann conditions at $M = 3.0$ . . . 12
2.6 Pressure-deflection polars in the dual solution domain and at the sonic condition at $M = 3.0$ 12
2.7 Pressure-deflection shock polar for a reflection at the detachment condition at $M = 1.93$ . . . 13
2.8 Theoretical ϕ_N and ϕ_D between $M = 1.6$ and 10.0 for air with $\gamma = 1.4$ . . . 16
2.9 Pressure deflection shock polar for the asymmetric case at $M = 4.96$, $\theta_1 = 35.0°$ and $\theta_2 = 14.58°$ 18
2.10 Direct and inverse Mach reflections possible in a steady supersonic free stream . . . 18
2.11 A series of schlieren images from the experiment of Mouton & Hornung [36] demonstrating hysteresis in the dual solution domain at $M = 4.0$ . . . 21
2.12 Measured transition results from the dynamic experiment by Mouton & Hornung [36] . . . 21
2.13 Periodic formation of compression and expansion waves generated by wedge oscillation about its leading edge with amplitude = 0.5°; wedge rotation speed, $\Omega = 8 \cdot 10^3$ deg/s published by Markelov et al. [34] . . . 23
2.14 Curvature on the incident wave of a RR due to rapid wedge rotation, $M = 5.0$, $g/w = 0.42$ and rotation speed $M_T = 0.1$ at $\theta_w = 24.0°$ [28] . . . 23
2.15 Computed effect of rapid wedge rotation on ϕ_T for RR → MR transition published by Felthun & Skews [12], $M = 3.0$, $h/w = 0.9$, $\theta_{wi} = 20.0°$ . . . 24
2.16 Predicted and measured dynamic Mach stem development by Mouton & Hornung [36] at $M = 4.0$, $g/w = 0.3907$, $\theta_w = 23.0°$, $\gamma = 1.4$ . . . 25

3.1 Two and three-dimensional Mach stem measurements from experiments and Euler predictions published by Ivanov et al. [24] for a static wedge at $M = 4.0$, $g/w = 0.56$ . . . 30
3.2 Side view of supersonic wind tunnel facility at the CSIR, South Africa . . . 31
3.3 Simplified schematic indicating tunnel nozzle shape control . . . 32
3.4 Schematic of stagnation temperature probe in settling chamber . . . 34
3.5 (a) Sample total temperature probe measurement and (b) magnified view of select data range 34
3.6 Schematic of schlieren flow visualisation setup (colour mask and high-speed camera not shown) 36
3.7 Sample images obtained with various colour masks . . . 38

3.8 Image of (a) 5 mm × 5 mm square calibration grid with locating markers and the (b) test image captured with the high-speed camera at 512 x 512 pixel resolution used for all dynamic experiments . . . 39
3.9 Distribution of deviation from target angle . . . 39
3.10 Photograph of the Photron Ultima APX-RS high speed camera with a UV filter to protect the imaging sensor and an aspherical achromatic lens for focussing. The schlieren colour mask is positioned ahead of the focussing lens. . . . 40
3.11 Schematic of a section of the supersonic tunnel with walls removed showing available tunnel support systems for the mounting of the rig (image provided courtesy of the CSIR) . . . 42
3.12 Envelope of operating conditions in CSIR supersonic wind tunnel in terms of total pressure (gauge) . . . 44
3.13 Illustrations of rig installed in the CSIR supersonic wind tunnel . . . 45
3.14 Symmetric wedge arrangement and the drive path highlighted in grey . . . 46
3.15 Servo motor driven actuator for steady state, baseline experiments . . . 48
3.16 The spring driven actuator and latch mechanism for the dynamic experiment. The actuator is assembled for the dynamic RR → MR experiment. . . . 50
3.17 Sectioned view illustrating jacking nut/screw and thrust bearing arrangement to arm the actuator . . . 51
3.18 A series of CAD drawings illustrating the operation of the latch release mechanism . . . 52
3.19 Actuator arrangement for dynamic MR → RR experiments . . . 54
3.20 Sample data acquisition readings acquired during an experiment . . . 55
3.21 Sample image captured during a dynamic experiment and prepared for measurements. The image was captured with the high-speed digital camera at 10000 frames per second with a 1/20000 s exposure time. Image resolution : 512 × 512 pixels. . . . 56
3.22 Comparison of frontal area profiles in the streamwise direction . . . 58
3.23 First rig design is considerably larger than the final version of the rig. Blockage was sufficiently large to prevent tunnel startup. . . . 58
3.24 (a) Illustration and (b) photograph of the second rig design with (c) a schlieren image of the reflection pattern indicating poor optical magnification . . . 59
3.25 A series of high-speed schlieren images showing the early release of the drive train and wedges due to failure of the latch mechanism on tunnel startup. The detached bow wave, after the flow conditions stabilised, can be seen on the last frame, well after the latch has been released. The new optics have the desired magnification. . . . 60

4.1 (a) Conformal mesh topology in the in-house Euler code compared to (b) the non-conformal mesh topology in Fluent for mesh refinement in the region of the incident wave at the wedge leading edge . . . 65
4.2 Sample spurious flow feature in Fluent flow solution due to poor mesh quality in the vicinity of the reflection point . . . 66
4.3 Schematic of computational model for simulation of the experiment . . . 66
4.4 Series of images illustrating the successive adaption of an initial coarse mesh to establish an initial, grid independent, steady solution. Corresponding computed density contours appear on the right hand side. . . . 68
4.5 Results from CFD grid sensitivity assessment for a static and dynamic simulation . . . 69
4.6 Computed density contours showing RR → MR transition close to the detachment condition condition. $M = 2.98$, $M_E = +0.001$, fixed $h/w = 0.91$. . . . 71
4.7 Computed density contours showing MR → RR transition close to the von Neumann condition. $M = 2.98$, $M_E = -0.001$, fixed $h/w = 0.91$. . . . 72

5.1 Typical 3D geometry of shock wave reflections at $M = 4.0$, computed by Ivanov et al. [24] . . 75
5.2 Computed and measured spanwise Mach stem height variation in a $M = 4.0$ free stream published by Ivanov et al. [24] . . . 75
5.3 Identification of 3D reflection structures on schlieren images from the steady state experiment at $M = 1.93$ . . . 77

5.4 View of CAD model of wedge illustrating the location of counterbores on the stream facing surface of the wedge . . . 78
5.5 Isometric and top view identifying location of reflection point on symmetry plane with respect to sonic cone from wedge face counterbores at the detachment condition, $M = 1.93$ . . . 79
5.6 High-speed images from steady state experiment at $M = 1.93$ . . . 81
5.7 Magnified view : schlieren image of MR at $M = 2.98$, indicating the maximum Mach stem height in the wedge vertical plane of symmetry and the shear layer in the plane of the minimum Mach stem height (indicated on the bottom half of the reflection only) . . . 82
5.8 High-speed images from steady state experiment at $M = 2.98$ . . . 83
5.9 Measured and computed Mach stem development at $M = 1.93$, $g/w \approx 0.6$. The solid lines are second-order polynomial fits to each data set used to extrapolate ϕ_T at zero m/w. The uncertainty in $\delta\phi$ and $\delta m/w$ for the experimental data is omitted to prevent cluttering on the graph. . . . 85
5.10 Measured and computed Mach stem development at $M = 2.98$, $g/w \approx 0.6$. The solid lines are second-order polynomial fits to each data set used to extrapolate ϕ_T at zero m/w. The uncertainty in $\delta\phi$ and $\delta m/w$ for the experimental data is omitted to prevent cluttering on the graph. . . . 86

6.1 High-speed images for dynamic RR → MR transition at $M = 1.93$ . . . 90
6.2 Measurements from the dynamic experiment at $M = 1.93$ . . . 91
6.3 High-speed images for dynamic RR → MR transition at $M = 2.98$ . . . 92
6.4 Measurements from the dynamic experiment at $M = 2.98$ . . . 93
6.5 Experimental and CFD results for steady and dynamic RR → MR transition at $M = 1.93$. Solid lines are second-order polynomial fits through each data set and are used to predict ϕ_T at zero m/w. . . . 96
6.6 Experimental and CFD results for steady and dynamic RR → MR transition at $M = 2.98$. Solid lines are second-order polynomial fits through each data set and are used to predict ϕ_T at zero m/w. . . . 97
6.7 Critical pressure-deflection shock polars for steady reflection at $M = 2.98$ . . . 98
6.8 Computed density contours showing the flow field development for $M_E = +0.1$, $\theta_{wi} = 19.0°$ at $M = 2.98$, $g/w \approx 0.6$. The Mach stem is indicated "ms" only where clearly visible. This is not to be mistaken to indicate the point of transition. . . . 99
6.9 Closeup views of computed density contours showing the first traces of the shear layer from the triple point as the reflection transitions to MR . . . 100
6.10 Mach stem development for impulsive rotation at $M_E = +0.1$ with $\theta_{wi} = 19.0°$ compared to results from the experiment and 2D CFD results. $M = 2.98$, $g/w \approx 0.6$. . . . 101
6.11 Computed pressure traces through the reflection point as the wedge rotates from $\theta_{wi} = 19.0°$ at $M_E = +0.1$ about the model pivot point at $M = 2.98$, $g/w \approx 0.6$ . . . 102
6.12 Computed density contours showing the development of the subsonic region downstream of reflection point before transition at $M = 2.98$, $M_E = +0.1$, $\theta_{wi} = 19.0°$. The subsonic region downstream of the reflection point is shaded black. . . . 104
6.13 Computed density contours showing the development of the subsonic region downstream of the reflection point between θ_S and θ_C at $M = 1.93$, $M_E = +0.05$, $\theta_{wi} = 8.0°$. The subsonic region downstream of the reflection point is shaded black. . . . 105
6.14 Estimated location of length scale information on the shortest line between the leading edge of the expansion and the subsonic region at $\theta_{WT} = 17.6°$. The early development of the shear layer from the triple point is also visible. . . . 106
6.15 θ_{WT} and ϕ_T vs. M_E at $M = 1.93$, $\theta_{wi} = 8.0°$ . . . 110
6.16 θ_{WT} and ϕ_T vs. M_E at $M = 2.98$, $\theta_{wi} = 19.0°$ . . . 111
6.17 Dynamic Mach stem development for impulsive rotation about the wedge trailing edge at $M = 1.93$. Solid lines are second-order polynomial fits through each data set. . . . 112
6.18 Dynamic Mach stem development for impulsive rotation about the wedge trailing edge at $M = 2.98$. Solid lines are second-order polynomial fits through each data set. . . . 113

7.1 High-speed images showing the initial, steady, disgorged wave system at $M = 1.92$ being swallowed as the wedge incidence decreases rapidly 118
7.2 High-speed images from dynamic MR → RR experiment at $M = 3.26$ 120
7.3 Measurements from the dynamic experiment at $M = 3.26$. The time of MR → RR transition is estimated from the images and is indicated on each graph with a broken line. 121
7.4 Mach stem development from experiment and CFD for dynamic MR → RR transition at $M = 3.26$, $g/w \approx 0.6$. The dashed and solid lines represent first and second-order fits respectively, only for $\phi \leq 38.0°$, to their respective data sets and are used to extrapolate ϕ_T at zero m/w. The offset from the steady data due to rapid rotation of the wedge is labelled "A". 122
7.5 Computed variation of m/w with θ_w for impulsive rotation at $M_E = -0.075$. $M = 1.93$, $\theta_{wi} = 13.4°$, $h/w = 0.84$. The dashed line represents a linear fit of the data for $\theta_w \leq 4.5°$ and is used to estimate θ_{WT} at zero m/w for the rapidly rotating wedge. The solid line represents a second order fit of the steady data. 125
7.6 Computed variation of m/w with ϕ for impulsive rotation at $M_E = -0.075$. $M = 1.93$, $\theta_{wi} = 13.4°$, $h/w = 0.84$. The solid line represents a second order fit of the steady data. The data points from the unsteady simulation are connected with a dashed line to clarify the sequence of events. 126
7.7 Computed variation of m/w with ϕ for impulsive rotation at $M_E = -0.075$. $M = 1.93$, $\theta_{wi} = 13.4°$, $g/w = 0.6$. The solid lines represent a second order fit of the steady and unsteady data. For the unsteady case, only data for $\theta_w \leq 5.0°$ is used to estimate θ_{WT}. . . . 128
7.8 Computed variation of m/w with ϕ for impulsive rotation at $M_E = -0.075$. $M = 1.93$, $\theta_{wi} = 13.4°$, $g/w = 0.6$. The solid line represents a second order fit of the steady data. The data points from the unsteady simulation are connected with a dashed line to clarify the sequence of events. 129
7.9 Computed variation of m/w with θ_w for rapid, impulsive rotation. $M = 1.93$, $\theta_{wi} = 13.4°$, $h/w = 0.84$ (for rotation about the leading edge), $g/w = 0.6$ (for rotation about the trailing edge). Dashed lines represent linear fits used to estimate θ_{WT} for $M_E = -0.01$ and -0.05. Solid lines are second-order polynomial fits used to estimate θ_{WT} for $M_E = -0.1$ and the steady state case. 130
7.10 Computed variation of m/w with ϕ for rapid, impulsive rotation. $M = 1.93$, $\theta_{wi} = 13.4°$, $h/w = 0.84$ (for rotation about the leading edge), $g/w = 0.6$ (for rotation about the trailing edge). The solid line is a second-order polynomial fit used to estimate θ_{WT} for the steady state case. The dashed line joins the data points in each data set to aid visualisation. ϕ_T was measured from the flow solution at θ_{WT} in each case. 131
7.11 Computed pressure contours for impulsive rotation at $M_E = -0.1$. $M = 1.93$, $\theta_{wi} = 13.4°$, $h/w = 0.84$. 132
7.12 θ_{WT} and ϕ_T vs. M_E at $M = 1.93$ 133
7.13 θ_{WT} and ϕ_T vs. M_E at $M = 2.98$ 135
7.14 Computed variation of Mach stem height with θ_w for rapid, impulsive rotation. $M = 2.98$, $\theta_{wi} = 24.5°$, $h/w = 1.01$ (for rotation about the leading edge), $g/w = 0.6$ (for rotation about the trailing edge). Dashed lines represent linear fits used to estimate θ_{WT} for $M_E = -0.01$, -0.05 and -0.01. Solid lines are second-order polynomial fits used to compute θ_{WT} for the steady state case. 136
7.15 Computed variation of Mach stem height with ϕ for rapid, impulsive rotation. $M = 2.98$, $\theta_{wi} = 24.5°$, $h/w = 1.01$ (for rotation about the leading edge), $g/w = 0.6$ (for rotation about the trailing edge). The solid line is a second-order polynomial fit to compute ϕ_T for the steady state case. ϕ_T is measured at θ_{WT}. 137
7.16 Steady, 3D reflection pattern computed with an Euler code by Ivanov et al. [24]. $M = 4.0$, $\phi = 35.5°$, $b/w = 3.75$, $g/w = 0.3$. 139
7.17 Computed pressure contours at (a) $\theta_{wi} = 13.4°$ and (b) $\theta_w = 13.0°$ for impulsive rotation about the wedge leading edge at $M_E = -0.075$. $M = 1.93$, $\theta_{wi} = 13.4°$, $h/w = 0.84$. 142

7.18 Computed pressure contours at (a) $\theta_w = 11.5°$ and (b) $\theta_w = 11.0°$ for impulsive rotation about the wedge leading edge at $M_E = -0.075$. $M = 1.93$, $\theta_{wi} = 13.4°$, $h/w = 0.84$. 143
7.19 Computed pressure contours at (a) $\theta_w = 10.0°$ and (b) $\theta_w = 8.5°$ for impulsive rotation about the wedge leading edge at $M_E = -0.075$. $M = 1.93$, $\theta_{wi} = 13.4°$, $h/w = 0.84$. 144
7.20 Computed pressure contours showing decreasing Mach stem height between $\theta_w = 7.0°$ and $\theta_w = 1.0°$ for impulsive rotation about the wedge leading edge at $M_E = -0.075$. $M = 1.93$, $\theta_{wi} = 13.4°$, $h/w = 0.84$. 145
7.21 Development of flow field in the vicinity of the reflection point after transition to RR between (a) $\theta_w = 0.5°$ and (b) $\theta_w = 0.1°$ for impulsive rotation about the wedge leading edge at $M_E = -0.075$. $M = 1.93$, $\theta_{wi} = 13.4°$, $h/w = 0.84$. 146
7.22 Computed pressure contours at (a) $\theta_{wi} = 13.4°$ and (b) $\theta_w = 13.0°$ for impulsive rotation about the wedge trailing edge at $M_E = -0.075$. $M = 1.93$, $\theta_{wi} = 13.4°$, $g/w = 0.6$. 147
7.23 Computed pressure contours at (a) $\theta_w = 12.5°$ and (b) $\theta_w = 12.0°$ for impulsive rotation about the wedge trailing edge at $M_E = -0.075$. $M = 1.93$, $\theta_{wi} = 13.4°$, $g/w = 0.6$. The disturbance propagates down the length of the incident wave and the compression waves from the wedge surface continue propagating away from the surface. The solid red line indicates the position of the incident wave at the initial condition. 148
7.24 Computed pressure contours at (a) $\theta_w = 11.6°$ and (b) $\theta_w = 10.0°$ for impulsive rotation about the wedge trailing edge at $M_E = -0.075$. $M = 1.93$, $\theta_{wi} = 13.4°$, $g/w = 0.6$. The solid red line indicates the position of the incident wave at the initial condition. 149
7.25 Computed pressure contours at (a) $\theta_w = 9.5°$ and (b) $\theta_w = 8.5°$ for impulsive rotation about the wedge trailing edge at $M_E = -0.075$. $M = 1.93$, $\theta_{wi} = 13.4°$, $g/w = 0.6$. Between $\theta_w = 9.5°$ and $7.5°$ the Mach stem height is constant at approximately δm below the initial Mach stem height. The discontinuity on the incident wave continues to move towards the triple point. The solid red line indicates the position of the incident wave at the initial condition. . 150
7.26 Computed pressure contours at (a) $\theta_w = 7.0°$ and (b) $\theta_w = 5.0°$ for impulsive rotation about the wedge trailing edge at $M_E = -0.075$. $M = 1.93$, $\theta_{wi} = 13.4°$, $g/w = 0.6$. The discontinuity on the incident wave has reached the triple point and the incident wave is curved along its entire length. The Mach stem height decreases until transition to RR. The solid red line indicates the position of the incident wave at the initial condition. 151
7.27 Computed pressure contours at (a) $\theta_{WT} = 2.4°$, (b) $\theta_w = 1.5°$ and (c) $\theta_w = 1.1°$ for impulsive rotation about the wedge trailing edge at $M_E = -0.075$. $M = 1.93$, $\theta_{wi} = 13.4°$, $g/w = 0.6$. . 152

8.1 Measured ϕ_T from experiments compared to analytical steady transition criteria 155

A.1 Druck Digital Pressure Indicator 605 159
A.2 Calibration and regression for pressure transducers 161
A.3 Schematic of stagnation temperature probe in settling chamber 169
A.4 Transducer response supplied by WIKA Instruments 170
A.5 Sample total temperature probe measurement (magnified view of select data range on the right hand side) 171
A.6 Data Acquisition Architecture 172

B.1 Schlieren system light source 174
B.2 Machined collar for laser pointer to replace slit mount on schlieren light source for system alignment 175
B.3 Custom collimator for adjustment of second mirror 175
B.4 Wyler and Pro3600 Inclinometers 176

C.1 Data used to determine the maximum permissable model cross sectional area extracted from a US Naval Ordnance Report [43]. 180
C.2 Schematic showing derivation of actuator force 180

C.3 Lead screw and bearing assembly to convert rotational motion of the DC servo motor to horizontal motion of the actuator required to pitch the wedges. The image is taken from the Rexroth Bosch Group product catalogue on precision ball screw assemblies. 183
C.4 Solution of the one dimensional ordinary differential equation for the spring mass system with $m = 1.0$ kg, $k = 72 \times 10^3$ N/m, $x_o = 13.0$ mm and zero initial speed 185
C.5 Contours showing the distribution of computed stress in the latch and release pillar. The region of maximum stress at approximately 354 MPa is indicated. The FEM analysis was performed by Ryan Raath at the CSIR, Pretoria. 187
C.6 Control and electrical connections interface for actuators 189
C.7 Electrical circuit for operation of servo-motor showing current direction for wedge pitch up and pitch down 190
C.8 (a) Front and (b) top views of control interface for spring-driven actuator 191
C.9 Solenoid circuit for the operation of the safety pin in the spring-driven actuator 192
C.10 Latch release circuit diagram for the spring-driven actuator 193
C.11 Actuators for (a) steady state, baseline experiments and (b) dynamic experiments 194
C.12 Rig used for dynamic shock wave reflection experiments. Cover plates are installed and the release actuator has been removed. 194
C.13 Rig with cover plates removed and release actuator installed. The actuator is assembled to execute the dynamic RR → MR transition experiment. 195
C.14 Closeup view of the spring-driven actuator with the release actuator installed. The actuator is assembled to execute the dynamic RR → MR transition experiment. 195
C.15 Closeup view of wedges 195
C.16 Stream wise view of the rig installed in tunnel test section 196

List of Tables

3.1 Results from a calibration check on a test image for measurements between $-20.0°$ and $40.0°$ 37
3.2 Summary of statistics for angular measurement error . . . 37
3.3 Calibration check for measurement uncertainty on distance . . . 38
3.4 Summary of measurement uncertainties . . . 41
3.5 A summary of results from a sample dynamic experiment at $M = 3.0$ . . . 56

4.1 Computed Mach stem heights compared to simulation results published by Ivanov et al. [24] for a stationary 2D wedge at $M = 4.0$, $g/w = 0.56$ . . . 70
4.2 Computed values for ϕ_T for the incidence-induced hysteresis test at $M = 2.98$ in comparison to steady state, theoretical values for RR $\leftrightarrow$ MR transition . . . 71

5.1 Summary of steady state results from experiment and CFD at $M = 1.93$ and 2.98, $g/w \approx 0.6$ 87

6.1 Experimental test conditions for dynamic RR $\rightarrow$ MR experiments, $g/w \approx 0.6$ . . . 90
6.2 Summary of ϕ_T from steady and dynamic experiments and CFD at $M = 1.93$, $g/w \approx 0.6$ . . 95
6.3 Summary of ϕ_T from steady and dynamic experiments and CFD at $M = 2.98$, $g/w \approx 0.6$ . . 95
6.4 Summary of results for dynamic simulations at $M = 1.93$ and $M = 2.98$ to investigate the dynamic RR $\rightarrow$ MR transition mechanism . . . 106
6.5 θ_{WT} and ϕ_T at $M = 1.93$, $\theta_{wi} = 8.0°$ . . . 109
6.6 Effect of initial incidence on ϕ_T and θ_{WT} at $M = 1.93$, $M_E = +0.1$ . . . 109
6.7 θ_{WT} and ϕ_T at $M = 2.98$, $\theta_{wi} = 19.0°$ . . . 109
6.8 Effect of initial incidence on ϕ_T and θ_{WT} at $M = 2.98$, $M_E = +0.1$ . . . 109

7.1 Experiment test conditions for dynamic MR $\rightarrow$ RR transition experiments, $g/w \approx 0.6$ . . . 119
7.2 Experimental and CFD results for steady and dynamic MR $\rightarrow$ RR transition at $M = 3.26$, $g/w \approx 0.6$. . . . 121
7.3 Experimental and CFD results for steady and dynamic MR $\rightarrow$ RR transition at $M = 2.96$, $g/w \approx 0.6$. . . . 123
7.4 Wedge and shock incidence at transition : M 1.93, $\theta_{wi} = 13.4°$ . . . 134
7.5 Wedge and shock incidence at transition : $M = 2.98$, $\theta_{wi} = 24.5°$ . . . 134
7.6 Sensitivity of $\delta\theta_{WT}$ and $\delta\phi_T$ to pivot point and θ_{wi} for $M_E = -0.1$ at $M = 2.98$ . . . 136

A.1 Technical specifications of the Druck DPI605 . . . 159
A.2 Pressure Transducer Specifications . . . 160
A.3 Total pressure transducer calibration: High Range . . . 160
A.4 Total pressure transducer calibration: Low Range . . . 160
A.5 Static pressure transducer calibration . . . 161
A.6 Atmospheric pressure transducer calibration . . . 161
A.7 Summary of pressure transducer regression statistics . . . 162
A.8 CSIR tunnel test section calibration . . . 167

B.1 Optical parameters of schlieren system . . . 176
B.2 Technical specifications of high speed camera . . . 176

B.3 Technical specifications of the Wyler Bubble Inclinometer 177
B.4 Calibration check of Pro3600 digital Protractor 177

C.1 Technical specifications for DC servo motor 183
C.2 Technical specifications for the lead screw and bearing arrangement 183
C.3 Technical specifications for safety pin solenoid 186
C.4 Technical specifications for release actuator 186

Abstract

There have been numerous studies on the steady state transition criteria between regular reflection (RR) and Mach reflection (MR) of shock waves for a stationary, two-dimensional (2D) wedge in a steady supersonic free stream since the original shock wave reflection research by Ernst Mach in 1878. The steady, 2D transition criteria between RR and MR are well established. There has been little done to consider the dynamic effect of rapid wedge rotation on RR $\leftrightarrow$ MR transition.

This thesis presents the results of an investigation of the effect of rapid wedge rotation on transition between 2D regular and Mach reflection in the weak and strong-reflection ranges, with experiment and computational fluid dynamics. A novel facility was designed to rotate a pair of large aspect ratio wedges in a 450 mm $\times$ 450 mm supersonic wind tunnel at wedge rotation speeds up to 11000 deg/s resulting in wedge tip speeds approximately 3.3 % of the free stream acoustic speed. Steady state, baseline experiments, in which the wedges were rotated very gradually, were also completed. High-speed images and measurements are presented for the steady and dynamic experiments. Numerical solution of the inviscid governing flow equations was used to model the steady case and to mimic the experimental motion in the dynamic experiments. The two-dimensional, Euler CFD code was developed at the University of the Witwatersrand.

Steady state experiments were completed in the weak and strong-reflection ranges and transition measurements were compared to 2D steady, theoretical values and Euler computations. There was close agreement between theoretical, computational and experimental transition for the steady case, with the following exception. Due to the levels of free stream noise in the supersonic wind tunnel, incidence-induced hysteresis was not observed in the strong-reflection region and transition occurred at the von Neumann condition for increasing and decreasing incidence. In the ideal case, RR $\rightarrow$ MR transition occurs at the detachment condition and the reverse transition occurs at the von Neumann condition. Therefore, there is discrepancy between steady theory/CFD and experiment for RR $\rightarrow$ MR transition in the strong-reflection range only, which is consistent with observations in other facilities with sufficient levels of free stream noise.

Dynamic RR $\rightarrow$ MR Transition : Rapid wedge rotation did generate a measurable dynamic effect on RR $\rightarrow$ MR transition. This thesis presents the first experimental evidence of RR $\rightarrow$ MR reflection transition

beyond the steady detachment condition in the weak and strong-reflection ranges. In all instances, there was good agreement between experiment and 2D CFD, including dynamic RR → MR transition in the strong-reflection region. The agreement between the experiment, in which small perturbations are always present in the free stream, and the CFD, in which the free stream is without perturbations, implies that RR → MR transition in the strong-reflection region becomes insensitive to free stream noise above a certain critical rotation speed. Due to the close agreement between CFD and experiment, the Euler code was also applied to scenarios beyond the limits of the current facility to explore the influence of variables in the parameter space, viz. rotation speed, initial incidence and rotation centre. CFD was also used to investigate the dynamic transition mechanism over a limited number of simulations. For dynamic RR → MR transition, a distinction is drawn between the sonic, length scale and detachment conditions. The point at which the flow downstream of the reflection point goes sonic is not necessarily the point at which the wedge length scale, from the wedge trailing edge expansion, is communicated to the reflection point. There is evidence to support that the RR → MR transition criteria for the rapidly rotating wedge is neither the sonic or length scale conditions, but rather the condition at which the reflected wave can no longer satisfy the boundary condition at the reflection point. Dynamic simulations showed that RR could be maintained with a length scale present at the reflection point. Other dynamic simulations showed, for the first time, that transition to MR was possible without the wedge length scale being communicated to the reflection point.

Dynamic MR → RR transition : Rapid wedge rotation generated a measurable effect on MR → RR transition. The first experimental evidence of MR → RR transition below the steady von Neumann condition is presented. Once again, there was good agreement between experiment and 2D CFD. CFD was used to investigate the sensitivity of transition to rotation speed, initial incidence and rotation centre in the strong and weak-reflection ranges. Due to impulsive wedge start and rapid wedge rotation, there are very marked dynamic effects on the variation of Mach stem height with wedge incidence and the deviation from the steady transition conditions is significant. The MR → RR transition was found to be dependent on the initial condition and the transient variation of Mach stem height with wedge incidence.

Published Works

Aspects of this work have been accepted for publication in the Journal of Fluid Mechanics:

1. Naidoo K, Skews BW. Dynamic effects on transition between two-dimensional regular and Mach reflection of shock waves in an ideal steady supersonic free stream. *Original submission 22 October 2010; revised 8 January 2011; accepted 29 January 2011.* DOI:10.1017/jfm.2011.58.

Various aspects of this work have been published in the following conference articles:

1. Naidoo K, Skews BW. Dynamic shock reflection phenomena in ideal, two-dimensional flows. In *Proceedings 25th International Symposium on Shock Waves*, (edited by G Jagadeesh, E Arunan, K P J Reddy), Bangalore, India, EAN 9788173715716, Paper 1187, 2005.

2. Naidoo K, Skews BW. Characterisation of unsteady shock wave reflection phenomena. In *Proceedings of the 5th South African Conference on Computational and Applied Mechanics* (edited by T M Harms), Cape Town, South Africa, CD-ROM, ISBN 1-919966-01-3, 292-299, 2006.

3. Naidoo K, Skews BW. Computational and experimental investigation of dynamic shock reflection phenomena. In *Proceedings 26th International Symposium on Shock Waves* (edited by K Hannemann and F Seiler), Göttingen, Germany, ISBN 978-3-540-85180-6, 1377-1382, 2007.

4. Naidoo K, Skews BW. High-speed imaging of dynamic shock wave reflection phenomena. In *Proceedings 28th International Congress on High-speed Imaging and Photonics* (edited by H Kleine and M P B Guillen), Canberra, Australia, ISBN 9780819473608, Paper 71260E, 2008.

5. Naidoo K, Skews BW. Experimental investigation of dynamic shock wave reflection phenomena. In *Proceedings 27th International Symposium on Shock Waves*, St. Petersburg, Russia, 289-294, 2009.

6. Naidoo K, Skews BW. High-speed imaging of dynamic shock wave reflection phenomena. In *Proceedings 29th International Congress on High-speed Imaging and Photonics* (edited by E Sato, T G Etoh, K Nagayama, H Shiraga, T Saito, N Yokoyama, S Suzuki, T Aoki), Morioka, Japan, ISBN 978-4-905149-01-9, Paper C03, 2010.

Chapter 1

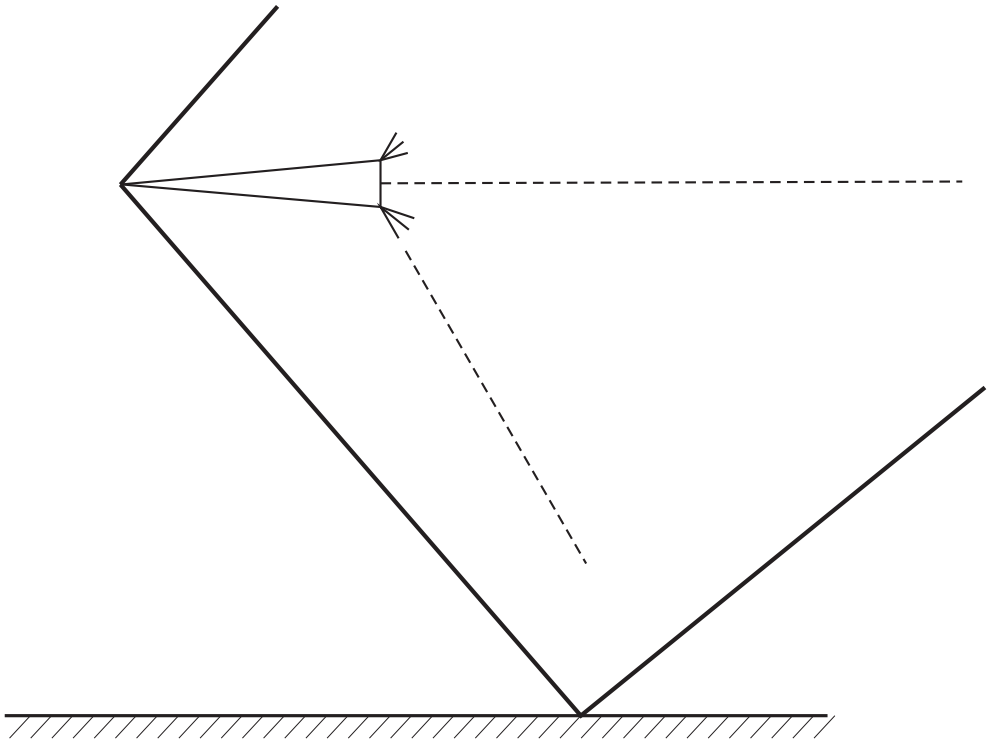
Introduction

1.1 Background

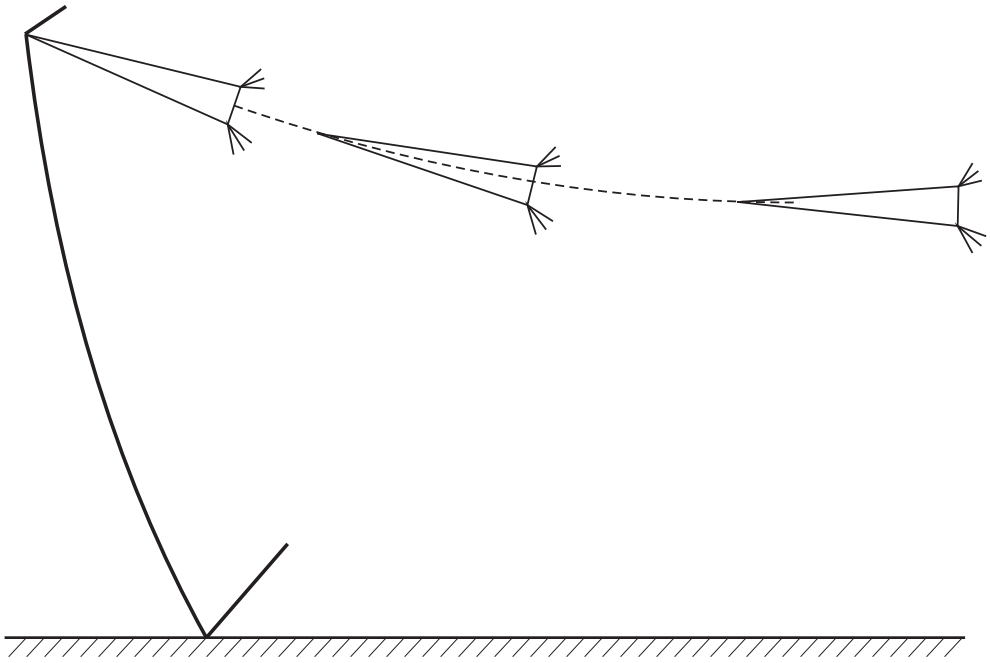
Consider the shock wave system generated by a flight vehicle in steady, level supersonic flight as illustrated in figure 1.1. The regular and Mach reflection possible on the ground plane as well as the transition conditions between idealised versions of these two configurations (figure 1.2) has been researched since the early work of Ernst Mach in 1878. The primary interest in the last 30 years has been the establishment of the steady state transition criteria between regular and Mach reflection in the strong-reflection range, i.e. free stream Mach number, $M \geq 2.202$, for air with a ratio of specific heats, $\gamma = 1.4$. To date there has been little published research that is relevant to the dynamic development of the reflection pattern as the flight vehicle increases its pitch orientation rapidly.

1.2 Ideal, Steady, Two-Dimensional Shock Wave Reflection Transition

Typically, steady shock wave reflection research has considered the shock wave pattern in the reference frame of a simplified wedge for the purpose of fundamental analysis and experiment. Since the gas medium ahead of the reflection pattern has no velocity relative to the ground plane in reality, there is no boundary layer ahead of the reflection point. Therefore, in the reference frame of the wedge, the ground plane is approximated by an idealised, frictionless surface. For the range of positive incidence of the wedge for which the incident shock wave is attached to the wedge leading edge, there are two possible reflection patterns, viz. a two-shock system or regular reflection (figure 1.2(a)) and a three-shock system or Mach reflection (figure 1.2(b)). In the case of a regular reflection (RR), the incident wave, "i", deflects the free stream flow towards the reflection plane and the reflected wave, "r", returns the flow parallel to the reflection plane. In

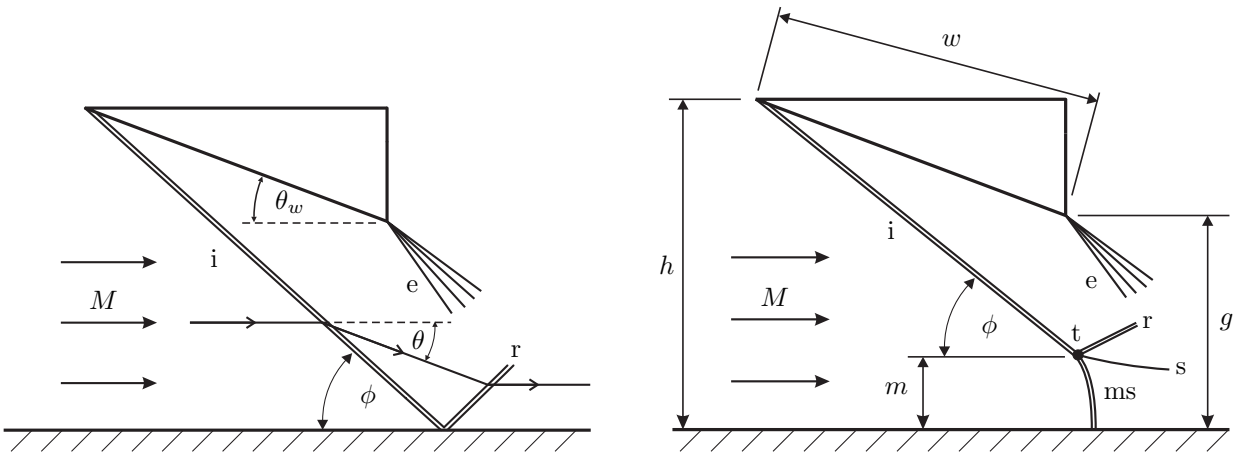


(a)



(b)

Figure 1.1: Simplified schematic of (a) steady shock wave reflection with the flight vehicle in steady, level flight and (b) dynamic shock wave reflection when the vehicle increases its pitch orientation rapidly



(a) Regular reflection

(b) Mach reflection

Figure 1.2: Simplified schematics of regular and Mach reflection generated by a wedge in a steady supersonic free stream

the case of Mach reflection (MR), the incident wave, reflected wave, Mach stem, "ms", and the shear layer, "s" meet away from the reflection plane at the triple point, "t". Figure 1.2 also includes definitions for the flow deflection angle, θ, wedge incidence, θ_w, shock incidence, ϕ, Mach stem height, m, wedge chord, w, as well as the leading and trailing edge separation from the reflection plane, g and h.

Steady state transition criteria between RR and MR generated by a wedge of infinite span in an ideal, steady supersonic flow are derived by taking into account local flow conditions at the reflection/triple point only and were published by Ben-Dor [3]. As the wedge incidence is increased gradually from an initial, steady RR, such that the reflection pattern approximates steady state at each point in time, there is a critical incidence beyond which transition to MR occurs. As the wedge incidence is decreased gradually from an initial, steady MR, such that the reflection is approximately steady at each instant, there is a critical incidence below which transition to RR occurs.

For $M \geq 2.202$, steady RR $\rightarrow$ MR transition is predicted at the sonic/detachment condition and the reverse transition occurs at the von Neumann condition (see Ben-Dor [3]). This incidence-induced hysteresis phenomenon was confirmed experimentally by Ivanov et al. [22] and by various researchers with numerical simulation (for example Ben-Dor [2]). In the weak-reflection range, below $M = 2.202$, there is no von Neumann condition and transition occurs at the sonic/detachment condition in both directions. The difference between the sonic and detachment conditions is very small and is usually neglected in practice. The theoretical, transition criteria were derived specifically for ideal, steady flows and are invalid for the dynamic case of interest.

1.3 Problem Statement

There have been many experimental, numerical and analytical studies on various aspects of steady, two and three-dimensional shock wave reflections. But, there has been little published research to consider the effect of rapid wedge rotation on transition and the dynamic development of the wave pattern. There are a handful of publications that consider dynamic phenomena on shock wave reflections in steady flows. However, most of these focus on the prediction and observation of the incidence-induced hysteresis phenomenon in the steady case for $M \geq 2.202$.

The theoretical, transition criteria were derived specifically for steady flows and are invalid for the dynamic case of interest. Felthun & Skews [12] simulated a rapidly rotating, two-dimensional wedge in a $M = 3.0$ free stream with an Euler CFD code and predicted significant deviation from the steady state, theoretical, transition criteria. Curvature was observed on the incident wave as illustrated in figure 1.3.

The incident shock wave incidence, ϕ, at the reflection/triple point at transition was compared to the steady transition criteria and they predicted RR $\rightarrow$ MR transition beyond the steady detachment condition and MR $\rightarrow$ RR transition below the steady von Neumann condition. To date there has been no published experiment that has explored this finding. The only relevant, published dynamic experiment was conducted by Mouton & Hornung [36]. They demonstrated with a single, rapidly rotating wedge in a $M = 4.0$ free stream (asymmetric double wedge arrangement) the persistence of RR further into the dual solution domain with increasing wedge rotation speed. However, RR was not observed up to or beyond the steady detachment condition.

An experimental and computational investigation of the dynamic flow field generated by a rapidly rotating wedge, with particular attention to two-dimensional RR $\leftrightarrow$ MR transition and Mach stem development in the strong and weak-reflection ranges is proposed. Definitions for the strong and weak-reflection ranges are presented in Chapter 2.

For the sake of clarity, when the incident shock is curved in the dynamic case, ϕ will refer to the shock incidence angle at the reflection point as indicated in figure 1.3. The wedge and shock incidence at transition are labelled θ_{WT} and ϕ_T respectively. A dimensionless parameter, M_E, is defined to quantify the wedge rotation speed in terms of the free stream acoustic speed, viz. $M_E = V_E/a_\infty$, where V_E is the wedge edge speed of the leading or trailing edge, depending on the rotation centre, and a_∞ is the free stream acoustic speed. A simple convention for the sign of V_E is used to indicate the direction of wedge incidence change, viz. $V_E > 0$ for increasing wedge incidence and $V_E < 0$ for decreasing wedge incidence. This results in $M_E > 0$ for increasing wedge incidence and $M_E < 0$ for decreasing wedge incidence. With respect to the experiment, the reflection pattern in the streamwise vertical plane of symmetry is of primary interest. All measurements

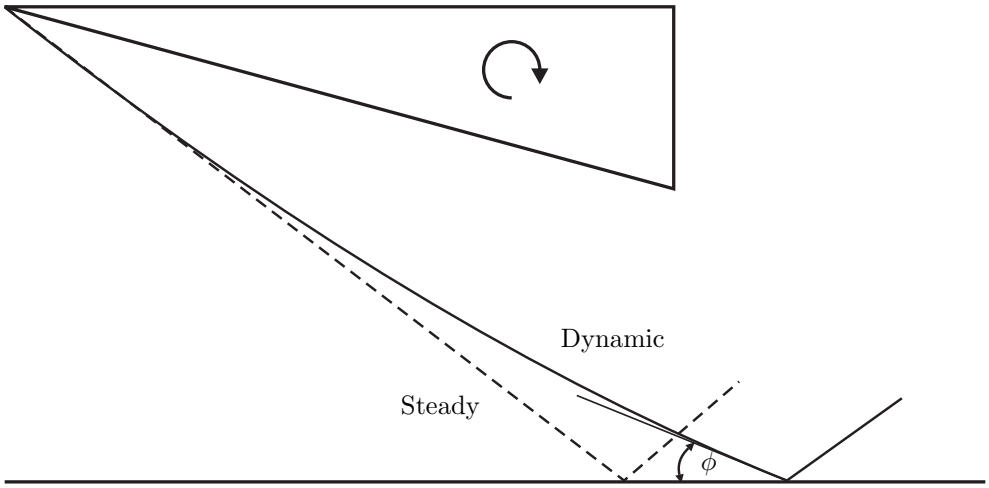


Figure 1.3: Typical curvature observed in flow computations by Felthun & Skews [12] for rapid increasing wedge incidence

are made on this vertical symmetry plane and all results will refer to the measurements made in this plane unless otherwise stated.

1.4 Objectives

The broad objectives of this study are as follows:

- To develop an experimental facility and appropriate computational models for the investigation of two-dimensional, dynamic shock wave reflection generated by a rapidly rotating wedge in the strong and weak-reflection ranges
- To measure and compute the dynamic effect of rapid wedge rotation on transition between two-dimensional regular and Mach reflection of shock waves in an ideal, steady, supersonic free stream.
- To explore the dynamic RR $\leftrightarrow$ MR transition mechanism to identify transition criteria for the rapidly rotating wedge
- To explore the effect of other critical variables in the relevant parameter space with the aid of computational modelling

More detail on these objectives are presented after the theory and literature review in chapter 2.

1.5 Chapter Overviews

Chapter 2 presents the current theory for ideal, steady, two-dimensional shock wave reflection. Steady RR $\leftrightarrow$ MR transition criteria are derived with pressure-deflection shock polars in the weak and strong-reflection ranges. Chapter 2 also summarises the few publications relevant to dynamic effects on shock wave reflection in steady supersonic flows. The research gaps are identified and more detail is provided on the objectives listed above.

Chapter 3 describes the experimental setup. The method of measurement for the tunnel flow conditions is presented. The optical measurement technique and calibration of the schlieren system for accurate shock incidence and Mach stem height measurement are discussed. The design, development and operation of the experimental test rig are discussed in some detail. Data reduction from sample measurements are included.

Chapter 4 documents details of the computational model. It also includes a brief description of the CFD codes used and results of a grid sensitivity study.

Chapter 5 presents results from steady state experiments and two-dimensional computations in the strong and weak-reflection ranges. The transition point between RR and MR in a wind tunnel, in the strong-reflection range, is facility dependent as documented by Ben-Dor [4] and Ivanov et al. [22] and had to be determined for the CSIR tunnel. Transition and Mach stem height measurements for the steady state, baseline experiments are compared to theory and CFD calculations.

Chapter 6 documents measurements and simulation results for the investigation of dynamic RR $\rightarrow$ MR transition in the strong and weak-reflection ranges. Comparisons are made with steady state, baseline measurements. This chapter includes results of computations applied to scenarios beyond the capability of the existing experimental setup to explore the effect of other dependent variables in the parameter space. It also investigates the mechanism for dynamic RR $\rightarrow$ MR transition.

Chapter 7 documents measurements and simulation results for the investigation of dynamic MR $\rightarrow$ RR transition in the strong-reflection range for the purpose of code validation. The code is applied to scenarios beyond the capability of the existing experimental setup to explore the effect of other dependent variables in the parameter space. Some ideas on three-dimensional effects are presented.

Chapter 8 summarises the significant findings and makes recommendations for future work.

Chapter 2

Literature Survey

2.1 Introduction

This chapter reviews the relevant steady state theory and literature relevant to the dynamic shock wave reflection phenomena generated by a rapidly rotating wedge. Critical pressure-deflection shock polars are considered briefly to establish the steady state transition criteria for the ideal, steady, two-dimensional case. The source of the earliest known requirement for the rapid wedge rotation case is traced back to steady state experimental work started more than 30 years ago. The literature relevant to the rapidly rotating wedge is summarised, though spread over a few publications. Most of the research relevant to the dynamic case of interest was directed to the investigation of the well known incidence-induced hysteresis problem in the strong-reflection region. The research gaps and opportunities are identified and motivated. Research findings for consideration in the design of experiment and the computational method will be presented in chapters 3 and 4.

2.2 Steady, Two-Dimensional, Theory

Currently there is no unsteady theory for the dynamic case of interest. However, the steady theory may be used to assist in the interpretation of the dynamic flow field. For the range of wedge incidence, θ_w, for which the incident wave is attached to the wedge, there are two possible reflection configurations, viz. the RR shown in figure 2.1 and the MR in figure 2.2.

The two and three-shock theory of von Neumann (see Ben-Dor [3]) may be used to calculate the flow states in the vicinity of the reflection point of a RR and in the vicinity of the triple point of a MR. The theory is based on the following simplifying assumptions:

- steady flow

- the discontinuities at the reflection/triple point are straight
- the flow obeys the equation of state
- the flow is inviscid
- the flow is thermally nonconductive
- the contact discontinuity at the triple point is infinitely thin

At the reflection point, "R", of the idealised RR shown in figure 2.1, the free stream flow in region 1 is deflected θ_2 towards the reflection surface by the incident wave, "i", and the reflected wave, "r", returns the flow parallel to the reflection surface by deflecting the flow downstream of the reflected wave θ_3 away from the reflection surface. There is a zero net flow deflection at the reflection point, i.e.

$$\theta_2 - \theta_3 = 0 \tag{2.1}$$

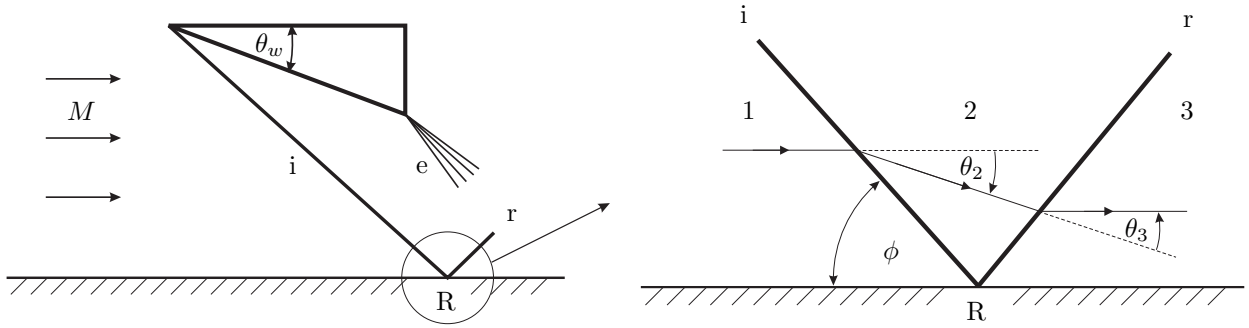
The idealised MR in figure 2.2 consists of an incident wave, "i", a reflected wave, "r", a Mach stem, "ms", and a contact surface or slipstream, "s". The point of confluence of the three shocks is the triple point, "t". The contact surface arises where the flow downstream of the reflected wave and the Mach stem meet, i.e. where regions 3 and 4 meet. The flow on either side of the shear layer at the triple point has the same direction. Therefore, at the triple point of the MR:

$$\theta_4 = \theta_2 - \theta_3 \tag{2.2}$$

The trailing edge expansion introduces a curvature on the reflected wave and the contact surface. The curvature on the shear layer generates a converging nozzle in which the flow, bounded by the Mach stem and shear layer, accelerates from subsonic to sonic at the minimum nozzle area (see Hornung & Robinson [19]).

As the wedge incidence is increased gradually from an initial, steady RR, such that the reflection pattern approximates steady state at each point in time, there is a critical incidence beyond which transition to MR occurs. As the wedge incidence is decreased gradually from an initial, steady MR, such that the reflection is approximately steady at each instant, there is a critical incidence below which transition to RR occurs. Steady state transition criteria between RR and MR for a steady wedge of infinite span in a steady supersonic flow are derived by taking into account local flow conditions at the reflection/triple point only. Ben-Dor [3] includes a detailed treatment of the analytical, two and three-shock theory presented by von Neumann [44].

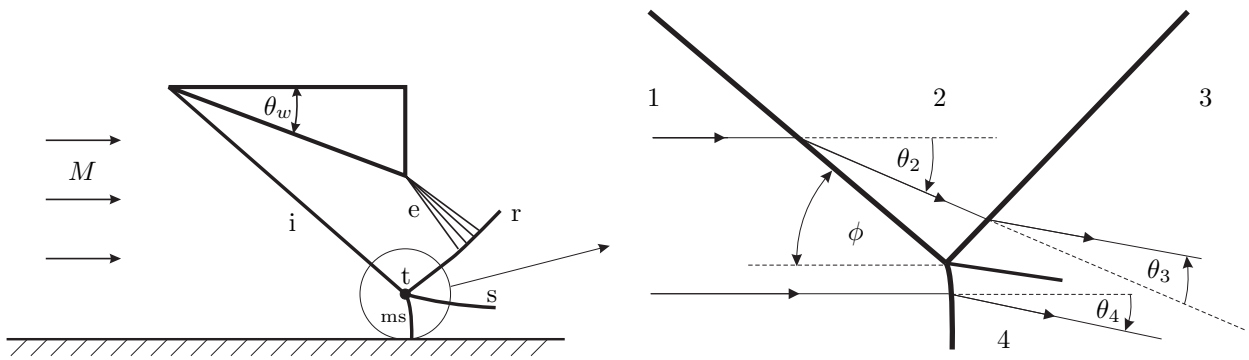
Pressure-deflection shock polars are a convenient, effective, graphical means of representing the analytical solution for ideal, steady, two-dimensional RR and MR. They are presented here to illustrate the derivation



(a) Schematic of RR

(b) Flow in the vicinity of the reflection point

Figure 2.1: Simplified schematic of idealised regular reflection and flow conditions in the vicinity of the reflection point



(a) Schematic of MR

(b) Flow in the vicinity of the triple point

Figure 2.2: Simplified schematic of idealised Mach reflection and flow conditions in the vicinity of the triple point

of the steady RR $\leftrightarrow$ MR transition criteria. Ben-Dor [3] and Chapman [5] may be consulted for more detail on pressure-deflection shock polars. Sample pressure-deflection shock polars for a $M = 3.0$ free stream are presented for illustrative purposes. The polar in figure 2.3 represents the static pressure rise, P/P_∞, that can be achieved through an incident oblique shock wave at $M = 3.0$ for a range of flow deflections, θ. P_∞ is the free stream static pressure and P is the static pressure downstream of the incident wave. In the ideal case, the incident wave deflects the flow parallel to the wedge surface and θ equals θ_w. The flow deflection at point "M" is the maximum deflection possible by an oblique wave at $M = 3.0$. For larger values of θ, the oblique wave is detached. The largest pressure rise possible through an oblique wave is at zero flow deflection, corresponding to the normal shock solution, i.e. the intersection of the incident polar with the vertical axis at point "N". The sonic point on the polar, labelled "S", separates the polar into supersonic and subsonic segments where the downstream flow is supersonic or subsonic respectively ("O" to "S" : supersonic segment; "N" to "S" : subsonic segment). For smaller values of flow deflection, there are two solutions for

each value of θ and the downstream flow can be either subsonic or supersonic. Usually, in practice, the downstream flow is supersonic as in the case of interest here and the segment of the polar between "S" and "O" is applicable.

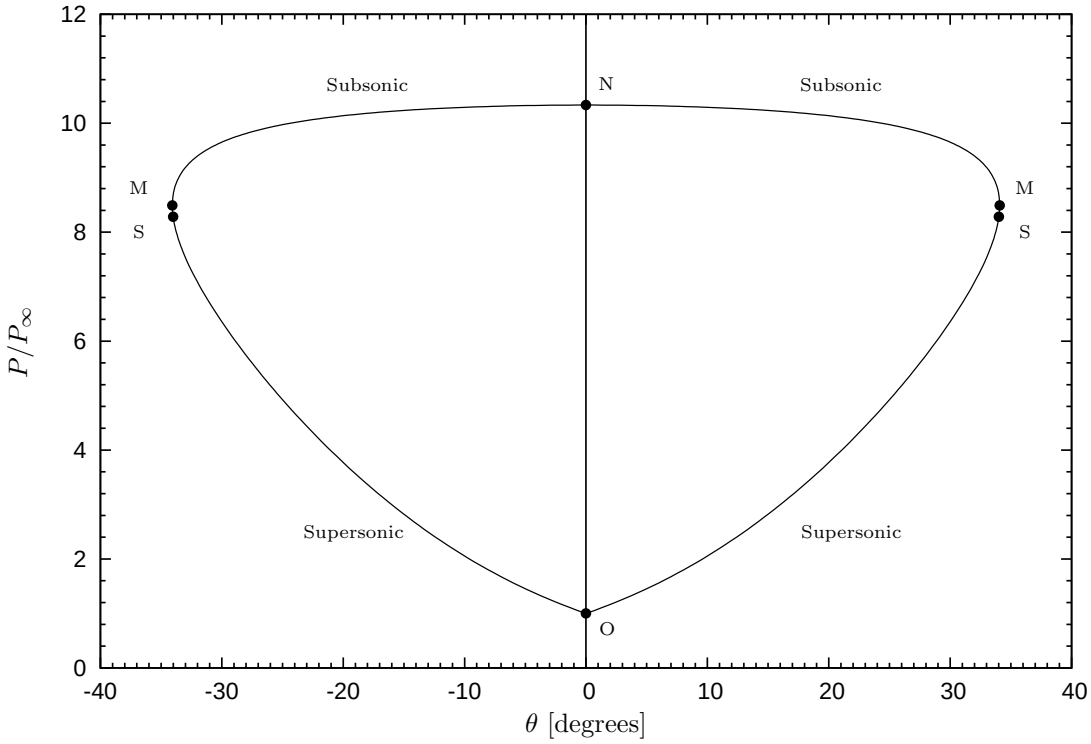
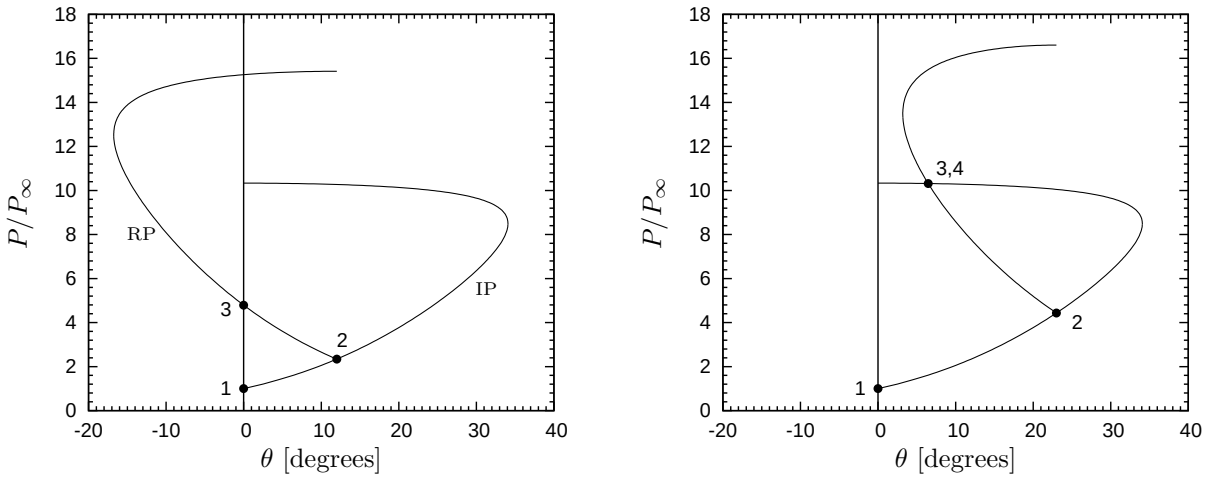


Figure 2.3: Locus of flow conditions that can be achieved through an oblique shock wave in a $M = 3.0$ free stream

The flow conditions downstream of the reflection/triple point are determined by superimposing pressure-deflection polars for the incident and reflected waves. Figure 2.4(a) includes the polar for the incident wave, "IP", and the polar for the reflected wave, "RP", corresponding to a RR at $\theta_w = 12.0°$ at $M = 3.0$. Only half of the incident and reflected polars are shown for the analysis of a single wedge. Since the incident wave turns the incident flow parallel to the wedge surface ($\theta = \theta_w = \theta_2$), the wedge incidence determines the location of the origin of the reflected polar with respect to the incident polar.

State 3 of the RR is given by the intersection of "RP" with the *y-axis*, since there is a zero net flow deflection in region 3. State 3 is a weak solution for the reflected wave and the downstream flow is supersonic. The strong solution for the reflected wave, where the reflected polar intersects the *y-axis* on the subsonic segment of the polar, though theoretically possible, is not stable as was demonstrated by Hornung [17].

Figure 2.4(b) includes the incident and reflected polars corresponding to a MR at $\theta_w = 23.0°$ at $M = 3.0$. Flow states 3 and 4 of the MR are given by the intersection of the reflected polar with the incident polar.



(a) Regular reflection at $\theta = 12.0°$

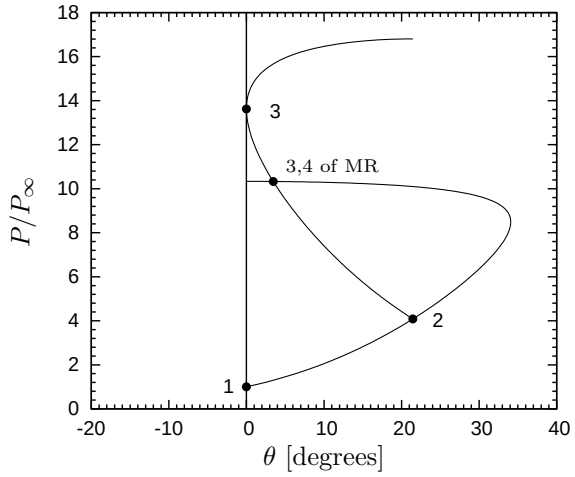
(b) Mach reflection at $\theta = 23.0°$

Figure 2.4: Sample pressure-deflection polars for regular and Mach reflection at $M = 3.0$

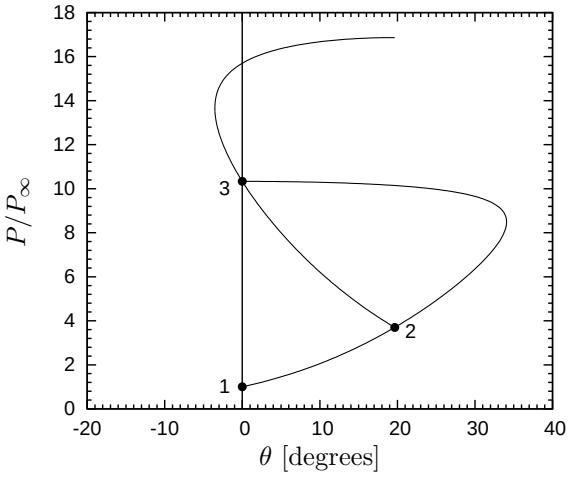
RR is theoretically possible as long as the reflected polar intersects the *y-axis*. There is a maximum flow deflection, $\theta = \theta_D$, beyond which RR is not possible, i.e. the detachment condition shown in figure 2.5(a). At the detachment condition, the maximum deflection point on the reflected polar is tangent to the *y-axis*. Beyond $\theta = \theta_D$ the reflected wave of a RR can no longer satisfy equation 2.1 and only MR is possible, i.e. the reflected wave is not able to return the flow in region 3 parallel to the reflection plane. The smallest flow deflection at which MR is theoretically possible is $\theta = \theta_N$, corresponding to the steady von Neumann condition shown in figure 2.5(b). At the von Neumann condition, the reflected polar intersects the *y-axis* at the normal shock solution of the incident polar. MR is not possible for $\theta < \theta_N$. In air, with gamma = 1.4, there is no von Neumann condition below $M = 2.202$.

In summary, for $M > 2.202$, both RR and MR are possible for $\theta_N < \theta < \theta_D$, also termed the dual solution domain. Figure 2.6(a) includes a sample polar in the dual solution domain. The intersection of the reflected polar with the *y-axis* is the solution for the flow state in region 3 of the RR. The indicated MR solution for the flow in regions 3 and 4, downstream of the reflected wave and Mach stem respectively, is given by the intersection of the reflected polar with the incident polar (also applicable to figures 2.5(a) and 2.6(b)). The difference between the von Neumann and detachment conditions increases with free stream Mach number as shown in figure 2.8, plotted in terms of ϕ.

The detachment condition also happens to be very close to the sonic condition shown in figure 2.6(b). At the sonic condition, corresponding to θ_S, the flow downstream of the reflection point of a RR is sonic. For $\theta < \theta_S$ the flow downstream of the reflection point of a RR is supersonic.

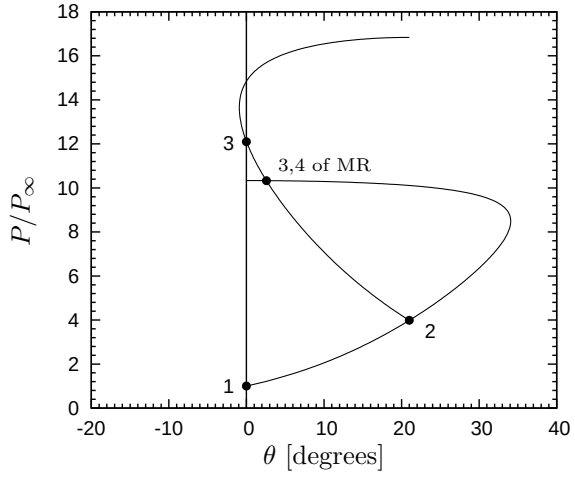


(a) Detachment condition at $\theta = \theta_D = 21.5°$

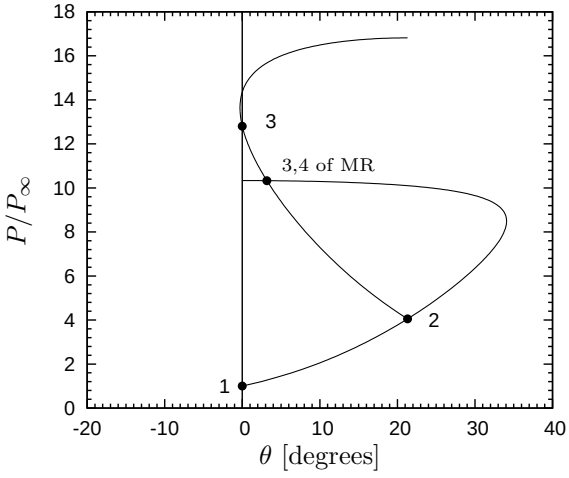


(b) von Neumann condition at $\theta = \theta_N = 19.7°$

Figure 2.5: Pressure-deflection at the detachment and von Neumann conditions at $M = 3.0$



(a) Sample polar in the dual solution domain at $\theta = 21.0°$



(b) Sonic condition at $\theta = \theta_S = 21.3°$

Figure 2.6: Pressure-deflection polars in the dual solution domain and at the sonic condition at $M = 3.0$

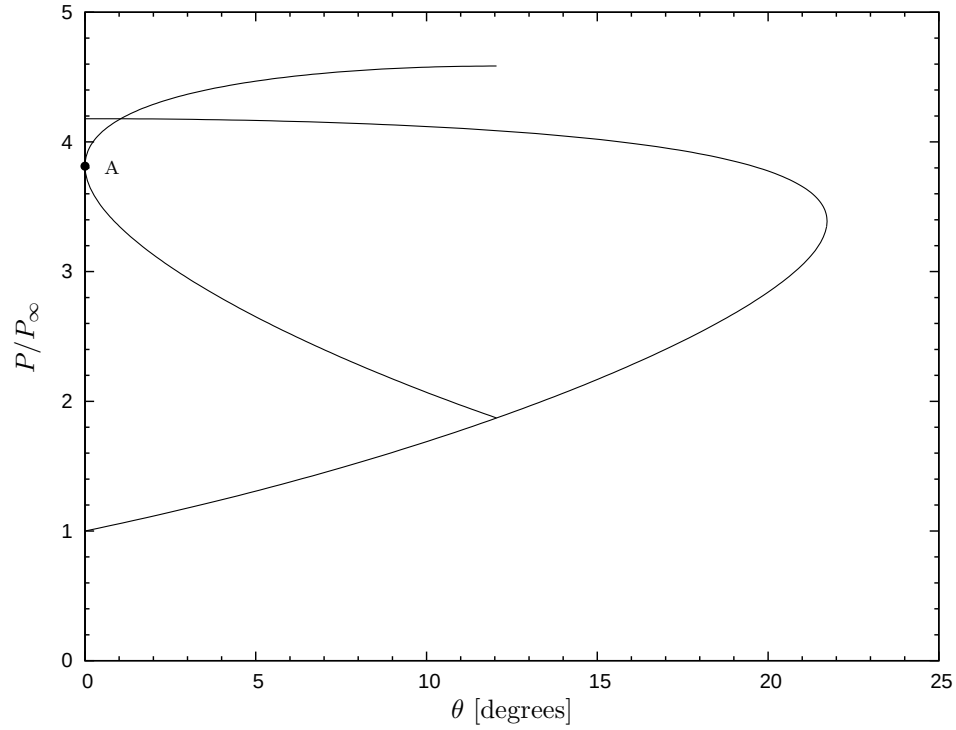


Figure 2.7: Pressure-deflection shock polar for a reflection at the detachment condition at $M = 1.93$

2.3 Ideal, Steady, Two-dimensional RR $\leftrightarrow$ MR Transition Criteria

In air, with $\gamma = 1.4$, there is no von Neumann condition below $M = 2.202$. A sample reflected polar corresponding to the detachment condition at $M = 1.93$ is shown in figure 2.7. Hornung [16] defines "weak" and "strong" reflections in terms of the location of the maximum deflection point on the reflected polar at the detachment condition with respect to the normal shock solution on the incident polar. For example, in figure 2.7, the detachment point "A", lies below the normal shock solution on the incident polar and the reflection is termed a weak reflection. In contrast, at $M = 3.0$, the detachment point "3" in figure 2.5(a) lies above the normal shock solution of the incident wave and the reflection is termed a strong reflection. At $M = 2.202$ the point of maximum flow deflection on the reflected wave at the detachment condition is co-incident with the normal shock solution on the incident polar. Accordingly, $M < 2.202$ is referred to as the weak-reflection range and $M > 2.202$ is referred to as the strong-reflection range.

Perhaps, the significance of whether the reflection is regular or Mach in the dual solution domain is best considered at this point. Consider the polars in figure 2.5. The difference in pressure across the reflection point between the von Neumann condition and the detachment condition is approximately $3.3 \times P_\infty$. This

difference increases to $12.9 \times P_\infty$ at $M = 4.0$. The point of transition is important in determining the maximum pressure rise through the reflection and may be applied to investigations of aircraft sonic boom, supersonic intake design, etc. Azevedo & Liu [1] highlighted the relatively large contribution of the subsonic region behind the Mach stem of a MR to acoustic levels in comparison to the otherwise supersonic flow as applicable to supersonic engine intakes and supersonic vehicle design. Perhaps, this condition could be avoided or at least taken into account with a knowledge of the point of transition.

In an experiment, there is a boundary layer on the wedge surface and θ at the reflection/triple point is no longer equivalent to θ_w. Since flow deflection at the reflection/triple point cannot be measured directly, it is far more practical to refer to shock incidence at the reflection/triple point. The remaining discussion on transition criteria will refer to shock incidence at the reflection/triple point, ϕ, rather than flow deflection, θ. The shock incidence angle at the von Neumann, sonic and detachment conditions are labelled ϕ_N, ϕ_S and ϕ_D respectively.

Ben-Dor [3] may be consulted for a detailed review of the ideal, steady, two-dimensional RR $\leftrightarrow$ MR transition criteria. In the weak-reflection range RR $\leftrightarrow$ MR transition occurs at the sonic (or detachment) condition. In the strong-reflection range, both RR and MR are possible in the dual solution domain and and the shock incidence at transition, ϕ_T, depends on the direction of wedge incidence change.

2.3.1 RR to MR Transition in the Strong-Reflection Range

Both RR and MR are possible in the dual solution domain between the von Neumann and detachment conditions. The smallest shock incidence at which MR is theoretically possible is ϕ_N. The largest shock incidence at which RR is possible is ϕ_D.

Consider an initial, steady RR at an initial wedge incidence, θ_{wi}, with an initial shock incidence, ϕ_i, such that $\phi_i < \phi_N$ (for example figure 2.4(a) at $M = 3.0$). Increasing incidence gradually from this initial incidence, the smallest incidence at which MR is theoretically possible is when $\phi = \phi_N$ at the von Neumann condition. If transition to MR were to occur at this point, there would be a smooth pressure change across the reflection/triple point through the point of transition. For this reason, the von Neumann condition was also termed the mechanical equilibrium condition by Henderson [14].

Since there is a length scale associated with a Mach stem, Hornung et al. [18] proposed that RR $\rightarrow$ MR transition only occurs when conditions change such that the wedge length scale is communicated to the reflection point (through the expansion fan), also referred to as the "information" condition. In the ideal, steady case, the smallest incidence at which a communication path is established between the wedge and the reflection point is when the flow immediately downstream of the reflection point first goes sonic, $M = 1.0$

at ϕ_S, which is beyond the von Neumann condition. Since the flow downstream of the reflection point is supersonic for $\phi < \phi_S$ there can be no communication of the wedge length scale to the reflection point below ϕ_S. Although MR is theoretically possible for $\phi \geq \phi_N$, the RR $\rightarrow$ MR transition criteria for ideal, steady, two-dimensional flows in the strong-reflection region is the sonic condition at ϕ_S.

The sonic condition happens to be very close to the detachment condition, beyond which RR is not possible. It so happens in the ideal, steady case that the earliest incidence at which the length scale is visible to the reflection point is negligibly close to the incidence at which RR is no longer possible. In this case there has been no need to differentiate between the two as they are so close, e.g. at $M = 3.0$, $\phi_S = 39.3°$ and $\phi_D = 39.5°$. For all practical intents and purposes this difference is usually neglected.

In reality, if a disturbance in the free stream is strong enough to set up a temporary MR anywhere in the dual solution domain, the communication path is established and MR would be maintained since it is more stable than RR (see Hornung [17] and Hornung & Sudani [20]).

In the general case, the RR $\rightarrow$ MR transition criteria for steady, two-dimensional flows in the strong-reflection region is the length scale or information condition. In ideal flows this corresponds to the sonic condition. In real flows, it depends on the level of free stream turbulence and RR $\rightarrow$ MR transition could occur anywhere between ϕ_N and ϕ_D.

2.3.2 MR to RR Transition in the Strong-Reflection Range

Consider an initial, steady MR with θ_{wi} such that $\phi_i > \phi_D$ (for example figure 2.4(b)). Decreasing incidence gradually from this initial incidence, the wedge length scale is communicated to the triple point as long as MR is maintained, since the flow downstream of the Mach stem is subsonic. As the wedge incidence is reduced, the Mach stem height decreases and MR is maintained until the von Neumann condition at ϕ_N at which point the Mach stem height reduces to zero and the wedge length scale information disappears at the reflection point.

2.3.3 Summary of Transition Conditions

The steady state, theoretical transition conditions are summarised below.

- RR $\leftrightarrow$ MR transition in the weak-reflection range occurs at $\phi_S \approx \phi_D$
- RR $\rightarrow$ MR transition in the strong-reflection range occurs at $\phi_S \approx \phi_D$ in the ideal case and anywhere between ϕ_N and ϕ_D in the real case, depending on the levels of free stream turbulence
- MR $\rightarrow$ RR transition in the strong-reflection range occurs at ϕ_N

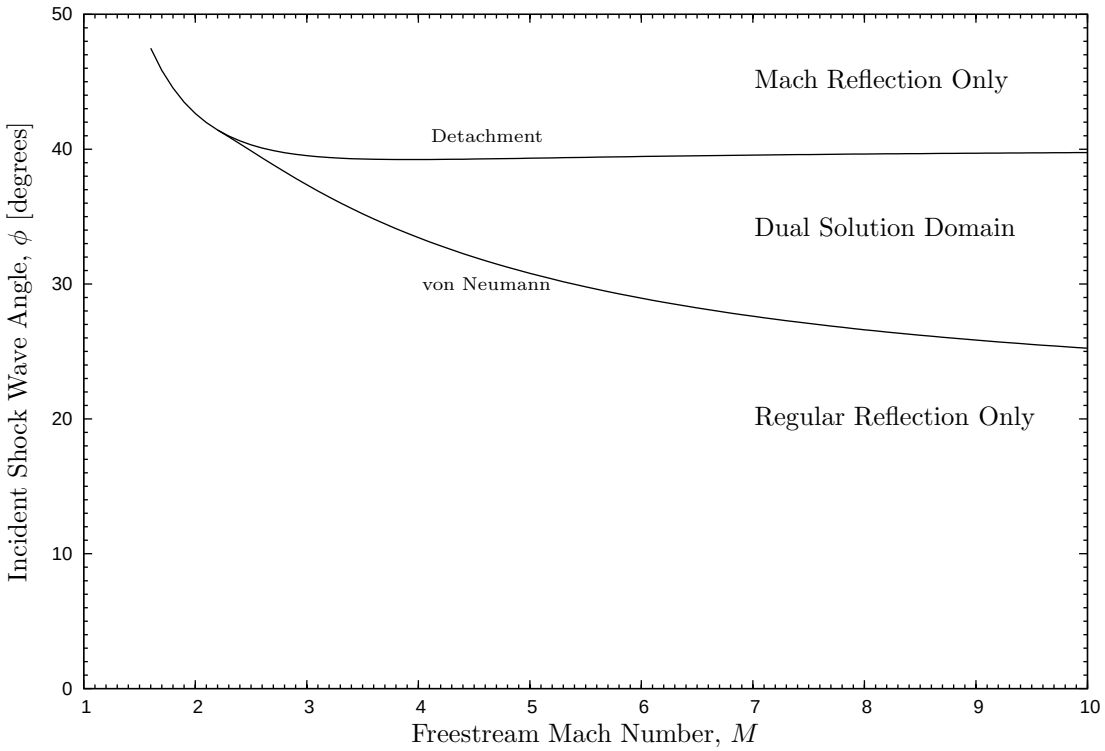


Figure 2.8: Theoretical ϕ_N and ϕ_D between $M = 1.6$ and 10.0 for air with $\gamma = 1.4$

The difference in ϕ_T for increasing and decreasing incidence in the strong-reflection region for the ideal case, is the well known hysteresis loop that was first suggested by Hornung et al. [18]. This was confirmed with numerical solution by various researchers (for example Ben-Dor [2]) and in an experiment in a low-noise supersonic tunnel by Ivanov et al. [22] in 2003.

2.4 The Persistence of Steady RR with a Length Scale Present at the Reflection Point

Li & Ben-Dor [31] proved with analytical means that RR was stable between the von Neumann and sonic conditions, but unstable in the small region between the sonic and detachment conditions. However, as discussed previously the difference between the sonic/length scale condition and detachment for the ideal, steady case is extremely small and it may be difficult to investigate the stability of RR in this region with experiment or computation.

In an experiment the ideal, horizontal reflection plane is set up with a symmetric wedge configuration. If the wedges are arranged asymmetrically, the reflection plane is not horizontal and the flow deflection at the reflection point is not parallel to the flow direction. Li et al. [32] considered various asymmetric

configurations with pressure deflection shock polars and identified a very narrow region in which it was theoretically possible to achieve an overall regular reflection with a weak reflected wave on one of the reflections and a strong reflected wave on the other. An example of such a polar for the overall regular reflection at $M = 4.96$ is shown in figure 2.9 in which $\theta_1 = 35.0°$ and $\theta_2 = 14.58°$, where θ_1 is the wedge incidence of the bottom wedge and θ_2 is the wedge incidence for the top wedge. The reflected polar, "RP_1", corresponds to θ_1, "RP_2" corresponds to θ_2 and the incident polar is annotated "IP". The sonic point on "RP_2" is labelled "S_2" and the detachment point on "RP_1" is labelled "D_1". For the setup shown in figure 2.9, the two possible RR configurations for RP_2 are weak in nature as both potential solutions are below its sonic condition. However, there is a weak and strong solution for RP_1, labelled "RR_{WS}" and "RR_{SS}" respectively. If θ_2 is increased there is a point beyond which there are two strong solutions for RP_1 and two weak solutions for RP_2. The flow does not have a choice except to set up one strong RR and one weak RR. The strong reflected wave would result in subsonic flow that would allow length scale information to be communicated to the reflection point from the leading edge of the trailing edge expansion. This demonstrates that it is theoretically possible to maintain RR in the presence of length scale information.

Khotyanovsky et al. [27] confirmed this with an Euler simulation at $M = 4.96$. They calculated the range for which one weak RR and one strong RR would be set up in an asymmetric arrangement, i.e. $15.595° < \theta_2 < 15.983°$ for $\theta_1 = 35.0°$ (a range of approximately 0.4°). Their simulations with $\theta_2 = 15.98°$ verified that it was indeed possible to set up such an arrangement. The important conclusion is that it is possible under specific conditions for RR to exist in the presence of length scale information.

2.5 MR Configurations in a Steady Supersonic Free Stream

There are texts that can be considered for details on the various Mach reflection configurations possible in steady, pseudo steady and unsteady flows (see Courant & Friedrichs [9] and Ben-Dor [3]). The configurations relevant to this investigation will be discussed briefly. The MR solution for $\phi > \phi_N$ in which the shear layer at the triple point is directed towards the reflection surface is referred to as Direct Mach reflection as shown in figure 2.10(a). In this case the intersection of the reflected and incident polars is at a positive incidence, to the right hand side of the *y-axis*. Stationary MR, in which the shear layer is parallel to the reflection plane at the triple point, is only possible at the von Neumann condition since there is a zero net flow deflection at this condition. An inverse MR shown in figure 2.10(b), has the slipstream directed away from the reflection surface. In this instance the intersection of incident and reflected polars is at a negative incidence. Sudani & Hornung [41] showed that it is possible to achieve a stable inverse MR with a steady wedge in a steady

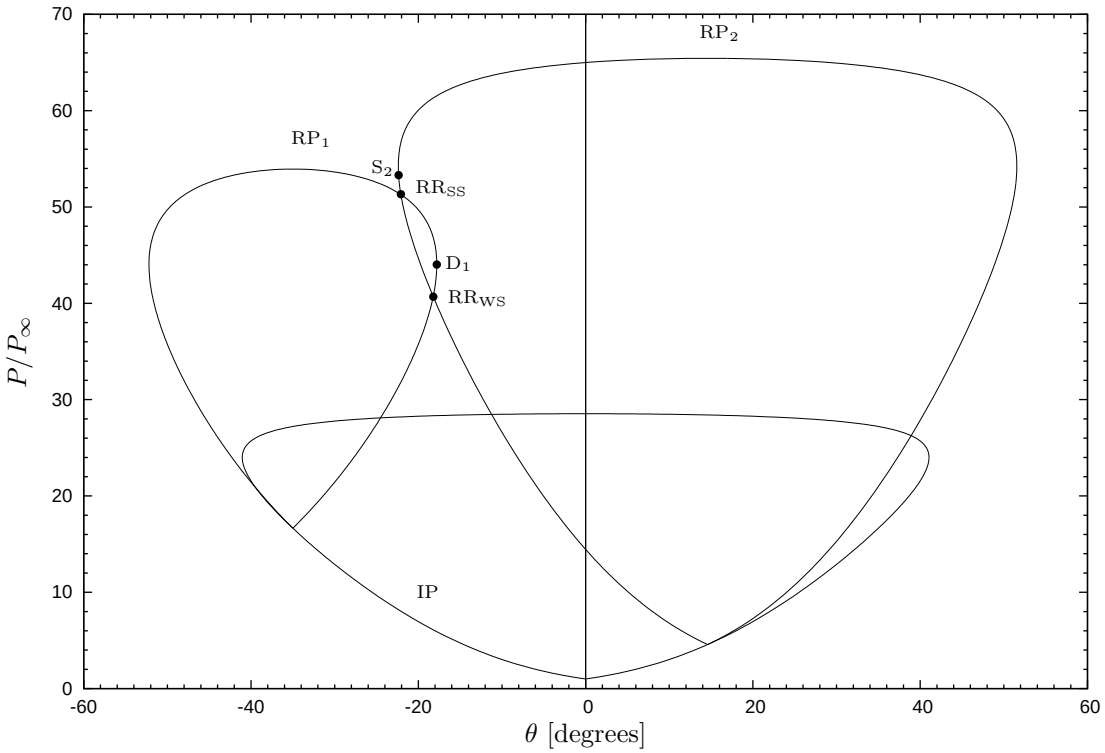
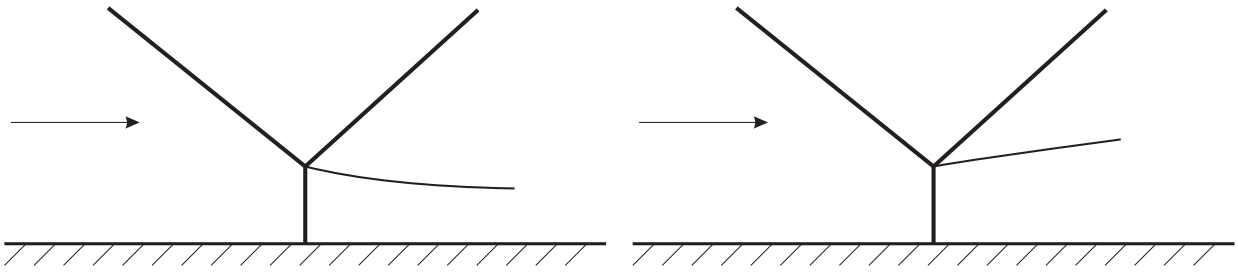


Figure 2.9: Pressure deflection shock polar for the asymmetric case at $M = 4.96$, $\theta_1 = 35.0°$ and $\theta_2 = 14.58°$

supersonic flow by maintaining a permanent deflection in the wall downstream of the reflection point. An inverse MR was also observed in an unsteady case investigated by Felthun & Skews [12] for dynamic MR → RR transition in a steady $M = 3.0$ free stream (see section 2.7).

2.6 Early Origins of Rapid Wedge Rotation

There are a handful of publications that investigate dynamic effects on shock wave reflections in steady flows. Most focus on the prediction and observation of the hysteresis phenomenon for the steady case in the



(a) Direct MR (b) Inverse MR

Figure 2.10: Direct and inverse Mach reflections possible in a steady supersonic free stream

strong-reflection range.

In 1979, Hornung et al. [18] first proposed the length scale transition criterion for RR → MR transition in steady flows, viz. the sonic condition in ideal flows. This hypothesis was supported by results from pseudosteady experiments in a shock tube in which RR → MR transition was observed close to the sonic condition. In their shock tube experiments, an incident planar shock travels through a stationary gas at constant speed over a plane wedge. The flow is termed pseudosteady because the RR that develops as the leading shock passes over the wedge is self-similar in time and the flow in the immediate vicinity of the reflection point in the reference frame of the reflection point is steady.

Henderson & Lozzi [15] also presented data that showed the persistence of RR beyond the von Neumann condition with the diffraction of strong shocks over surfaces in an unsteady flow field. In their shock tube experiments the wedge is concave and the shock incidence decreases as the shock passes over the wedge. In the reference frame of the reflection point the flow is changing with time and is considered unsteady.

These observations in pseudosteady and unsteady flows and the compelling physical arguments of Hornung et al. [18] led them to propose an incidence-induced hysteresis experiment in the dual solution domain for the steady case. It was predicted that RR → MR transition would occur at the sonic or detachment condition and the reverse transition would occur at the von Neumann condition.

In 1982, Hornung & Robinson [19] conducted a set of experiments in which the wedge incidence of a symmetric double wedge configuration, was increased and decreased gradually through the dual solution domain in steady, free stream conditions at $M = 2.84$, 3.49, 3.98 and 4.96. No hysteresis was observed and RR ↔ MR transition was observed repeatedly at the von Neumann condition, irrespective of the direction of incidence change. It was suggested that disturbances in the flow were sufficient to cause early RR → MR transition at the von Neumann condition.

Since 1995, there have been a number of publications on computational prediction and the experimental observation of hysteresis in the dual solution domain. Ben-Dor [3] includes a detailed review and bibliography of milestone publications in this field. Various computations with numerical solution of the Euler and Boltzmann equations supported the feasability of hysteresis (Vuillon et al. [45], Chpoun & Ben-Dor [7], Ivanov et al. [21],[25] and Ben-Dor [2]), due to the absence of free stream perturbations in the simulations. Flow simulations were successful in predicting hysteresis, but there was a failure to observe this phenomenon in an experiment.

Computations were done to determine the effect of free stream density, pressure and velocity perturbations by Ivanov et al. [23], Khotyanovsky et al. [28] and Kudryavtsev et al [30]. Results supported the hypothesis that free stream perturbations present in the experiment, not in the flow computations, would cause early

transition to MR.

In 1997, Hornung [17] suggested that it was possible that RR $\rightarrow$ MR transition would not be influenced by free stream disturbances in the experiment if the wedges were rotated sufficiently rapidly into the dual solution domain. He proposed establishing a steady RR before rotating the wedge rapidly into the dual solution domain, terminating the wedge motion just below the wedge incidence corresponding to detachment. This could prevent information of the wedge length scale from reaching the reflection point until the wedge was well into the dual solution domain. This is the earliest known published requirement for a rapid wedge rotation experiment, though its roots lie in the analysis of the steady problem.

The first experiment to consider this idea was published by Mouton & Hornung [36] in 2008. The experimental rig consisted of two wedges, one of which was actuated by a motor to demonstrate the effect of rapid pitch on transition. Figure 2.11 includes a series of schlieren images capturing the hysteresis phenomena at $M = 4.0$. The total motion was executed in approximately 90 ms. Though the wedge arrangement was asymmetric the transition criteria were recalculated as per the method published by Li et al. [32]. The results presented by Mouton & Hornung [36] in figure 2.12 support the hypothesis made by Hornung [17]. Rapid wedge rotation did indeed delay transition to MR and RR persisted further into the dual solution domain for increasing wedge rotation speeds, but not up to the detachment condition. They quantified wedge rotation speed with t/τ. $\tau = w/u_1$ is the characteristic flow time for the lower wedge, where w is the wedge chord, u_1 is the flow speed behind the incident shock of the lower stationery wedge and t is the time taken to rotate the upper wedge 10° from an initial wedge incidence, $\theta_{\text{wi}} = 20°$.

2.7 Computational Simulation of Wedge Vibration and Impulsive Wedge Rotation

By 1999, various experiments were being conducted in blow-down supersonic tunnels around the world that were attempting to observe the elusive hysteresis phenomena (see Fomin [13]). The failure to observe hysteresis was attributed to tunnel freestream noise. In contrast, continuum and kinetic models were quite successful in modelling the hysteresis phenomena, due to the absence of free stream noise (see Vuillon et al. [45], Chpoun & Ben-Dor [6], Ivanov et al. [21],[25] and Ben-Dor [2]). Experimental confirmation of hysteresis in the dual solution domain was not achieved until much later in 2003 when Ivanov et al. [22] conducted a series of experiments in a low-noise supersonic wind tunnel facility. Transition was observed repeatedly, close to the steady, theoretical conditions for RR $\leftrightarrow$ MR transition.

Prior to this result, the difference between results from steady simulation and experiment motivated

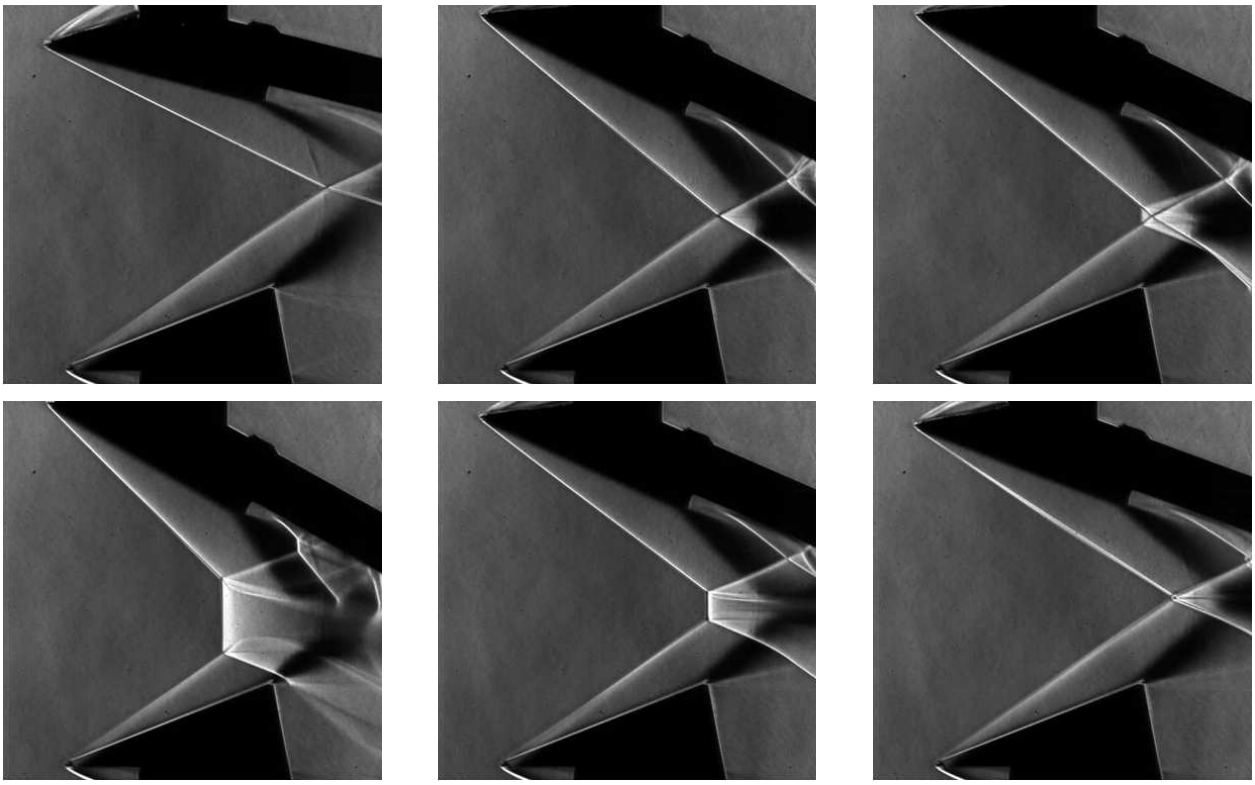


Figure 2.11: A series of schlieren images from the experiment of Mouton & Hornung [36] demonstrating hysteresis in the dual solution domain at $M = 4.0$

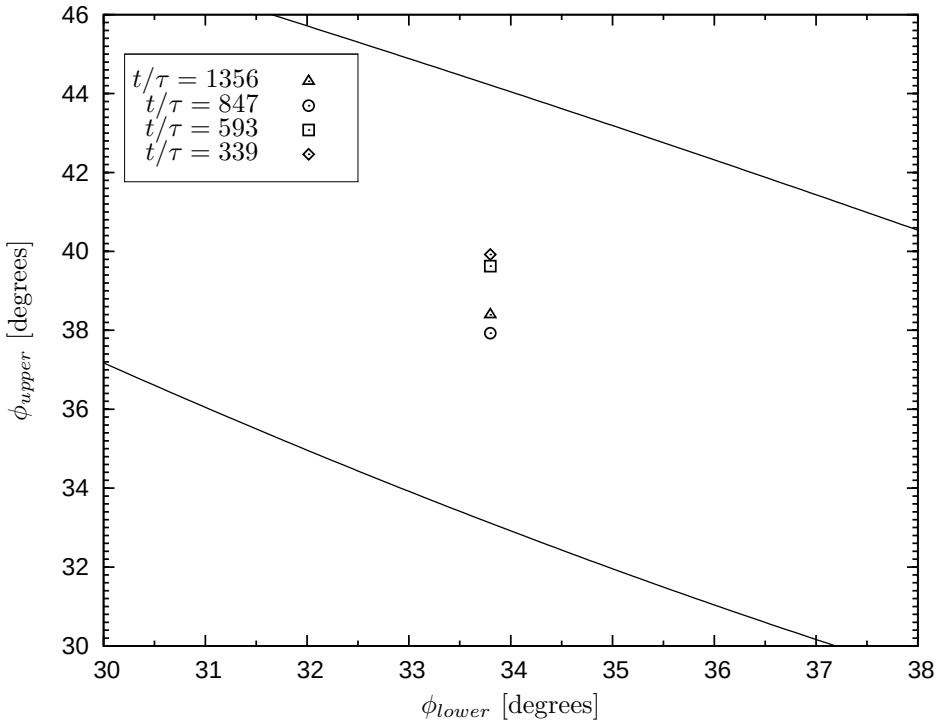


Figure 2.12: Measured transition results from the dynamic experiment by Mouton & Hornung [36]

Markelov et al. [34] to consider the effect of wedge vibration on RR → MR transition with impulsive and periodic wedge oscillations. They simulated a steady initial RR at M 4.96 just below the detachment condition at $\phi = 38.0°$, where $\phi_D = 39.33°$. The wedge was rotated impulsively at $\Omega = 3 \cdot 10^5$ deg/s for 1° about its trailing edge. Dynamic flow features were observed, but none significant enough to cause transition. However, impulsive rotation about the wedge leading edge did generate dynamic effects to the extent that it triggered transition. The impulsive start and stop resulted in an increased shock incidence at the reflection point and a substantial increase in pressure downstream of the reflected wave due to the interaction between the disturbing shock and the reflected wave. This substantial pressure rise was believed to be sufficient to trigger RR → MR transition.

They also simulated the effect of periodic wedge oscillation to determine the minimum wedge rotation speed required to trigger transition for various initial angles. A 1° amplitude oscillation about the wedge leading edge was simulated and this resulted in the periodic formation of compression and expansion waves as shown in figure 2.13. This led to a larger pressure rise downstream of the reflected wave than in the corresponding impulsive rotation case. Consequently, the minimum rotation speed required to trigger transition was lower than in the case of impulsive rotation. For reduced wedge rotation amplitudes, higher rotation speeds were required to trigger transition. The wedge rotation speeds used in the simulations were reported to be in the typical range of vibration frequencies of the test section of a typical blow-down wind tunnel facility during its operation. The results of this study supported the possibility that wedge vibration could be one of the reasons for differences between transition in experiment and simulation.

Concurrently, Khotyanovsky et al. [28] investigated the effect of continuous rapid wedge rotation on the point of transition with Euler CFD on moving meshes. In contrast to the work by Markelov et al. [34], Khotyanovsky et al. [28] considered larger movements of the wedge. Rather than to investigate the dynamic phenomena generated by a rapidly rotating wedge in particular, the objective of the study was to determine the maximum permissable pitch rate that could be used in simulation without introducing dynamic effects. It was an exercise to support the investigation of the steady case. Wedges were rotated about the trailing edge at $M_T = 0.0002, 0.002, 0.01, 0.1$ in a $M = 5.0$ free stream, where $M_T = w\omega/U_\infty$ (w = wedge chord; ω = wedge rotation speed [rad/s]; U_∞=free stream speed). At $M_T = 0.1$ there was significant curvature on the incident wave as illustrated in figure 2.14. Though the shock incidence at the reflection point did not correspond with the steady state shock angle for the same wedge incidence, the shock incidence at RR → MR transition was close to the detachment condition. Shock incidence at the triple point for MR → RR transition was not reported.

While the work of Markelov et al. [34] and Khotyanovsky et al. [28] investigated the effect of rapid wedge

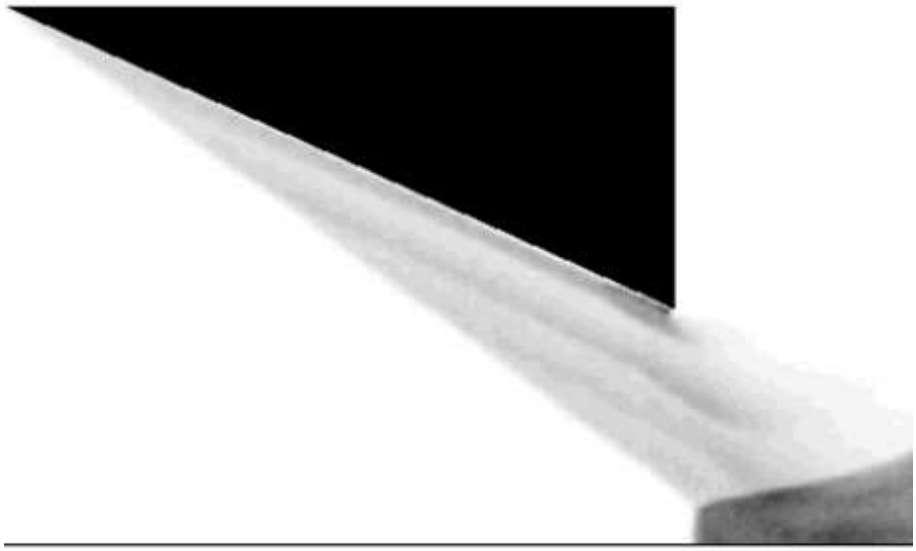


Figure 2.13: Periodic formation of compression and expansion waves generated by wedge oscillation about its leading edge with amplitude = 0.5°; wedge rotation speed, $\Omega = 8 \cdot 10^3$ deg/s published by Markelov et al. [34]

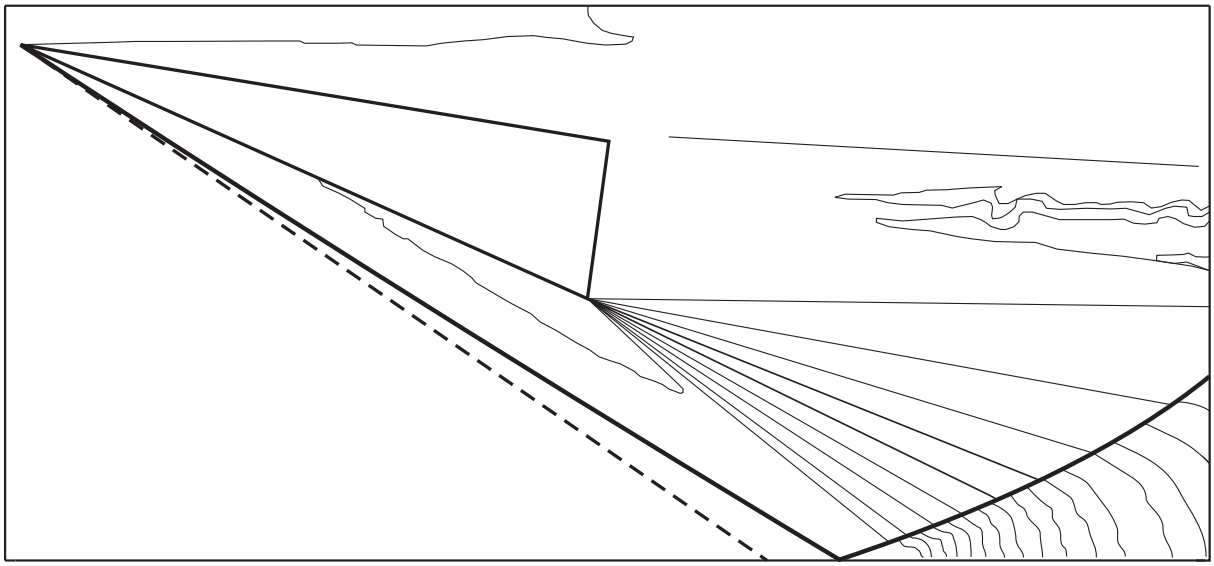


Figure 2.14: Curvature on the incident wave of a RR due to rapid wedge rotation, $M = 5.0$, $g/w = 0.42$ and rotation speed $M_T = 0.1$ at $\theta_w = 24.0°$ [28]

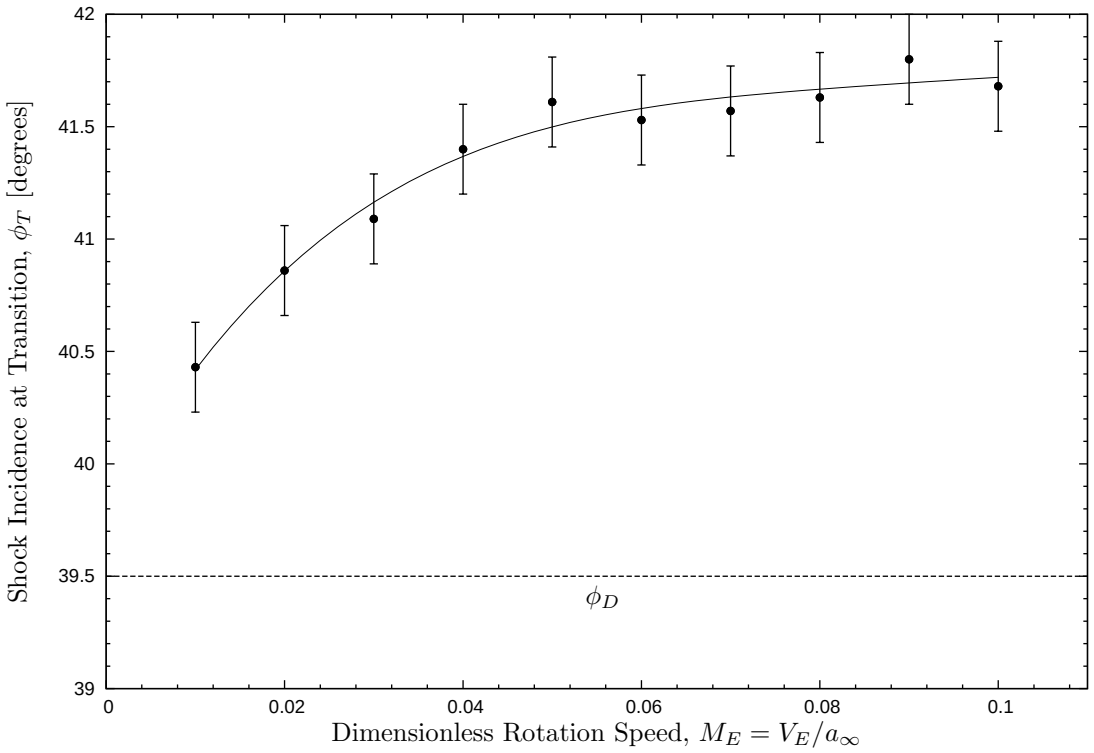


Figure 2.15: Computed effect of rapid wedge rotation on ϕ_T for RR $\rightarrow$ MR transition published by Felthun & Skews [12], $M = 3.0$, $h/w = 0.9$, $\theta_{wi} = 20.0°$

rotation with particular focus on the implications for the steady case, Felthun & Skews [12] specifically investigated the dynamics of the rapidly rotating wedge case. The wedge was rotated impulsively about its leading edge at various rotation speeds for increasing and decreasing incidence at $M = 3.0$ using Euler computations. Resultant trailing edge speeds, V_E, were between 1 and 10 % of the free stream acoustic speed. For increasing incidence, RR $\rightarrow$ MR transition was delayed beyond ϕ_D. Convex curvature was generated on the incident wave and transition was delayed further for increasing rotation speeds as shown in figure 2.15.

Felthun & Skews [12] also investigated the effect of rapid wedge rotation on MR $\rightarrow$ RR transition at a single test point with Euler CFD. A detailed parametric study was not conducted, only the general behaviour of the flow was observed. A steady MR was established at $\theta_{wi} = 23.0°$ at $M = 3.0$. The wedge was started impulsively and rotated at a constant rotation speed with $M_E = -0.05$ until $\theta_w = 16.0°$, by which time transition had not occurred. The evolution of the reflection pattern was observed until transition to MR while the wedge was maintained at $\theta_w = 16.0°$. The rapid rotation resulted in concave curvature on the incident wave and MR $\rightarrow$ RR transition was observed approximately 1.8° below ϕ_N. During the wedge motion, the shear layer was directed away from the reflection surface, indicating an inverse Mach reflection configuration. Due to the wedge impulsive startup, the expansion wave from the wedge surface had the

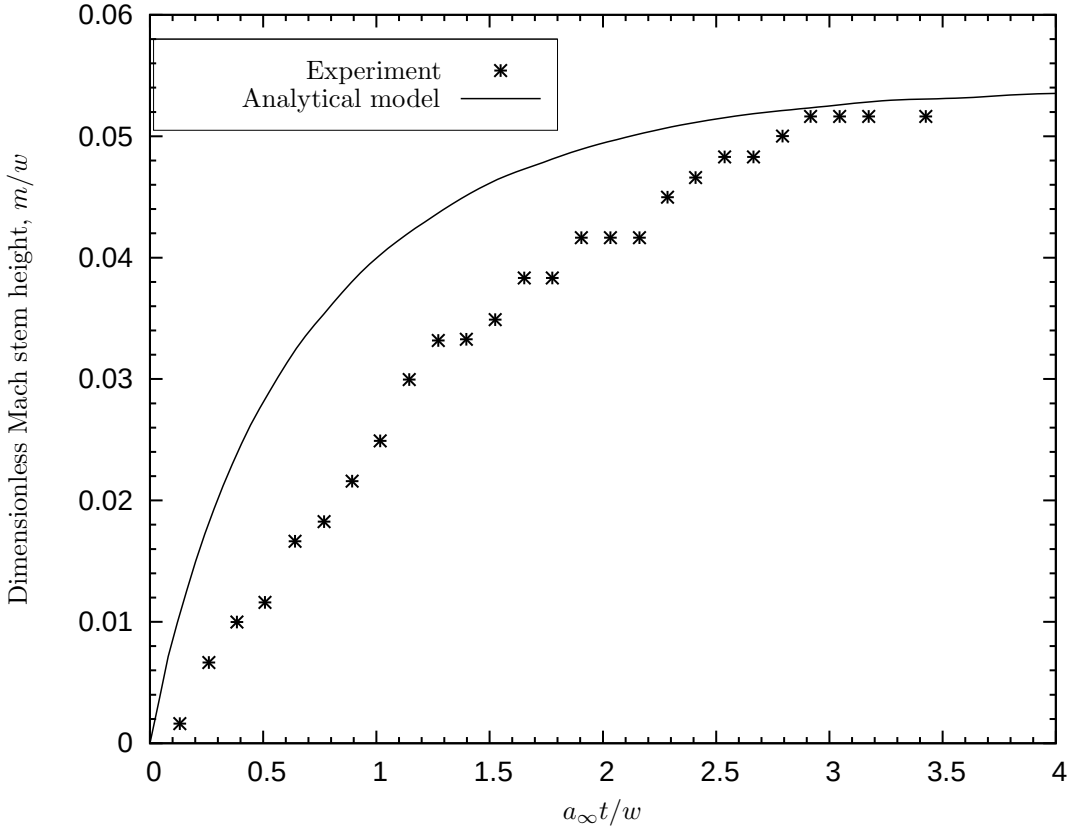


Figure 2.16: Predicted and measured dynamic Mach stem development by Mouton & Hornung [36] at $M = 4.0$, $g/w = 0.3907$, $\theta_w = 23.0°$, $\gamma = 1.4$

initial effect of moving the triple point away from the reflection surface. No Mach stem measurements were made and no experiments were done to verify the computations.

2.8 Dynamic Mach Stem Development for a Stationery Wedge

Though not directly applicable to the continuously rotating wedge, the following work is highlighted as it represents one of the few pieces of research in the field of dynamic shock wave reflection. Mouton & Hornung [36] conducted another experiment in which an initial RR was setup within the dual solution domain. RR → MR transition was subsequently triggered with the deposition of laser energy on the wedge surface and the dynamic Mach stem development was measured and compared to results of a moving triple point analysis published earlier by the same authors [35]. This is the first analytical model for the prediction of time dependent Mach stem growth for a stationary wedge. There was close agreement between the experiment and the analytical solution shown in figure 2.16 at $M = 4.0$, $g/w = 0.3907$, $\theta_w = 23.0°$, $\gamma = 1.4$.

2.9 Research Gap

The following research gaps have been identified and will be investigated in this work. All aspects will be conducted in the strong and weak-reflection ranges unless specified otherwise.

1. An experimental investigation into the effect of a rapidly rotating, symmetric wedge configuration on two-dimensional RR → MR transition in the strong and weak-reflection ranges will be conducted. The effect of rapid rotation on MR → RR transition will also be considered. This requires the development of a novel facility to generate and measure the dynamic phenomena of interest. An Euler CFD code, developed by Felthun [11] at the University of the Witwatersrand, will be used to simulate all experiments. This experiment will potentially address two gaps in the published literature. Both are listed subsequently.

2. The first, is an experimental verification of the dynamic phenomena published by Felthun & Skews [12]. They reported computational results of a rapidly rotating wedge in a steady $M = 3.0$ free stream that showed RR → MR transition beyond the steady detachment condition at ϕ_D and MR → RR transition below the steady von Neumann condition at ϕ_N. To date there has been no experimental confirmation of the predicted dynamic effect.

3. The proposed experiment may also address aspects of the original idea proposed by Hornung [17] in relation to the observation of RR (or lack thereof) in the dual solution domain in a facility where small perturbations are always present. Mouton & Hornung [36] demonstrated with a single, rapidly rotating wedge that it was indeed possible to maintain RR further into the dual solution domain for increasing wedge rotation speeds but RR was not maintained until detachment. If the free stream noise levels in the facility employed are indeed sufficient to prevent hysteresis in the strong-reflection range, is it possible to maintain RR until ϕ_D with a larger wedge rotation speed? How do Euler computations and measurements from experiment compare under these circumstances? On the other hand, if the free-stream noise levels in the facility employed are significantly small such that hysteresis is observed for the steady case, how does rapid wedge rotation effect transition?

4. The mechanism for ideal, two-dimensional, RR ↔ MR transition in the dynamic case with rapid wedge rotation will be investigated and compared to the steady transition criteria, viz. the steady sonic/detachment condition and the mechanical equilibrium/von Neumann condition.

5. Mach stem measurements will be made for the rapidly rotating wedge and compared with two-dimensional computations. These will be considered in view of the difference in trend observed between

the steady, two and three-dimensional result reported by Ivanov et al. [22] (discussed in chapter 4).

6. Computational simulations will be used to investigate the effect of pivot point, wedge rotation speed and initial incidence not considered previously in the strong and weak-reflection regions.

Chapter 3

Experimental Method

3.1 Introduction

The dynamic effect of rapid wedge rotation on the transition between two-dimensional (2D) regular and Mach reflection of shock waves in an ideal, steady, supersonic free stream is of primary interest in this investigation. This is explored with experimental and numerical methods. The numerical method is discussed in chapter 4. Background literature relevant to the experiment is reviewed briefly. This chapter presents details of the experimental setup which includes a rig to generate the dynamic phenomena of interest in the weak and strong-reflection ranges. All experiments were done in the blow-down supersonic wind tunnel at the CSIR. The facility and the measurement of tunnel conditions are discussed. A schlieren flow visualisation system was developed for these experiments and images of the dynamic flow field were recorded with a high-speed digital camera. The optical measurement technique and its calibration are outlined. The rig design, development and operation are described in some detail. Sample experimental data is presented to demonstrate the data reduction process. Uncertainties for all measured quantities are calculated and summarised.

3.2 Background

3.2.1 Simulation of the Ground Plane

In reality, the gas medium ahead of the supersonic flight vehicle is stationary and there is no boundary layer on the ground plane. In an experiment, the ideal, frictionless reflection plane is generated with a double wedge configuration arranged symmetrically about a horizontal plane. This is a widely adopted approach and has been used extensively in the shock wave community (see Hornung & Robinson [19] for example). The symmetric arrangement of the wedges about a horizontal image plane sets up a perfectly rigid, frictionless

and adiabatic wall. This ensures that the reflection point is not contaminated by a boundary layer that would develop on a surface in the tunnel. This implies that the rig must consist of two wedges arranged and actuated symmetrically about a horizontal reflection plane.

3.2.2 Evaluation of Free Stream Turbulence Levels in the Supersonic Facility

Many attempts were made to observe the elusive hysteresis phenomena since the early analytical work by von Neumann [44] and the experimental work by Henderson & Lozzi [15], Hornung et al. [18] and Hornung & Robinson [19]. Since 1995, there have been a number of publications and considerable debate on the computational prediction and observation of hysteresis in the strong-reflection range. Ben-Dor [3] includes a detailed review and bibliography of milestone publications in this field. Since the gas medium ahead of the flight vehicle is stationary, the transition criteria in a free stream without perturbations are correct.

In general, Euler codes are able to model hysteresis due to the absence of free stream perturbations (see Vuillon et al. [45], Chpoun et al. [6], Ivanov et al. [21], [25] and Ben-Dor [2]). Sudani et al. [42] were able to observe both RR and MR in the dual solution domain, though not repeatable, and demonstrated that hysteresis could not be observed with a perturbed free stream flow by introducing water droplets into the free stream. In 2003, Ivanov et al. [22] published the first set of repeatable, experimental data that confirmed the hysteresis phenomena originally proposed by Hornung et al. [18] more than 20 years earlier. The experiment was conducted at $M = 4.0$, with wedges of an aspect ratio of 3.37, in a low noise supersonic tunnel.

All experiments in this work were done in the 450 mm $\times$ 450 mm supersonic wind tunnel at the Council for Scientific and Industrial Research, South Africa. As steady state RR $\rightarrow$ MR transition is dependent on the level of free stream turbulence in the strong-reflection range, the steady transition conditions for the CSIR facility must be determined. This is an indirect measurement of the level of free stream turbulence in the facility. This baseline was used to evaluate the results from the dynamic experiments.

3.2.3 Three-Dimensional Wedge Edge Effects

Skews [40], [39] highlighted the issue of three-dimensional (3D) influences, from the wedge corner signal, on the reflection pattern in the streamwise vertical plane of symmetry. Care must be taken to ensure that the transition angle, ϕ_T, is not influenced by 3D wedge edge effects, by testing with sufficiently large aspect ratio wedges.

Ivanov et al. [24] published 2D and 3D computational and experimental data. The data presented here was estimated from the publication and is shown in figure 3.1. Figure 3.1 shows the close agreement between

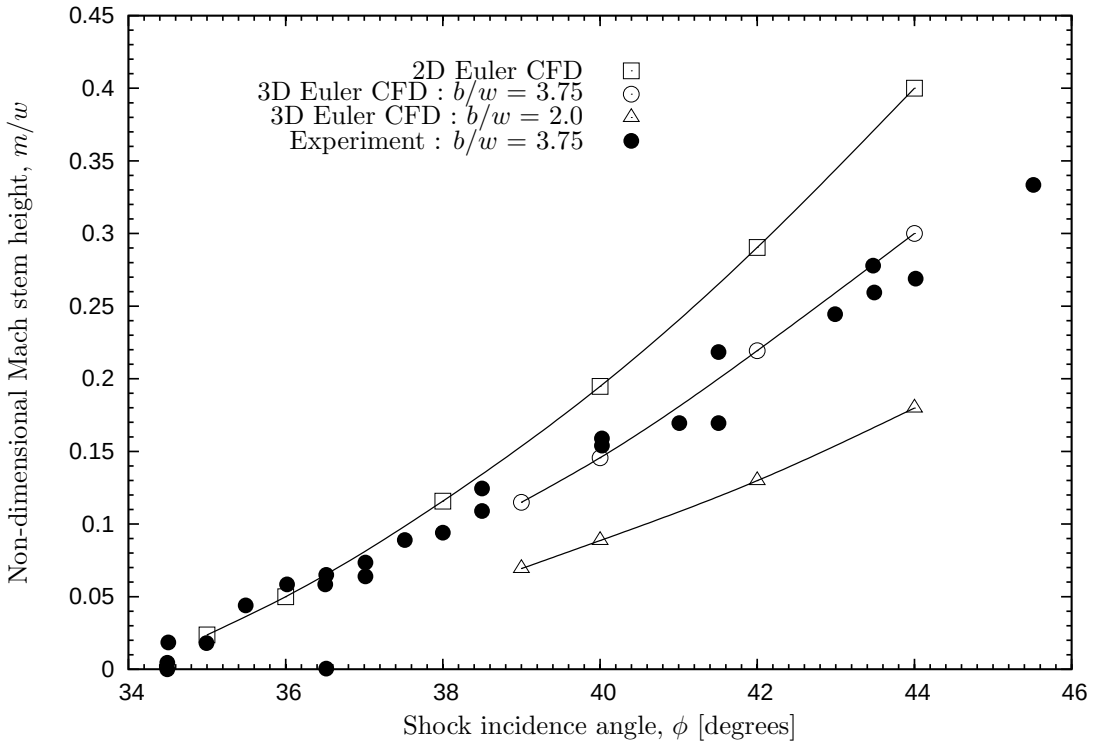


Figure 3.1: Two and three-dimensional Mach stem measurements from experiments and Euler predictions published by Ivanov et al. [24] for a static wedge at $M = 4.0$, $g/w = 0.56$

the 3D Euler CFD predictions of Ivanov et al. [24] and their measurements from experiments with the finite aspect ratio wedge. This agreement established confidence in their 2D Mach stem predictions with Euler CFD. Results show that there are 3D effects on the Mach stem height even for a wedge with an aspect ratio of 3.75. In an experiment, the flow downstream of the Mach stem is subsonic and 3D downstream influences are always present. Though the point of transition for large aspect ratio wedges approaches the theoretical, 2D transition value, the Mach stem height is always influenced by 3D effects and is always smaller than the 2D result. The difference in Mach stem height between the 2D and 3D result for the same shock incidence must be considered when comparing 2D computed results with measurements from experiments. Figure 3.1 serves as a useful summary of the expected difference between steady 2D CFD and 3D experimental results.

3.3 Supersonic Wind Tunnel

All experiments in this work were conducted in the blow-down, supersonic wind tunnel facility at the Council for Scientific and Industrial Research in Pretoria, South Africa illustrated in figure 3.2. The wind tunnel has a 450 mm $\times$ 450 mm test section and a free stream speed range of $0.6 \leq \mathrm{M} \leq 4.3$. Supersonic flow conditions

in the test section are achieved with a semi-flexible nozzle upstream of the test section (see figure 3.3). The nozzle consists of two stainless steel plates (top and bottom wall) fastened to a pair of "nozzle throat blocks", positioned symmetrically about the tunnel horizontal centre plane, at the nozzle minimum cross sectional area. The supersonic test section Mach number is achieved by controlling the vertical position of the throat blocks (and hence the nozzle throat area) with two large hydraulic jacks. The steel plates are shaped with 7 additional hydraulic cylinders per plate to achieve the required nozzle shape at each set point. The shape of the throat blocks is fixed and they are re-oriented at each set point to ensure a smooth transition between the blocks and the steel plates.

A 500kW compressor pressurises 4 large tanks, with a total volume of approximately 350m^3, to 12.0 bar before each experiment. This provides approximately 20 - 30 seconds of useful test time and depends on the experiment test conditions. This is adequate for the purposes of this experiment as the motion of interest requires less than 20 msec of steady flow. An air dryer, installed between the compressor and storage tanks, ensures that dry air is delivered to the test section. At tunnel startup a shutoff valve discharges the compressed air into the tunnel. A hydraulically actuated pressure control valve controls the stagnation pressure in the settling chamber and test section. A single honeycomb mesh, positioned in the settling chamber, pre-conditions the flow to reduce the turbulence in the test section. The test section turbulence levels are unknown at this stage.

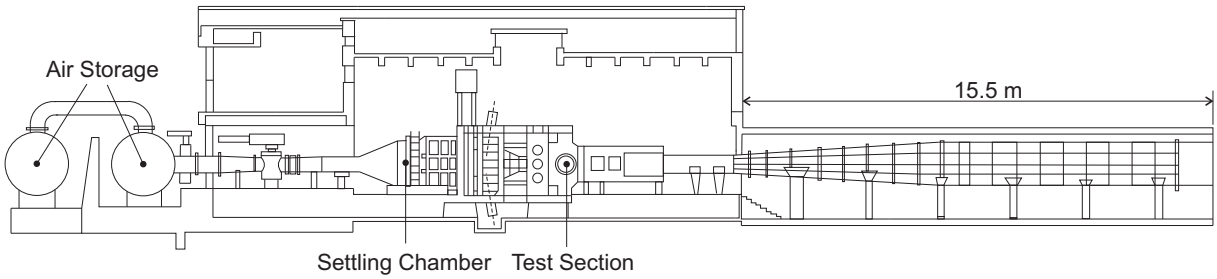


Figure 3.2: Side view of supersonic wind tunnel facility at the CSIR, South Africa

The tunnel control is automated and consists of a National Instruments based control system. The wind tunnel is operated remotely during the experiments from a Labview interface. Tunnel transducer data is acquired at 500Hz with a National Instruments data acquisition system, i.e. total pressure, test section static pressure, atmospheric pressure and total temperature. A more detailed description of the acquisition system is included in Appendix A. Technical specifications of all the pressure transducers and the pressure calibration standard may also be found in Appendix A. Pressure transducer calibrations were conducted before the experiments and the calculated calibration coefficients and linear regression statistics are included

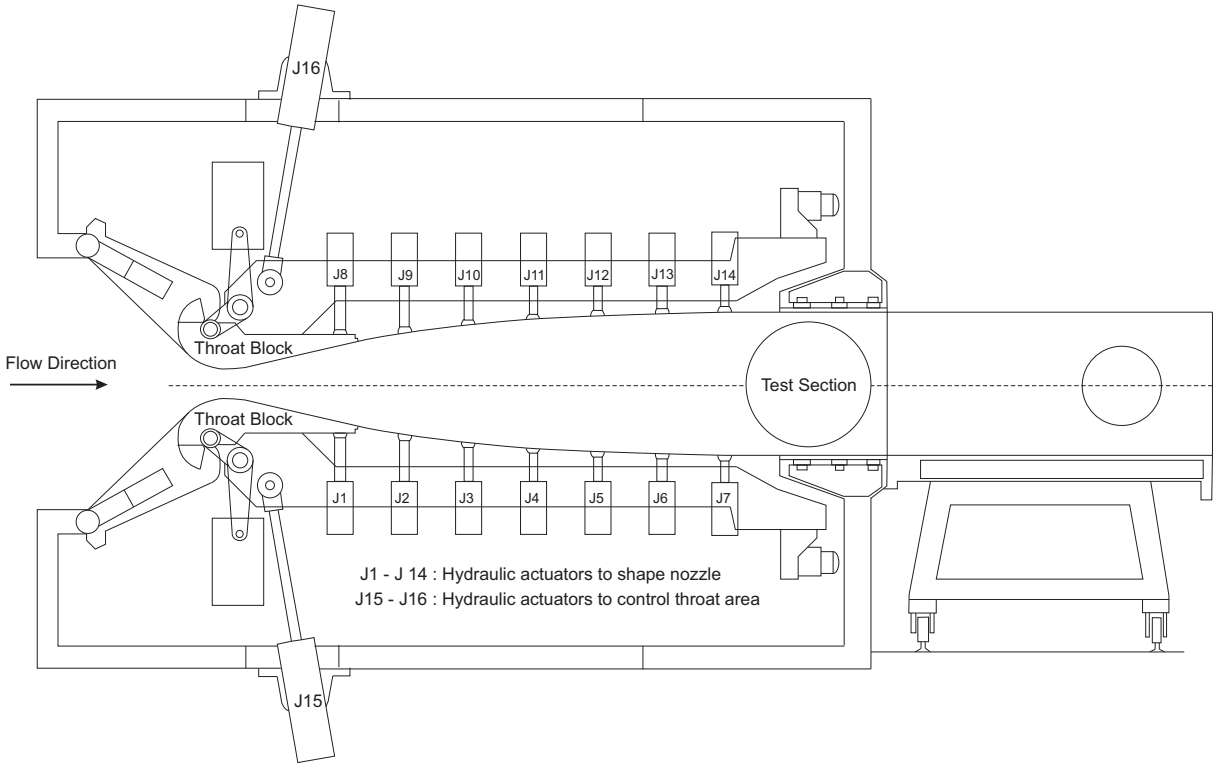


Figure 3.3: Simplified schematic indicating tunnel nozzle shape control

in Appendix A. All rig and high-speed imaging operations were conducted remotely from the tunnel control room, due to Environment Health and Safety regulations at the CSIR.

3.3.1 Mach Number Measurement

Mach number control in the test section is achieved with accurate control of the nozzle throat area through accurate positioning of the throat blocks. The test section Mach number is governed, to a large extent, by the area ratio between the nozzle throat and the tunnel test section. The following ideal, isentropic relation provides an estimate of the required area ratio between the nozzle throat and the test section (see Zukrow & Hoffman [46]):

$$M = \frac{A^*}{A}\left\{\frac{2}{\gamma+1}\left(1+\frac{\gamma-1}{2}M^2\right)\right\}^{\frac{(\gamma+1)}{2(\gamma-1)}} \tag{3.1}$$

The following relationship between the stagnation pressure, static pressure and test section Mach number is applicable to isentropic flows (Zukrow and Hoffman [46]):

$$M = \left[\left\{ \left(\frac{P_O}{p} \right)^{\frac{\gamma-1}{\gamma}} - 1 \right\} \left\{ \frac{2}{\gamma - 1} \right\} \right]^{\frac{1}{2}} \tag{3.2}$$

Assuming isentropic conditions between the settling chamber and the test section, the stagnation pressure is constant from settling chamber to test section. A Mach number measurement on the test section wall is derived from the stagnation pressure measurement in the settling chamber and a static pressure measurement on the wall of the test section upstream of the model of interest. The CSIR tunnel calibration requires the application of a correction factor to the wall measurement to derive the test section Mach number. All applicable correction factors are included in Appendix A. All tunnel transducers were calibrated by the author as part of the experimental setup, but the current CSIR test section calibration is assumed. From the uncertainty in the most recent pressure transducer calibrations and the CSIR test section calibration, a value for Mach number uncertainty is estimated. The uncertainty calculation is documented in Appendix A. A Mach number uncertainty of $\delta M = \pm 0.03$ is assumed across the range of experimental test conditions.

3.3.2 Stagnation Temperature Measurement

In the unsteady case, the propagation speed of information in the gas medium with respect to the rotation speed is an important parameter. Since the acoustic speed is dependent on the static temperature in the test section, a static temperature measurement was required.

The flow between the settling chamber and test section is assumed isentropic. Given that:

$$\frac{T_O}{T} = 1 + \frac{\gamma - 1}{2} M^2 \tag{3.3}$$

, the test section static temperature was derived from a settling chamber temperature measurement (close to total temperature) and the derived test section Mach number.

Due to the contraction ratio from the settling chamber to the test section (≈ 6.22), the Mach number in the settling chamber is very small, and the difference in total and static air temperature in the settling chamber is also very small. The largest issue for the total temperature measurement was the short duration test time. The test time was insufficient for the sensor reading to stabilise in some instances (see figure A.5). The stagnation temperature probe is shown in figure A.3. It consists of an entrance hole that faces the oncoming flow and a bleed hole on the leeward side. The probe houses a PT100 RTD (resistance temperature detector) sensor in the gas path between the entrance and bleed holes. A custom PT100 with an aerated tip was acquired for these experiments to maximise the heat transfer rate to the sensor. Details of the sensor and calibration data are included in Appendix A.

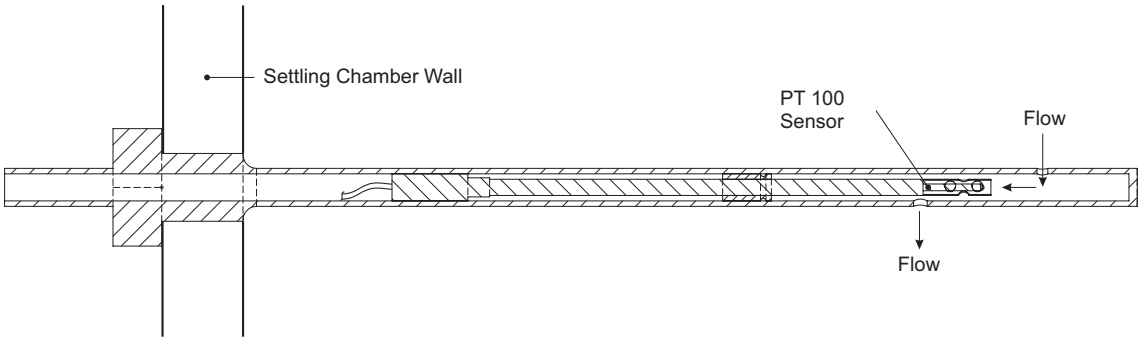
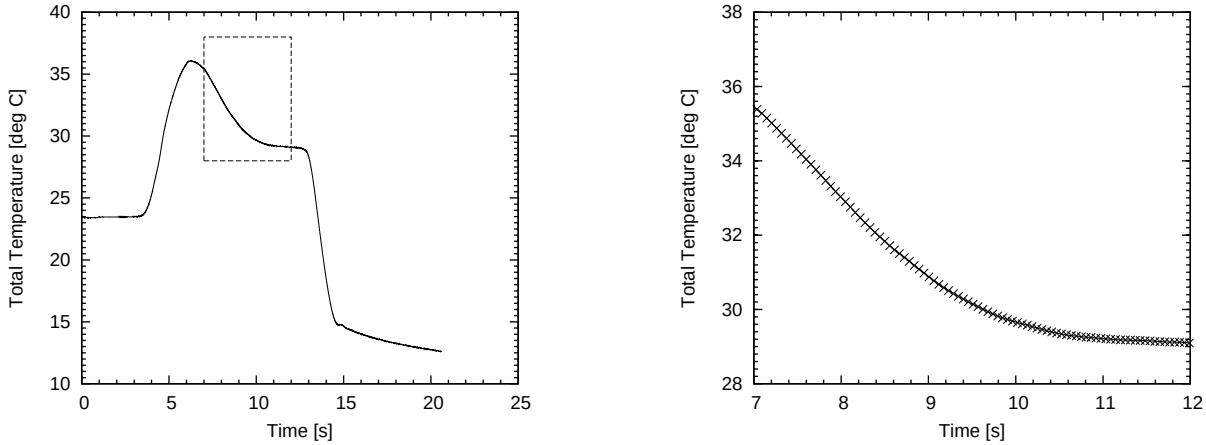


Figure 3.4: Schematic of stagnation temperature probe in settling chamber



(a) (b)

Figure 3.5: (a) Sample total temperature probe measurement and (b) magnified view of select data range

A sample probe measurement from an experiment is shown in figure 3.5. Before the experiment the temperature reading was relatively constant at approximately 296.6 K. At tunnel startup there was a rapid rise in temperature as the startup shock passed through the settling chamber. As the tunnel flow stabilised the probe temperature measurement dropped and began to stabilise. It is assumed that the transient is only due to the short test time, i.e. the variation in actual total temperature in the settling chamber is small in comparison to the probe transients. From the data between the highlighted markers, it is possible to extrapolate a settling temperature of approximately $29.0°C$. The total temperature measurement quoted for each experiment was determined in a similar manner. The sharp drop in temperature at the end of the experiment was due to rapid heat transfer between the air in the settling chamber and the relatively cold air in the test section as the supply air is turned off.

With $T_O = 29.0 \pm 0.5°C$ and $M = 3.0 \pm 0.03$, this results in a maximum uncertainty of approximately $\pm 0.75\%$ on the acoustic speed. For any value of wedge rotation speed this translates to an uncertainty of

approximately ±0.75% on wedge rotation speed and dimensionless rotation speed, $M_E = V_E/a_\infty$. Sample calculations may be found in Appendix A. This uncertainty would have a negligible effect on the transition point for the dynamic case.

3.4 Flow Visualisation

A standard, z-type schlieren system (see Settles [37]) was designed for these experiments. The system is shown in figure 3.6. The optical design was done in accordance with the guidelines provided by the Eastman Kodak company [8]. There was a limited budget on this project and every attempt was made to minimise cost. Parabolic mirrors (6 inch in diameter, f/8) were acquired from a telescope retailer . Old mirror mounts were salvaged and new stands were designed. Stands were designed to be sufficiently heavy and were mounted on rubber dampers to eliminate the possibility of system vibration during testing. The light source from the previous system was used. The arrangement of optical components attempted to maximise coverage on the camera imaging sensor. Various colour masks were tested at the cutoff plane (see Fig. 3.7). The multi-coloured mask provided more qualitative information on the three-dimensional nature of the flow field than the standard three-colour mask (discussed in chapter 5). The technical specification of the schlieren system is documented in Appendix B. Alignment of the schlieren system was done in accordance with the guidelines of Settles [37]. See Appendix B for more detail on the procedure and alignment equipment employed.

3.5 Image Calibration Technique

Accurate measurement of θ_w, ϕ and Mach stem height, m, from images was important to this investigation. The calibration of the schlieren optics for angular and co-ordinate measurements involved imaging a 5 mm $\times$ 5 mm uniform grid on the test section window (see figure 3.8). There is no visible pin cushion or barrel distortion. The grid was generated with CAD software and printed on a transparency with a laser printer. The transformation from the image co-ordinate system to the object co-ordinate system is known from an image of the calibration grid.

An image of the calibration grid was captured before each experiment. The maximum image resolution during the dynamic experiments was 512 $\times$ 512 pixels at the required frame rate (discussed later in this chapter). Absolute orientation of the uniform grid was measured with a calibrated digital inclinometer (see Appendix B for technical specifications and calibration). Locating markers were fixed on the test section window and were imaged for the calibration and during the experiments. The camera was stationary between the time the calibration grid was imaged and the experiment was completed. The locating markers were

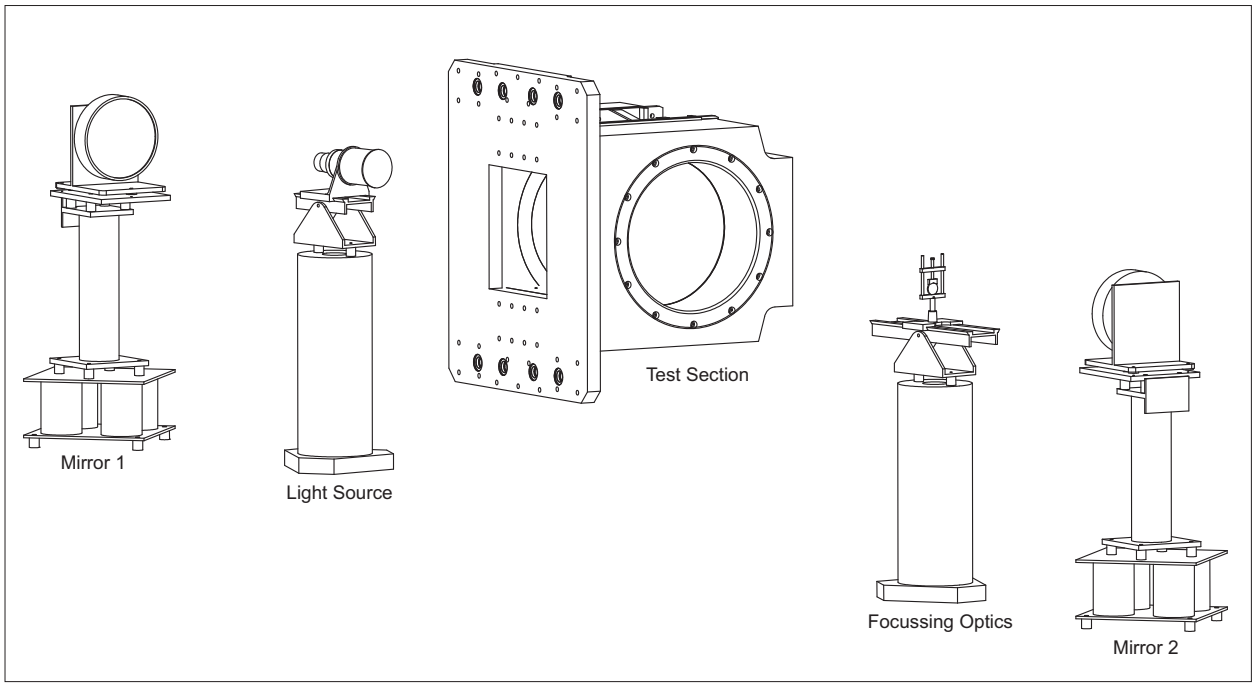


Figure 3.6: Schematic of schlieren flow visualisation setup (colour mask and high-speed camera not shown)

used to determine if there was any camera movement between calibration and testing.

Co-ordinates of points not co-incident with the grid were calculated with linear interpolation from the four closest grid points. A software routine was written to transform pixel co-ordinates to object space co-ordinates. The calculation routine is documented in Appendix B. This procedure enabled the accurate measurement of ϕ, θ_w and m from images. A critical and limiting factor in the uncertainty estimation of spatial measurements is the available resolution and object magnification. The uncertainty of spatial measurements using this method increases with a decrease in image resolution and a decrease in imaging sensor coverage.

The uncertainty in the measurement technique was determined from angle and distance measurements on the test image shown in figure 3.8(b). The test pattern consists of lines at known angular orientations. With the exception of the lines at $\pm 2.5^\circ$ and $\pm 177.5^\circ$, the remaining lines are oriented at $\pm 5^\circ$ intervals.

Pixel co-ordinates of 10 points along lines of interest were transformed to object space co-ordinates to determine the orientation of each line with a linear regression of the measured points. Results of a calibration check are documented in table 3.1. A summary of statistics on the measurements are documented in table 3.2. From the summary statistics in table 3.2 the uncertainty in angular measurement is estimated at approximately $\pm 0.3^\circ$, a value slightly larger than 95% of the calculated errors.

The uncertainty of distance measurement was estimated by measuring the distance between the ends of

Table 3.1: Results from a calibration check on a test image for measurements between $-20.0°$ and $40.0°$

Data Point	**Calculated Angle** ($0.0°$)	**Error**	**Calculated Angle** ($10.0°$)	**Error**
1	0.104	-0.104	9.930	0.070
2	0.066	-0.066	9.800	0.200
3	0.123	-0.123	9.892	0.108
4	0.051	-0.051	10.001	-0.001
5	0.041	-0.041	9.921	0.079
Data Point	**Calculated Angle** ($20.0°$)	**Error**	**Calculated Angle** ($30.0°$)	**Error**
1	20.000	0.000	30.176	-0.176
2	20.121	-0.121	30.174	-0.174
3	19.889	0.111	29.943	0.057
4	19.956	0.044	30.289	-0.289
5	19.911	0.089	30.248	-0.248
Data Point	**Calculated Angle** ($40.0°$)	**Error**	**Calculated Angle** ($-5.0°$)	**Error**
1	40.030	-0.030	-4.925	-0.075
2	39.978	0.022	-4.967	-0.033
3	40.061	-0.061	-5.150	0.150
4	40.130	-0.130	-5.275	0.275
5	40.166	-0.166	-5.156	0.156
Data Point	**Calculated Angle** ($-10.0°$)	**Error**	**Calculated Angle** ($-20.0°$)	**Error**
1	-10.076	0.076	-20.093	0.093
2	-10.283	0.283	-20.196	0.196
3	-10.283	0.283	-20.015	0.015
4	-10.222	0.222	-20.316	0.316
5	-10.143	0.143	-20.291	0.291

Table 3.2: Summary of statistics for angular measurement error

Mean Error	$0.035°$
Standard Deviation	$0.155°$
Maximum Error	$0.316°$
95% **of Calculated Errors**	$< 0.28°$

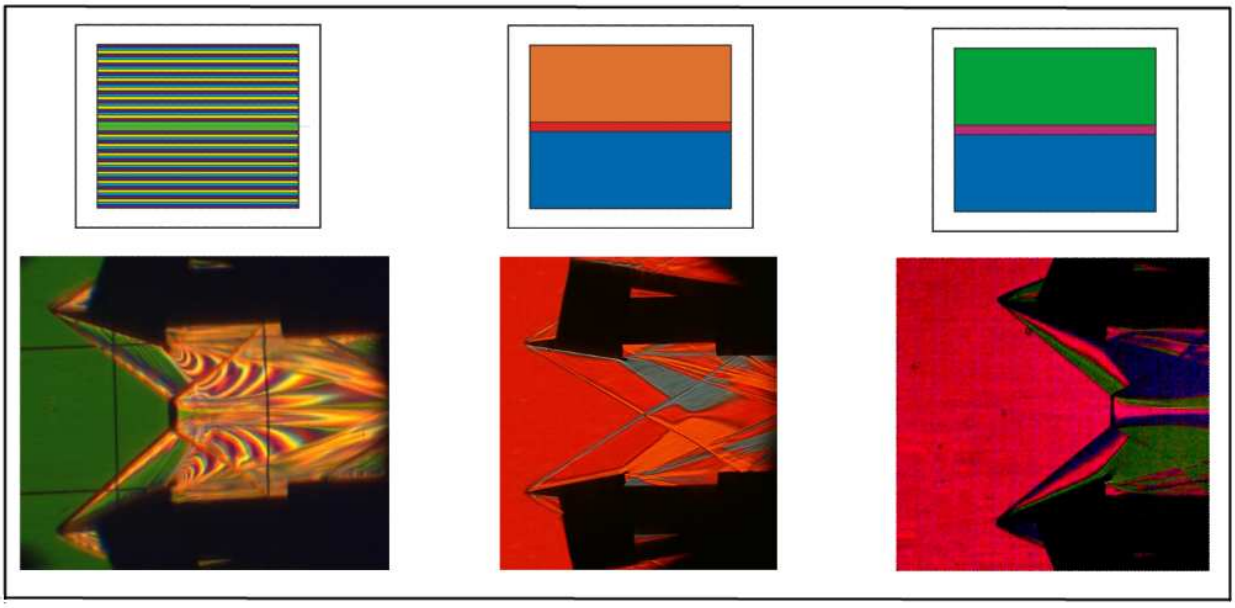


Figure 3.7: Sample images obtained with various colour masks

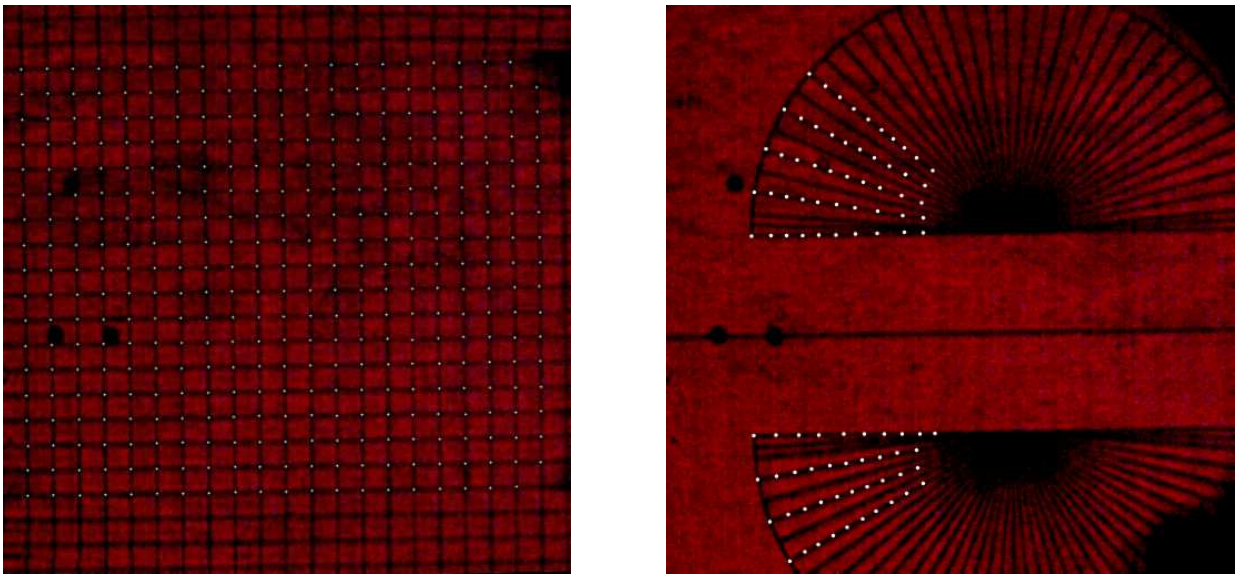
Table 3.3: Calibration check for measurement uncertainty on distance

Data Point	**Measured Distance [mm]**	**Error [mm]**
1	4.426	0.064
2	4.442	0.080
3	4.301	0.061
4	4.417	0.055
5	4.297	0.065
6	4.422	0.060
7	4.435	0.073
8	4.305	0.057

any two lines bounding a five degree arc on the test image and comparing the result with the true value (approximately 4.362 mm). Results are presented in table 3.3. The maximum error was approximately 0.08 mm. This translates to a measurement uncertainty on m/w of approximately ± 0.002. This does not necessarily account completely for the uncertainty in locating the triple point on an image of a MR. By considering images of a MR, the uncertainty in the non-dimensional Mach stem height measurement is estimated at approximately $\delta m/w = \pm 0.004$, 0.4% of the wedge chord.

3.6 High-Speed Image Acquisition

High-speed schlieren images of the dynamic flow field were captured with the Photron Ultima APX-RS high-speed digital camera. The camera has a 10-bit CMOS sensor with 1024 × 1024 pixels, with a pixel size



(a) (b)

Figure 3.8: Image of (a) 5 mm × 5 mm square calibration grid with locating markers and the (b) test image captured with the high-speed camera at 512 x 512 pixel resolution used for all dynamic experiments

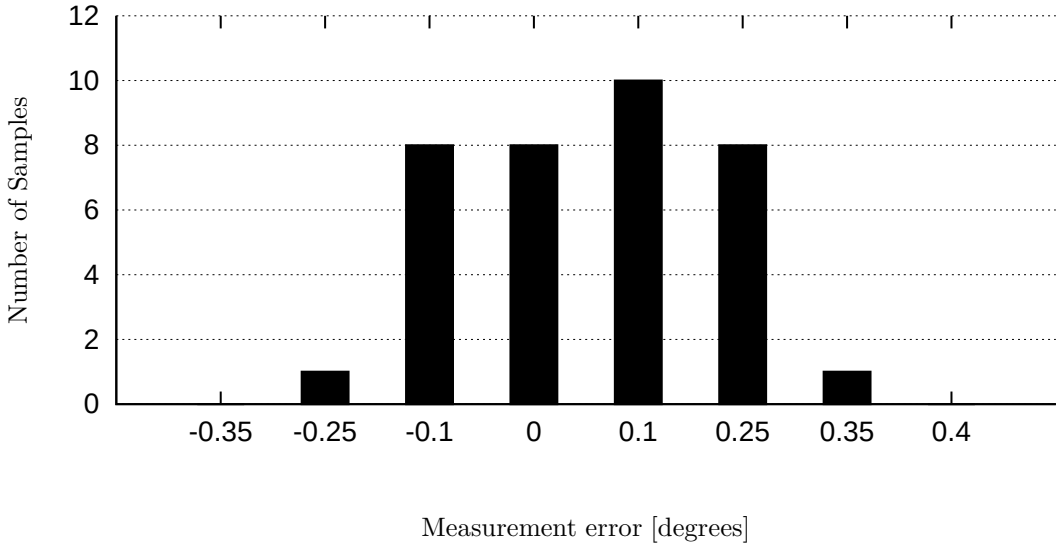


Figure 3.9: Distribution of deviation from target angle

of 17μm. Image focussing onto the camera CCD chip was achieved with a 100mm focal length aspherical achromatic lens. The larger radius of curvature on the achromatic lens faces the larger conjugate on the optical axis, i.e. the test object. The smaller radius of curvature faces the camera CCD chip. The camera opening to the lens was covered with a UV filter to protect the imaging chip as seen in figure 3.10. Specifications of the camera and focussing lens are documented in Appendix B. Images were captured at the camera's maximum resolution (1024 x 1024 pixels) at 250 frames per second for the steady state experiments and at 10000 frames per second (512 x 512 pixels) for the dynamic experiments. Shutter speed was reduced to 1/20000s for the dynamic experiments to reduce motion blur that resulted from the rapid rotation of the wedge.

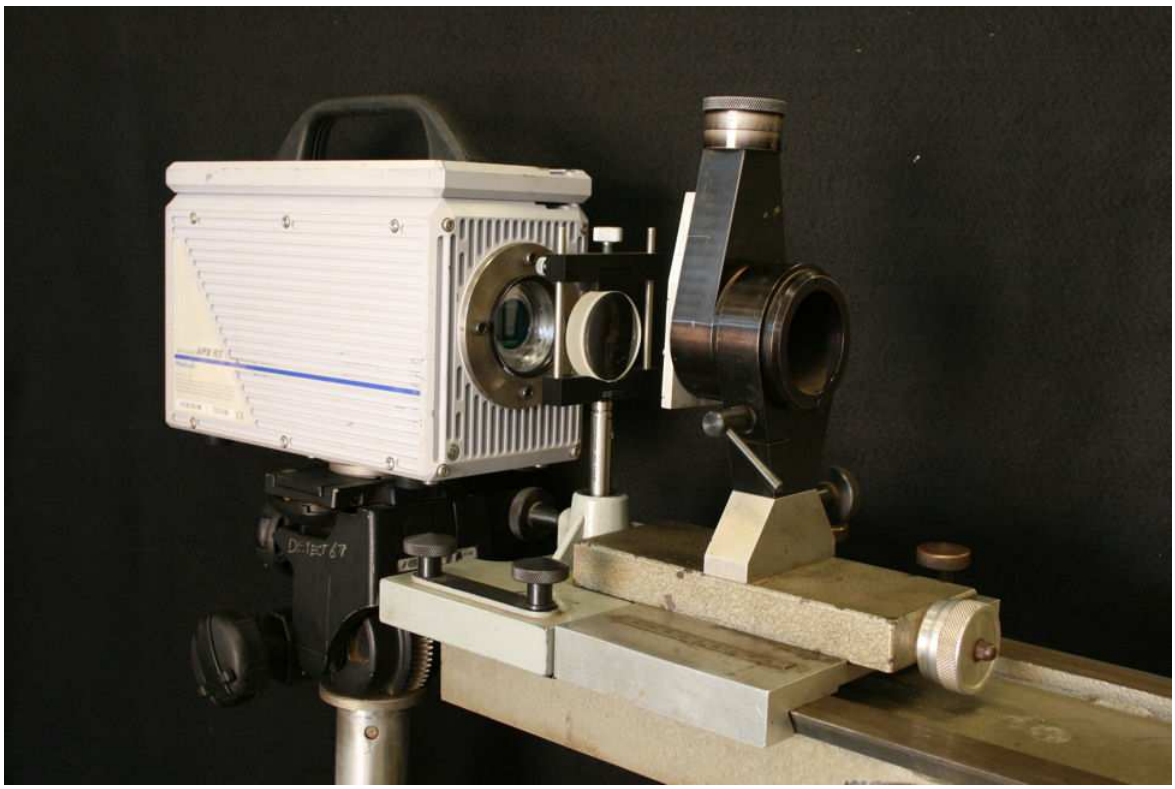


Figure 3.10: Photograph of the Photron Ultima APX-RS high speed camera with a UV filter to protect the imaging sensor and an aspherical achromatic lens for focussing. The schlieren colour mask is positioned ahead of the focussing lens.

3.7 Summary of Measurement Uncertainties

Values for δM, δT_O, $\delta m/w$ and $\delta\phi$ (or $\delta\theta_w$) are summarised in table 3.4.

Table 3.4: Summary of measurement uncertainties

Quantity	Value
δM	± 0.03
δT_O	$\pm 0.5K$
$\delta\phi$, $\delta\theta_w$	$\pm 0.3°$
$\delta m/w$	± 0.004

3.8 Dynamic Shock Wave Interaction Rig

This section presents various aspects of the rig design. Critical aspects of the system requirements specification, design considerations and constraints are documented. Four versions of the rig were tested in the facility before a final, satisfactory design was achieved. A brief summary of the development history of the rig is also presented. A limited series of drawings are presented in the body of this work for the purpose of illustration. Calculations for the sizing of the actuators are included in Appendix C.

3.8.1 System Requirements Specification

The following basic requirements were used to develop the design concept. These include requirements/constraints gathered from the literature.

Functional and Performance Requirements

1. The rig shall rotate the wedges to achieve increasing and decreasing incidence
2. The rig shall enable wedge rotation between 0° and approximately 40°
3. The wedge shall rotate about its trailing edge
4. The rig shall generate steady state data as well as dynamic data (not in the same experiment)
5. The wedge rotation speed for the steady state experiments shall not result in $|M_E| > 0.001$
6. The required order of magnitude for the wedge rotation speed in the dynamic experiments shall result in $M_E \geq +0.01$

Interface Requirements

1. The rig shall be designed for installation and operation in the CSIR supersonic blow-down facility illustrated in figure 3.2.
2. The rig shall be mounted on either the existing tunnel pitch sector and/or the tunnel cart shown in figure 3.11.

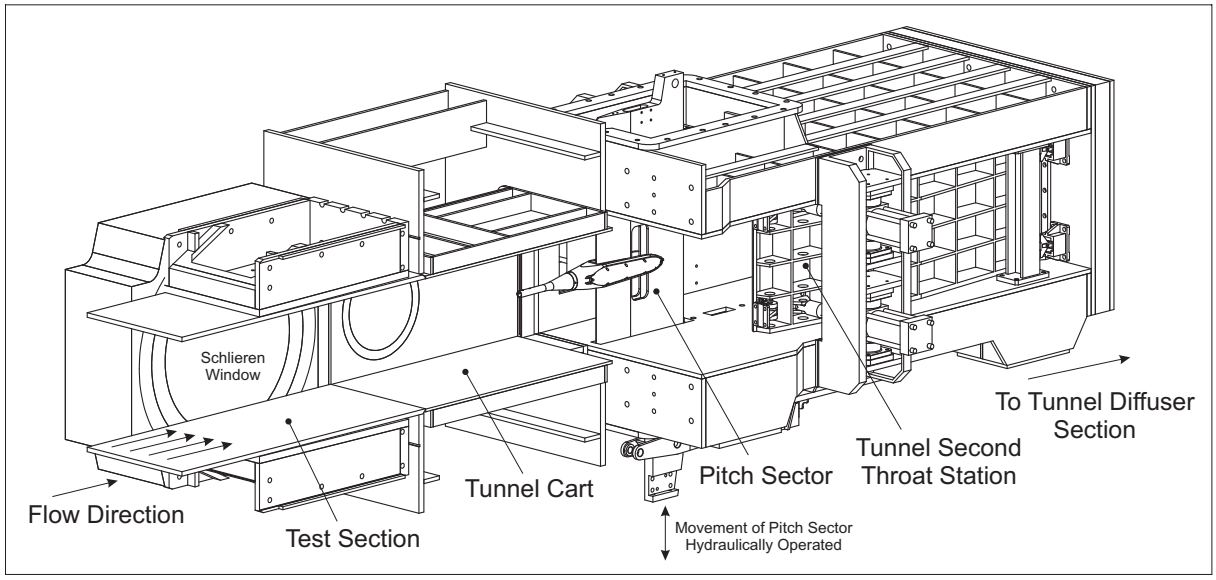


Figure 3.11: Schematic of a section of the supersonic tunnel with walls removed showing available tunnel support systems for the mounting of the rig (image provided courtesy of the CSIR)

3. The rig shall be designed such that the wedges and the reflection pattern are visible to the schlieren system through the glass windows in the test section.

4. Rig and camera operations shall be conducted remotely from the tunnel control room during the experiment. A rig control interface shall be developed.

5. The high speed camera shall be triggered manually or automatically.

6. Rig installation and operation shall be safe.

Constraints

1. The rig shall consist of a double, symmetric wedge configuration

2. Both wedges shall be arranged and actuated symmetrically about a horizontal, symmetry plane, parallel to the tunnel free stream

3. The vertical separation between the wedge and the reflection plane shall ensure that the reflected wave does not intersect the wedge surface and the expansion fan from the wedge trailing edge does not intersect the reflection/triple point at $M = 2.0$ and $M = 3.0$

4. Each wedge shall have a minimum aspect ratio, $b/w = 4.0$, where b is the wedge span and w is the wedge chord

5. The rig cross sectional area shall not cause blockage to the extent that the tunnel does not start. Guidelines provided in a Naval Ordnance Report [43] may be used to estimate this maximum permissable blockage (see Appendix C)

6. The rig shall be designed such that shock waves from the test article or rig, on reflection from the test section wall, must not interfere with the test article or flow phenomena of interest

7. Each experiment shall not exceed 15 seconds due to the limit on stored air

Environmental Conditions

1. The rig shall be designed to operate between $M = 2.0$ and $M = 3.0$

2. The rig shall operate within the envelope in figure 3.12. The lower boundary of the test envelope represents the minimum pressure required for tunnel startup. The upper boundary represents the maximum design strength of the schlieren windows in the test section. Curves for $P_O = 600$ to 1000 kPa are not shown as they would not be applicable for the range of free stream conditions required

3. The rig and test article shall be designed to withstand the aerodynamic load experienced on tunnel startup as the startup shock passes downstream

4. The total temperature ranges from 0.0°C to 35.0°C

3.8.2 Design Description

The rig consists of two large aspect ratio, symmetrically opposed wedges, a support structure and an actuator as illustrated in figure 3.13. The wedges are mounted on the support structure and are actuated symmetrically about a horizontal plane of symmetry. The use of finite aspect ratio wedges, as opposed to wedges spanning the entire test section, are necessary to avoid the complex shock-boundary layer interaction on the test section window, which will produce confusing features on the schlieren images. The approach adopted in this investigation was to actuate both wedges symmetrically rather than a single wedge with corrected, theoretical transition criteria to account for the asymmetry. With the adopted design approach the wedges may also be mounted asymmetrically. Each wedge has an aspect ratio of $b/w = 4.25$ with w=40.0 mm and this is sufficient to ensure 2D RR $\leftrightarrow$ MR transition for $2.0 < M < 3.0$.

The wedge pivot point was maintained as close to the trailing edge as possible and was selected to minimise the vertical movement of the trailing edge. The vertical movement of the trailing edge between wedge incidence, $\theta_w = 2.0°$ and $\theta_w = 25°$ is approximately 2.1% of the wedge chord. This variation is small,

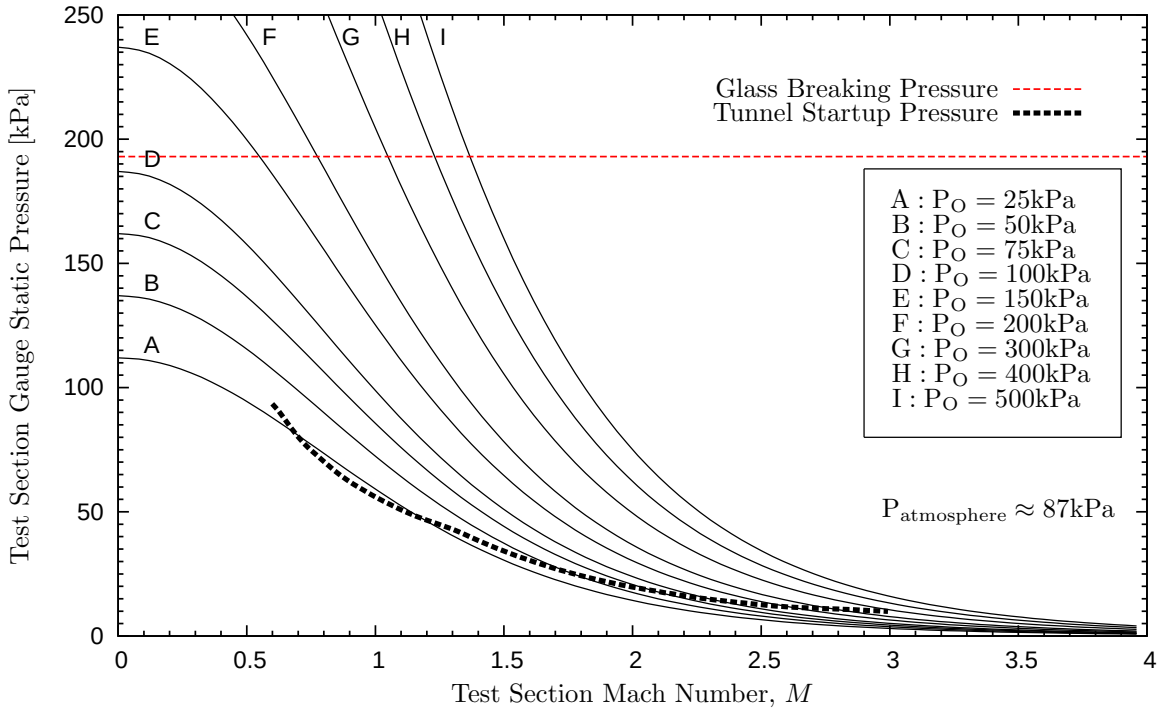


Figure 3.12: Envelope of operating conditions in CSIR supersonic wind tunnel in terms of total pressure (gauge)

but its effect on transition is addressed with numerical simulation in Chapters 6 and 7. The trailing edge separation from the symmetry plane, g, was calculated to prevent the intersection of the expansion fan with the reflection point ($g/w \approx 0.6$ for all experiments) and to prevent intersection of the reflected wave with the wedge chord.

The drive path from the actuator to the wedges is highlighted in grey in figure 3.14 and consists of a vertical bar that synchronizes the horizontal motion of two drive shafts that result in synchronized rotation of the wedges. The wedges were rotated gradually, with a servo motor, between 5.0 and 10 deg/s to generate steady state data (see figure 3.15). This rotation speed is sufficiently small such that the reflection pattern is approximately steady at each point in time. The wedges were rotated at larger rotation speeds with a spring-driven actuator to investigate the dynamic case (see figure 3.16). The spring-driven actuator is assembled to achieve either rapid increasing or decreasing incidence. Photographs of the hardware are included in Appendix C.

3.8.3 Actuator for Steady State Experiments

As illustrated in figure 3.15, the actuator for the steady state experiments consists of a DC servo motor and lead screw arrangement that rotates the wedges gradually between 5 and 10 deg/s. This is sufficiently

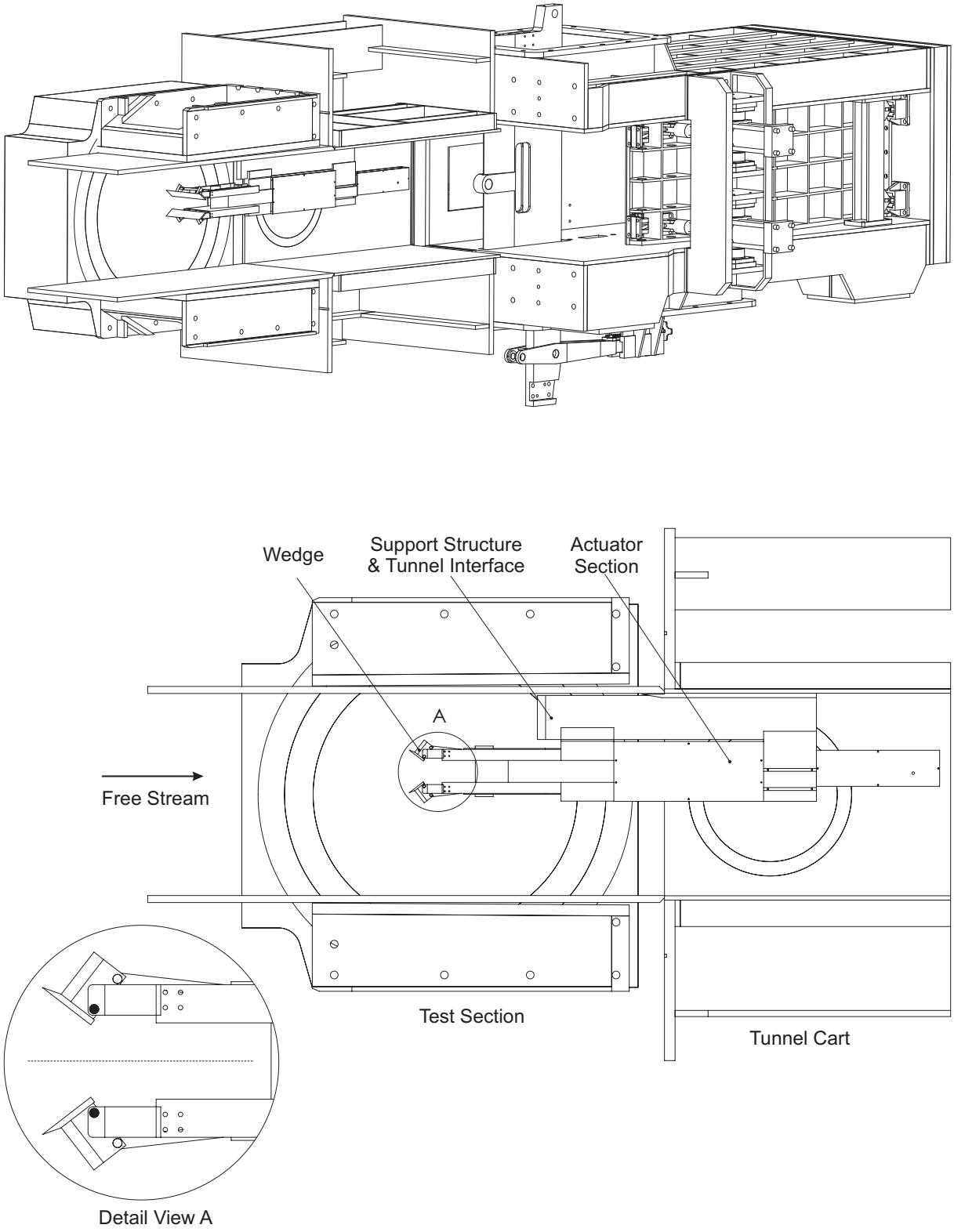


Figure 3.13: Illustrations of rig installed in the CSIR supersonic wind tunnel

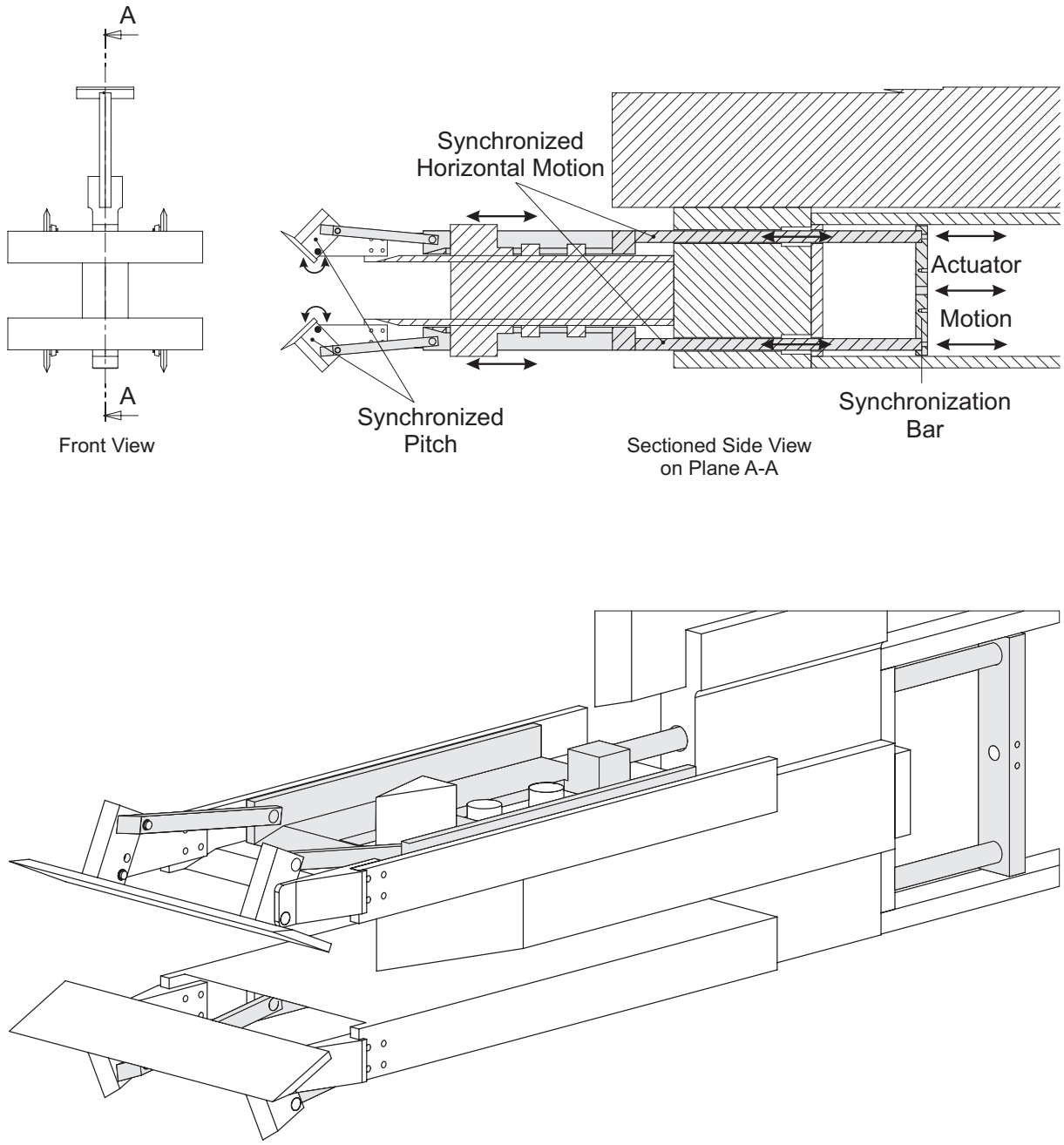


Figure 3.14: Symmetric wedge arrangement and the drive path highlighted in grey

slow not to generate any dynamic effects on the transition point and the Mach stem development. The synchronisation bar has an embedded bearing arrangement that houses the lead screw. Rotation of the lead screw through the bearing is translated to horizontal movement of the synchronisation bar and drive shafts that result in wedge rotation. At the time of design, available commercial off the shelf DC motors were not able to withstand the predicted axial loads at tunnel startup. A custom thrust bearing arrangement was designed to transfer the axial load on the drive shafts to the support bracket. The arrangement decouples the motor shaft from the lead screw in the axial direction, but maintains rotational coupling. Calculations for the motor selection are included in Appendix C. Details and drawings of the lead screw and bearing arrangement are also included in Appendix C. A control interface was developed for remote control of the servo-motor, which includes control to reverse the motor direction. Illustrations of the control interface and circuit diagrams are included in Appendix C.

3.8.4 Actuator for Dynamic Experiments

Wedge rotation speeds that were used in simulations by Felthun & Skews [12] resulted in wedge trailing edge speeds up to 10% of the free stream acoustic speed. The wedge was started impulsively (with an initial, established steady RR) and rotated at a constant rotation speed. In a typical supersonic blow down wind tunnel at $M = 3.0$, using air stored at 300.0 K, with $w = 40.0$ mm, this required starting the wedge impulsively and rotating it at a constant rotation speed of approximately 30000 deg/s. Evidently, the validation of this type of numerical simulation with an experiment is not possible as it requires infinite acceleration at startup. Only finite acceleration could be considered in the experiment and this has been mimicked in the computations.

Various concepts were considered to realise the rotation speeds required, viz. spring-driven, electric, dynamic impact, pyrotechnics, pneumatics and hydraulics. As these experiments were the first of their kind in the CSIR tunnel, a spring-driven mechanism was considered primarily for the sake of simplicity and cost. The actuator was designed to achieve movement of the wedges in one direction only per experiment, i.e. rapid increasing or decreasing incidence per experiment, but not both in the same experiment. The actuator must be configured appropriately to achieved the required rotation direction. The actuator for rapid increasing incidence is shown in figure 3.16. The required arrangement for the reverse motion is shown in figure 3.19. All components in the drive path are highlighted in grey and are coupled to the horizontal movement of the synchronisation bar and drive shafts. A pair of compression springs were designed to generate an average $M_E = +0.01$ over a 25° rotation range. Calculations are presented in Appendix C. Though this wedge rotation speed is smaller than the maximum rotation speed investigated with computational simulation by

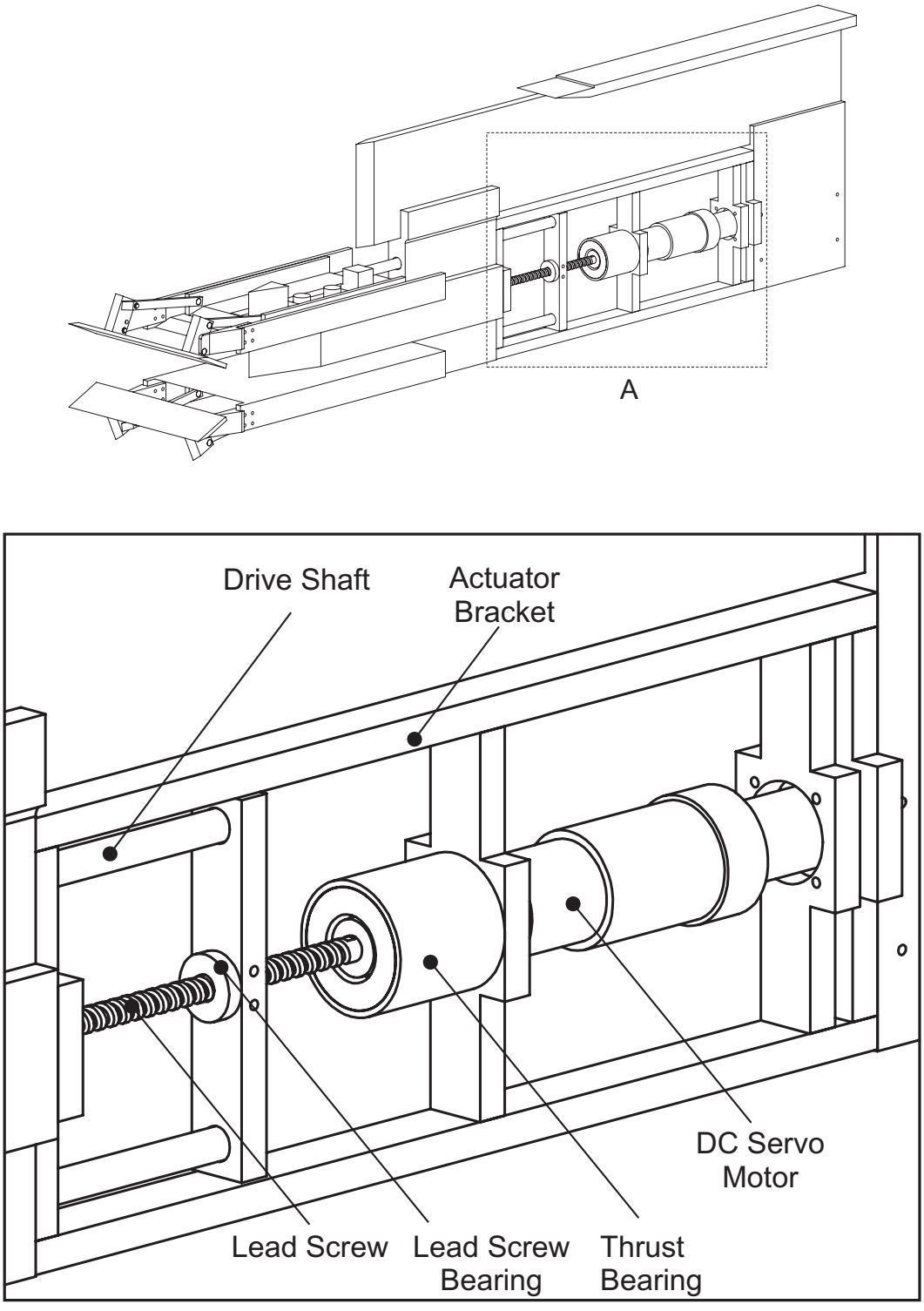


Figure 3.15: Servo motor driven actuator for steady state, baseline experiments

Felthun & Skews [12], it was considered sufficient to provide the necessary validation data.

In the configuration shown in figure 3.16 the springs are energised by moving the synchronisation bar upstream until it is secured with the latch mechanism. During the experiment the latch mechanism is released remotely and the drive path accelerates downstream resulting in the required rapid wedge rotation. With an initial spring load of 1000 N, the drive train is accelerated at approximately 1000m.s^{-2} and the motion is completed in approximately 6.0 ms. Depending on the experimental test conditions a maximum instantaneous $M_E \approx +0.033$ was achieved, i.e. approximately 11000 deg/s.

The linear potentiometer in figure 3.16 is coupled to one of the drive shafts and its signal is acquired along with tunnel Mach number. The potentiometer signal is used to identify the start of the wedge motion on the Mach number trace as illustrated in figure 3.20.

Arming the Actuator

The springs are energised with the jacking nut on the screw thread shown in figure 3.17. The jacking nut is turned against the cover (jacking surface) of the thrust bearing arrangement on the synchronisation bar. The springs are compressed until the latch mechanism secures the synchronisation bar as shown in figure 3.16. Before releasing the latch mechanism, the jacking nut is turned away from the synchronisation bar to ensure sufficient clearance for the actuator stroke during an experiment.

Securing the Actuation Load

The latch mechanism shown in figure 3.18 was designed to hold the required actuation load until released remotely from the control room. This was a particularly important aspect of the design as experiments with an earlier version of the mechanism resulted in early release of the load as the startup shock moved through the test section (see figure 3.25). The current design ensures that the actuation load is secure during tunnel startup. When the actuator is armed (figure 3.18(a)), the actuation load is held in position with a latch that is engaged against the shoulder of a release pillar. The shoulder of the release pillar and the mating surface on the latch were designed with the same radius of curvature. The centre of curvature of both surfaces in the locked position is the rotation centre of the release pillar. Therefore, the distributed load on the latch at the shoulder acts through the centre of the release pillar, cancelling any moment that may tend to rotate the release pillar. In this way, the latch is self-locking by design and will not release the load due to any sudden load application. The latch and the release pillar were precision wire cut from 8 mm thick 174 Ph Stainless Steel (1000 MPa yield strength after heat treatment) to ensure an ideal mating surface at the shoulder. The mechanism includes a redundant safety pin, shown in figure 3.16, that prevents movement of the release

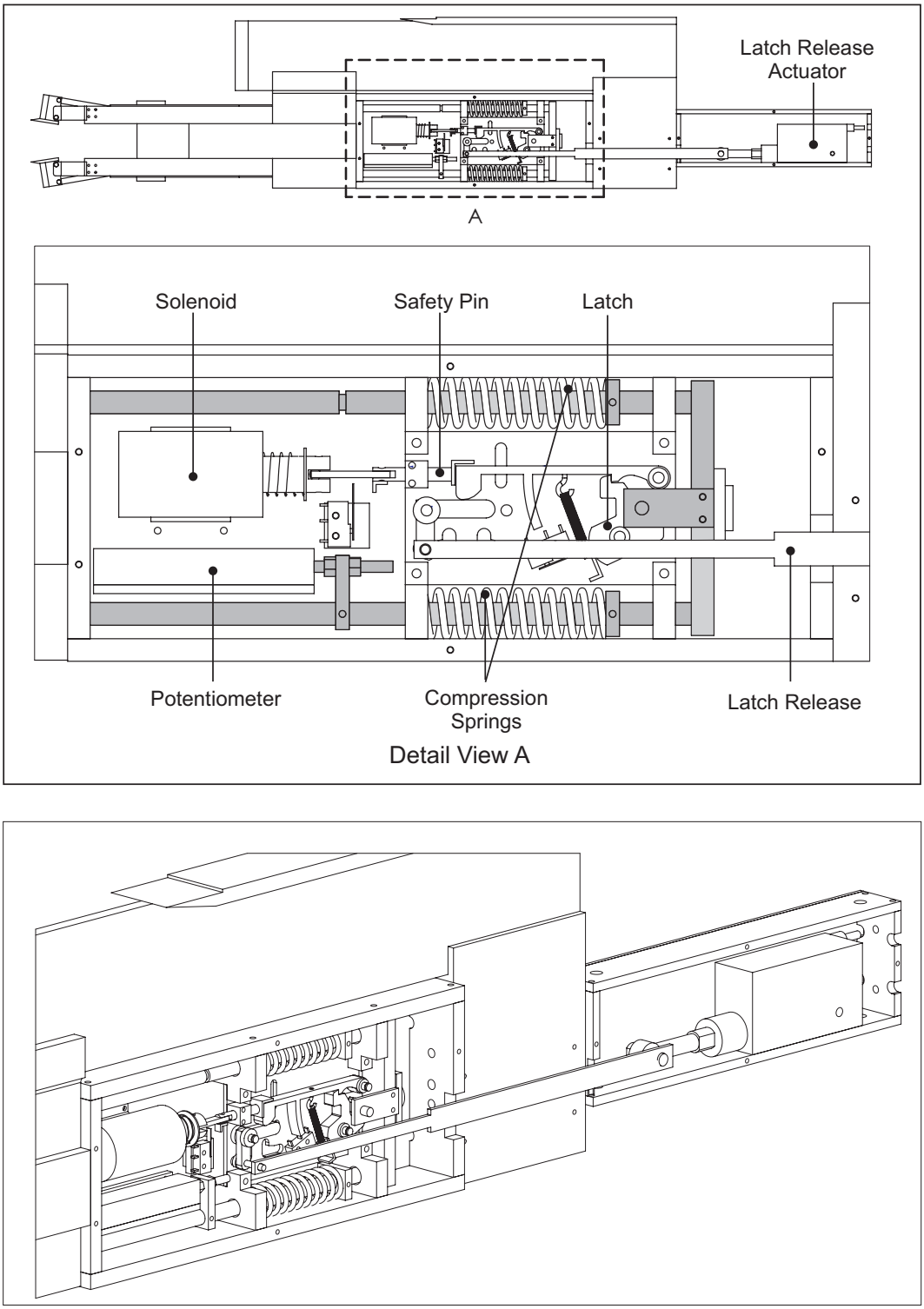
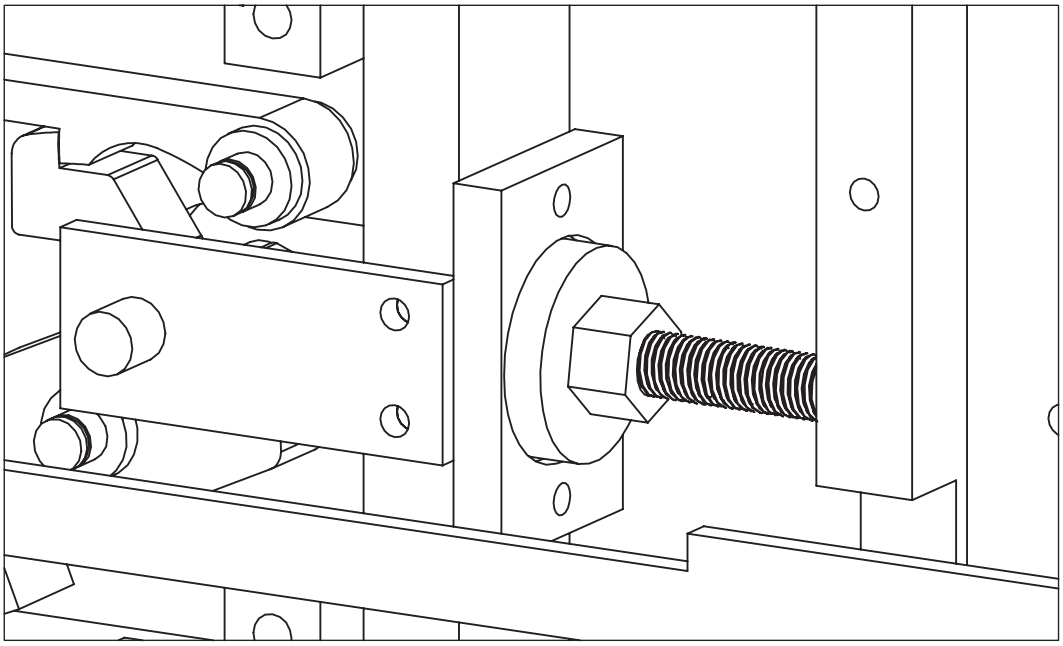
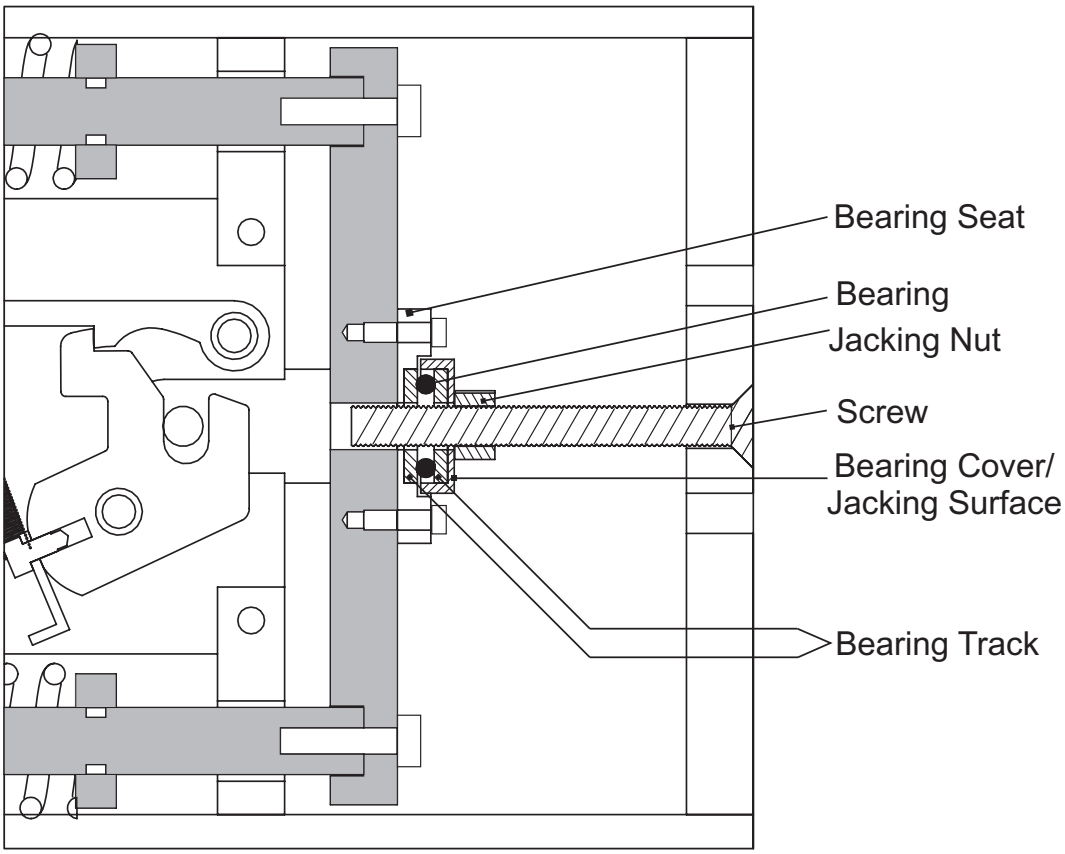


Figure 3.16: The spring driven actuator and latch mechanism for the dynamic experiment. The actuator is assembled for the dynamic RR → MR experiment.

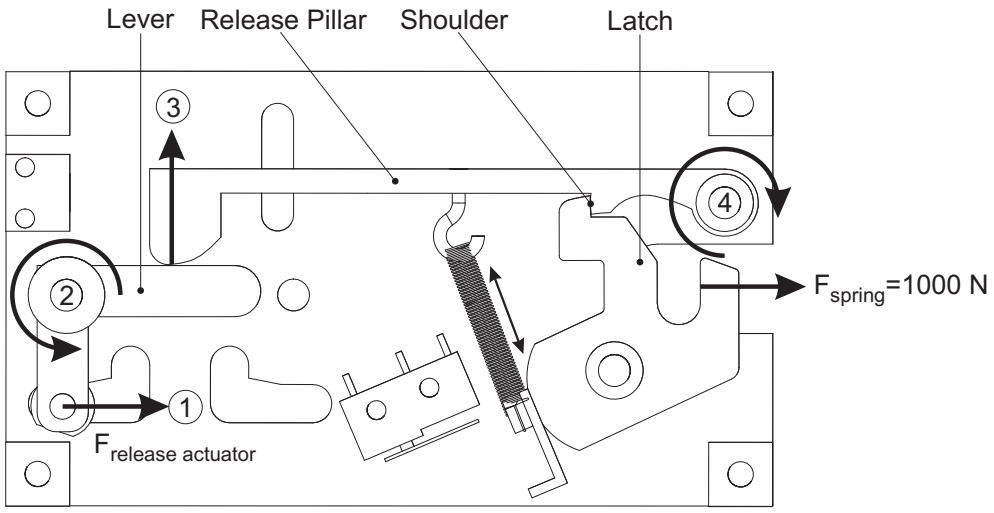


Rear Isometric View

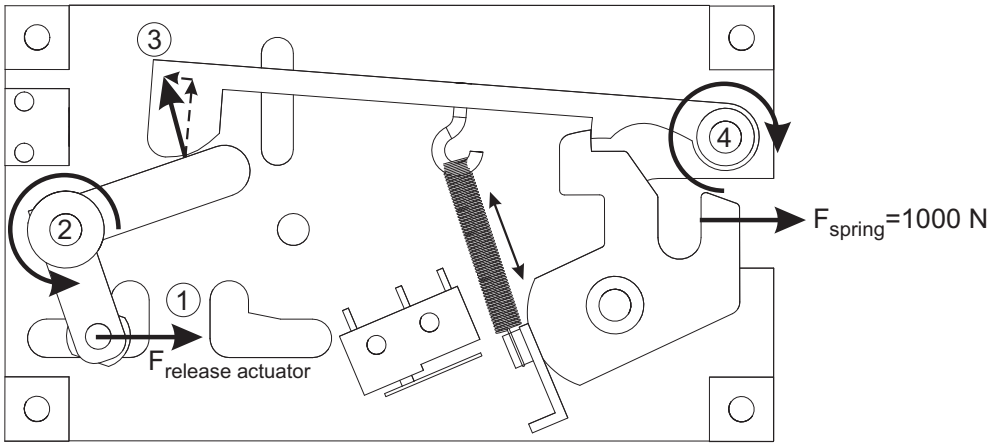


Sectioned Side View

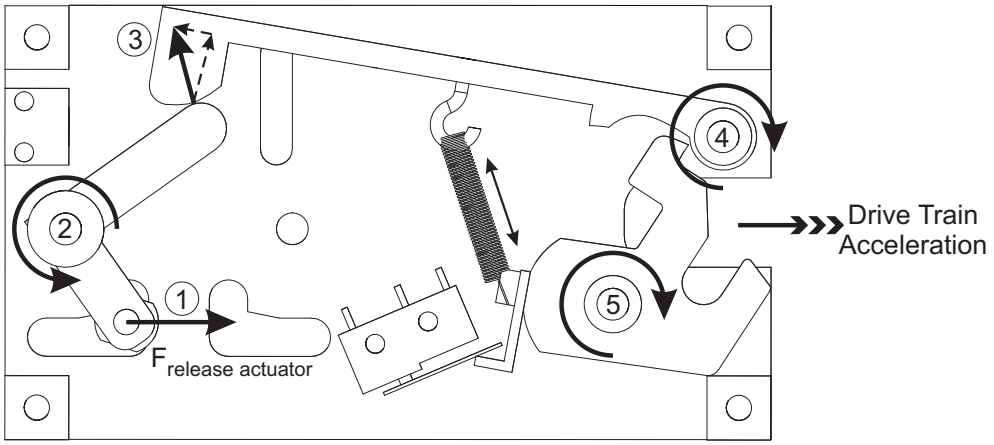
Figure 3.17: Sectioned view illustrating jacking nut/screw and thrust bearing arrangement to arm the actuator



(a) Latch in locked position under actuator load, F_{spring}



(b) 1. Movement of latch release actuator → 2. Rotation of lever → 3. Lever acting on release pillar → 4. Rotation of release pillar away from latch



(c) The release pillar is moved sufficiently away from the latch to release the actuator load

Figure 3.18: A series of CAD drawings illustrating the operation of the latch release mechanism

pillar when engaged. During an experiment the safety pin is disengaged only after the free stream flow has stabilised, before the latch mechanism releases the wedge actuation load. The safety pin is disengaged remotely by energising a solenoid. Technical specifications of the solenoid are included in Appendix C.

Releasing the Actuation Load

Figure 3.18 illustrates the sequence of events, labelled 1 - 5, that describe the operation of the latch mechanism to release the spring load, F_{spring}. The latch may be released by rotating the release pillar about its pivot point away from the latch. This is achieved with the actuation of a lever that acts against the release pillar. When the shoulder of the release pillar is moved sufficiently far away from the latch mating surface the latch is free to rotate about its own rotation centre under F_{spring}. The lever is actuated with the latch release actuator installed at the rear of the rig shown in figure 3.16.

Dynamic Actuator Control Interface

The actuator is operated remotely from the tunnel control room. A control interface was designed to:

- Indicate the status of the latch mechanism to the rig operator, i.e. latched or unlatched
- Indicate the status of the safety pin to the rig operator, i.e. engaged or disengaged
- Indicate the status of the solenoid, i.e. power on or off
- Indicate the status of the release actuator, i.e. power on or off
- Switch power to the safety pin solenoid
- Switch power to the release actuator

Limit switches are installed at appropriate locations on the actuator to indicate the status of the latch mechanism and the safety pin. Illustrations of the control interface and circuit diagrams are included in Appendix C.

Operational Test Procedure

Before tunnel startup, the actuator is armed, the actuation load is secured and the safety pin is engaged. The rig cover plates are installed and the tunnel is prepared for the experiment. The tunnel operator, rig operator and camera operator are positioned in the control room. After tunnel startup, the rig operator waits for the tunnel free stream conditions to stabilise before disengaging the safety pin. When the actuator

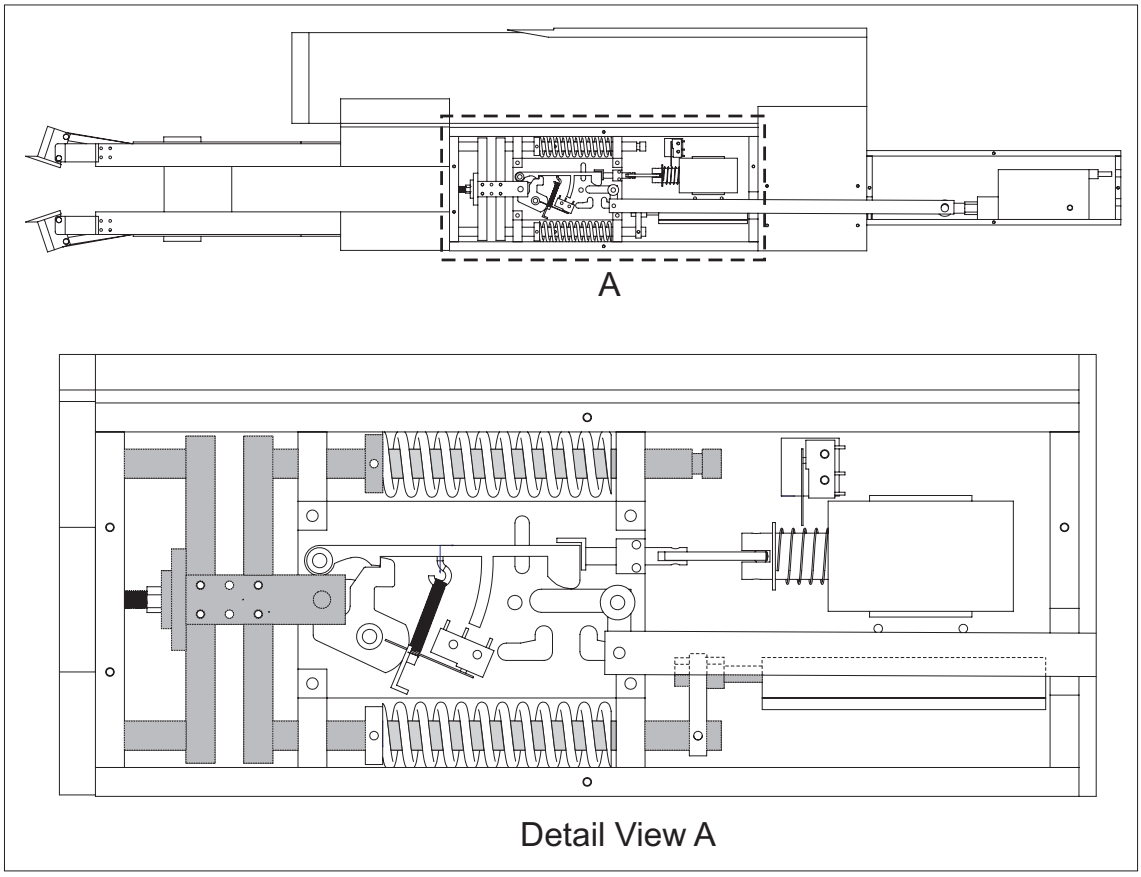


Figure 3.19: Actuator arrangement for dynamic MR → RR experiments

control interface indicates that the safety pin is disengaged, the operator drives the latch release actuator installed at the rear of the rig shown in figure 3.16, the load is released and the drive train is accelerated to achieved the required wedge rotation. The actuator control interface indicates the latch release and the camera is triggered manually. The camera is setup to capture an equal number of images on either side of the triggering event.

3.9 Sample Image and Data Reduction

Data acquisition signals from an experiment are presented in figure 3.20 for illustrative purposes. Images were prepared for measurements as shown in figure 3.21. Wedge and shock incidence measurements were made as described previously. A summary of results is presented in table 3.5. The start of the wedge rotation is indicated by the movement of the potentiometer as discussed earlier.

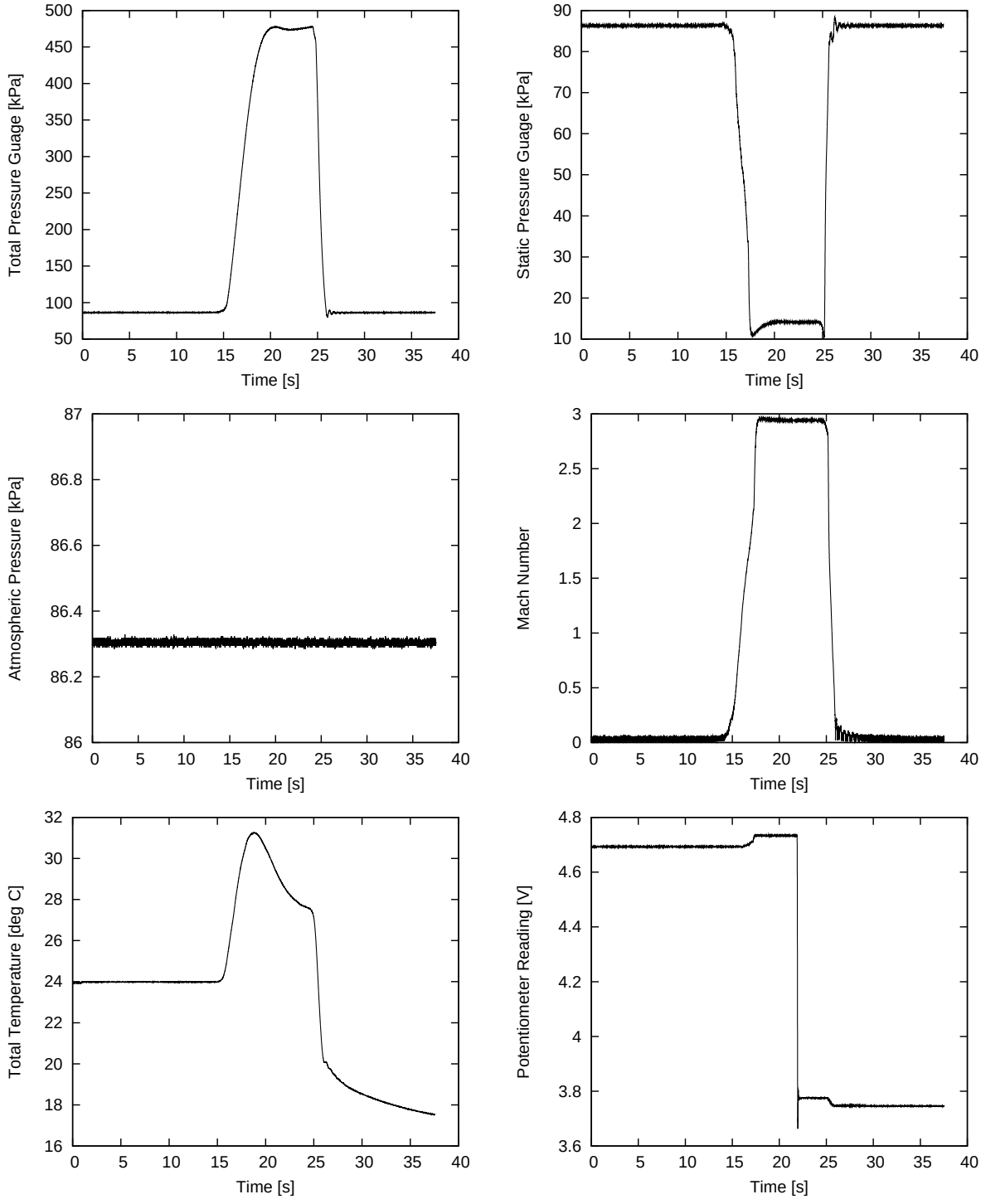


Figure 3.20: Sample data acquisition readings acquired during an experiment

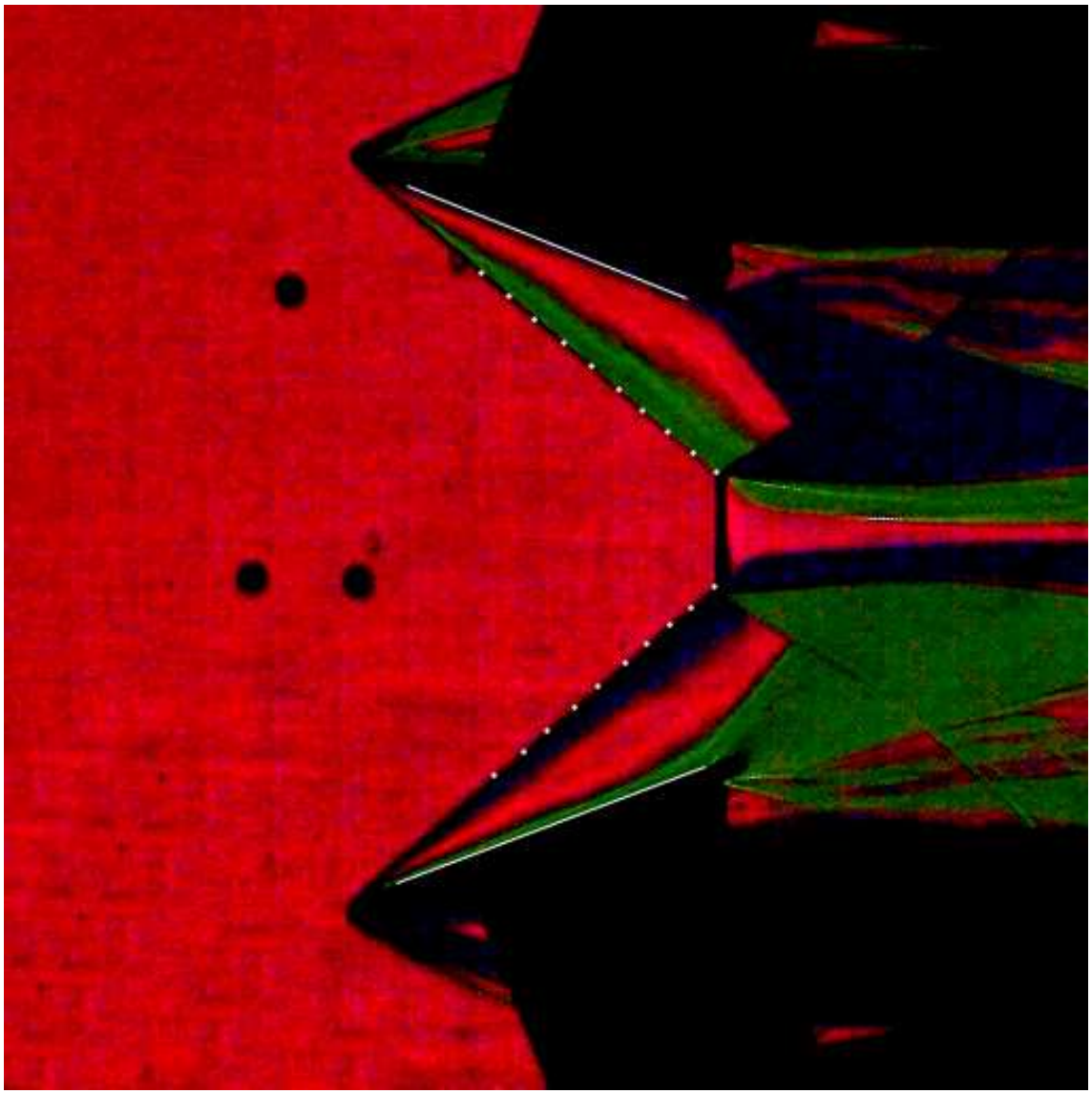


Figure 3.21: Sample image captured during a dynamic experiment and prepared for measurements. The image was captured with the high-speed digital camera at 10000 frames per second with a 1/20000 s exposure time. Image resolution : 512 × 512 pixels.

Table 3.5: A summary of results from a sample dynamic experiment at $M = 3.0$

Quantity	**Value**
Mach Number, M	2.956 ± 0.03
Total Temperature, T_O	$27.85 \pm 0.5°\text{C} = 301.0 \pm 0.5\text{K}$
Top Wedge Angle	$21.3 \pm 0.30°$
Bottom Wedge Angle	$22.0 \pm 0.30°$
Top Incident Shock Angle	$41.2 \pm 0.30°$
Bottom Incident Shock Angle	$41.6 \pm 0.30°$
Mach stem height, m	$5.8 \pm 0.16\text{mm}$
m/w	0.145 ± 0.004

3.10 Rig Development History

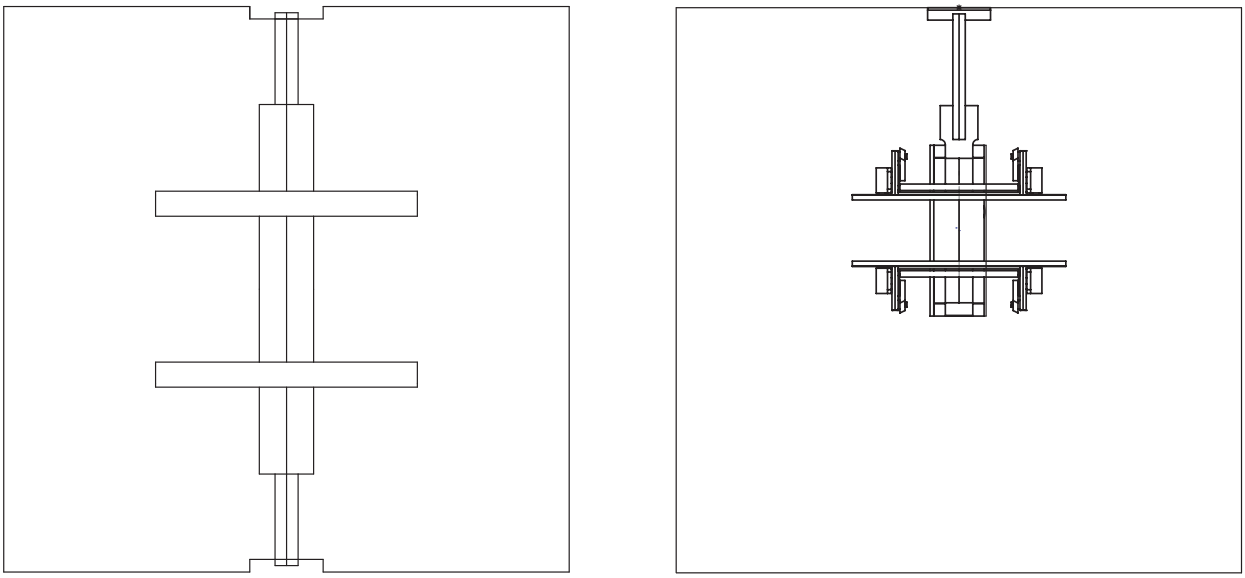
The current rig design evolved over a number of unsuccessful tunnel tests. The various previous designs will be presented briefly. Videos of the previous unsuccessful experiments are included on a data disc accompanying this thesis.

1. The first design shown in figure 3.23 was designed to accelerate larger wedges (chord = 50 mm; span = 200mm) at larger rotation speeds (maximum instantaneous wedge rotation speed = 30000 deg/s) to achieve an average $M_E = +0.1$. This required actuation loads in the order of 10000N and a larger dynamic actuator was designed. Each wedge had four drive shafts to ensure sufficient support along the span. The resultant blockage was sufficient to prevent tunnel startup. Also, the actuation loads raised concerns of operator safety and this rig was abandoned.

2. The blockage may have been reduced with a smaller, spring-driven actuator that would achieve smaller rotation speeds or with a high-density energy actuation concept that required a smaller volume, e.g pyrotechnics or hydraulics. The spring-driven actuator concept was maintained for mechanical simplicity. As shown in figure 3.24, the rig support structure was streamlined to reduce model frontal area and a smaller actuator was designed. The wedge had $w = 20$mm with $b = 93$mm. The blockage problem was resolved, but the size of the flow field of interest in comparison to the total image area was too small. At this time, the larger CSIR schlieren system, with 600 mm mirrors, was used for the experiments.

3. Subsequently, a larger wedge design was considered, i.e. $w = 40$mm and $b = 170$mm span. This required modifying the support system. This is the current version of wedge and support system shown in figure 3.14. A smaller schlieren system was also designed and a focussing lens was selected to maximise sensor coverage. From the images in figure 3.25 the magnification and image quality of the new system was satisfactory. However, the latch mechanism for the dynamic actuator failed on tunnel startup. At this time, there was no safety pin and the mating surfaces on the latch and release pillar were not manufactured to the correct specification.

4. A safety pin was added to the latch mechanism and stringent manufacturing tolerances were specified to ensure a self-locking mechanism.



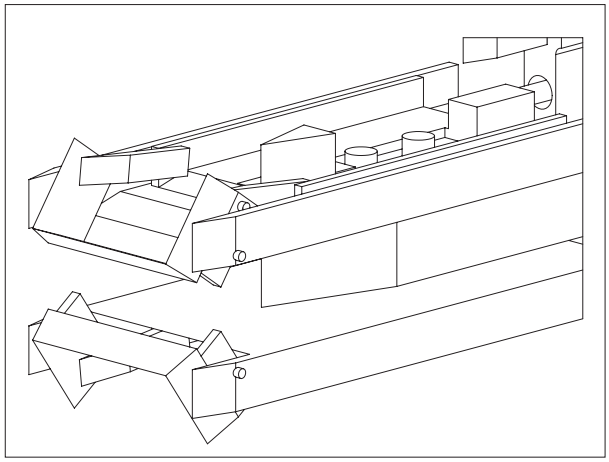
(a) First rig design

(b) Current rig design

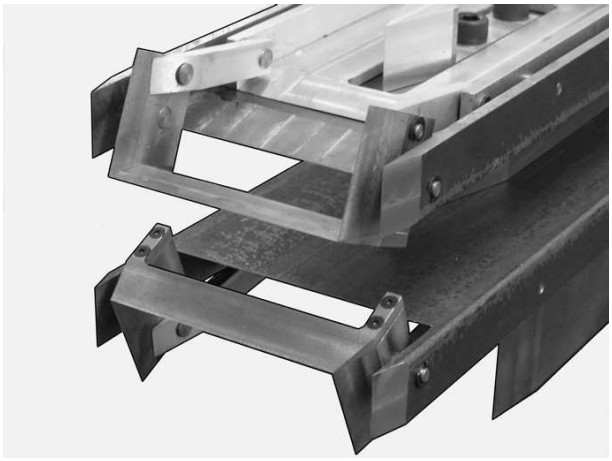
Figure 3.22: Comparison of frontal area profiles in the streamwise direction



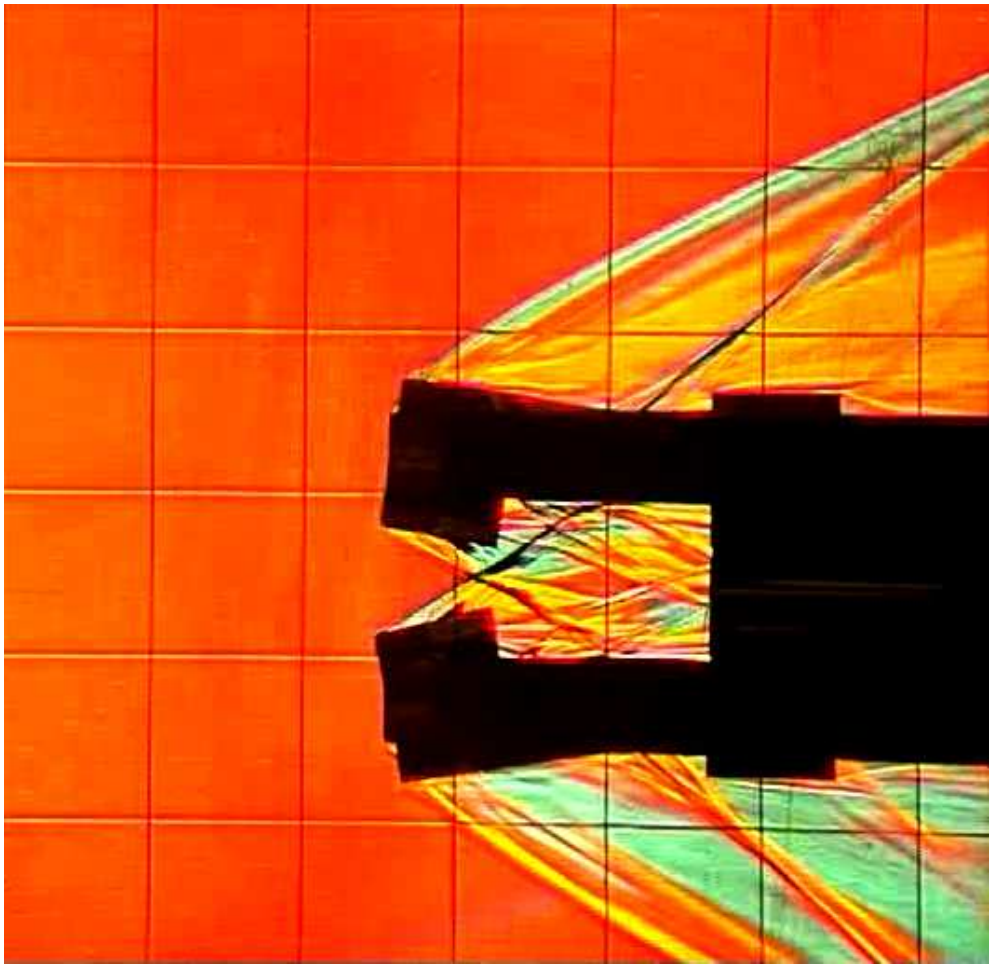
Figure 3.23: First rig design is considerably larger than the final version of the rig. Blockage was sufficiently large to prevent tunnel startup.



(a)

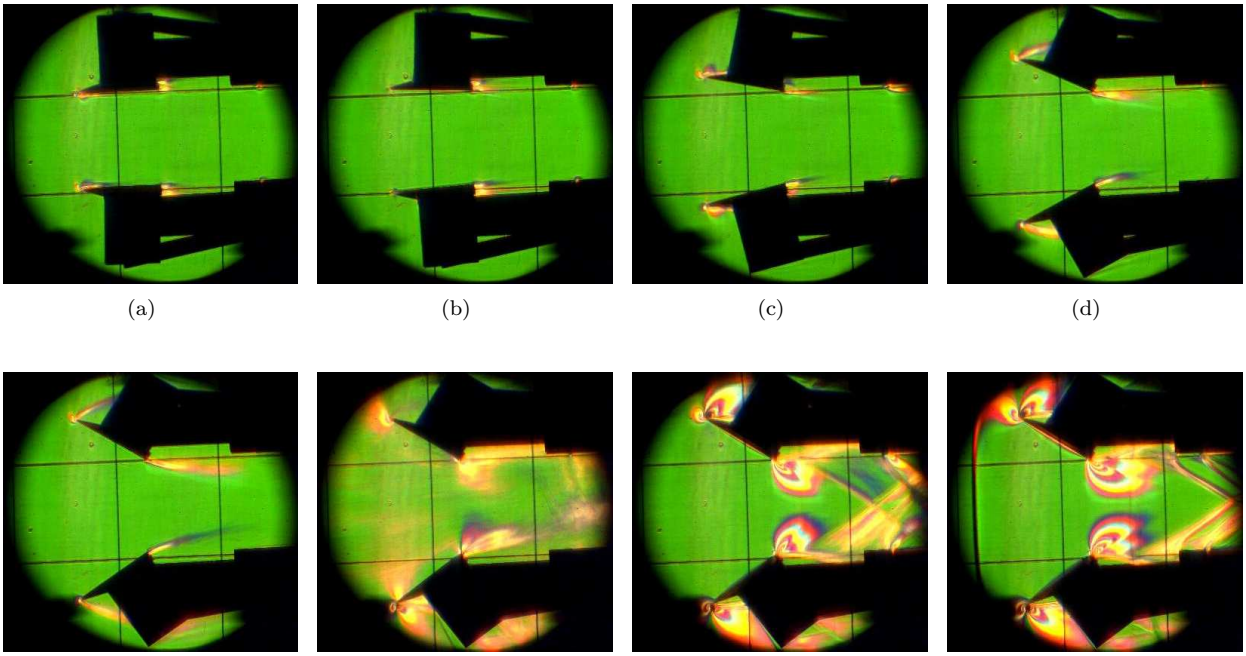


(b)



(c)

Figure 3.24: (a) Illustration and (b) photograph of the second rig design with (c) a schlieren image of the reflection pattern indicating poor optical magnification



(a) (b) (c) (d)

(e) (f) (g) (h)

Figure 3.25: A series of high-speed schlieren images showing the early release of the drive train and wedges due to failure of the latch mechanism on tunnel startup. The detached bow wave, after the flow conditions stabilised, can be seen on the last frame, well after the latch has been released. The new optics have the desired magnification.

3.11 Conclusion

All experiments were conducted in the 450mm × 450mm blow-down supersonic wind tunnel at the Council for Scientific and Industrial Research in South Africa at approximately $M = 2.0$ and 3.0. Free stream tunnel conditions were acquired with a National Instruments data acquisition system, viz. test section static pressure, total pressure and total temperature. Test section Mach number and static temperature were derived. Flow-visualisation was achieved with a standard z-type schlieren system. High-speed imaging was done with a Photron-Ultima APX-RS at 10000 fps for the dynamic experiments and at 250 fps for the steady state experiments. The optical measurement technique was presented and the uncertainties in angular and distance measurements were quantified, i.e. $\delta\theta_w, \delta\phi = \pm 0.03^\circ$ and $\delta m/w = \pm 0.004$. The rig consists of two large aspect ratio wedges with $b/w = 4.25$, arranged and actuated symmetrically about a horizontal image plane. The rig includes a servo-driven actuator that rotates the wedges gradually between 5 and 10 deg/s to generate steady state data and a spring-driven actuator to generate rapid wedge rotation in the dynamic experiments. The actuator for the dynamic experiments accelerated the drive train at approximately 1000m.s^{-2} at release and the wedges achieved a maximum instantaneous rotation speed of approximately 11000 deg/s i.e. $M_E = +0.033$.

Chapter 4

Computational Method

4.1 Introduction

The dynamic effect of rapid wedge rotation on the transition between two-dimensional (2D) regular and Mach reflection of shock waves in an ideal, steady, supersonic free stream is of primary interest in this investigation. This is explored with experimental and numerical methods. The experimental method was discussed in chapter 3. This chapter presents details of the numerical method.

Numerical solution of the 2D Euler equations are used to simulate the dynamic experiments and to extend the investigation beyond the capability of the existing experimental facility to investigate the effect of pivot point, initial incidence and rotation speed on RR $\leftrightarrow$ MR transition.

An Euler code was developed at the University of Witwatersrand by Felthun [11] and was used for all transient flow simulations in this work. The use of Fluent V 12.0 was explored to model viscous effects in the dynamic case, but was eventually only used for steady state, inviscid simulations where required. This chapter describes the relevant aspects of both codes briefly. Relevant modelling issues identified in Fluent are discussed. Results of grid sensitivity studies are also presented.

4.2 Code Description : Euler Code

The Euler code used in this investigation was developed specifically for the solution of moving boundary problems in compressible flows. It was previously used to simulate the rapidly rotating wedge (see Felthun & Skews [12]). The code is a vertex centred, arbitrary Lagrangian Eulerian finite volume scheme for unstructured triangular meshes. The Euler equations are solved with second-order accuracy. AUSM+ as formulated by Liou [33] is implemented for the calculation of convective fluxes across cell interfaces. Node redistribution during boundary movement is implemented every time step with Laplacian smoothing. A

mesh adaption routine was implemented to avoid excessive element deformation. The mesh adaption routine includes point insertion (for mesh refinement), edge collapsing (for mesh coarsening) and edge swapping (to optimise element quality). The in-house code was not optimised for solver speed, and Fluent V 12.0 was used for all steady state, inviscid flow calculations. Fluent V 12.0 has a compressible, density-based solver for the Euler and Navier-Stokes equations with adaptive refinement for the resolution of flow field gradients. First-order accuracy on triangular meshes was used. The Euler code has proved practical for the solution of 2D problems, but has limitations in solving three-dimensional (3D) problems adequately. Three-dimensional computations are beyond the scope of this work.

4.3 Code Description : Fluent V 12.0

Fluent has a 2D and 3D compressible, density based solver for the Euler and Navier-Stokes equations on structured and unstructured meshes. It has a first, second and third-order accurate solver with a custom version of AUSM+, suited to shock capture. Mesh adaption is also available.

The second and third order schemes proved unstable for the simulation of a steady MR. The solver instability arises from the shear layer instability downstream of the triple point. Only the first order scheme proved stable in this case. Fluent has been developed for parallel computing and has a faster solver than the available in-house code.

The moving mesh capability was explored for the rapidly rotating wedge case. Fluent incorporates spring-based mesh smoothing and a remeshing algorithm for transient, moving boundary problems. In the spring-based model of Farhat [10] the entire meshed domain is viewed as a structural system with stiffness provided by the element edges. Each edge is modelled as a spring with stiffness inversely proportional to the element edge length. As the edge shortens, its stiffness increases, reducing further deformation of the edge. This method is successful in cases with small boundary movement, but does not avoid edge crossing for larger boundary movement. Fluent rebuilds/remeshes areas of the domain where elements violate a user-specified edge size range and skewness value to prevent edge crossing. However, the remeshing algorithm itself does not have explicit control of the size and skewness of the new elements.

On their own, mesh smoothing and remeshing in Fluent were able to redistribute nodes and remesh the entire domain appropriately for the rapidly rotating wedge. However, adaptive refinement was necessary in conjunction with mesh smoothing and remeshing to resolve the shock wave system adequately, while maintaining practical solution times. The addition of mesh refinement introduced a modelling issue. Fluent performs mesh adaption with a non-conformal mesh topology as opposed to the conformal topology used

in the in-house Euler code as illustrated in figure 4.1. In the former approach, data must be interpolated across non-conformal interfaces in the mesh. Spurious flow features were generated in regions of the mesh with excessive skewness, especially those regions in proximity of the non-conformal interfaces (see figure 4.2). Currently, there is insufficient control of element quality to model the rapidly rotating wedge in Fluent. The remeshing algorithm only has implicit control of the element quality as mentioned earlier. Due to this limitation, Fluent was used for steady state simulations only and the in-house code for all dynamic simulations.

4.4 Computational Model

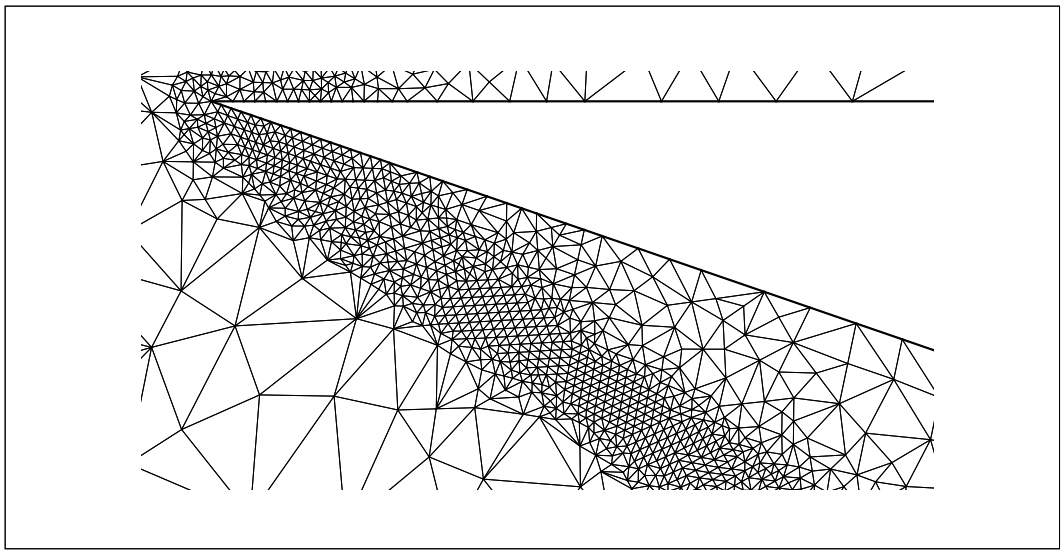
The steady state cases were simulated in Fluent and all dynamic cases were simulated with the in-house Euler code developed by Felthun [11]. Felthun & Skews [12] previously demonstrated the ability of the in-house Euler code to predict the theoretical RR $\leftrightarrow$ MR transition conditions at $M = 3.0$.

A fundamental issue is the modelling of the steady RR $\rightarrow$ MR transition experiment in the strong-reflection region in a facility with sufficient free stream noise to suppress hysteresis. If the free stream noise levels are large enough, RR $\rightarrow$ MR transition will occur at the von Neumann condition, whereas an Euler or Navier-Stokes CFD code will predict transition at the detachment condition. The effect of rapid rotation on RR $\rightarrow$ MR transition as well as the validity of the Euler equations under these conditions will be assessed and discussed in chapter 6.

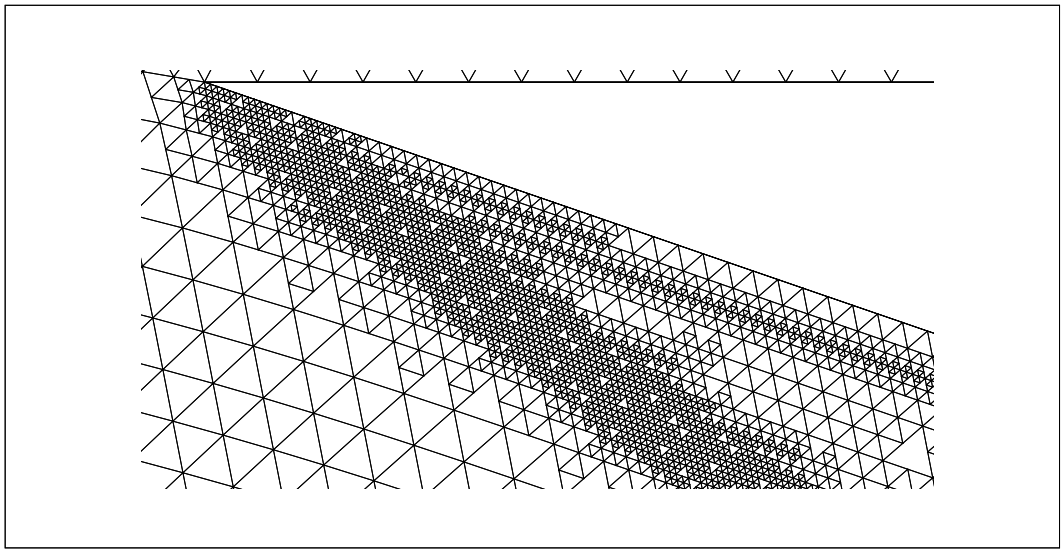
For steady MR $\rightarrow$ RR transition, Ivanov et al. [24] demonstrated close agreement in ϕ_T between experimental measurements and Euler simulation results at $M = 4.0$. Both results recorded $\phi_T \approx \phi_N$, indicating that the Euler equations are sufficient to predict ϕ_T for MR $\rightarrow$ RR transition. The effect of rapid rotation on MR $\rightarrow$ RR transition and the validity of the Euler equations here will be evaluated in chapter 7.

Figure 4.3 illustrates the flow domain boundaries of the grid for the experimental model. As the flow at the trailing edge is supersonic, the geometry downstream of the wedge was not modelled. As the wedge wake flow was not modelled, the exit dimensions change during the simulation. The flow was modelled as inviscid and all solid surfaces were modelled as "slip" walls.

The model rotation centre in the experiment is indicated in figure 4.3. The vertical movement of the trailing edge between $\theta_w = 2.0°$ and $\theta_w = 25°$ is approximately 2.1% of the wedge chord. This variation is small, but its effect on transition is addressed in Chapter 6 with the aid of numerical simulation.

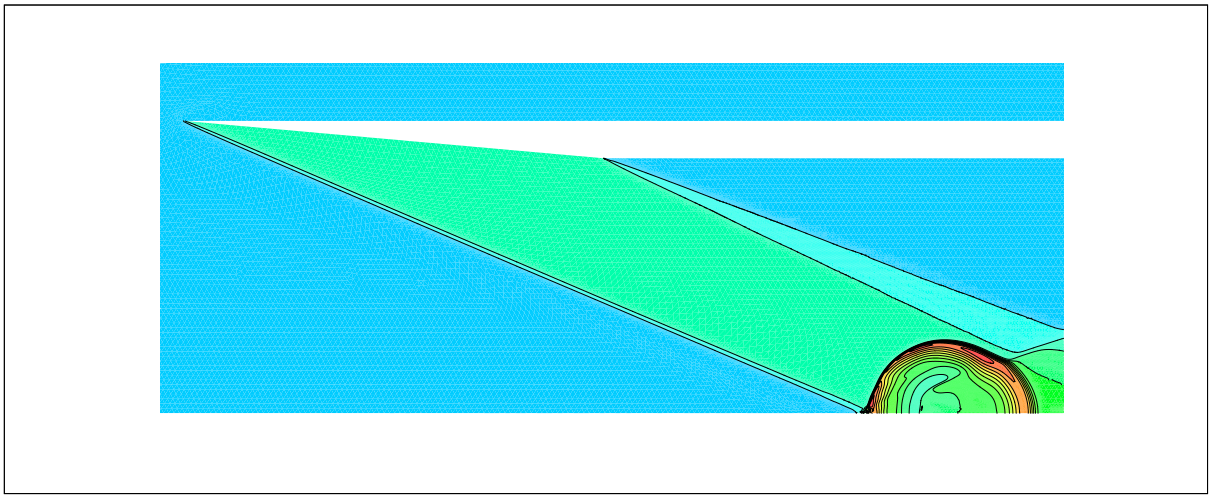


(a)

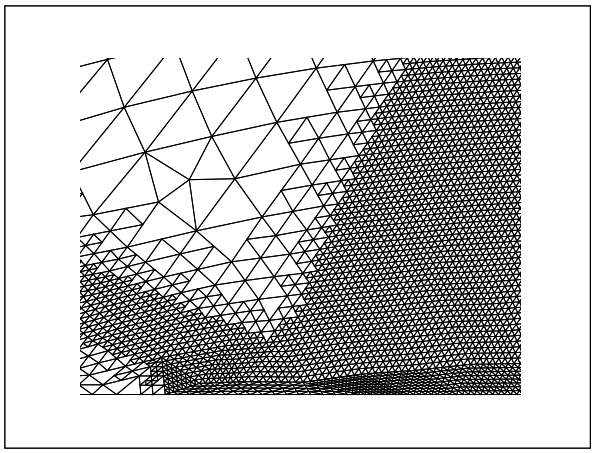


(b)

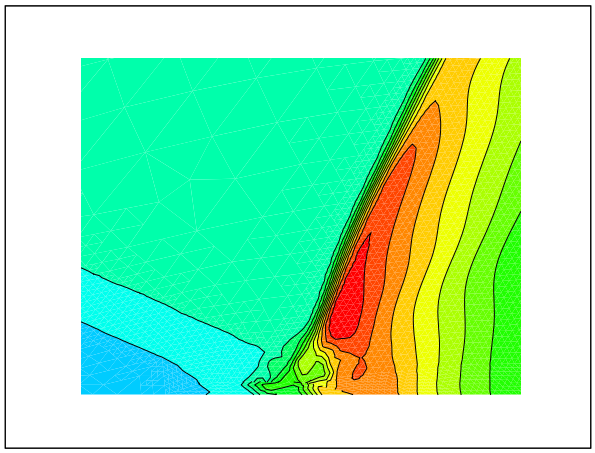
Figure 4.1: (a) Conformal mesh topology in the in-house Euler code compared to (b) the non-conformal mesh topology in Fluent for mesh refinement in the region of the incident wave at the wedge leading edge



(a) Spurious flow feature arising due to poor mesh quality in the region of the reflection point



(b) Mesh near reflection point



(c) Flow field contours near reflection point

Figure 4.2: Sample spurious flow feature in Fluent flow solution due to poor mesh quality in the vicinity of the reflection point

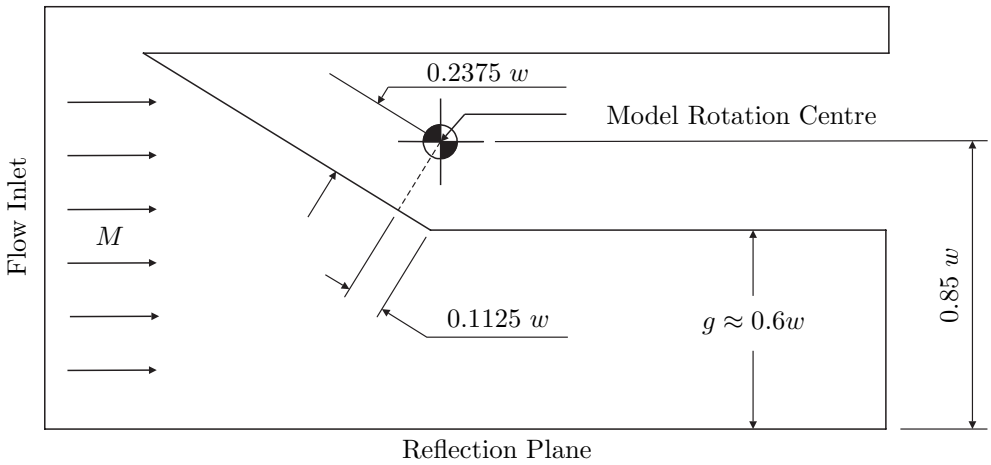


Figure 4.3: Schematic of computational model for simulation of the experiment

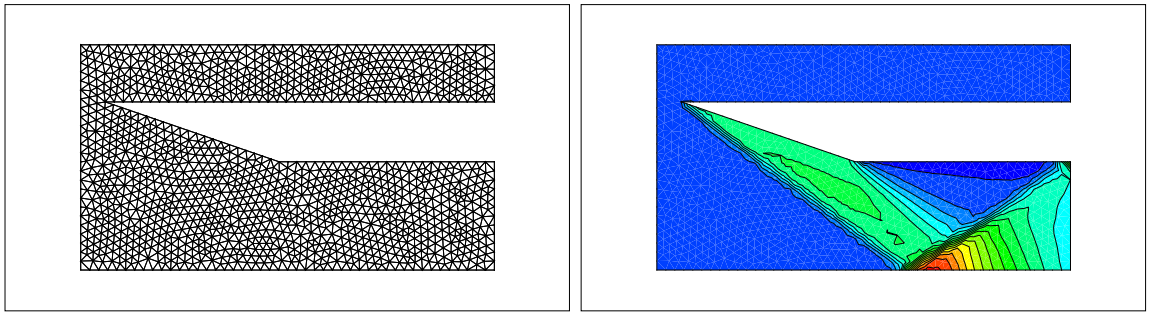
4.5 Dynamic Solution Procedure

For each dynamic simulation, a steady, initial, grid independent solution was computed before the wedge was moved. This was achieved by computing a solution on a coarse mesh and performing successive mesh refinements (and mesh coarsenings) to resolve the flow field adequately. The flow solver is run between successive passes of the mesh adaption routine to recalculate the flow field on the adapted mesh. Figure 4.4 illustrates how each pass of the adaption routine halves the previous minimum element size, d, in the regions of high flow gradients. The routine also coarsens regions of the mesh without strong flow gradients. During wedge movement, Laplacian smoothing is executed at each time step and the adaption routine is executed at user-specified intervals. For the modelling of flows with an initial Mach stem, long computation times and fine mesh resolution was necessary to achieve a steady, grid independent result.

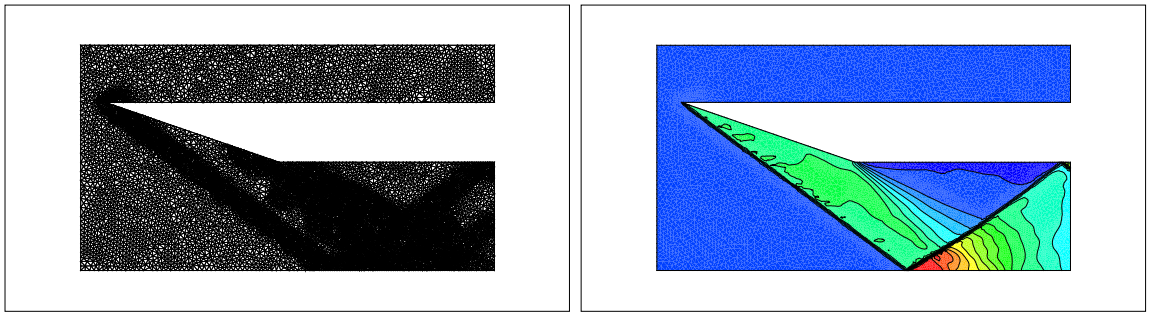
4.6 Grid Sensitivity Studies

Fluent was used for all steady state simulations and the in-house Euler code was used for all dynamic simulations. A grid sensitivity study was performed on a static, 2D wedge with $g/w = 0.56$ and $\phi = 40.0°$ at $M = 4.0$ in Fluent to determine the sensitivity of computed Mach stem height to grid element size. Ivanov et al. [24] published the result of a 2D Euler calculation of the Mach stem height for this configuration (see figure 3.1 in Chapter 3). Figure 4.5(a) shows the convergence of computed Mach stem height with the reduction in minimum element size. There is also close agreement to the predicted Mach stem height published by Ivanov et al. [24].

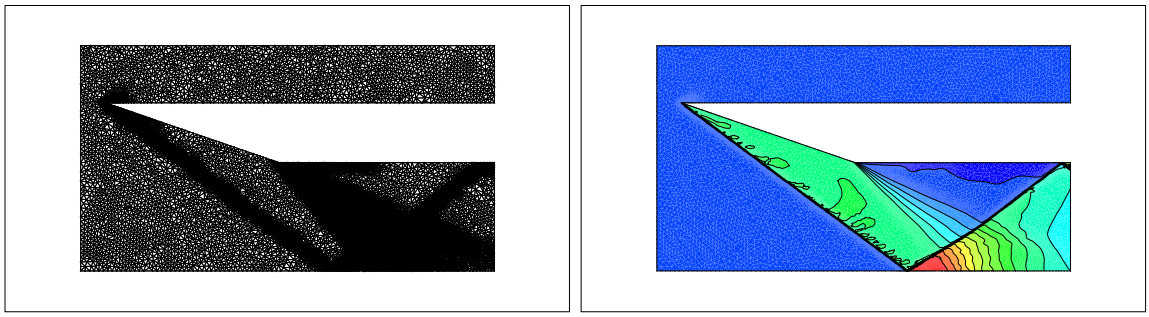
In addition, simulations of a rapidly rotating wedge, with varying minimum element size were done with the in-house Euler code to determine the dependence of the computed dynamic RR $\rightarrow$ MR transition point on minimum mesh element size. A steady RR was established at an initial wedge incidence, $\theta_{wi} = 19.0°$, in a $M = 2.98$ free stream and the wedge incidence was increased rapidly at $M_E = +0.1$ until transition to MR. The rotation point was the same as the model in the experiment shown in figure 4.3. The variation of ϕ_T with minimum element size is shown in figure 4.5(b). The difference in ϕ_T with the two finest grid resolutions is approximately 0.1°. At zero element size, the extrapolated $\phi_T \approx 40.57°$, 0.03° less than ϕ_T with the finest grid. Uncertainty in shock incidence measurement from flow field contours is estimated at approximately $\delta\phi = \pm 0.2°$.



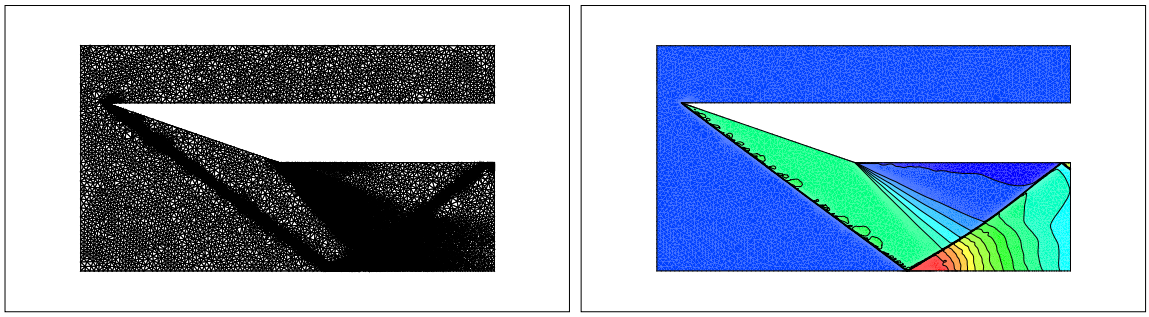
(a) Initial coarse mesh and solution without local refinement, $d/w = 0.05$



(b) The first pass of the mesh adaption routine refines the background mesh such that $d/w = 0.025$ in the background and elements within the shocks and expansion fan are halved such that $d/w = 0.0125$

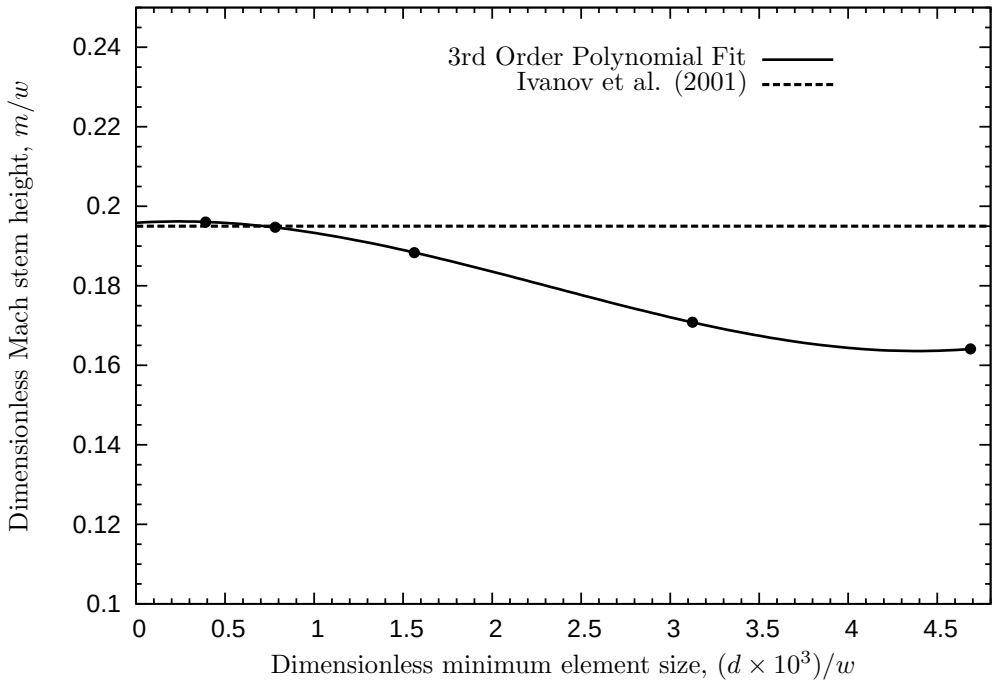


(c) The second pass of the mesh adaption routine refines elements within the shocks and expansion fan only, $d/w = 0.00625$

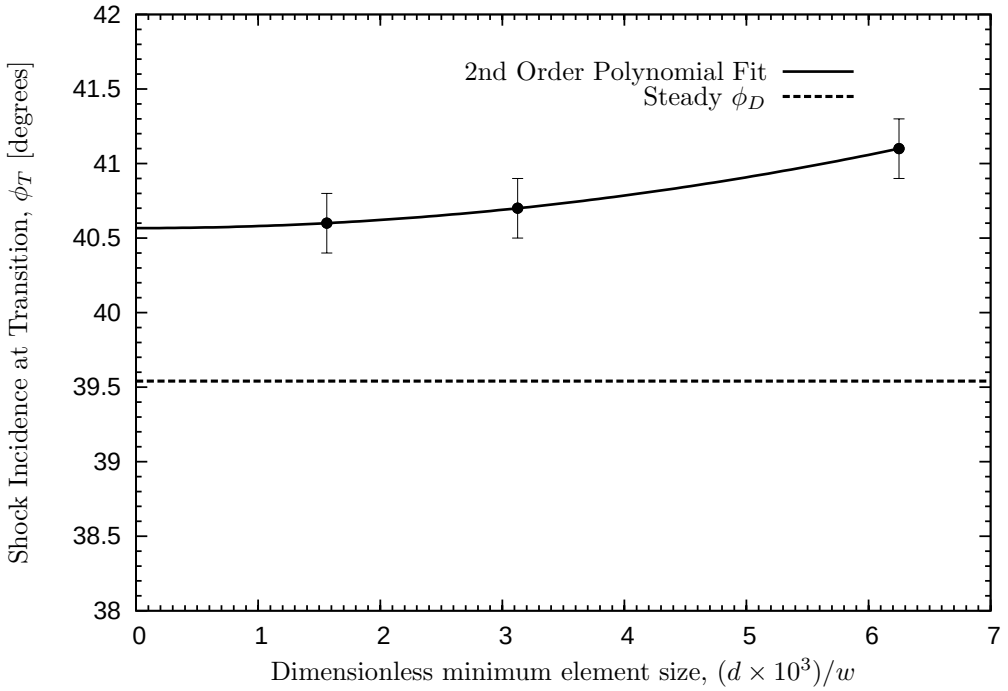


(d) The third pass of the mesh adaption routine refines elements within the shocks and expansion fan only, $d/w = 0.003125$

Figure 4.4: Series of images illustrating the successive adaption of an initial coarse mesh to establish an initial, grid independent, steady solution. Corresponding computed density contours appear on the right hand side.



(a) Computed Mach stem height variation with minimum element size in Fluent at $\phi = 40.0°$, $M = 4.0$, $g/w = 0.56$. The solid line is a third-order polynomial fit to the data and is used to extrapolate m/w at zero d.



(b) Variation of computed ϕ_T with minimum element size with the in-house Euler code for $M_E = +0.1$ at $M = 2.98$. The solid line is a second-order polynomial fit to the data and is used to extrapolate ϕ_T at zero d.

Figure 4.5: Results from CFD grid sensitivity assessment for a static and dynamic simulation

Table 4.1: Computed Mach stem heights compared to simulation results published by Ivanov et al. [24] for a stationary 2D wedge at $M = 4.0$, $g/w = 0.56$

ϕ	Computed m/w	Published m/w	$\mid \Delta m \mid$ [% of w]	CFD Code
36.0°	0.048825	0.05	0.1	Fluent
40.0°	0.196	0.195	0.1	Fluent
44.0°	0.40415	0.4	0.4	Fluent
44.0°	0.404	0.4	0.4	In-house

4.7 Fluent Benchmarking

In addition to the steady configuration modelled in section 4.6, Ivanov et al. [24] also published 2D, steady Mach stem height data at $\phi = 36.0°$, within the dual solution domain, and at $\phi = 44.0°$, outside the dual solution domain (see figure 3.1 in Chapter 3). There is confidence in their 2D Euler predictions due to the close agreement between results of the 3D simulations and experiments with the finite aspect ratio wedge on the same graph. Both cases were modelled in Fluent. The in-house Euler code was used to simulate the wedge with $\phi = 44.0°$ only. Simulation results are summarised in table 4.1. There is good agreement between the predictions made here and the published data, with the maximum deviation, Δm approximately 0.4% of the wedge chord. The favourable comparison provides confidence in the ability of Fluent to model the steady state case of interest.

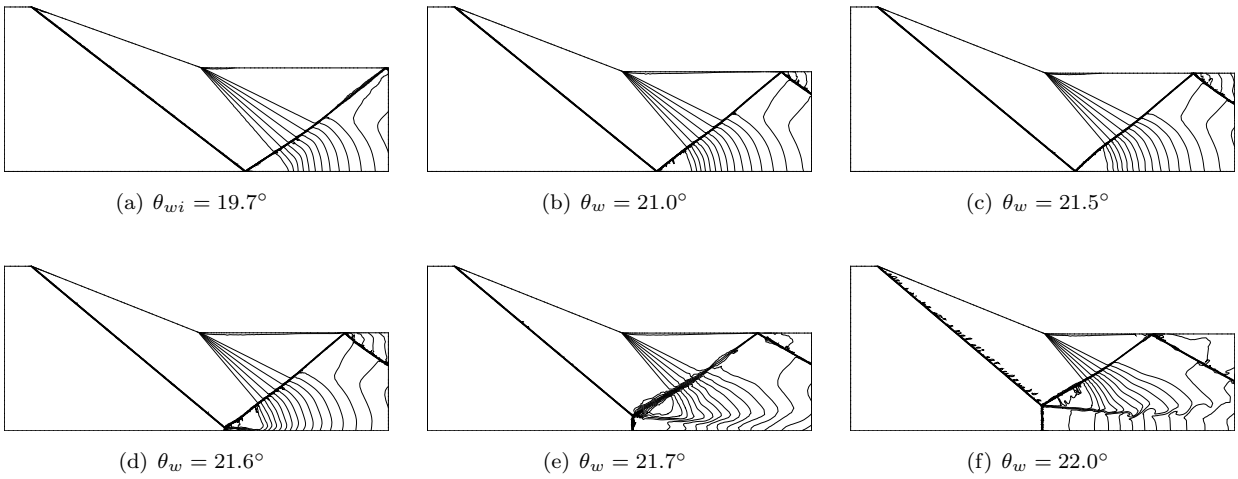
4.8 The Incidence-Induced Hysteresis Test

In the incidence-induced hysteresis test, originally proposed by Hornung et al. [18], a steady RR is established below ϕ_N and the wedge incidence is increased gradually until transition to MR. The wedge incidence is subsequently decreased until transition to RR. Ideally, RR $\rightarrow$ MR transition must occur at ϕ_D as there are no free stream disturbances in the flow simulation and the reverse transition must occur at ϕ_N. Felthun & Skews [12] previously demonstrated the ability of the in-house Euler code to model the hysteresis test at $M = 3.0$. This was repeated here at $M = 2.98$ to benchmark the CFD model rather than the code. Results are summarised in table 4.2. Computed density contours are included in figures 4.6 and 4.7.

A steady RR is established at $\phi < \phi_N$ in figure 4.6(a) and θ_w is increased at $M_E = +0.001$ such that there is no observable dynamic effect on the reflection pattern. RR was maintained through the dual solution domain. Figure 4.6(d) shows the earliest traces of a shear layer on the reflection plane. Transition is assumed 0.1° before the first appearance of the shear layer on the reflection plane at $\theta_w = 21.5°$. For RR $\rightarrow$ MR transition, $\phi_T = 39.7°$, 0.2° larger than ϕ_D. The Mach stem development beyond transition can be seen in figures 4.6(d) to 4.6(f) as θ_w increases to 22.0°.

Table 4.2: Computed values for ϕ_T for the incidence-induced hysteresis test at $M = 2.98$ in comparison to steady state, theoretical values for RR $\leftrightarrow$ MR transition

	Computed ϕ_T	Theoretical ϕ_T
RR $\rightarrow$ MR transition	39.7°	$\phi_D = 39.5°$
MR $\rightarrow$ RR transition	37.3°	$\phi_N = 37.5°$



(a) $\theta_{wi} = 19.7°$ (b) $\theta_w = 21.0°$ (c) $\theta_w = 21.5°$

(d) $\theta_w = 21.6°$ (e) $\theta_w = 21.7°$ (f) $\theta_w = 22.0°$

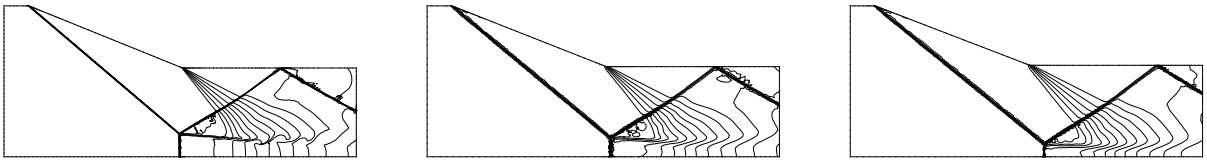
Figure 4.6: Computed density contours showing RR $\rightarrow$ MR transition close to the detachment condition condition. $M = 2.98$, $M_E = +0.001$, fixed $h/w = 0.91$.

The wedge incidence is subsequently decreased at $M_E = -0.001$ (see figures 4.7(a) to 4.7(f)) and transition to RR was observed at $\theta_w \approx 19.4°$ with $\phi_T = 37.3°$, 0.2° below ϕ_N. The deviation from ϕ_D and ϕ_N is within the value of uncertainty for shock incidence measurement of $\delta\phi \pm 0.2°$.

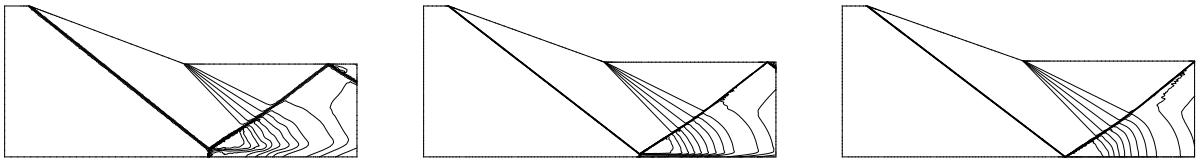
4.9 Compensation for Boundary Layer Deflection

The measured wedge motion from all dynamic experiments were used as inputs to the CFD. However, due to the boundary layer on the wedge surface in the experiment, ϕ is larger in the experiment than in the Euler simulation for the same value of θ_w. Since the flow conditions at the reflection point are critical to RR $\leftrightarrow$ MR transition, ϕ at the reflection point is critical rather than θ_w. If ϕ and consequently ϕ_T are sensitive to the time history of the flow field, it is crucial that ϕ_i and the time history of ϕ is the same between the experiment and the computation, rather than θ_{wi} and the time history of θ_w.

The value of θ_{wi} required in the inviscid simulation to match ϕ_i in the experiment is calculated from the following well-known oblique shock relation for isentropic flow (see Anderson [26]) :



(a) $\theta_{wi} = 22.0°$ (b) $\theta_w = 21.5°$ (c) $\theta_w = 21.0°$



(d) $\theta_w = 20.5°$ (e) $\theta_w = 20.0°$ (f) $\theta_w = 19.6°$

Figure 4.7: Computed density contours showing MR → RR transition close to the von Neumann condition. $M = 2.98$, $M_E = -0.001$, fixed $h/w = 0.91$.

$$\tan\theta_{wi} = \frac{(M_1^2 \sin^2\phi_i - 1)\cot\phi_i}{1 + (\frac{1}{2}(\gamma+1) - \sin^2\phi_i)M_1^2} \tag{4.1}$$

The difference between θ_{wi} derived from equation 4.1 and the measurement from experiment is the flow deflection caused by the boundary layer at the start of the motion and is labelled $\delta\theta_{BL}$. As a first approximation, it is assumed that there is no significant change in $\delta\theta_{BL}$ until transition and the measured motion profile (measured wedge incidence with time) is offset by $\delta\theta_{BL}$ to ensure that ϕ_i is matched between simulation and experiment.

It must be noted that even with this correction there must still be a difference in initial Mach stem height between the 3D experiment and the 2D simulation as discussed in chapter 3. It is incorrect to adjust θ_{wi} to achieve the measured initial Mach stem height in the experiment.

4.10 Conclusion

The in-house Euler code was used for all dynamic simulations and Fluent V 12.0 (inviscid model only) was used for all steady state predictions. The Navier-Stokes solver in Fluent was also considered initially to model the dynamic case. Numerical issues were identified that disqualified its use for the dynamic case of interest. The Euler equations are sufficient to predict steady RR ↔ MR transition. Their ability to predict dynamic RR ↔ MR transition will be explored in later chapters.

A steady and dynamic grid sensitivity study was completed with Fluent and the in-house code respectively

to determine the minimum required mesh element size.

Fluent was benchmarked against the steady, 2D Mach stem height data published by Ivanov et al. [24] for three configurations at $M = 4.0$. There was close agreement with the published data in all three cases with the maximum deviation in predicted Mach stem height, approximately 0.4% of wedge chord.

The in-house code was successfully benchmarked previously by Felthun [11] to model the incidence-induced hysteresis test originally proposed by Hornung et al. [18]. This exercise was repeated to test the integrity of the CFD model developed for this work. Steady RR $\rightarrow$ MR transition was predicted close to the detachment condition and the reverse transition was observed close to the von Neumann condition.

The Euler simulations do not account for the flow deflection caused by the wedge surface boundary layer. A simple method was proposed to correct the measured wedge motion profile used in the CFD simulations to match the initial shock incidence measured in the experiment.

Chapter 5

Steady State RR $\leftrightarrow$ MR Transition

5.1 Introduction

This chapter presents results from experiments and computations on steady, two-dimensional RR $\leftrightarrow$ MR transition in the weak and strong-reflection regions. The primary objective of the steady experiments were to determine if hysteresis could be observed in the strong-reflection region in the CSIR tunnel. Since the wedge aspect ratio is larger than 4.0, it was expected that ϕ_T would not be influenced by three-dimensional (3D) effects. These experiments were done with the servo-driven actuator described in chapter 3. Wedges were rotated symmetrically about a horizontal plane between approximately 5.0 and 10.0 deg/sec, sufficiently slow to ensure an approximately steady reflection pattern at each instant. Schlieren images were captured with the Photron Ultima APX-RS at 250 frames per second at 1024×1024 pixel resolution. Aspects of the 3D structure of the reflections will be highlighted where necessary. Movies of the experiments may be found on the accompanying data disc. Only selected images are presented in this chapter. Steady, two-dimensional (2D), Euler computations were done with Fluent and results were compared with the measurements from experiments. In this chapter, the streamwise vertical plane of symmetry will simply be referred to as the symmetry or central plane and the horizontal plane of symmetry will be referred to as the reflection plane.

5.2 A Brief Summary: The Three-Dimensional Nature of Wave Systems in an Experiment

The multi-coloured mask shown in figure 3.7(a) was used at the schlieren cut-off and limited 3D information of the reflection pattern could be inferred from the schlieren images. Relevant literature on 3D shock wave reflection is reviewed briefly.

Ivanov et al. [24] computed the 3D reflection pattern generated by a large aspect ratio, steady wedge in

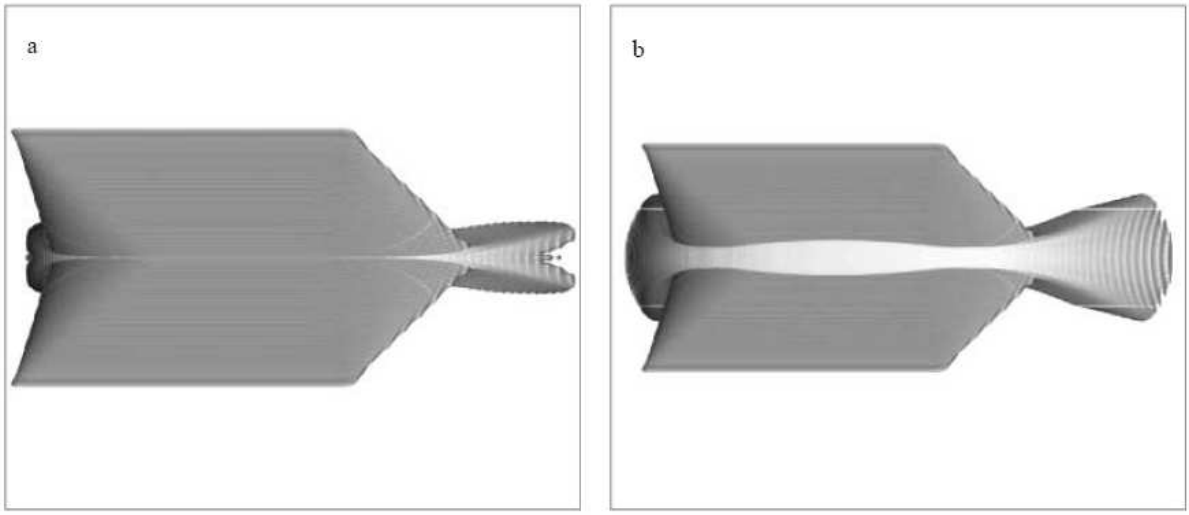


Figure 5.1: Typical 3D geometry of shock wave reflections at $M = 4.0$, computed by Ivanov et al. [24]

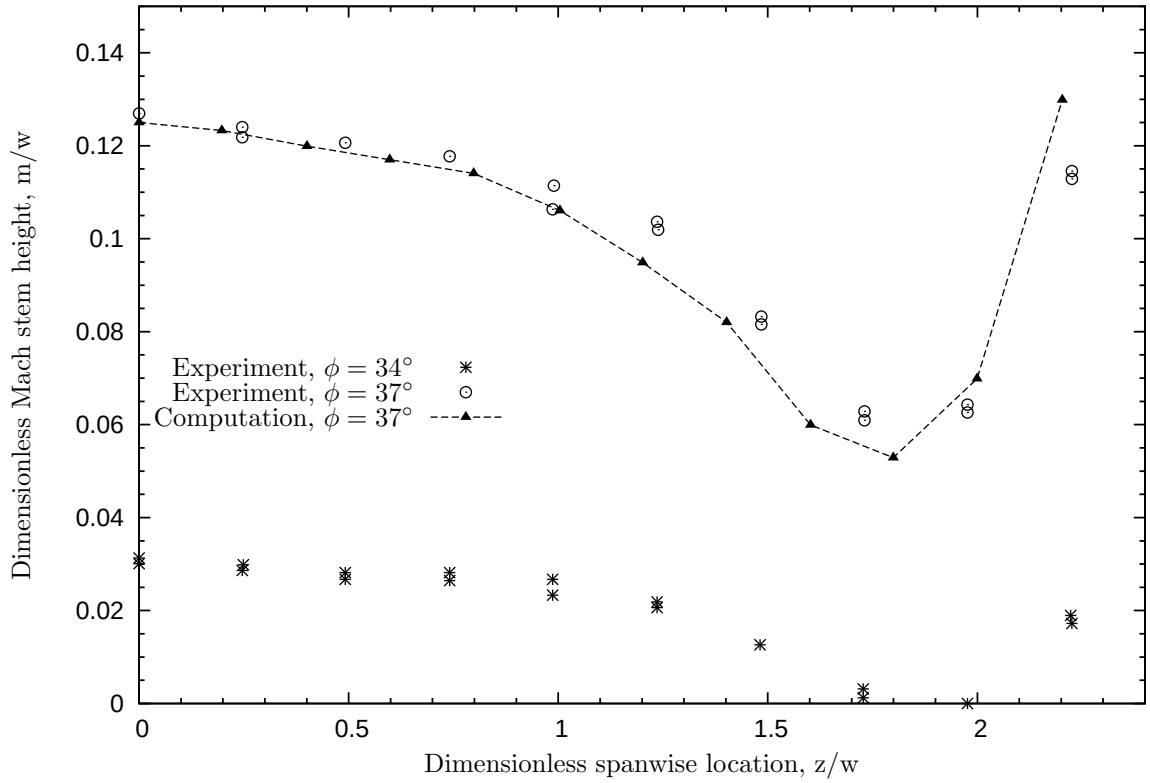


Figure 5.2: Computed and measured spanwise Mach stem height variation in a $M = 4.0$ free stream published by Ivanov et al. [24]

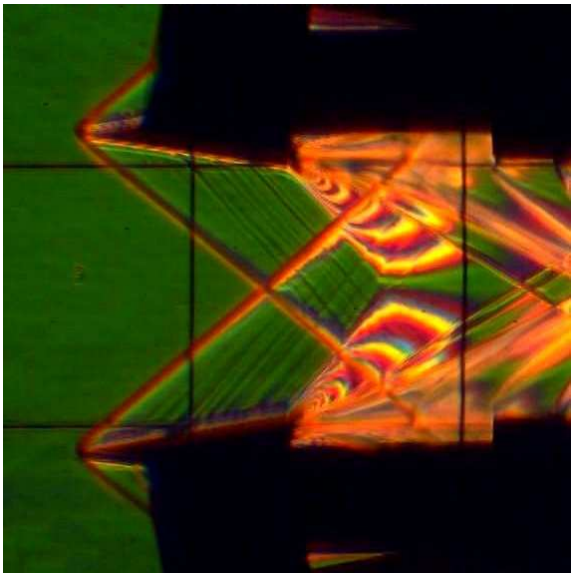
a $M = 4.0$ free stream as illustrated in figure 5.1. Spanwise Mach stem height was measured and compared to 3D computations in figure 5.2 and there was good agreement between computation and experiment and provided confidence in the 2D computations. These simulations were completed at $M = 4.0$ and effectively illustrated the 3D geometry of the reflection pattern in an experiment. In figure 5.1(a), the reflection in the plane of symmetry is RR. As one moves towards the periphery, the pattern transitions to MR close to the wedge corner. In figures 5.1(b) and 5.2, the maximum Mach stem height is in the plane of symmetry. As one moves towards the periphery there is a decrease in the Mach stem height until the minimum Mach stem height is achieved and this is followed by an increase in Mach stem height toward the periphery. There are no published results for 3D computations or experiments in the weak shock region.

5.3 Steady State Experiment in the Weak-Reflection Region

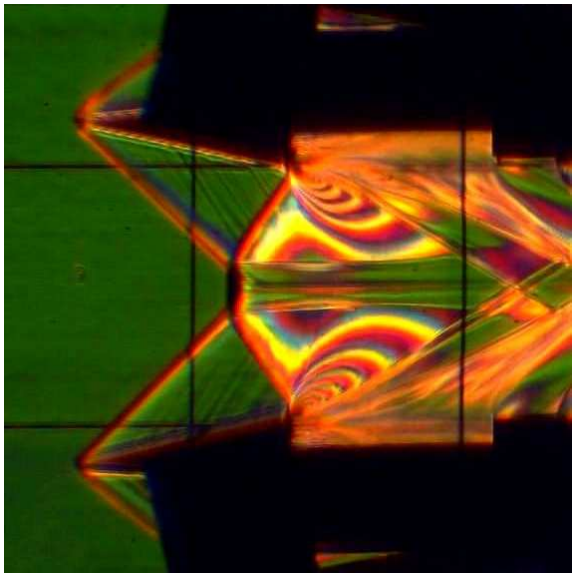
A steady state experiment was conducted in the weak-reflection range at approximately $M = 1.93$. Figure 5.6 presents a series of images from the experiment, showing the development of the reflection pattern. An initial, steady RR is established after tunnel startup. The servo motor is initially driven to increase θ_w until transition to MR. Subsequently, θ_w is reduced until transition to RR. In the weak-reflection region there is no von Neumann condition and there is a single theoretical transition point between RR and MR for the steady case, viz. the detachment condition (see figure 2.7 in chapter 2).

5.3.1 Three-dimensional Wave Structure

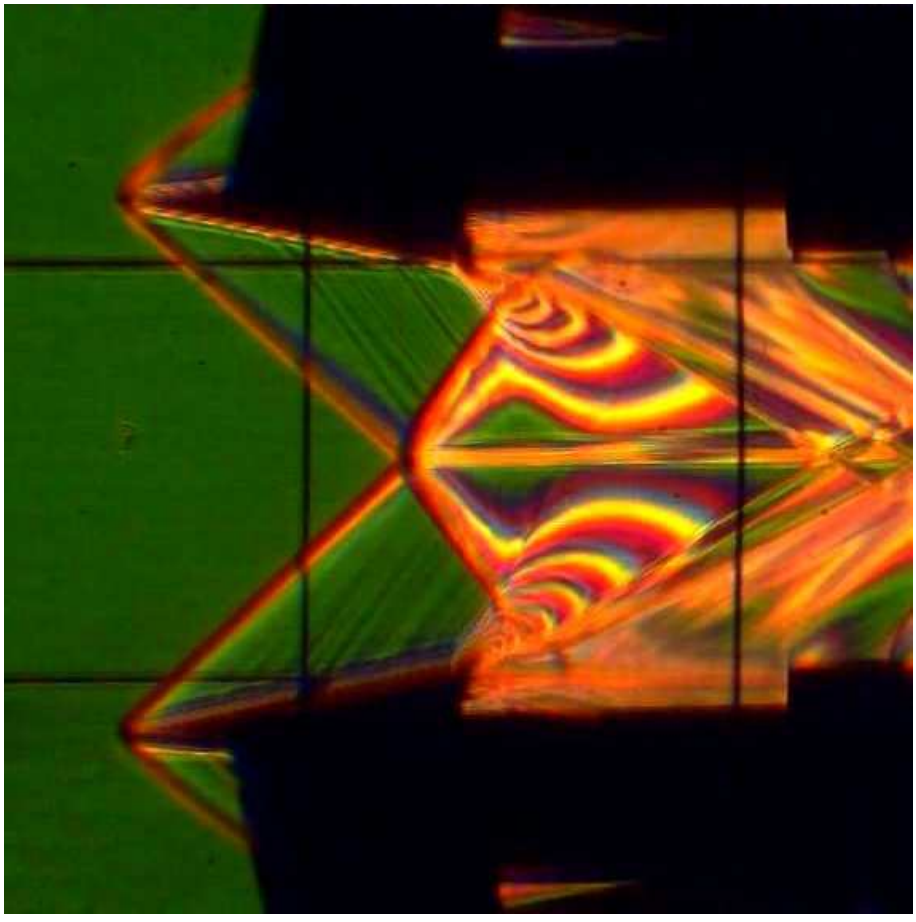
Figures 5.3(a) - 5.3(c) are sample images from the experiment and highlight particular 3D features (not shown in order). In figure 5.3(a), there is no shear layer visible, and there is RR in the plane of symmetry as well as in the wedge spanwise direction. For a larger wedge incidence in figure 5.3(c) a shear layer is observed in proximity of the reflection plane. The shear layer could emanate from the triple point of a MR at any spanwise location. The reflection in the symmetry plane (the most upstream wave front on the image) is still RR. Therefore, MR must occur elsewhere in the spanwise direction. At an even larger wedge incidence in figure 5.3(b) MR is also evident in the symmetry plane. The variation in Mach stem height in the spanwise direction is visible from the shear sheet emanating from the locus of triple points in the spanwise direction ("triple curve"). At $M = 1.93$, unlike the case investigated by Ivanov et al .[24] in figure 5.1, the minimum Mach stem height is in the symmetry plane. In this case, identifying the 2D transition point from the first appearance of the shear layer for increasing incidence is incorrect. The transition point must be extrapolated from the variation of Mach stem height with ϕ or θ_w.



(a) Central RR peripheral RR



(b) Central MR peripheral MR



(c) Central RR peripheral MR

Figure 5.3: Identification of 3D reflection structures on schlieren images from the steady state experiment at $M = 1.93$

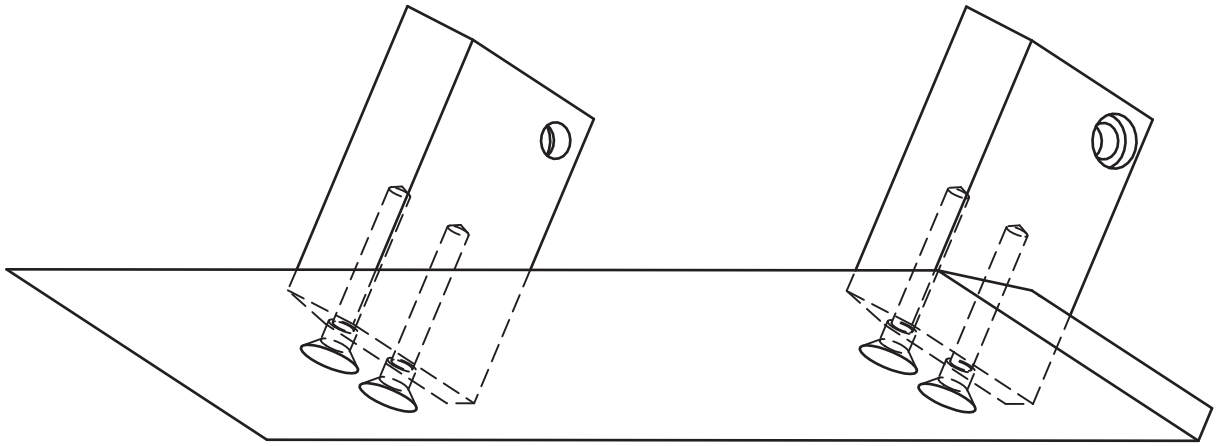


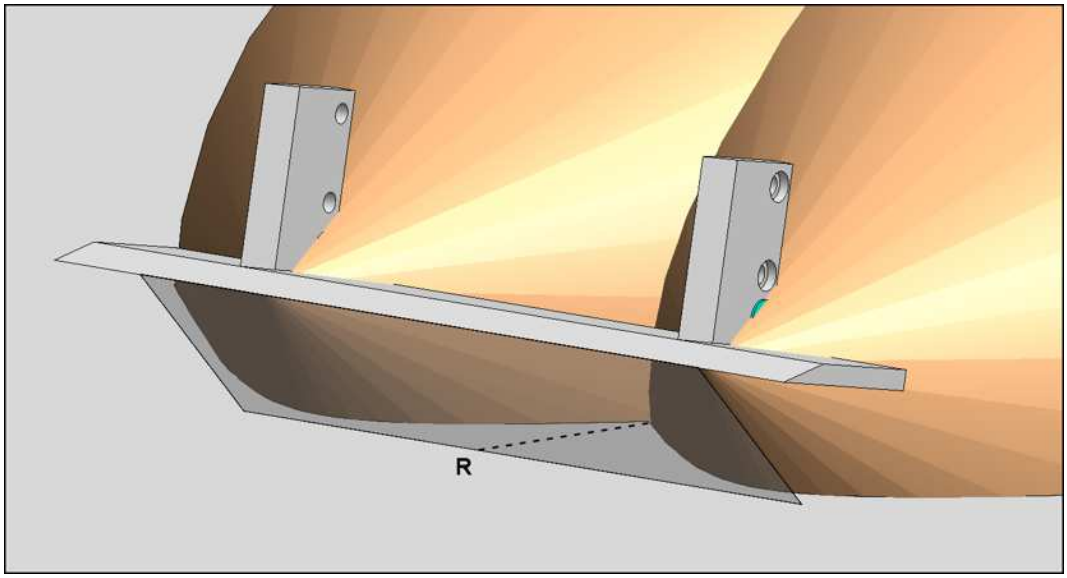
Figure 5.4: View of CAD model of wedge illustrating the location of counterbores on the stream facing surface of the wedge

5.3.2 Weak Surface Waves

The weak waves from the wedge in figures 5.3(a) to 5.3(c) are in fact generated by surface flaws. The wedge supports are attached to the wedge from the stream facing surface with countersunk screws (counterbored) as illustrated in figure 5.4. The weak waves arise from the imperfect application of wax to fill the counterbores. Figure 5.5 illustrates the boundaries of the sonic cone from the surface disturbances at the detachment condition at $M = 1.93$, i.e. $\theta \approx 12.1°$. From the 2D schlieren image, the intersection of the sonic cone on the reflection plane outside the symmetry plane can be mistaken as an interaction on the symmetry plane. In reality the sonic cone intersects the symmetry plane downstream of the reflection point on the symmetry plane and does not interact with the flow at the reflection point. At $M = 2.98$, the separation between the reflection point and the sonic cone intersection on the symmetry plane is larger. The counterbores were filled with silver-solder and polished for the dynamic experiments presented in chapters 6 and 7.

5.3.3 Experimental Results

In figure 5.6(a) a steady RR was established, before the wedge incidence was increased gradually. RR was maintained until MR developed on the periphery in frame 185. The peripheral Mach stem grew until the central reflection pattern transitioned to MR. By frame 235 the entire reflection is MR. Eventually the reflected wave intersected the deflection surface. As the wedge incidence increased further, the wave system disgorged within 3 frames, i.e. frames 256 to 258. There is a small wedge incidence range between transition and disgorge (approximately 2.0°). Subsequently, the motor direction was reversed to decrease the wedge incidence. Between frames 731 and 732 the wave system is swallowed and only RR can be seen in the plane of symmetry and MR on the periphery. By frame 780 the entire pattern transitioned to RR. The change



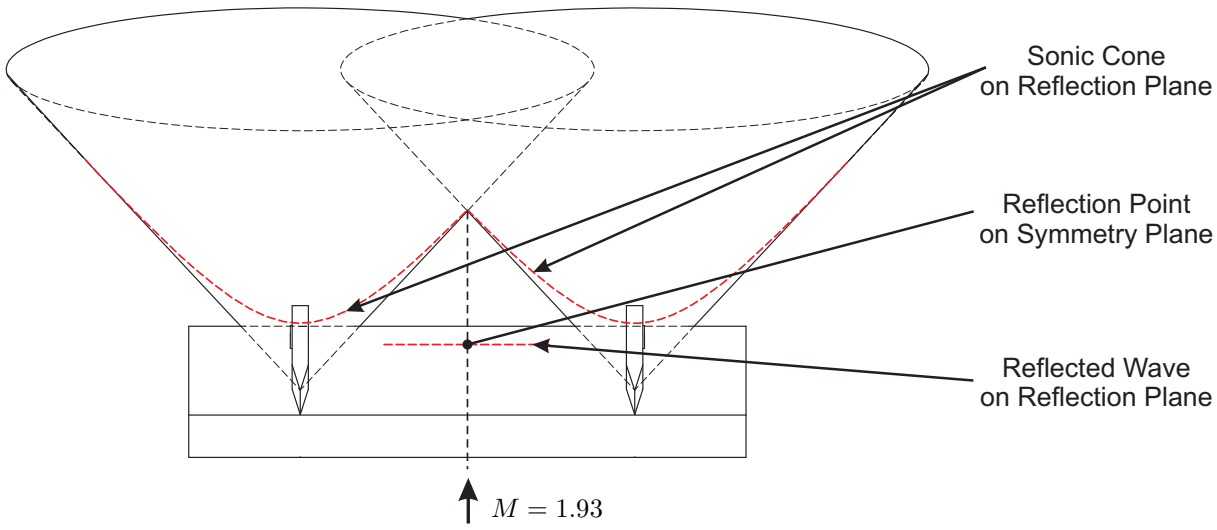


Figure 5.5: Isometric and top view identifying location of reflection point on symmetry plane with respect to sonic cone from wedge face counterbores at the detachment condition, $M = 1.93$

in incidence between frames 731 and 732 is in the order of magnitude of $\approx 0.1^\circ$ and it is unlikely that a steady MR was established in the central plane in the time between those frames. It is evident that there is hysteresis in the phenomena of shock disgorge and shock swallow, i.e. the Mach stem height just prior to disgorge is not the same as just after the wave system is swallowed. The hysteresis associated with shock disgorge and swallow, though interesting, is beyond the scope of this work and will not be investigated further.

The implication of not having observed MR in the plane of symmetry for decreasing incidence, is that it will not be possible to setup an initial, steady MR at this free stream condition with a fixed initial incidence with this setup. Due to the way in which the tunnel flow starts, the flow would setup an initial disgorged wave system or a steady RR in the plane of symmetry for a fixed initial incidence.

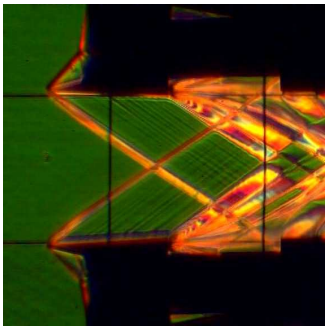
Fluent was used to simulate the steady case. Results are summarised in table 5.1 and figure 5.9.

5.4 Steady State Experiment in the Strong-Reflection Region

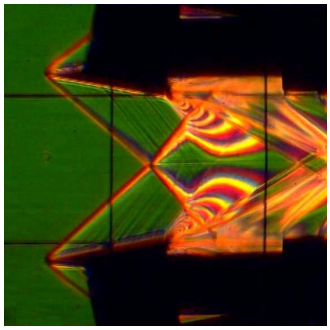
A steady experiment was conducted in the strong-reflection region at approximately $M = 2.98$. Figure 5.8 presents a series of images from the experiment, showing the development of the reflection pattern from an initial steady RR as the wedge incidence is increased beyond transition and decreased subsequently.

5.4.1 Theoretical Transition

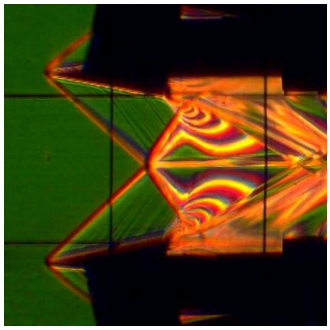
In the strong-reflection region, the dual solution domain is bounded by the von Neumann and detachment conditions as illustrated by the pressure-deflection shock polars in figure 2.5. The early steady state experiments by Hornung & Robinson [19] observed RR $\leftrightarrow$ MR transition at the von Neumann condition irrespective of the direction of incidence change, though the theory supported RR $\rightarrow$ MR transition at detachment. The observance of hysteresis or lack thereof was postulated to be dependent on the level of free stream turbulence. This was confirmed with the experiments of Ivanov et al. [22] in which the elusive hysteresis phenomenon was observed in a low noise wind tunnel facility. The RR $\rightarrow$ MR transition point in the strong-reflection region is dependent on the level of tunnel free stream turbulence and can vary between wind tunnels. In an experiment, provided the wedge aspect ratio is sufficiently large, transition to MR may occur anywhere between the von Neumann and detachment conditions. In a low turbulence facility, with low levels of vibration, MR can be maintained until the detachment condition. Apart from the single honeycomb mesh in the settling chamber of the CSIR tunnel, there are no additional mechanisms for turbulence or vibration reduction.



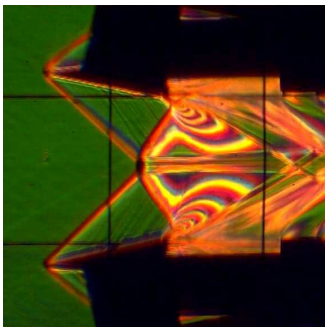
(a) Frame 1, $t = 0.0$ s



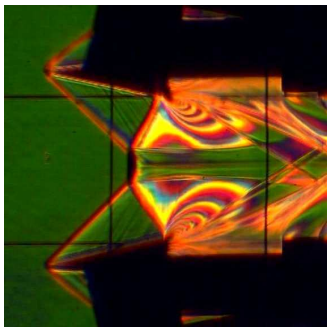
(b) Frame 185, $t = 0.736$ s



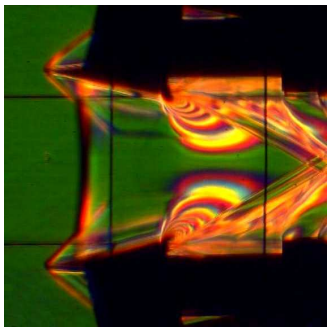
(c) Frame 211, $t = 0.84$ s



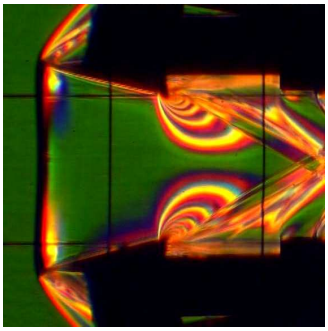
(d) Frame 235, $t = 0.936$ s



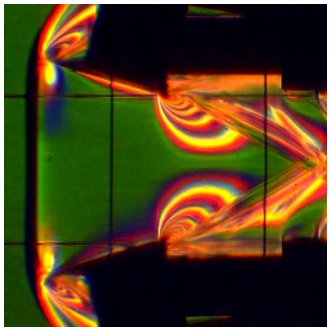
(e) Frame 256, $t = 1.02$ s



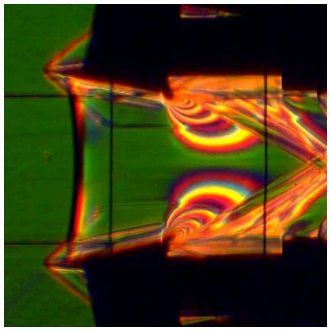
(f) Frame 257, $t = 1.024$ s



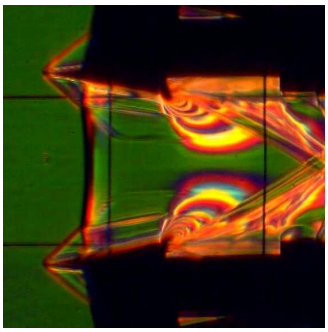
(g) Frame 258, $t = 1.028$ s



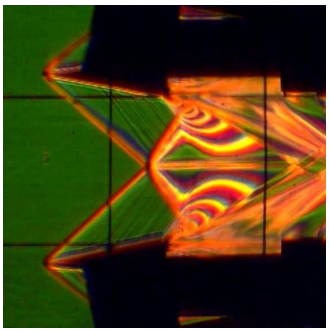
(h) Frame 334, $t = 1.332$ s



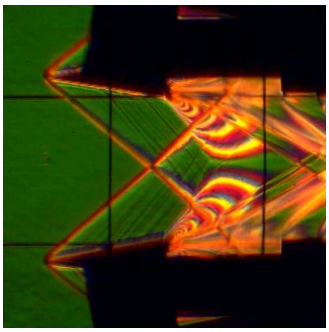
(i) Frame 730, $t = 2.916$ s



(j) Frame 731, $t = 2.92$ s



(k) Frame 732, $t = 2.924$ s



(l) Frame 780, $t = 3.116$ s

Figure 5.6: High-speed images from steady state experiment at $M = 1.93$

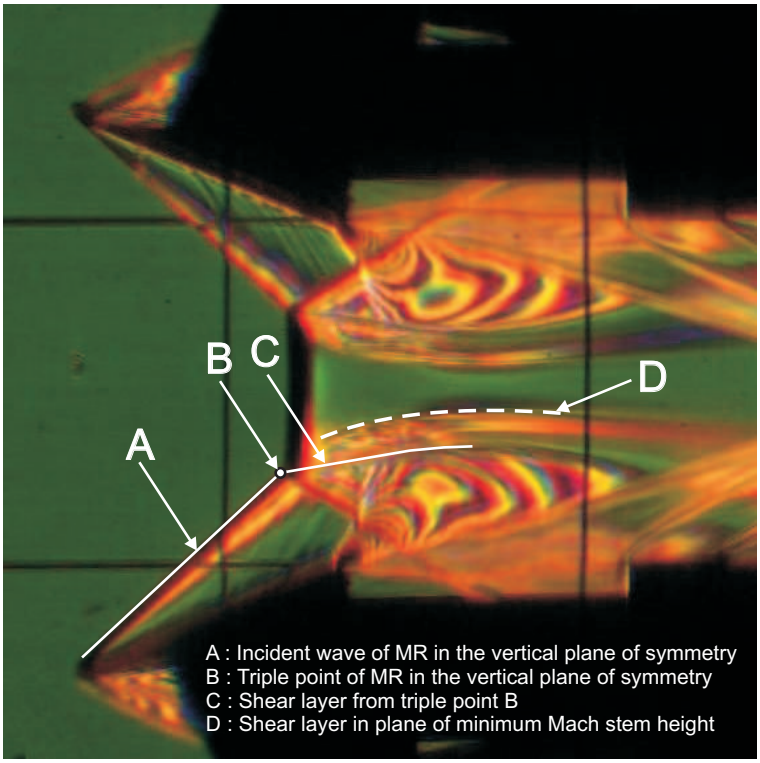


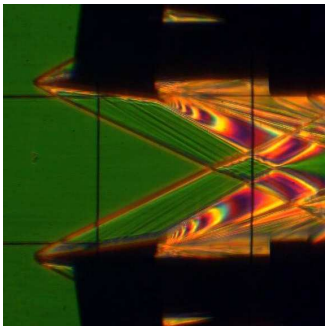
Figure 5.7: Magnified view : schlieren image of MR at $M = 2.98$, indicating the maximum Mach stem height in the wedge vertical plane of symmetry and the shear layer in the plane of the minimum Mach stem height (indicated on the bottom half of the reflection only)

5.4.2 Three-dimensional Wave Structure

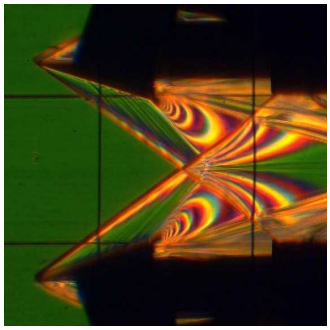
In figure 5.7, one can identify the leading edge of the incident oblique wave in the plane of symmetry. The intersection of the incident oblique wave with the leading edge of the Mach stem identifies the triple point in this plane. In contrast to the $M = 1.93$ case, the Mach stem decreases in the spanwise direction and a minimum Mach stem height can be seen. The 3D reflection pattern could be similar to that computed by Ivanov et al. [24] in figure 5.1. This may be verified with high-resolution 3D CFD simulations, but is not necessary for this investigation. As the maximum Mach stem height occurs in the plane of symmetry it is likely, though it cannot be confirmed, that the appearance/disappearance of the shear layer downstream of the reflection point, may be an accurate estimate of transition for increasing/decreasing incidence. Transition was extrapolated from Mach stem data.

5.4.3 Experimental Results

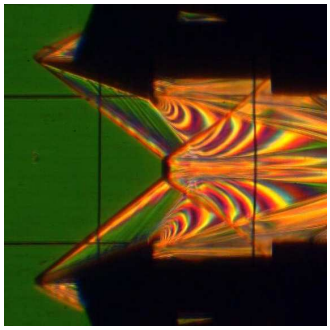
A steady RR can be seen in frame 1 of figure 5.8. The wedge incidence was increased gradually beyond transition to MR. Mach stem growth was continuous with an increase in wedge incidence (see frames 429 -



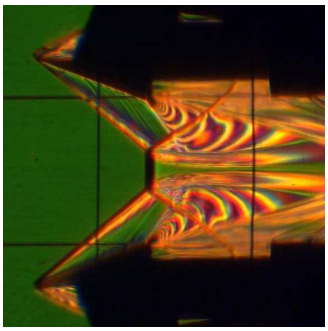
(a) Frame 1, $t = 0.0$ s



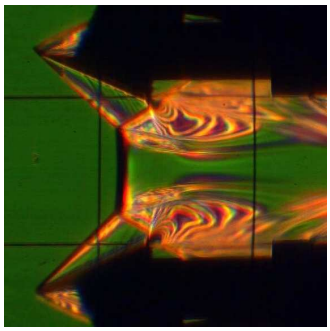
(b) Frame 380, $t = 1.516$ s



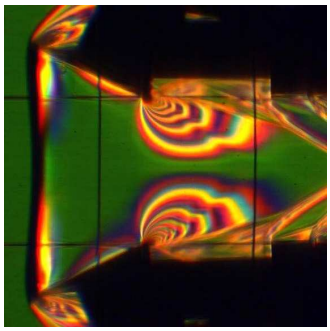
(c) Frame 429, $t = 1.712$ s



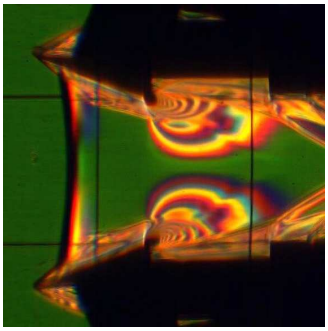
(d) Frame 480, $t = 1.916$ s



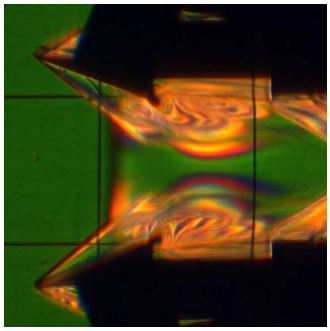
(e) Frame 579, $t = 2.312$ s



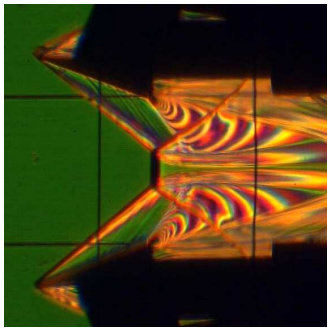
(f) Frame 665, $t = 2.656$ s



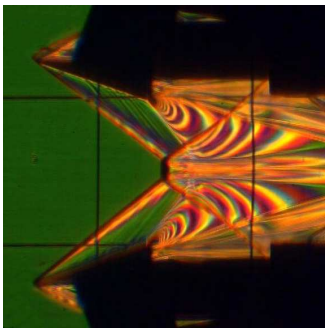
(g) Frame 806, $t = 3.22$ s



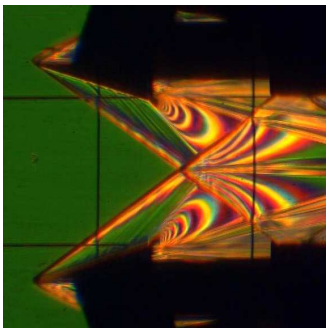
(h) Frame 807, $t = 3.224$ s



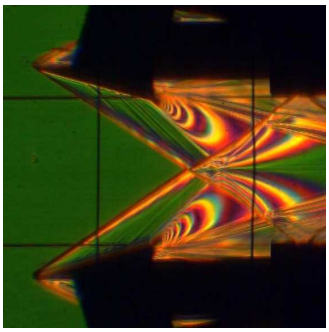
(i) Frame 808, $t = 3.228$ s



(j) Frame 849, $t = 3.392$ s



(k) Frame 900, $t = 3.596$ s



(l) Frame 979, $t =3.912$ s

Figure 5.8: High-speed images from steady state experiment at $M = 2.98$

579), indicating that the tunnel free stream turbulence is sufficient to trigger transition at the von Neumann condition. The wedge incidence was increased until the wave system disgorged in frame 665. As θ_w was decreased the wave system was swallowed and a steady MR was established in the central plane as seen in frames 806-808. Further decrease in θ_w resulted in transition to RR. There is hysteresis in the phenomena of shock disgorge and shock swallow as observed at $M = 1.93$. Incidence-induced RR $\leftrightarrow$ MR transition hysteresis was not observed in the CSIR facility. Fluent was used to simulate the steady case. Results are summarised in table 5.1 and figure 5.10.

5.5 Results

Transition results for both experiments are summarised against the steady state transition criteria in table 5.1. The shock incidence at transition was extrapolated from a second-order polynomial fit of the Mach stem growth data. At $M = 1.93$, there is good agreement in ϕ_T between experiment and CFD at $M = 1.93$. Transition was measured in the experiment and computed at approximately $\phi_T = 43.4°$, $0.2°$ beyond ϕ_D, which is within the uncertainty value of $\delta\phi$ for measurements from experimental images and computed flow field contours. The difference in Mach stem growth with ϕ between experiment and CFD in figure 5.9 was expected as demonstrated previously by Ivanov et al. [24] in figure 3.1, i.e. the Mach stem height is always smaller in a 3D experiment than the ideal, 2D case for any $\phi > \phi_T$. The results of the 2D CFD and experiments converge at ϕ_T.

In the ideal case in the strong-reflection range, RR $\rightarrow$ MR transition occurs at the detachment condition and the reverse transition occurs at the von Neumann condition. For $\phi > \phi_D$ the Mach stem height is independent of the direction of incidence change. Figure 5.10 shows the hysteresis loop predicted by CFD at $M = 2.98$. However, hysteresis was not observed in the experiment and transition occurred close to the von Neumann condition in both directions, which indicates that there is sufficient noise in the free stream to suppress hysteresis. Due to the level of free stream noise, there is disagreement between the steady theory/CFD and experiment for RR $\rightarrow$ MR transition, but good agreement for the reverse transition. The CFD result and the experiment are within $0.1°$ of the von Neumann condition for steady MR $\rightarrow$ RR transition. This is consistent with observations in all supersonic wind tunnels without special noise and vibration reduction measures. Once again, the difference in Mach stem height between CFD and experiment was observed for $\phi > \phi_T$. Transition results from both experiments indicate that the wedge aspect ratio is sufficient to ensure that ϕ_T in the wedge vertical plane of symmetry is close to the 2D result.

These steady state experiments employed a lower quality imaging lens (bi-convex) and a coarser calibra-

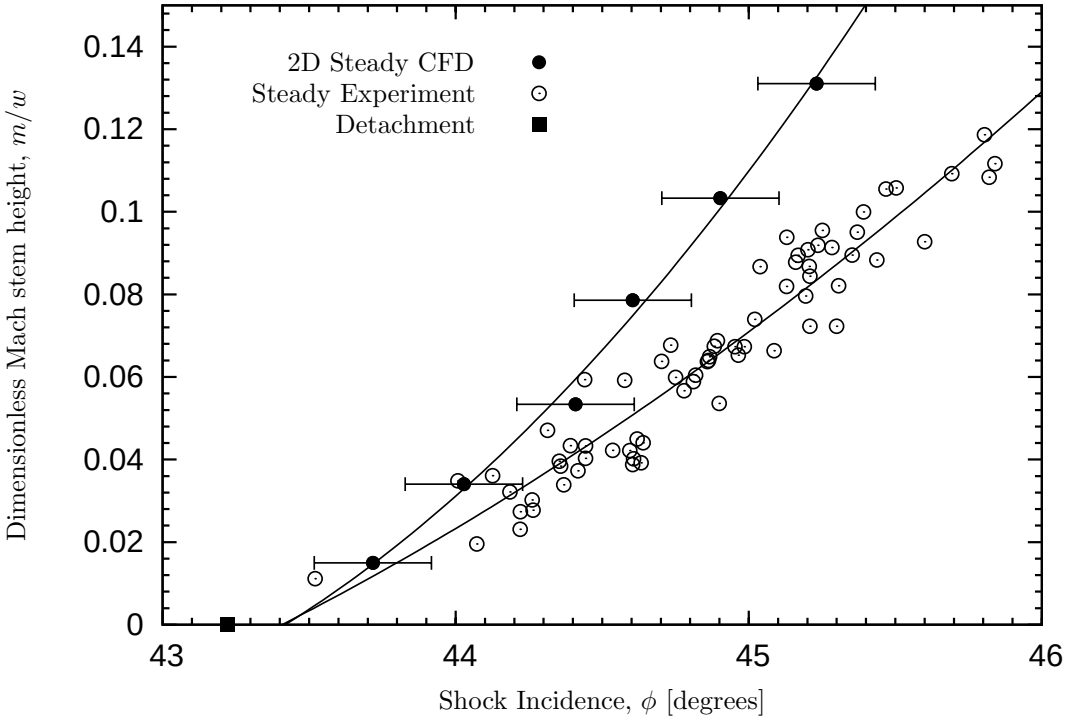


Figure 5.9: Measured and computed Mach stem development at $M = 1.93$, $g/w \approx 0.6$. The solid lines are second-order polynomial fits to each data set used to extrapolate ϕ_T at zero m/w. The uncertainty in $\delta\phi$ and $\delta m/w$ for the experimental data is omitted to prevent cluttering on the graph.

tion grid than that reported in sections 3.5 and 3.6. They were considered sufficient for the purpose of these baseline experiments. The finer calibration grid and aspherical achromatic lens documented in sections 3.5 and 3.6 were used for the dynamic experiments presented in chapters 6 and 7.

5.6 Conclusion

Steady state, baseline experiments and computations were done to determine the 2D RR $\leftrightarrow$ MR transition points in the weak and strong-reflection ranges. RR $\rightarrow$ MR was observed close to the detachment condition at $M = 1.93$ and close to the von Neumann condition in both directions at $M = 2.98$. The free stream noise in the CSIR supersonic tunnel is sufficient to suppress incidence-induced hysteresis in the strong-reflection region. There was good agreement between theory, computation and experiment for the transition point at both free stream conditions with the exception of RR $\rightarrow$ MR transition at $M = 2.98$ due to the level of free stream noise. The wedge aspect ratio was sufficient to ensure that ϕ_T in the wedge vertical plane of symmetry approximates the 2D result. The expected difference in Mach stem growth with shock incidence between the 2D CFD result and the 3D experimental measurement was observed and exhibits identical characteristics to

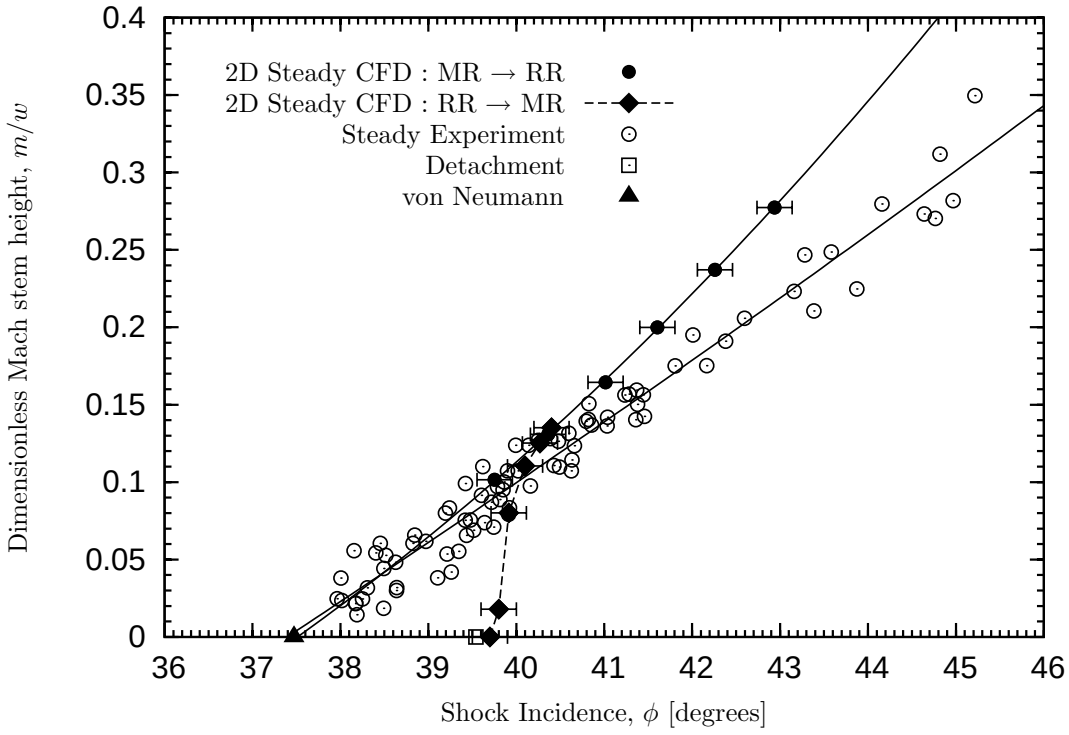


Figure 5.10: Measured and computed Mach stem development at $M = 2.98$, $g/w \approx 0.6$. The solid lines are second-order polynomial fits to each data set used to extrapolate ϕ_T at zero m/w. The uncertainty in $\delta\phi$ and $\delta m/w$ for the experimental data is omitted to prevent cluttering on the graph.

Table 5.1: Summary of steady state results from experiment and CFD at $M = 1.93$ and 2.98, $g/w \approx 0.6$

	$M = 1.93$	$M = 2.98$
Analytical ϕ_T	43.2°	$\phi_N = 37.5°$, $\phi_D = 39.5°$
2D Euler CFD : ϕ_T	43.4°	MR → RR : 37.5°; RR → MR : 39.7°
Experiment : ϕ_T	43.4°	37.4°

the data published by Ivanov et al. [24]. Some interesting 3D wave features were identified. At $M = 1.93$, the minimum Mach stem height is in the streamwise vertical plane of symmetry, not on the periphery as observed at $M = 2.98$. The optical calibration and imaging optics, though sufficient for these steady state experiments, were improved for the dynamic experiments.

Chapter 6

Dynamic Two-Dimensional Regular to Mach Reflection Transition in an Ideal Steady Supersonic Free Stream

6.1 Introduction

This chapter presents results from experiments and computations to investigate the effect of rapid wedge rotation on two-dimensional RR → MR transition in an ideal, steady, supersonic free stream. The investigation was conducted in the weak and strong-reflection regions. Results for the steady state experiments and two-dimensional (2D) Euler computations were presented in chapter 5. The spring-driven actuator was installed and configured for dynamic RR → MR transition experiments. The wedges achieved a maximum instantaneous rotation speed of approximately 11000 deg/s resulting in $M_E \approx +0.033$. Schlieren images were captured with the Photron Ultima APX-RS at 10000 frames per second at 512 × 512 pixel resolution. The counterbores on the wedge surface identified in chapter 5 were filled with silver solder to remove the surface disturbances observed in the steady state experiments. The evolution of the reflection pattern was acquired over several high-speed images. Selected images are presented here. Movies with the complete sequence of images are included on an accompanying data disc. The measured wedge motion was mimicked in the Euler code developed by Felthun [12]. The code was also applied to scenarios beyond the capability of the current facility to investigate the dependence of dynamic RR → MR transition on other variables in the parameter space. These include pivot point, initial incidence, rotation speed and Mach number. The dynamic RR → MR transition mechanism was also investigated. Reference will only be made to the reflection pattern in the streamwise vertical plane of symmetry unless otherwise stated.

6.2 Experimental Results for Dynamic RR to MR Transition

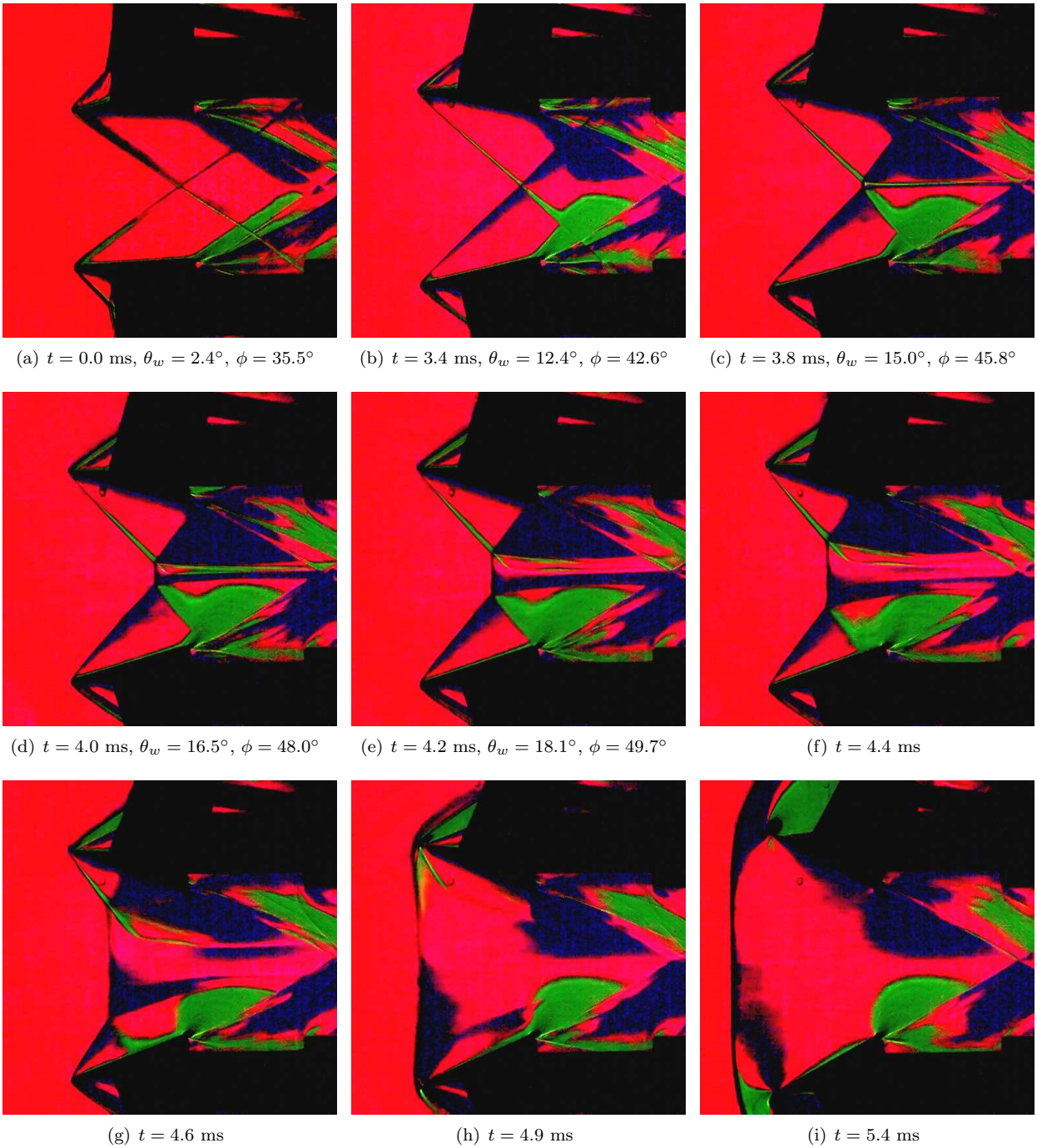
Experiments to observe the dynamic RR → MR transition of interest were conducted in the weak and strong-reflection ranges at $M = 1.93$ and 2.98 respectively. The spring-driven actuator was installed to increase wedge incidence rapidly on latch release. Table 6.1 includes measured test conditions, viz. M, stagnation temperature (T_O), stagnation pressure (P_O) and the initial shock incidence (ϕ_i). Selected high-speed images from both experiments are presented in figures 6.1 and 6.3. Zero time corresponds to the image frame just before any wedge movement is visible on the high-speed images. The measured wedge motion (θ_w vs. time), variation of shock incidence (ϕ vs. time), variation in Mach stem height (m/w vs. time) and the streamwise movement of the reflection/triple point (x/w vs. time) is included in figures 6.2 and 6.4. The motion after the reflected wave of the MR intersects the wedge surface is not of interest here and was not analysed. Each frame before this time includes a value of time, t, as well as θ_w and ϕ. Images from both experiments at $M = 1.93$ and 2.98 contain a similar sequence of events and the following qualitative description is applicable to both experiments, unless otherwise specified.

After tunnel startup a steady, initial RR is established (see figures 7.1(a) and 6.3(a)) after which time the latch mechanism restraining the actuation load is released. Initially, as the wedges rotate, there is little streamwise movement of the reflection point as the measurements show in figures 6.2(d) and 6.4(d). Both graphs show a distinct upstream movement only after approximately 2.5 - 2.6 ms of wedge motion. In this time the wedge has changed incidence by approximately 5.5° at $M = 1.93$ and 7.0° at $M = 2.98$. As θ_w increases, transition to MR occurs and the triple point moves upstream. The Mach stem and the shear layer of the MR is visible in figures 7.1(c) and 6.3(c). In particular, at $M = 2.98$, the streamwise speed of the triple point after transition is different from the streamwise speed of the reflection point before transition and is evident from the change in gradient after transition in figure 6.4(d). As the θ_w increases further, the reflected wave of the MR intersects the wedge surface (figure 7.1(e) and 6.3(g)) and the wave system disgorges. The wedge motion terminates and a steady disgorged wave is established as seen in figures 6.1(i) and 6.3(i). The motion of interest is completed in approximately 4.5 ms at $M = 1.93$ and in approximately 5.5 ms at $M = 2.98$.

The speed of the reflection point at transition is used to calculate the effective local free stream speed at the reflection point at transition and the steady, analytical transition criteria are corrected accordingly. The shock incidence at the corrected von Neumann and detachment conditions will be referred to as ϕ_{NC} and ϕ_{DC} respectively. The measured test conditions in table 6.1 and wedge motion were used as inputs to the Euler simulations.

Table 6.1: Experimental test conditions for dynamic RR → MR experiments, $g/w \approx 0.6$

M	P_O [Pa]	T_O [K]	ϕ_i [degrees]
1.93	232.0	302.7	35.5
2.98	474.0	302.3	23.2

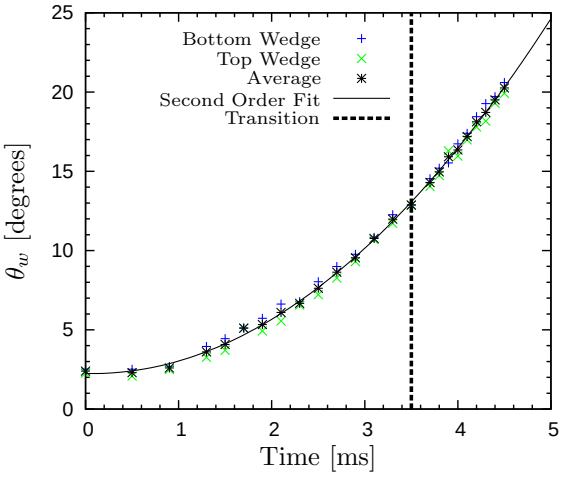


(a) $t = 0.0$ ms, $\theta_w = 2.4°$, $\phi = 35.5°$ (b) $t = 3.4$ ms, $\theta_w = 12.4°$, $\phi = 42.6°$ (c) $t = 3.8$ ms, $\theta_w = 15.0°$, $\phi = 45.8°$

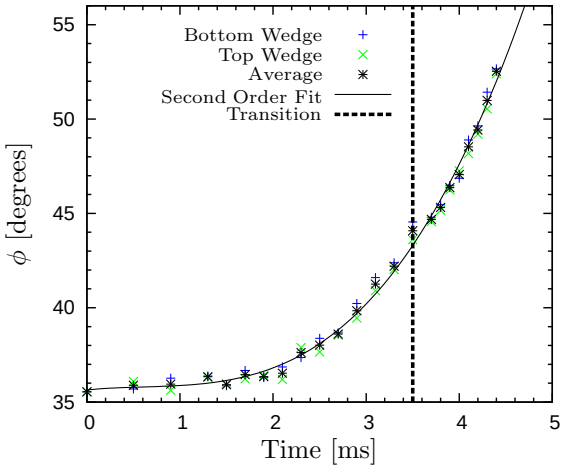
(d) $t = 4.0$ ms, $\theta_w = 16.5°$, $\phi = 48.0°$ (e) $t = 4.2$ ms, $\theta_w = 18.1°$, $\phi = 49.7°$ (f) $t = 4.4$ ms

(g) $t = 4.6$ ms (h) $t = 4.9$ ms (i) $t = 5.4$ ms

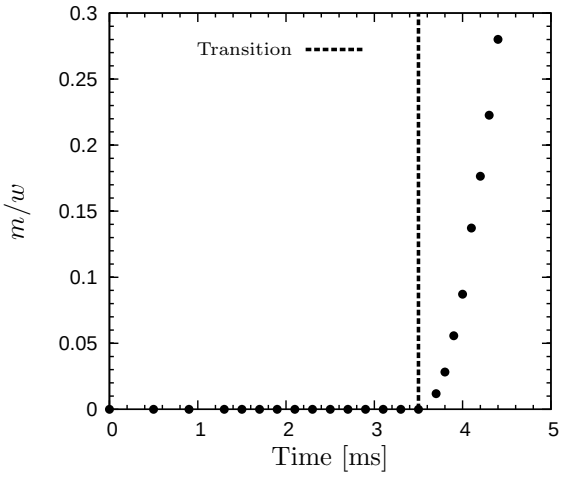
Figure 6.1: High-speed images for dynamic RR → MR transition at $M = 1.93$



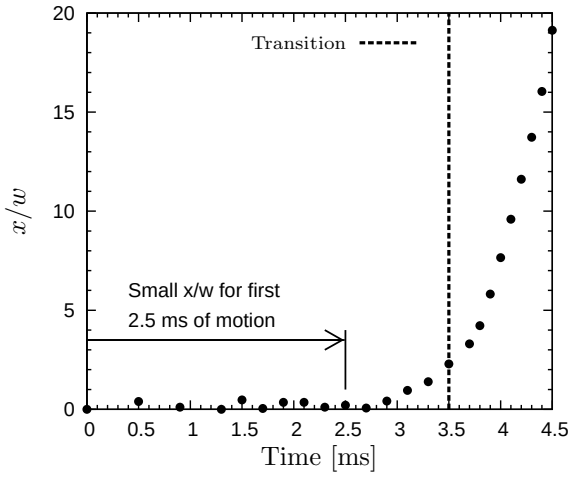
(a) θ_w vs time



(b) ϕ vs time

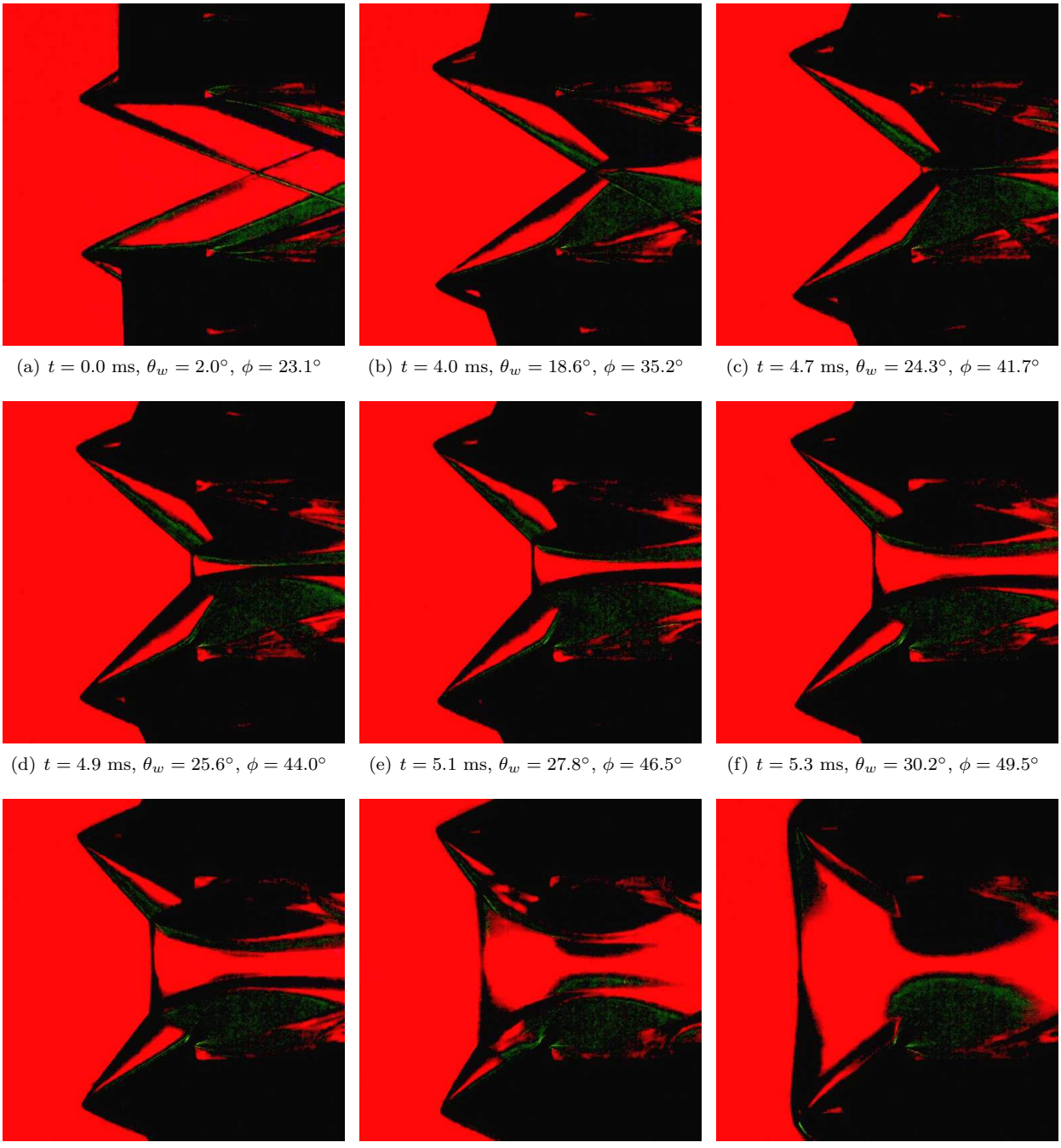


(c) m/w vs time



(d) x/w vs time

Figure 6.2: Measurements from the dynamic experiment at $M = 1.93$

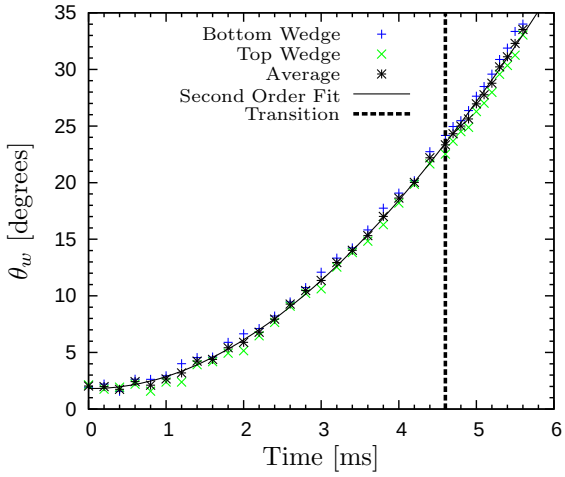


(a) $t = 0.0$ ms, $\theta_w = 2.0°$, $\phi = 23.1°$ (b) $t = 4.0$ ms, $\theta_w = 18.6°$, $\phi = 35.2°$ (c) $t = 4.7$ ms, $\theta_w = 24.3°$, $\phi = 41.7°$

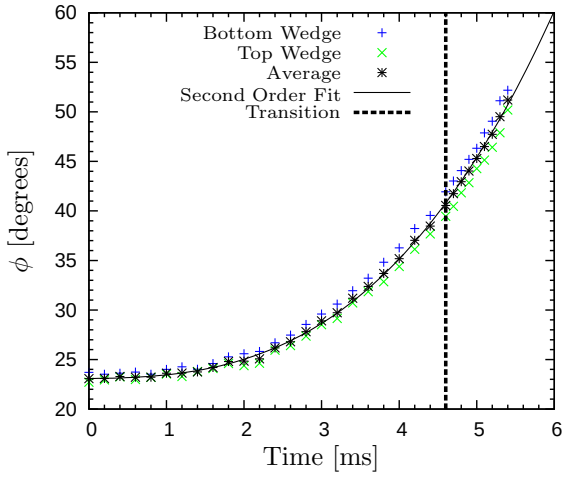
(d) $t = 4.9$ ms, $\theta_w = 25.6°$, $\phi = 44.0°$ (e) $t = 5.1$ ms, $\theta_w = 27.8°$, $\phi = 46.5°$ (f) $t = 5.3$ ms, $\theta_w = 30.2°$, $\phi = 49.5°$

(g) $t = 5.4$ ms, $\theta_w = 31.1°$, $\phi = 51.2°$ (h) $t = 5.7$ ms (i) $t = 6.0$ ms

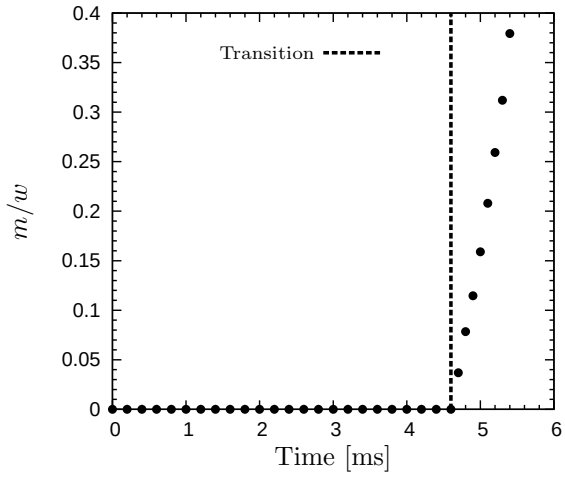
Figure 6.3: High-speed images for dynamic RR → MR transition at $M = 2.98$



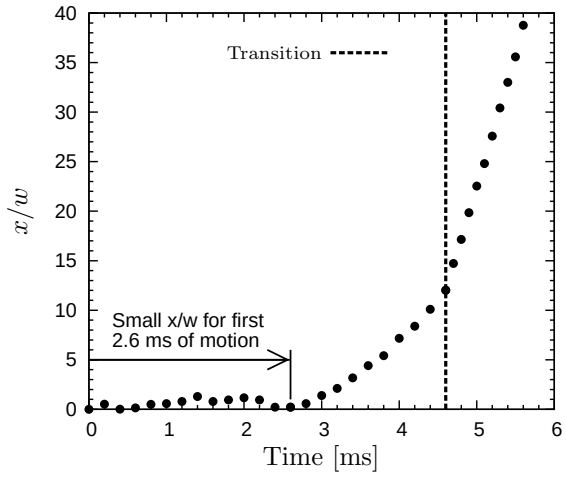
(a) θ_w vs time



(b) ϕ vs time



(c) m/w vs time



(d) x/w vs time

Figure 6.4: Measurements from the dynamic experiment at $M = 2.98$

6.2.1 Weak-Reflection Range

The measurements from experiments and computational results are presented in table 6.2 and figure 6.5. The solid lines in figure 6.5 are second-order polynomial fits through each data set and are used to extrapolate ϕ_T at zero m/w. The experimental and computed ϕ_T for the steady case are within 0.2° of ϕ_D. In the dynamic experiment, the wedge achieved an instantaneous rotation speed ($\approx$ 6300.0 deg/s) that resulted in $M_E = +0.02$ at the point of transition. The average M_E up to the point of transition was approximately + 0.011. The rapid rotation delayed transition in the experiment and CFD of the experiment beyond ϕ_{DC} by approximately $1.2° - 1.3°$. Values of ϕ_T from the dynamic experiment and simulation of the experiment are within 0.1° of each other. As expected (and discussed by Ivanov et al. [24]), there is the difference in Mach stem growth between the 2D computed result and the three-dimensional (3D) experimental measurement for the steady case. This characteristic is also evident in the dynamic case. The close agreement between experiment and computation lends confidence to the ability of the computational method to predict dynamic transition.

6.2.2 Strong-Reflection Range

The measurements from experiments and computational results are presented in table 6.3 and figure 6.6. As the point of transition in the strong-reflection range is dependent on the level of tunnel free stream turbulence and is tunnel dependent, baseline measurements for the steady experiment were necessary. In figure 6.6 the von Neumann and detachment conditions are indicated ϕ_N and ϕ_D respectively. The dual solution domain is $\phi_N < \phi < \phi_D$. The solid lines in figure 6.6 are second-order polynomial fits through each data set and are used to extrapolate ϕ_T at zero m/w. In the steady experiment, RR $\leftrightarrow$ MR takes place close to the von Neumann condition in both directions, indicating that the noise in the CSIR supersonic tunnel is sufficient to suppress hysteresis. The steady CFD successfully predicted the incidence-induced hysteresis loop. For the steady case, there is disagreement in ϕ_T between the steady experiment, in which free stream perturbations are always present, and the steady CFD, in which there are no perturbations in the free stream.

For the dynamic case the wedge achieved an instantaneous rotation speed ($\approx$ 9000.0 deg/s) that resulted in $M_E = +0.028$ at the point of transition. The average M_E up to the point of transition was approximately + 0.015. The measured ϕ_T for the dynamic experiment is labelled "X". Figure 6.6 shows, very clearly, that the rapid wedge rotation was sufficient to maintain RR past $\phi_T \approx \phi_N$ observed in the steady experiment, through the dual solution domain (as hypothesised by Hornung [17]) and even beyond ϕ_D. Both the experiment and CFD show that RR persisted approximately $0.9° - 1.2°$ beyond ϕ_{DC}. Even though there was disagreement between the steady experiment and CFD, there is close agreement between the experimental

Table 6.2: Summary of ϕ_T from steady and dynamic experiments and CFD at $M = 1.93$, $g/w \approx 0.6$

Analytical steady detachment condition, ϕ_D	43.2°
Measured relative Mach number of reflection point at transition	+ 0.017
Corrected analytical steady detachment condition, ϕ_{DC}	43.1°
Experiment : steady state ϕ_T	43.4°
Experiment : dynamic ϕ_T	44.4°
2D Euler CFD : steady state ϕ_T	43.4°
2D Euler CFD : dynamic ϕ_T	44.3°
Difference between dynamic ϕ_T and ϕ_{DC} (Experiment and CFD)	$\approx 1.2° - 1.3°$

Table 6.3: Summary of ϕ_T from steady and dynamic experiments and CFD at $M = 2.98$, $g/w \approx 0.6$

Analytical steady von Neumann condition, ϕ_N	37.5°
Analytical steady detachment condition, ϕ_D	39.5°
Measured relative Mach number of reflection point at transition	+ 0.046
Corrected analytical steady detachment condition, ϕ_{DC}	39.5°
Experiment : steady state ϕ_T	37.4°
Experiment : dynamic ϕ_T	40.75°
2D Euler CFD : steady state ϕ_T	37.5°
2D Euler CFD : dynamic ϕ_T	40.45°
Difference between dynamic ϕ_T and ϕ_{DC} (CFD and Experiment)	$\approx 0.9° - 1.2°$

and computed values of ϕ_T for the dynamic case. The agreement between the dynamic experiment, in which small perturbations are always present in the free stream, and the dynamic CFD, in which the free stream is without perturbations, implies that RR → MR transition in the strong-reflection region becomes insensitive to free stream noise above a certain critical rotation speed. This critical rotation speed may depend on the level of free stream noise and may vary between facilities.

The characteristic difference between the 2D and 3D result is also seen here. This result provides experimental evidence to support the dynamic effect originally presented by Felthun & Skews [12]. Rapid wedge rotation introduces a dynamic effect that delays RR → MR transition beyond the steady, theoretical transition condition.

6.3 Computational Simulation of Impulsive Rotation at $M = 2.98$

The close agreement between experiment and computation provides confidence in the use of flow simulations to investigate the dynamics of the flow field, including the dynamic RR → MR transition mechanism. This section analyses 2D Euler CFD results from the simulation of a rapidly rotating wedge in a $M = 2.98$ free stream. The wedge is started impulsively from a steady, initial RR, at an initial wedge incidence of $\theta_{wi} = 19.0°$ and rotated continuously at $M_E = +0.1$ (rotation speed = 32644 deg/s with $T_O = 302.3K$ and w= 40.0 mm) until transition to MR. The wedge is rotated about the model rotation centre in the

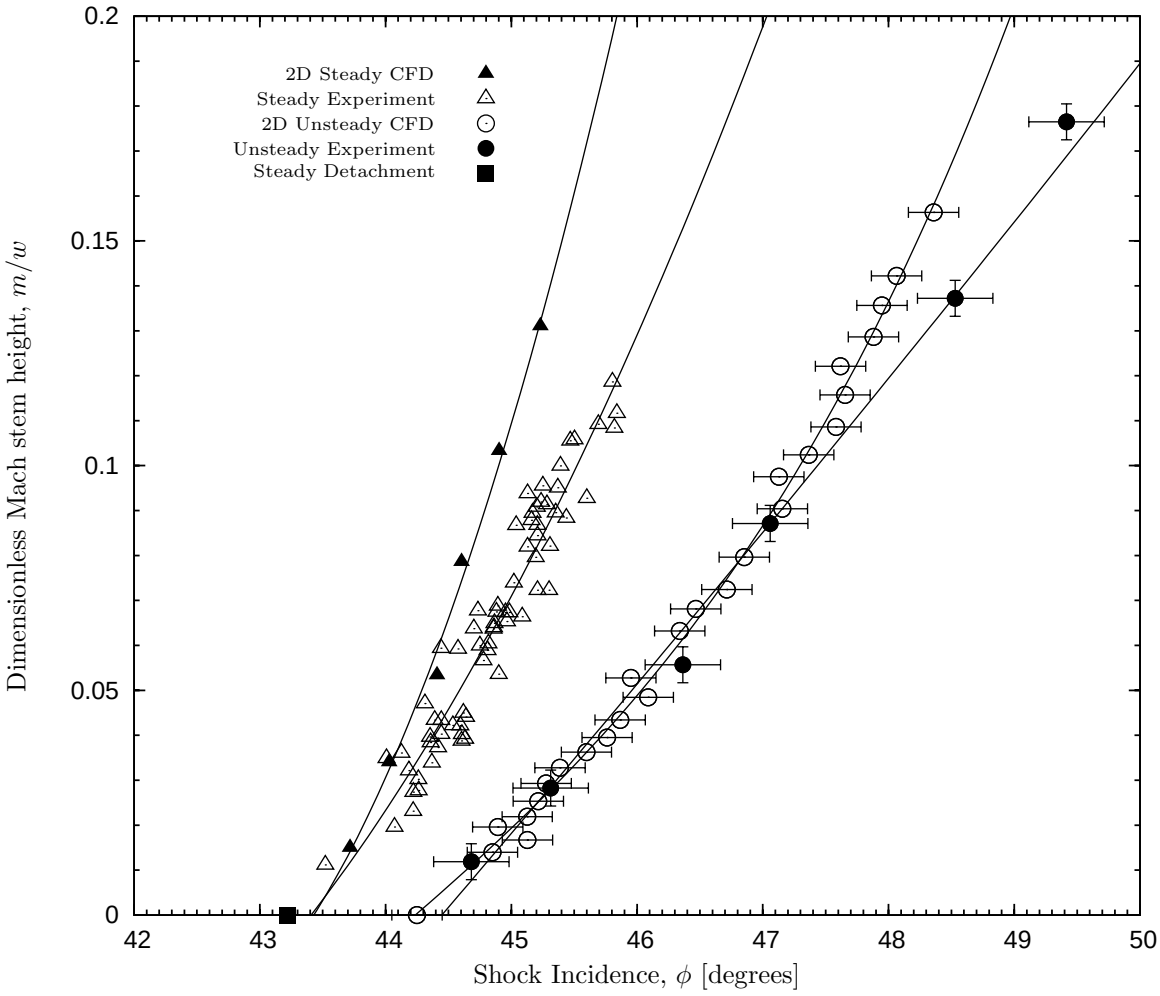


Figure 6.5: Experimental and CFD results for steady and dynamic RR → MR transition at $M = 1.93$. Solid lines are second-order polynomial fits through each data set and are used to predict ϕ_T at zero m/w.

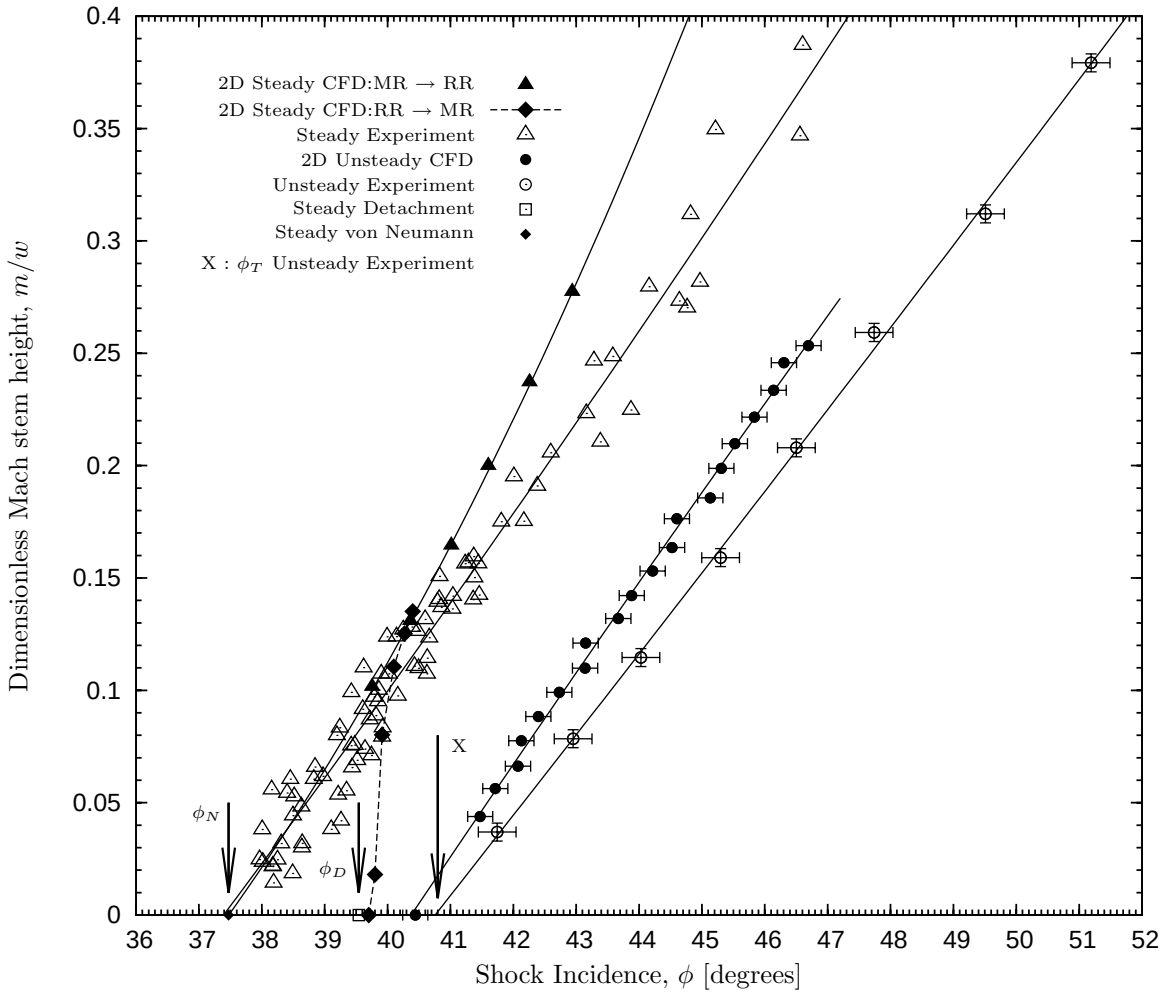


Figure 6.6: Experimental and CFD results for steady and dynamic RR → MR transition at $M = 2.98$. Solid lines are second-order polynomial fits through each data set and are used to predict ϕ_T at zero m/w.

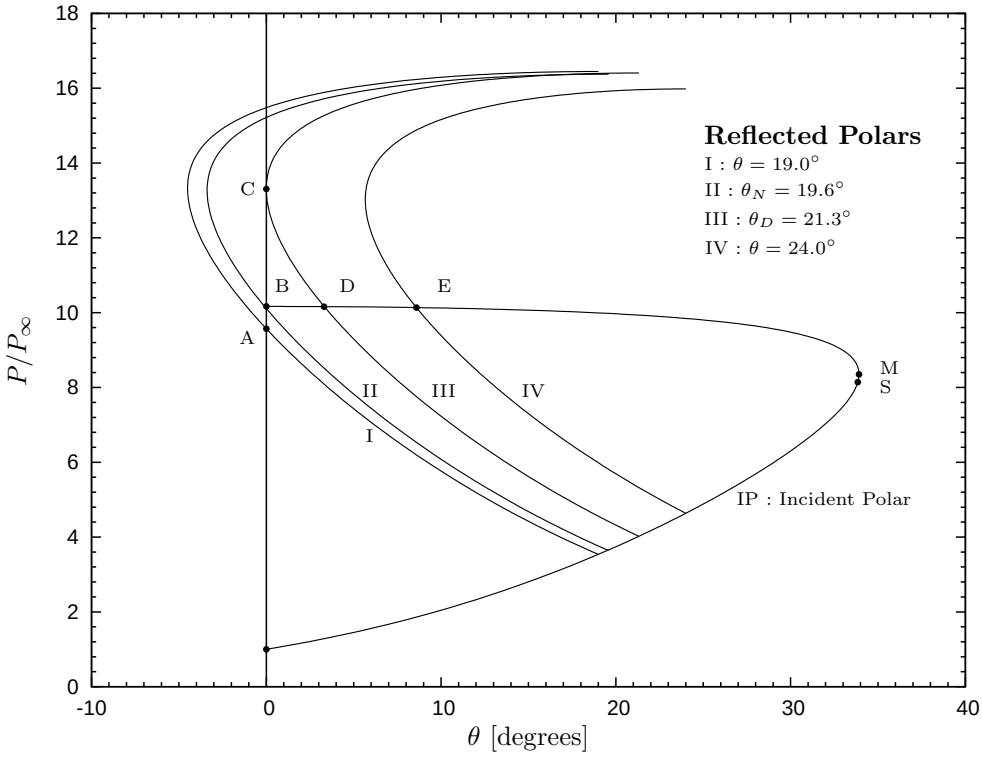
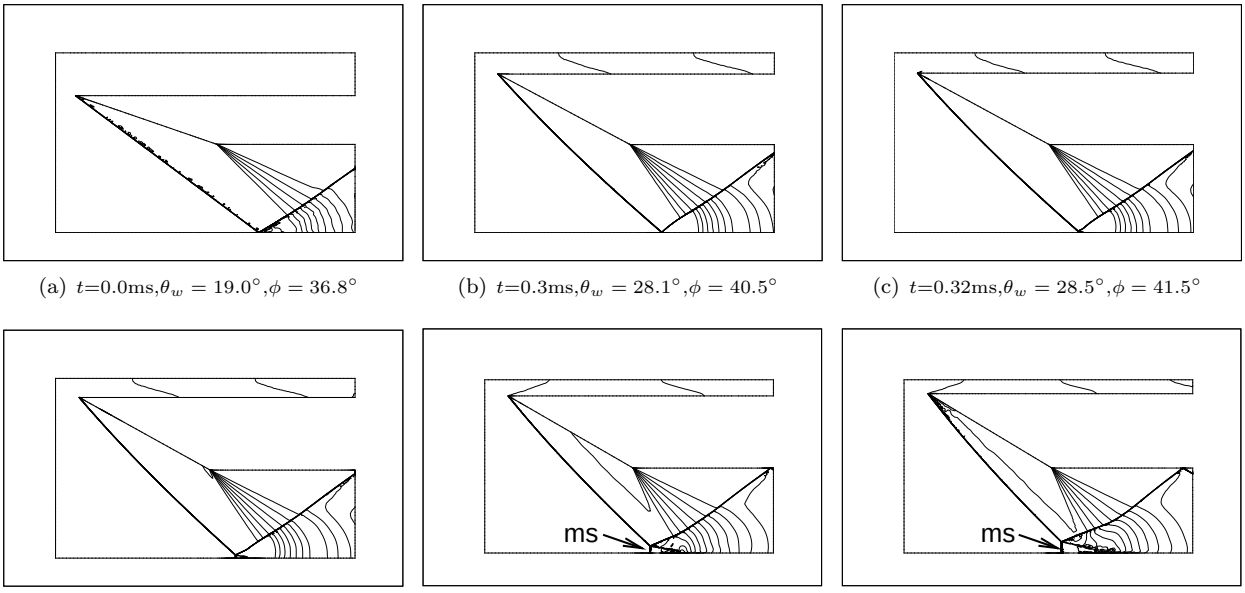


Figure 6.7: Critical pressure-deflection shock polars for steady reflection at $M = 2.98$

experiment. The large rotation speed is implemented deliberately to highlight the transient effects.

6.3.1 Steady Pressure-Deflection Shock Polars

As a prelude to the dynamic analysis, critical pressure-deflection shock polars for the ideal, steady case at $M = 2.98$ are reviewed briefly in figure 6.7. The incident polar is labelled "IP". "M" and "S" are the detachment and sonic points on "IP". At the initial wedge incidence, $\theta_{wi} = 19.0°$, only RR is possible and the pressure downstream of the reflection point is given by the intersection of the reflected polar, "I", with the *y-axis*, i.e. point A. As θ_w is increased from θ_{wi} very gradually, to ensure an approximately steady flow, the pressure rise through the reflection point increases as the intersection of the reflected polar with the *y-axis* moves towards point C. Points B and C on reflected polars "II" and "III" represent the pressure rise through the reflection point at the von Neumann and detachment conditions respectively ($\theta_N = 19.6°$ and $\theta_D = 21.3°$). As θ_w is gradually increased beyond the detachment condition, there is a marked drop in pressure rise across the reflection point from point C to point D as the reflection transitions to MR. At $\theta_w = 24.0°$, the pressure rise through the triple point of the MR is given by point "E" on polar "IV".



(a) t=0.0ms,$\theta_w = 19.0°$,$\phi = 36.8°$ (b) t=0.3ms,$\theta_w = 28.1°$,$\phi = 40.5°$ (c) t=0.32ms,$\theta_w = 28.5°$,$\phi = 41.5°$

(d) t=0.33ms,$\theta_w = 29.0°$,$\phi = 42.5°$ (e) t=0.37ms,$\theta_w = 30.0°$,$\phi = 43.3°$ (f) t=0.4ms,$\theta_w = 31.0°$,$\phi = 44.9°$

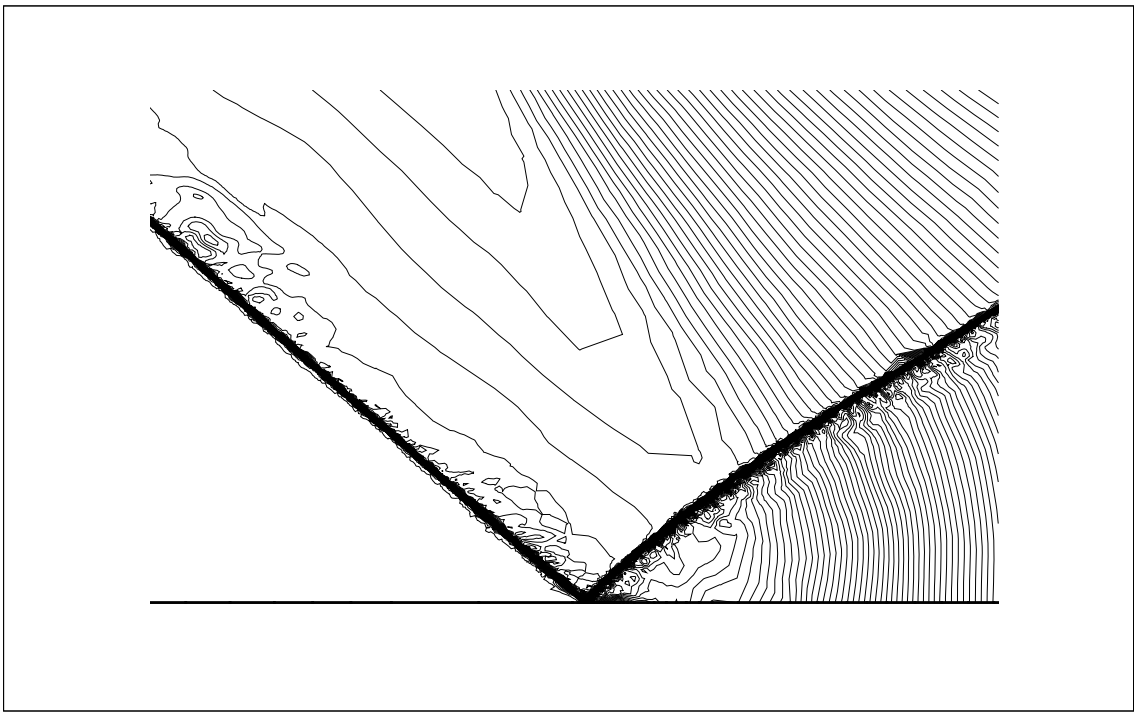
Figure 6.8: Computed density contours showing the flow field development for $M_E = +0.1$, $\theta_{wi} = 19.0°$ at $M = 2.98$, $g/w \approx 0.6$. The Mach stem is indicated "ms" only where clearly visible. This is not to be mistaken to indicate the point of transition.

6.3.2 Dynamic Flow Solution

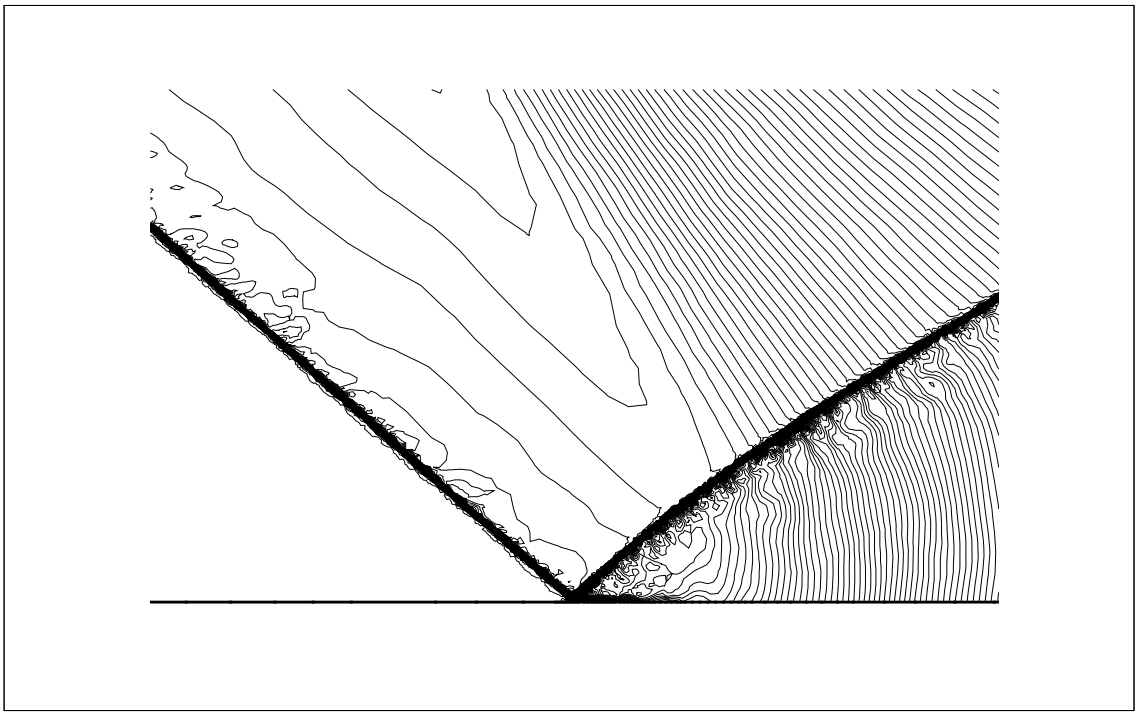
Selected images from the flow solution (flow field density contours) of the impulsive rotation case are presented in figure 6.8. An initial, steady RR is established at $\theta_{wi} = 19.0°$, before the wedge is started impulsively and rotated about its leading edge at a constant rotation speed with $M_E = +0.1$. As θ_w increases, curvature develops on the incident wave as observed previously by Khotyanovsky et al. [28] and Felthun & Skews [12]. The curvature and pressure gradient along the incident wave arise from the rapid wedge rotation and the interaction of the resultant compression and expansion waves with the incident wave. To date, there have been no detailed studies to quantify these effects. The visible Mach stems are indicated in figures 6.8(e) and 6.8(f). However, the point of transition cannot be identified accurately from the views presented in figure 6.8. Closeup views of the reflection pattern at $\theta_w = 28.0°$ and $\theta_w = 28.2°$ in figures 6.9(a) and 6.9(b) show the early development of the shear layer from the triple point as transition to MR occurs.

Transition is assumed when $\theta_w = 27.9°$, i.e. $0.1°$ before the appearance of the shear layer in figure 6.9(a). The corresponding $\phi_T \approx 40.5°$ and $\phi_{DC} = 39.4°$. Transition is delayed with respect to ϕ_{DC} by approximately $1.1°$.

The Mach stem development for this case is compared to the experimental/CFD results presented in section 6.2.2 in figure 6.10. The previous dynamic experiment at $M = 2.98$ and associated 2D CFD had a



(a) $\theta_w = 28.0^\circ$



(b) $\theta_w = 28.2^\circ$

Figure 6.9: Closeup views of computed density contours showing the first traces of the shear layer from the triple point as the reflection transitions to MR

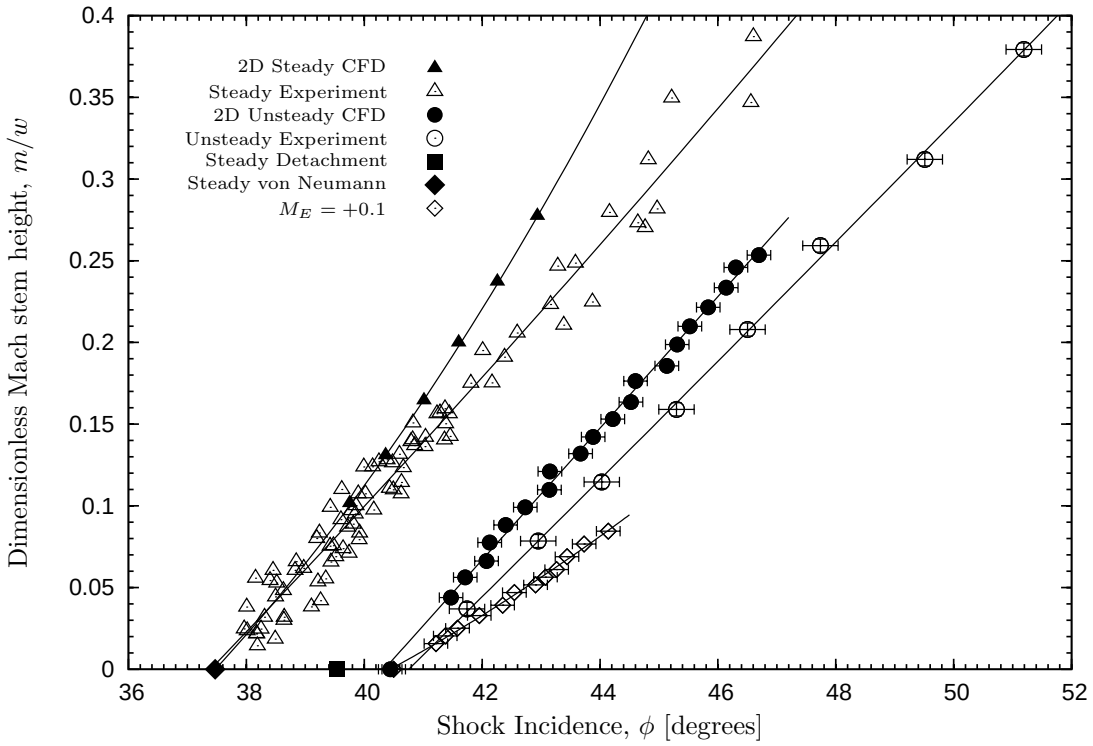


Figure 6.10: Mach stem development for impulsive rotation at $M_E = +0.1$ with $\theta_{wi} = 19.0°$ compared to results from the experiment and 2D CFD results. $M = 2.98$, $g/w \approx 0.6$.

significantly smaller and non-constant rotation rate. Due to the larger rotation rate here, the Mach stem height at any $\phi > \phi_T$, is smaller than previously observed. However, there is little difference in ϕ_T between the previous dynamic experiment and the impulsive rotation case presented here. The effect of rotation speed will be investigated in greater detail later in this chapter.

6.3.3 Transient Pressure Rise through the Reflection/Triple Point

Pressure traces through the reflection/triple point for the impulsive rotation case with $M_E = +0.1$ at $M = 2.98$ are analysed with respect to the steady state pressure-deflection shock polars presented earlier in figure 6.7. Consider the selection of pressure traces through the reflection/triple point in figure 6.11. The pressure rise through the reflection point at the steady, initial condition at $\theta_{wi} = 19.0°$ is close to the steady, analytical solution given by point "A" on reflected polar "I" in figure 6.7, i.e. $P/P_\infty = 9.6$. As the wedge incidence increases, the pressure rise through the reflection point increases and peaks at $\theta_w = 27.8°$ with $P/P_\infty \approx 19.0$ in comparison to 13.3 in the steady case (point "C" at the detachment condition on reflected polar "III"). Beyond $\theta_w = 27.8°$ there is a significant drop in pressure. The wedge incidence at which the maximum pressure rise through the reflection point was observed in figure 6.11 is close to the

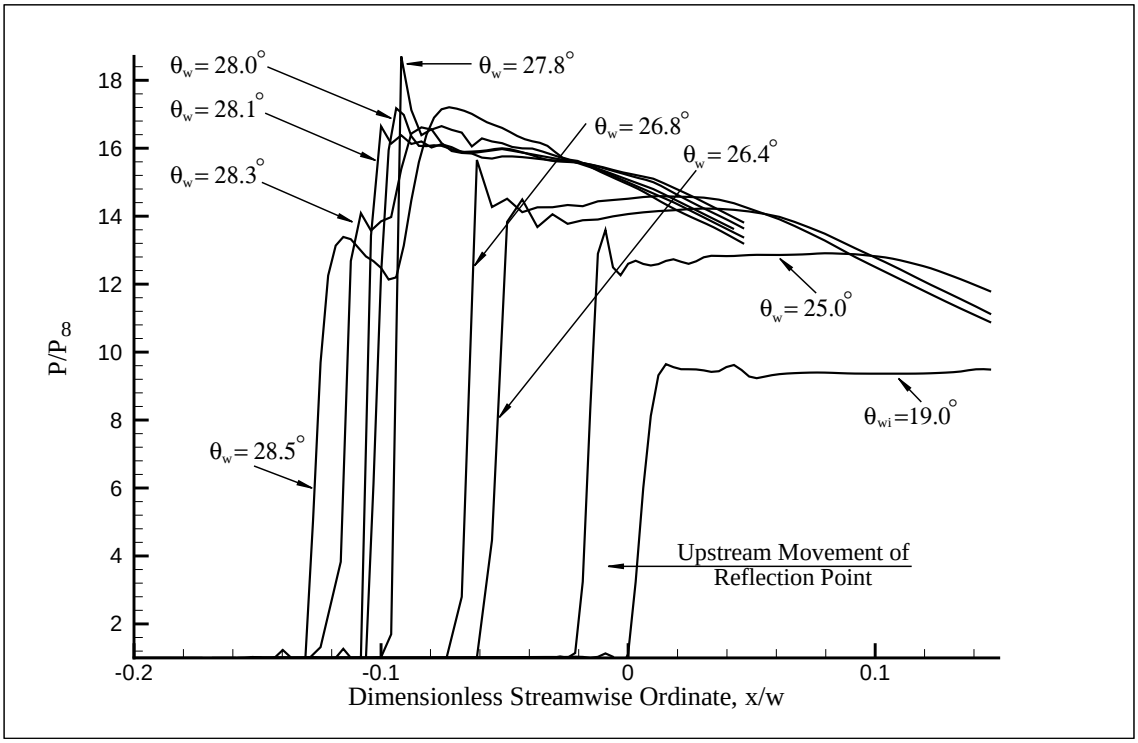


Figure 6.11: Computed pressure traces through the reflection point as the wedge rotates from $\theta_{wi} = 19.0°$ at $M_E = +0.1$ about the model pivot point at $M = 2.98$, $g/w \approx 0.6$

wedge incidence at which transition was assumed. It is reasonable to assume that the significant drop in pressure is associated with transition to MR, as in the steady case just beyond the detachment condition. Due to this similarity in trend between the dynamic and steady case, pressure-deflection shock polars may be useful in identifying the critical trend that highlights the point of transition.

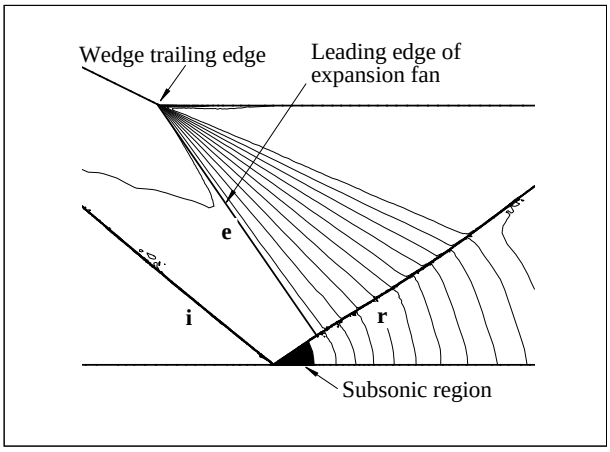
6.4 Transition Criteria and Mechanism for Dynamic RR to MR Transition

RR and MR are possible in the dual solution domain between the von Neumann and detachment conditions. The shock incidence at the von Neumann condition, ϕ_N, is the smallest incidence at which MR is theoretically possible. The shock incidence at the detachment condition, ϕ_D, is the largest incidence at which RR is possible. The length scale criteria or information condition proposed by Hornung et al. [18] states that RR $\rightarrow$ MR transition occurs at the point when flow conditions change such that there is communication of the wedge length scale to the reflection point (through the expansion fan). For the ideal, steady case, this is when the flow immediately downstream of the reflection point first goes sonic, i.e. M 1.0 at ϕ_S. Since the

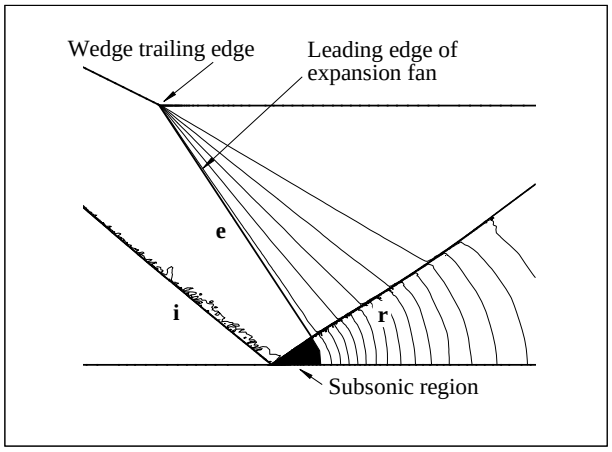
flow downstream of the reflection point is supersonic for $\phi < \phi_S$ there can be no communication of the wedge length scale to the reflection point below ϕ_S. This also happens to be very close to ϕ_D, beyond which RR is not possible. The difference between ϕ_D and ϕ_S is very small and is usually neglected, e.g. at $M = 4.0$, $\phi_D = 39.2°$ and $\phi_S = 39.1°$. It so happens in the ideal, steady case that the smallest incidence at which the length scale is visible to the reflection point is negligibly close to the incidence at which RR is no longer possible. In this case there has been no need to differentiate between the two as they are so close.

Once again, consider the impulsive rotation case at $M = 2.98$ in section 6.3 to explore the dynamic RR $\rightarrow$ MR transition mechanism. Transition was identified at $\theta_w = 27.9°$ in section 6.3.2. From observations of the Mach number contours in the CFD solution, the first time the flow downstream of the reflection point goes sonic is when $\theta_w \approx 26.2°$ as shown in figure 6.12(a), approximately 1.7° below transition. The subsonic region is highlighted in black as indicated. The leading edge of the expansion intersects the reflected wave downstream of this subsonic region and the length scale cannot be communicated to the reflection point. For convenience this will be referred to as the sonic condition and is labelled θ_S. As the wedge incidence increases, the leading edge of the expansion moves closer to the reflection point and the subsonic region grows until they interact at approximately $\theta_w = 26.4°$ in figure 6.12(b). This is the smallest incidence at which there is an established communication path between the trailing edge expansion and the reflection point and shall be referred to as θ_C for convenience. Taking into account the local acoustic speed in the subsonic zone, the wedge rotation speed and the finite time it takes the length scale information from the expansion fan to traverse the subsonic region, a prediction can be made as to when the length scale information reaches the reflection point. The wedge rotates to approximately $\theta_w = 26.8°$ as the length scale information reaches the reflection point, approximately 0.6° after the sonic condition. For convenience this will be referred to as the length scale condition and shall be identified by θ_L. Transition was identified in section 6.3.2 at $\theta_{WT} = 27.9°$, approximately 1.1° beyond the identified length scale condition at θ_L. Though the wedge length scale is visible at the reflection point from $\theta_L = 26.8°$, RR persists until transition at $\theta_w = \theta_{WT} = 27.9°$ (Khotyanovsky et al. [27] demonstrated, with CFD, the possibility of maintaining a steady overall RR in steady flow in the presence of length scale information - see section 2.4). Therefore, transition to MR must occur when the reflected wave can no longer turn the flow downstream of the incident wave parallel to the reflection plane at the reflection point, i.e. the dynamic equivalent of the detachment condition.

The difference between θ_S and θ_L was even more pronounced at $M = 1.93$ in which the wedge was rotated at a constant rotation speed about its trailing edge at $M_E = +0.05$ (≈ 18909 deg/s at $T_O = 302.7K$) with $\theta_{wi} = 8.0°$. Figure 6.13 shows the development of the subsonic region. The sonic condition is identified at



(a) Sonic condition at $\theta_w = \theta_S = 26.2°$

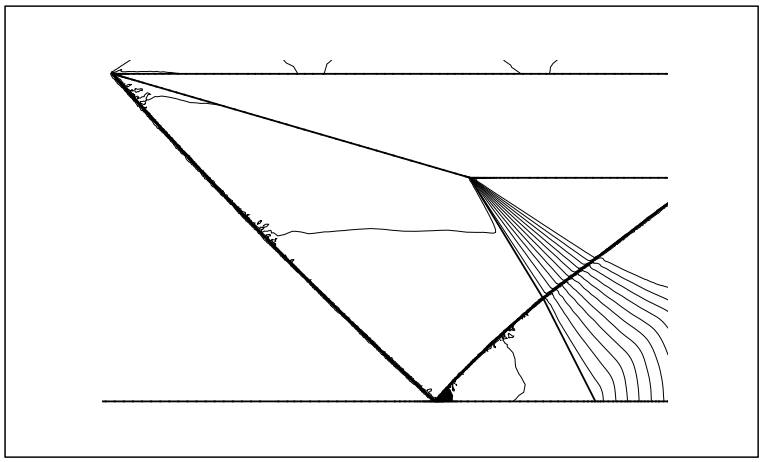


(b) Point of first contact between the expansion fan and the subsonic region at $\theta_w = \theta_C = 26.4°$

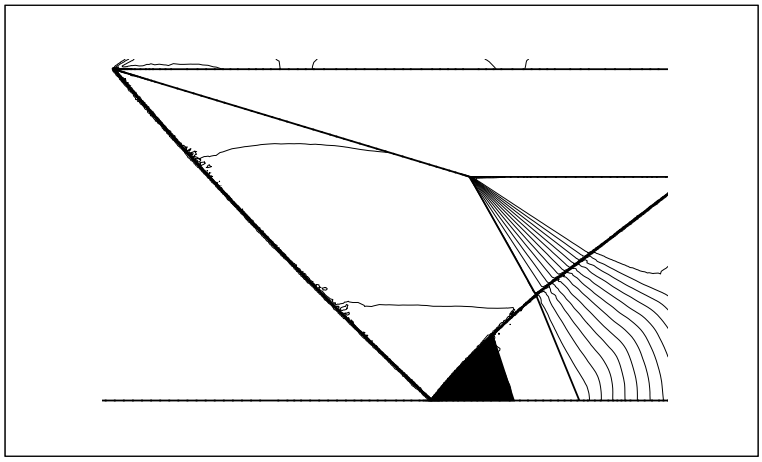
Figure 6.12: Computed density contours showing the development of the subsonic region downstream of reflection point before transition at $M = 2.98$, $M_E = +0.1$, $\theta_{wi} = 19.0°$. The subsonic region downstream of the reflection point is shaded black.

$\theta_S = 16.2°$. The subsonic region downstream of the reflection point grows until it meets the trailing edge expansion approximately 1.0° later at $\theta_C = 17.2°$. At this point information still has to traverse the subsonic patch before it reached the reflection point. Transition to MR was identified from the flow field contours at $\theta_{WT} = 17.5°$. The flow solution 0.1° later at $\theta = 17.6°$ is shown in figure 6.14. The first signs of the shear layer development at the triple point are visible. Taking into account the local sound speed, the length scale information only traverses approximately 40% of the subsonic region by the time transition has occurred. The red dot in figure 6.14 marks the estimated distance traversed by the length scale information on the shortest line between the leading edge of the expansion and the reflection point at transition. RR → MR transition has occurred without the presence of a length scale at the reflection point. As in the case at $M = 2.98$, transition must occur when the reflected wave can no longer maintain the boundary condition at the wall, i.e. the dynamic equivalent of the detachment condition. This particular result demonstrates that the length scale information from the trailing edge expansion to the reflection point was not necessary for RR → MR transition in this particular dynamic case. This is purely a dynamic effect introduced by the rapid wedge rotation. The various critical points in the flow field development for both impulsive test cases are summarised in table 6.4.

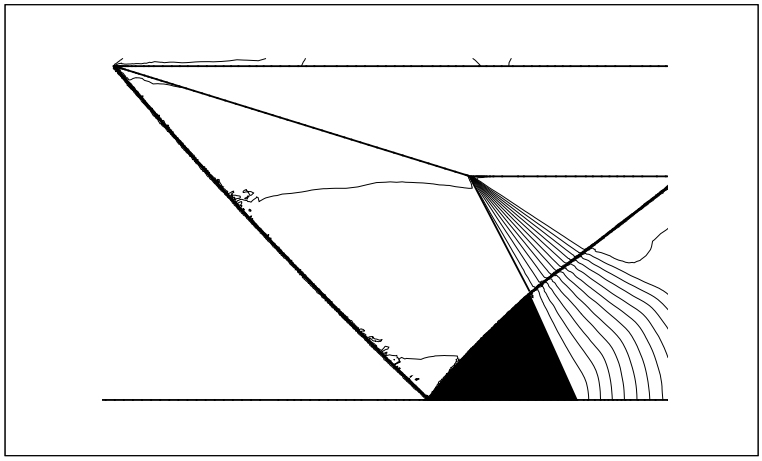
In the ideal, steady case the difference between the length scale and detachment conditions is negligible. However, these results show that the difference is more significant for the dynamic cases presented. Also, in the ideal steady case, the sonic condition and the length scale condition are synonymous. There is a difference between the two in the dynamic case due to the transient nature of the flow. As illustrated in



(a) $\theta_w = \theta_S = 16.2°$



(b) $\theta_w = 16.8°$



(c) $\theta_w = \theta_C = 17.2°$

Figure 6.13: Computed density contours showing the development of the subsonic region downstream of the reflection point between θ_S and θ_C at $M = 1.93$, $M_E = +0.05$, $\theta_{wi} = 8.0°$. The subsonic region downstream of the reflection point is shaded black.

Table 6.4: Summary of results for dynamic simulations at $M = 1.93$ and $M = 2.98$ to investigate the dynamic RR $\rightarrow$ MR transition mechanism

	$M = 1.93$, $M_E = +0.05$	$M = 2.98$, $M_E = +0.1$
θ_S	16.2°	26.2°
θ_C	17.2°	26.4°
θ_L	-	26.8°
θ_{WT}	17.6°	28.1°

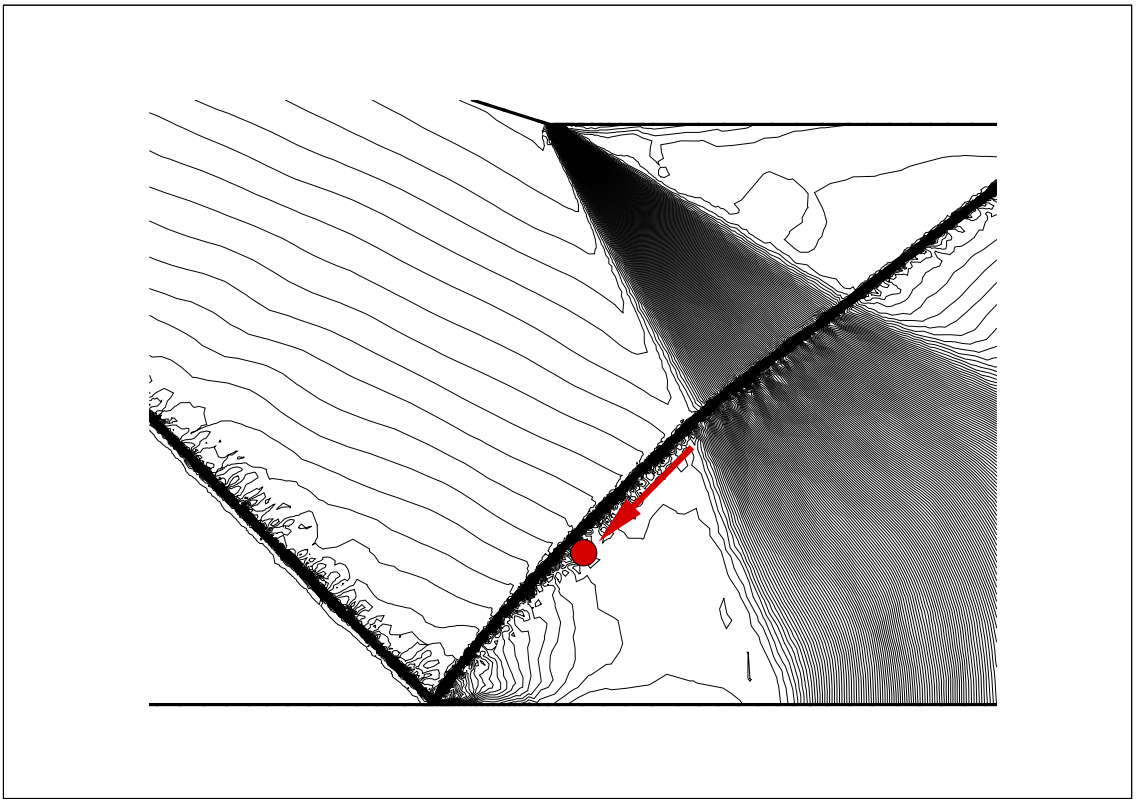


Figure 6.14: Estimated location of length scale information on the shortest line between the leading edge of the expansion and the subsonic region at $\theta_{WT} = 17.6°$. The early development of the shear layer from the triple point is also visible.

figure 6.13, it is possible to increase the time between the sonic condition and the length scale condition. Results for the dynamic case at $M = 2.98$ show that it is possible to maintain RR with a length scale visible at the reflection point. In addition, results for the dynamic case at $M = 1.93$ show that it is possible to achieve RR $\rightarrow$ MR transition without length scale information at the reflection point (from the wedge trailing edge expansion).

In summary, for the dynamic cases investigated here, the criterion for dynamic RR $\rightarrow$ MR transition is neither the sonic or length scale condition, but rather the dynamic equivalent of the detachment condition.

6.5 Parameter investigation for dynamic RR to MR transition

Euler simulations were used to determine the effect of various parameters, within a limited range, on ϕ_T and θ_{WT} at $M = 1.93$ and 2.98, viz. rotation speed, pivot point and initial incidence. Unless otherwise stated, $\theta_{wi} = 8.0°$, $g/w = 0.6$ for trailing edge pivot and $h/w = 0.74$ for leading edge pivot at $M = 1.93$. At $M = 2.98$, $\theta_{wi} = 19.0°$, $g/w = 0.6$ for trailing edge pivot and $h/w = 0.91$ for leading edge pivot unless otherwise stated. At $M = 1.93$ and 2.98, the dimensionless leading edge separation, h/w, for rotation about the leading edge was selected to match the value of h/w in the experimental setup at $\theta_w = \theta_{wi}$. The effect of moving the rotation point between the trailing edge and the model rotation centre is also investigated briefly.

The wedge and shock incidence at the steady detachment condition are annotated θ_D and ϕ_D respectively. Both are corrected to account for the increase in local Mach number at the reflection point due to streamwise movement of the latter and are annotated θ_{DC} and ϕ_{DC} respectively. The speed of the reflection point at transition is dependent on the pivot point and hence θ_{DC} and ϕ_{DC} are also dependent on the pivot point. The abbreviations TE, LE and EXP will be appended to labels of quantities to indicate the rotation centre, viz. wedge trailing edge (TE), wedge leading edge (LE) and the model rotation centre in the experiment (EXP). For example the corrected ϕ_D for rotation about the trailing edge is ϕ_{DC_TE}. The deviation from the corrected theoretical transition condition (corrected detachment condition in this case) is labelled $\delta\theta_{WT}$ and $\delta\phi_T$. Comments are only applicable for the range of simulations presented here, unless otherwise stated. The uncertainty in shock incidence measurement from flow field contours in the CFD solution was reported earlier in chapter 4 as $\delta\phi = \pm 0.2°$.

6.5.1 $M = 1.93$

Results for Euler simulations at $M = 1.93$ are presented in figure 6.15 and tables 6.5 - 6.6. Figures 6.15(a) and 6.15(b) include θ_{DC} and ϕ_{DC} to account for the streamwise movement of the reflection point at transition, e.g. at $M_E = +0.1$, $\phi_{DC_LE} \approx 41.8°$ in comparison to the uncorrected $\phi_D = 43.22°$, a difference of approximately 1.4°.

The results at $M = 1.93$ are summarised as follows :

1. For the range of rotation speeds investigated, $\delta\theta_{WT}$ increased with M_E for rotation about the wedge leading and trailing edges.
2. Across the range of simulated rotation rates, $1.3° \leq \delta\theta_{WT_TE} \leq 8.5°$ and $0.8° \leq \delta\theta_{WT_LE} \leq 5.4°$.
3. $\delta\phi_T$ also increased with M_E, for a given rotation centre and initial incidence.
4. $1.2° < \delta\phi_{T_TE} < 1.6°$ and $0.8° < \delta\phi_{T_LE} < 1.3°$, a similar order of magnitude observed in the experiment. The variation in $\delta\phi_T$ across the range of rotation speeds, is small at 0.4° for trailing edge pivot and 0.5° for leading edge pivot.
5. The dependency of $\delta\phi_T$ on rotation centre, for a given rotation speed, is also small, e.g. for $M_E = +0.1$, $\delta\phi_{T_LE} = 1.3°$ and $\delta\phi_{T_TE} = 1.6°$, a difference of 0.3°, just outside the uncertainty in shock incidence measurement of $\delta\phi = \pm 0.2°$.
6. The difference between ϕ_{T_TE} and ϕ_{T_EXP} is negligible for all practical purposes and within the uncertainty value of $\delta\phi = \pm 0.2°$
7. Table 6.6 indicates, that the dependency of θ_{WT} and ϕ_T on initial incidence, for a given rotation centre and rotation speed, is small and also within the uncertainty of $\delta\phi = \pm 0.2°$.

6.5.2 $M = 2.98$

Results are presented in figure 6.16 and tables 6.7 - 6.8. The corrections made to the steady detachment condition were smaller as the gradient of ϕ_D with Mach number is smaller around $M = 2.98$. For the range of simulations conducted at $M = 2.98$, there were many similarities in the results observed at $M = 1.93$. The only difference observed at $M = 2.98$ worth particular mention was in terms of $\delta\phi_T$, i.e. $0.6° < \delta\phi_{T_TE} < 1.4°$ and $0.4° < \delta\phi_{T_LE} < 1.3°$. The variation in $\delta\phi_T$ across the range of rotation speeds, for a given rotation centre and initial incidence, is larger than at $M = 1.93$, viz. 0.8° for trailing edge pivot and 0.9° for leading edge pivot. So, while the sensitivity of $\delta\phi_T$ to rotation speed, for a given rotation centre and initial incidence is small at $M = 1.93$, this is not generally true.

Table 6.5: θ_{WT} and ϕ_T at $M = 1.93$, $\theta_{wi} = 8.0°$

M_E	**+0.01**	**+0.03**	**+0.05**	**+0.075**	**+0.1**
θ_{T_TE} [degrees]	13.6	15.3	17.5	19.8	21.9
ϕ_{T_TE} [degrees]	44.2	44.4	44.3	43.9	43.9
θ_{T_LE} [degrees]	13.1	15.0	16.4	18.1	19.8
ϕ_{T_LE} [degrees]	43.8	43.7	43.7	43.5	43.1
θ_{T_EXP} [degrees]	-	-	17.8	-	22.8
ϕ_{T_EXP} [degrees]	-	-	44.3	-	43.7

Table 6.6: Effect of initial incidence on ϕ_T and θ_{WT} at $M = 1.93$, $M_E = +0.1$

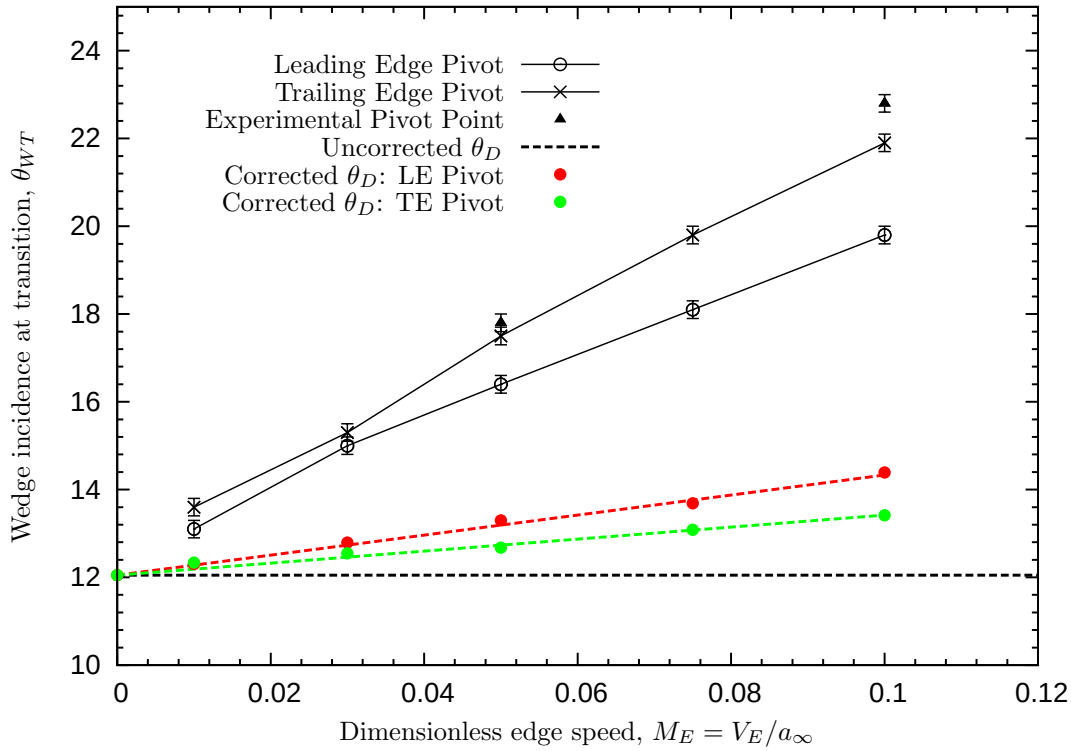
θ_{wi} [degrees]	Pivot Point	ϕ_T [degrees]	θ_{WT} [degrees]
2.0	Leading Edge	43.3	19.7
8.0	Leading Edge	43.1	19.8
2.0	Trailing Edge	43.8	22.0
8.0	Trailing Edge	43.9	21.9

Table 6.7: θ_{WT} and ϕ_T at $M = 2.98$, $\theta_{wi} = 19.0°$

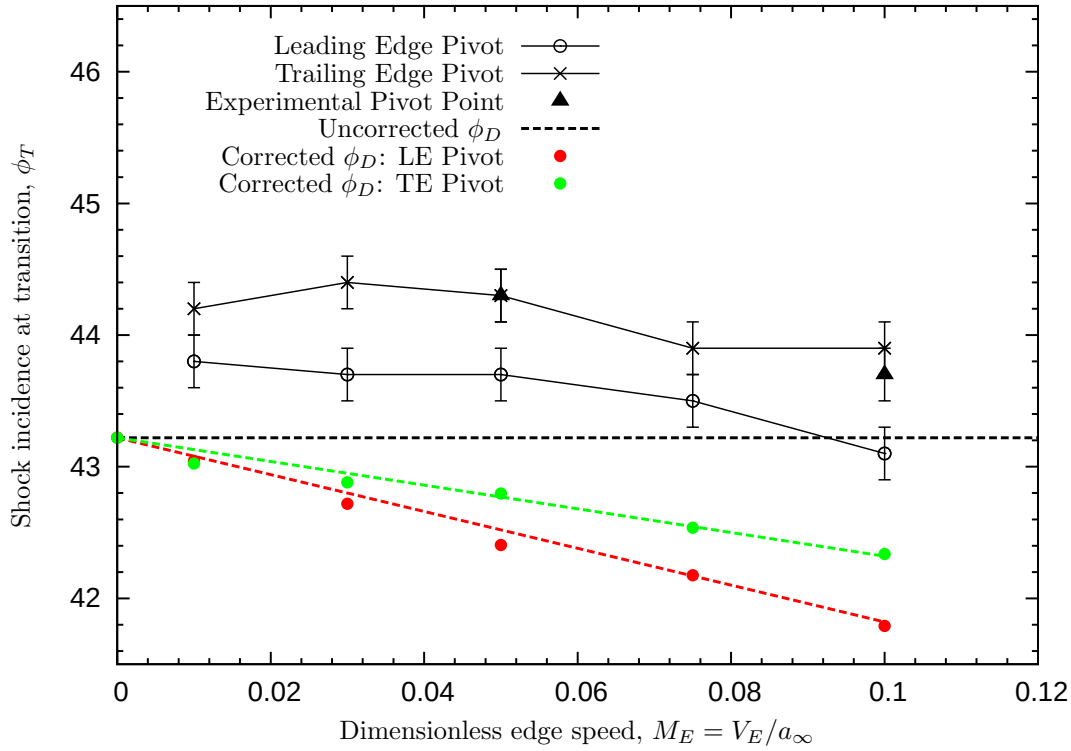
M_E	**+0.01**	**+0.03**	**+0.05**	**+0.075**	**+0.1**
θ_{T_TE} [degrees]	22.3	23.7	24.9	26.5	27.7
ϕ_{T_TE} [degrees]	40.1	40.4	40.5	40.6	40.8
θ_{T_LE} [degrees]	22.3	23.4	24.7	25.8	27.0
ϕ_{T_LE} [degrees]	39.9	40.5	40.4	40.6	40.7
θ_{T_EXP} [degrees]	-	-	25.3	-	28.1
ϕ_{T_EXP} [degrees]	-	-	40.6	-	40.7

Table 6.8: Effect of initial incidence on ϕ_T and θ_{WT} at $M = 2.98$, $M_E = +0.1$

θ_{wi} [degrees]	Pivot Point	ϕ_T [degrees]	θ_{WT} [degrees]
11.0	Leading Edge	40.6	27.0
19.0	Leading Edge	40.7	27.0
11.0	Trailing Edge	40.7	27.7
19.0	Trailing Edge	40.8	27.7

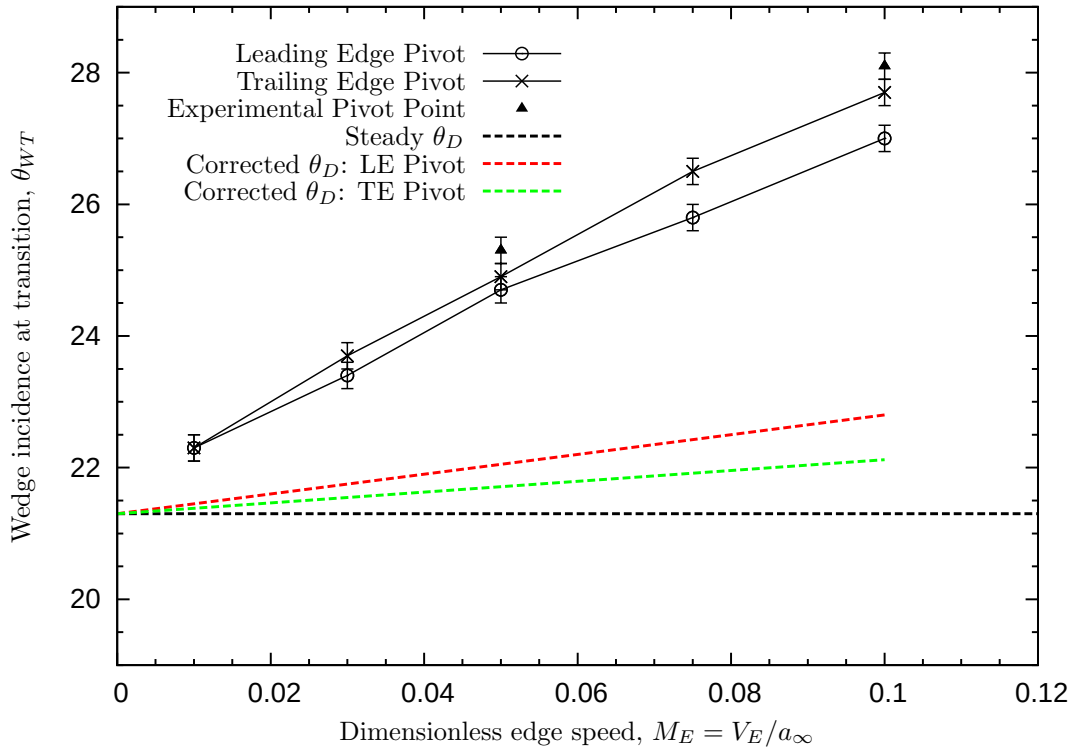


(a)

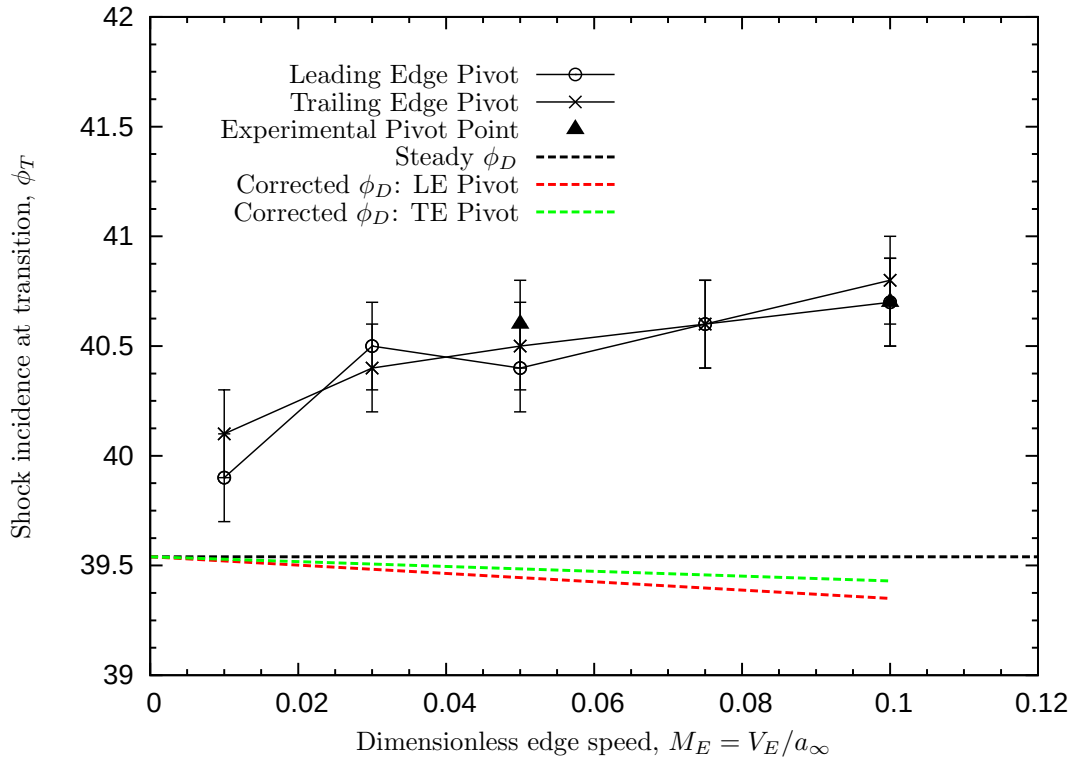


(b)

Figure 6.15: θ_{WT} and ϕ_T vs. M_E at $M = 1.93$, $\theta_{wi} = 8.0°$



(a)



(b)

Figure 6.16: θ_{WT} and ϕ_T vs. M_E at $M = 2.98$, $\theta_{wi} = 19.0°$

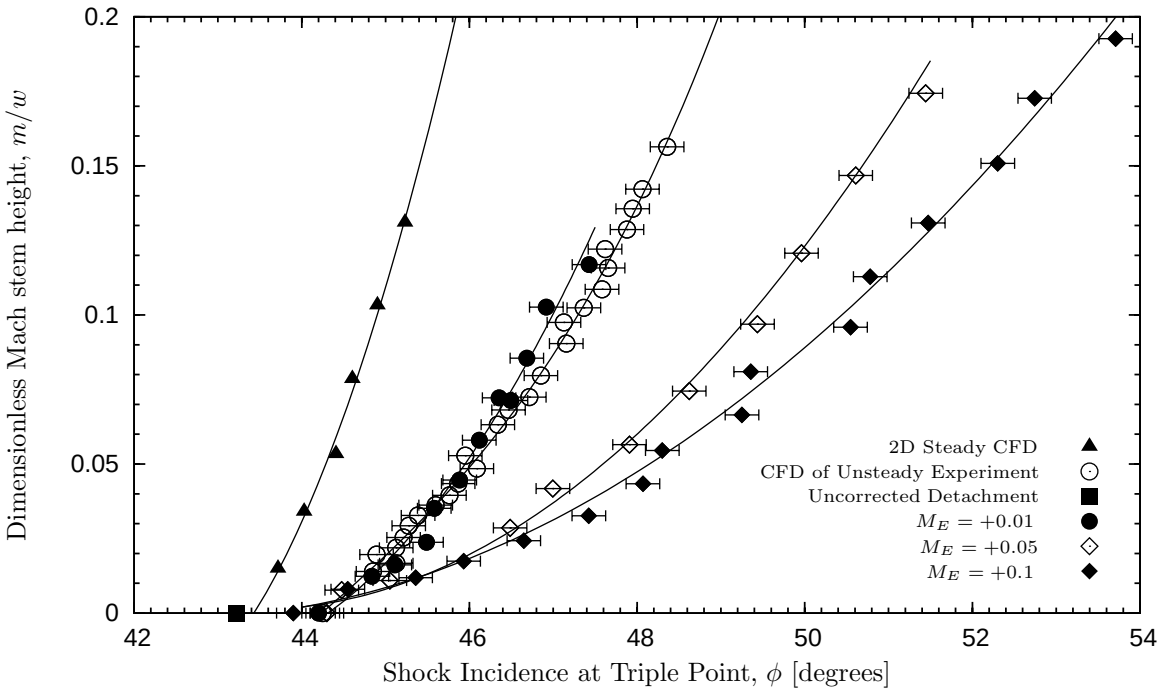


Figure 6.17: Dynamic Mach stem development for impulsive rotation about the wedge trailing edge at $M = 1.93$. Solid lines are second-order polynomial fits through each data set.

6.5.3 Dynamic Mach Stem Development

The dynamic Mach stem development for the various impulsive rotation cases at $M = 1.93$ and 2.98 are presented in figures 6.17 and 6.18 to visualise the effect of rotation speed on Mach stem growth with respect to ϕ at the triple point. The results from the steady CFD and the simulated experiments presented in sections 6.2.1 and 6.2.2 are overlayed. Only results for rotation about the wedge trailing are presented to indicate the general trend. At both free stream conditions, the second-order curve fit lies closer to the *x-axis* with an increase in rotation speed, i.e. for a given value of $\phi > \phi_T$, Mach stem growth is delayed further with an increase in rotation speed. At $M = 1.93$ there is little difference in the trend between the impulsively started wedge with $M_E = +0.01$ and the 2D CFD of the experiment (with average $M_E = +0.011$ up to transition). This is not the case at $M = 2.98$. The discrepency in trend between results for impulsive rotation with $M_E = +0.01$ and 2D CFD of the experiment (with average $M_E = +0.015$ up to transition) at $M = 2.98$ is rather curious. The trend has a negative second gradient in comparison to a positive second gradient for all the other cases. Though interesting, this particular feature lies beyond the scope of this work and is recommended for consideration in future investigations.

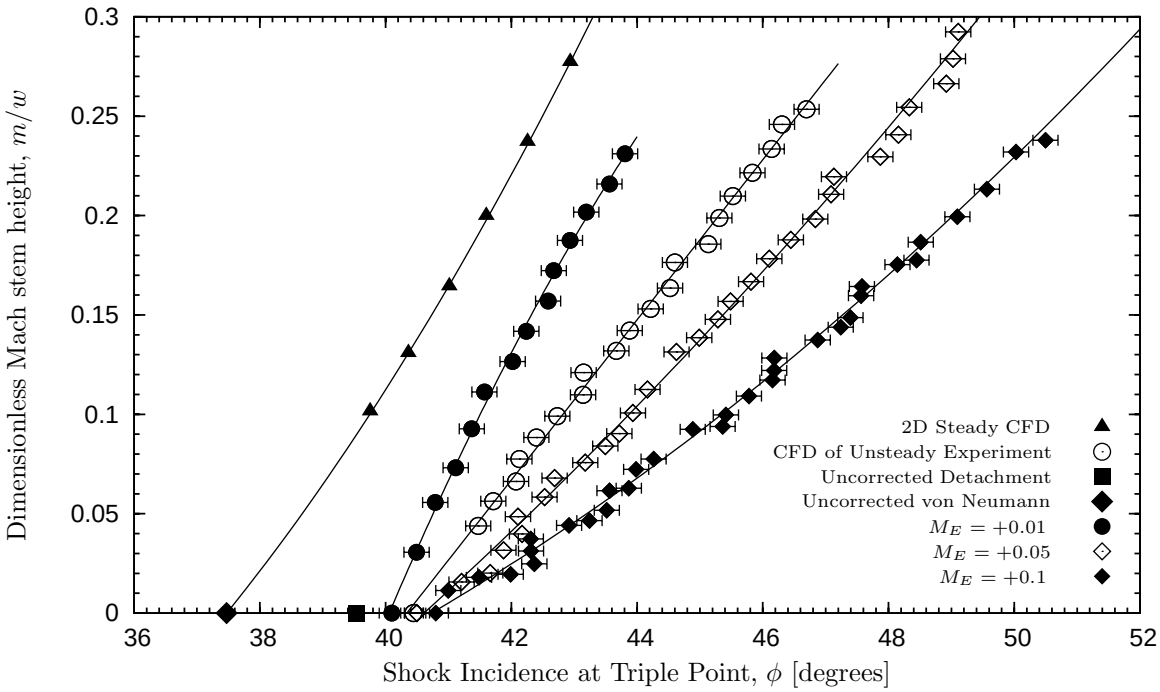


Figure 6.18: Dynamic Mach stem development for impulsive rotation about the wedge trailing edge at $M = 2.98$. Solid lines are second-order polynomial fits through each data set.

6.6 Conclusion

A rig was designed to investigate the dynamic effect of rapid wedge rotation on 2D RR to MR transition in a steady supersonic free stream. Experiments were completed in the weak and strong-reflection regions in the blow-down supersonic wind tunnel at the CSIR, South Africa. Results of steady state experiments, presented previously in chapter 5, showed that RR $\rightarrow$ MR transition occurs close to the detachment condition at $M = 1.93$ and close to the von Neumann condition at $M = 2.98$. With rapid wedge rotation at $M = 2.98$ it was possible to maintain RR through the dual solution domain, as originally proposed by Hornung [17], and even beyond steady detachment. Even though there was disagreement between the steady experiment and CFD in the strong-reflection region, there is close agreement between the experimental and computed values of ϕ_T for the dynamic case. This agreement implies that RR $\rightarrow$ MR transition in the strong-reflection region becomes insensitive to free stream noise above a certain critical rotation speed. In the dynamic experiments and computations of experiments at $M = 1.93$ and 2.98, RR persisted approximately $0.9^\circ - 1.3^\circ$ beyond ϕ_{DC}.

In all dynamic cases, there was good agreement in ϕ_T between the measurements in the experiments and predictions made by the Euler code developed by Felthun [11]. The measurements provide experimental evidence to support the dynamic effect originally presented by Felthun & Skews[12]. The close agreement

between experiment and computation provided confidence in the application of the Euler code to investigate particular aspects of the dynamic flow field.

As expected in the steady case (and discussed by Ivanov et al. [24]), for $\phi > \phi_T$, the difference in Mach stem height between the 2D computed result and the 3D experimental measurement was observed. This characteristic was also observed in the dynamic case at $M = 1.93$ and 2.98.

The dynamic RR $\rightarrow$ MR transition mechanism was investigated with 2D Euler CFD applied to the simulation of an impulsively rotated wedge at $M = 1.93$ and 2.98. For the dynamic cases investigated here, a distinction is drawn between the sonic, length scale and "detachment" conditions for dynamic RR $\rightarrow$ MR transition. Results show that the wedge length scale from the trailing edge expansion is not necessarily communicated to the reflection point as the flow downstream of the reflection point first goes sonic.

Computations at $M = 2.98$ also show that it is possible for RR to persist even though length scale information from the wedge trailing edge expansion is available at the reflection point. It is possible that RR is maintained beyond the length scale condition as long as the reflected wave is able to maintain the boundary condition at the reflection plane until the dynamic equivalent of the detachment condition.

Simulations at $M = 1.93$ show that it is also possible for RR $\rightarrow$ MR to occur without the presence of a length scale, perhaps due to the failure of RR to maintain the boundary condition at the reflection point. This is purely a dynamic effect due to the rapid wedge rotation.

Pressure traces through the reflection point show that rapid rotation increases the maximum achievable pressure rise through the reflection point of a RR in comparison to the steady case. As in the steady case, transition to MR in the strong-reflection region, is accompanied by a rapid decrease in pressure rise through the reflection/triple point. Due to the similarity in trend between the steady and dynamic cases, steady state shock polars may be useful in identifying the critical trend that highlights the point of transition in the dynamic case.

The parameter investigation at $M = 1.93$ showed, for $+0.01 < M_E < +0.1$, that there was a small dependence of $\delta\phi_T$ on rotation centre. Over the range of rotation speeds investigated, $0.8^\circ < \delta\phi_T < 1.6^\circ$, for both rotation centres. There was no significant change in θ_{WT} and $\delta\phi_T$ between the two values of initial incidence tested for rotation about the wedge leading and trailing edges at $M_E = +0.1$. For the range of simulations completed at $M = 2.98$ there is no fundamental difference in the results observed at $M = 1.93$. At $M = 2.98$, $0.4^\circ < \delta\phi_T < 1.4^\circ$, for both rotation centres. Graphs of dynamic Mach stem development at $M = 1.93$ and 2.98 show that an increase in rotation speed delays the development of the Mach stem with respect to ϕ at the triple point for a given value of $\phi > \phi_T$.

6.7 Recommendations for Future Work

The following items, though interesting, fall outside the scope of this thesis and are recommended for future work.

1. Determination of the minimum critical wedge rotation speed required such that transition is independent of free stream perturbations in the CSIR facility. This could be followed by a more general, but detailed investigation into the relationship between free stream noise and the minimum critical wedge rotation speed required to achieve RR $\rightarrow$ MR transition that is independent of the level of free stream noise and this could be applied to any facility.

2. An investigation to quantify the effect of rapid wedge rotation on the incident wave curvature and pressure gradient along the incident wave.

3. A detailed investigation into the "detachment" condition for the dynamic case.

4. Execution of the dynamic experiments at $M = 4.0$ in which the dual solution domain is larger. At $M = 4.0$ the difference between ϕ_D and ϕ_N is 5.8°.

5. Execution of the experiment described by Hornung [17]. Establish an initial, steady, RR below the dual solution domain, preferably at $M = 4.0$. Rotate the wedges rapidly and terminate the motion just below the detachment condition. The development of the reflection pattern would be of primary interest. The challenge, from an experimental perspective, lies in the termination of the wedge motion at the desired condition in a way that does not introduce vibration that influences transition or the development of the reflection pattern.

6. Investigation of the curious negative second gradient for Mach stem development against ϕ with $M_E = +0.01$ at $M = 2.98$.

7. The rig developed here may be applied to various interesting experimental studies, e.g. the effect of acceleration of finite aspect ratio wings in a steady, supersonic free stream on the unsteady evolution of the wing wake structure.

Chapter 7

Dynamic Two-Dimensional Mach to Regular Reflection Transition in an Ideal Steady Supersonic Free Stream

7.1 Introduction

This chapter presents results from experiments and computations to investigate the effect of rapid wedge rotation on two-dimensional (2D) MR $\rightarrow$ RR transition in an ideal, steady, supersonic free stream. A series of steady, baseline experiments were conducted with the servo-driven actuator, and results of the experiments and steady state computations were presented in chapter 5. The spring-driven actuator was installed and configured appropriately. Experiments were conducted at $M = 2.96$ and 3.26. The maximum rotation speed achieved at transition was approximately 2500 deg/s resulting in $M_E = -0.008$. Schlieren images were captured with the Photron Ultima APX-RS at 10000 frames per second at 512×512 pixel resolution. The measured wedge motion was mimicked in the Euler code developed by Felthun [11]. The dynamic Mach stem development as well as the measured and computed ϕ_T are compared to steady state results previously presented. The primary purpose of mimicking the experiment with CFD was to evalute the ability of the computational method to predict the gross dynamic effects and ϕ_T.

The 2D Euler code was also applied to scenarios beyond the experiments to investigate the dependence of dynamic MR $\rightarrow$ RR transition on other variables in the parameter space. These include pivot point, initial incidence, rotation speed at two free stream conditions, i.e. in the weak and strong-reflection ranges. The evolution of the reflection pattern and the development of the Mach stem due to impulsive rotation about the wedge leading and trailing edges is investigated. Reference will only be made to the reflection pattern in the streamwise vertical plane of symmetry unless otherwise stated. Thoughts on three-dimensional (3D) effects will be presented for consideration in future work.

7.2 Experimental Results

The wedge and shock incidence at the steady detachment condition are annotated θ_D and ϕ_D respectively. In a similar manner the wedge and shock incidence at the steady von Neumann condition are annotated θ_N and ϕ_N respectively.

7.2.1 Weak-Reflection Range

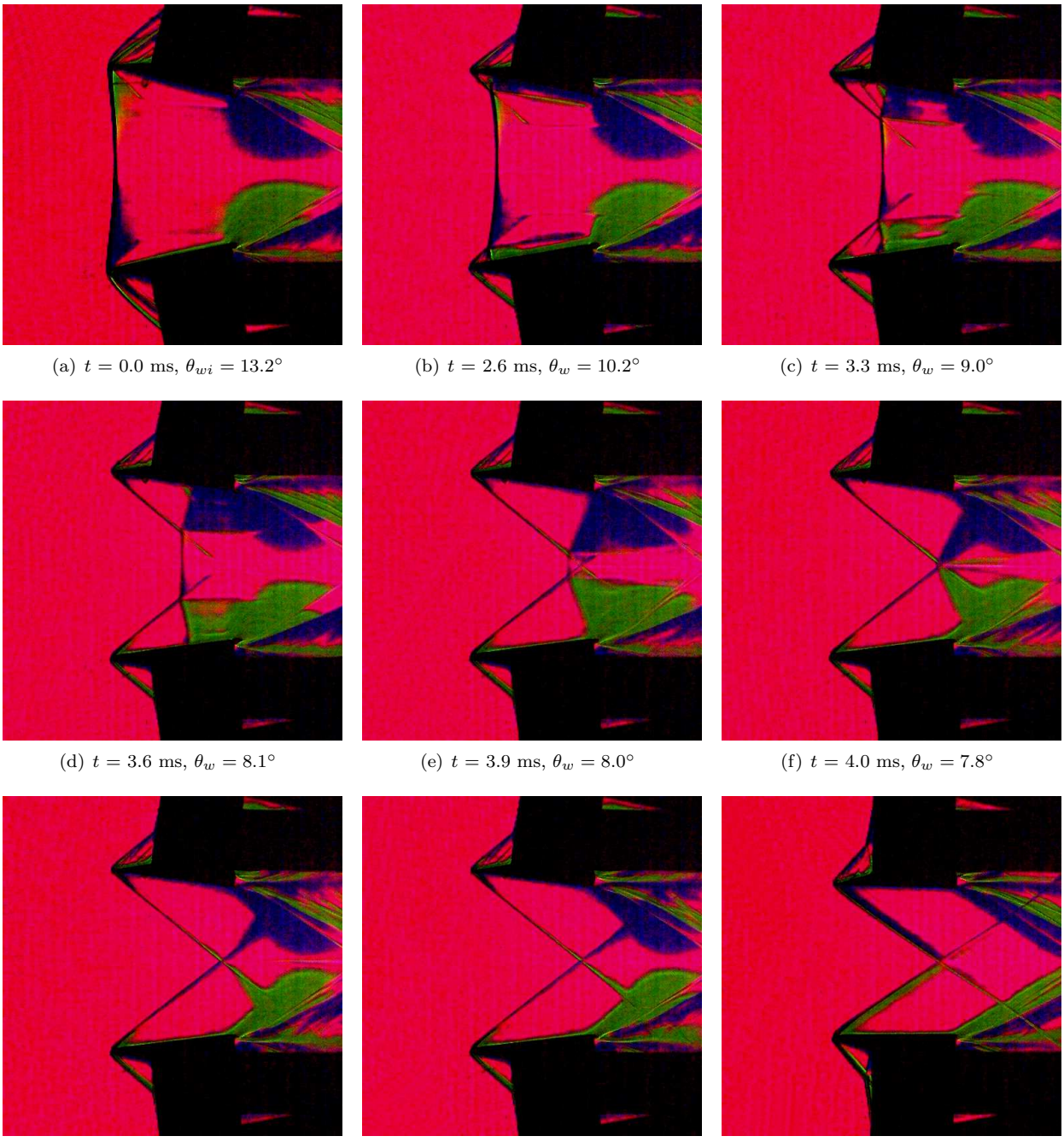
Due to the way in which the tunnel flow starts, the flow sets up an initial disgorged wave system or a steady RR in the plane of symmetry for a fixed initial wedge incidence at $M = 1.93$ (see results of the steady experiment in chapter 4). It was not possible to set up an initial, steady MR in the weak-reflection range and hence the dynamic MR $\rightarrow$ RR transition was not investigated with experiment. However, it was possible to set up an initial, steady MR in the strong-reflection region and experiments were completed at $M = 2.96$ and 3.26. These will be presented in the next section.

Figure 7.1 contains a selected sequence of images that show the initial, steady disgorged wave system at $M = 1.93$ and the development of the flow field as the spring-driven actuator decreases the wedge incidence rapidly. As the wedge incidence decreases the wave system is swallowed. A MR in which the reflected wave does not intersect the wedge surface can be seen in figure 7.1(e). Though visible, it cannot be considered steady state at this instant.

For dynamic RR $\rightarrow$ MR there was little dependence of ϕ_T on ϕ_i. However, for a steady, initial, disgorged wave system or MR, the flow downstream of the Mach stem is subsonic and the point of transition is likely to be very sensitive to ϕ_i. Since the flow field development from a steady, initial MR is of interest, this experimental data was not analysed further. Data from experiments in the strong-reflection range, presented in the next section, are considered sufficient to evaluate the computational method.

7.2.2 Strong-Reflection Range

Experiments for dynamic MR $\rightarrow$ RR transition were done at $M = 3.26$ and 2.96. In both experiments, an initial steady MR is set up and this is followed by the rapid decrease in wedge incidence until transition to RR. Experiment test conditions are documented in table 7.1. In both experiments RR persisted below ϕ_{NC}. There is no fundamental difference between the two cases in terms of flow physics. Hence, only results for the $M = 3.26$ case are analysed in some detail. Select high-speed images for the experiment at $M = 3.26$ are presented in figure 7.2. High-speed video from both experiments are included on the accompanying data disc. Zero time corresponds to the image frame just before any wedge movement is visible on the high-speed



(a) $t = 0.0$ ms, $\theta_{wi} = 13.2°$ (b) $t = 2.6$ ms, $\theta_w = 10.2°$ (c) $t = 3.3$ ms, $\theta_w = 9.0°$

(d) $t = 3.6$ ms, $\theta_w = 8.1°$ (e) $t = 3.9$ ms, $\theta_w = 8.0°$ (f) $t = 4.0$ ms, $\theta_w = 7.8°$

(g) $t = 4.1$ ms, $\theta_w = 7.1°$ (h) $t = 4.2$ ms, $\theta_w = 6.8°$ (i) $t = 5.9$ ms, $\theta_w = 1.2°$

Figure 7.1: High-speed images showing the initial, steady, disgorged wave system at $M = 1.92$ being swallowed as the wedge incidence decreases rapidly

Table 7.1: Experiment test conditions for dynamic MR → RR transition experiments, $g/w \approx 0.6$

M	P_O [Pa]	T_O [K]	ϕ_i [degrees]
3.26	616.0	302.0	40.2
2.96	474.0	301.0	41.2

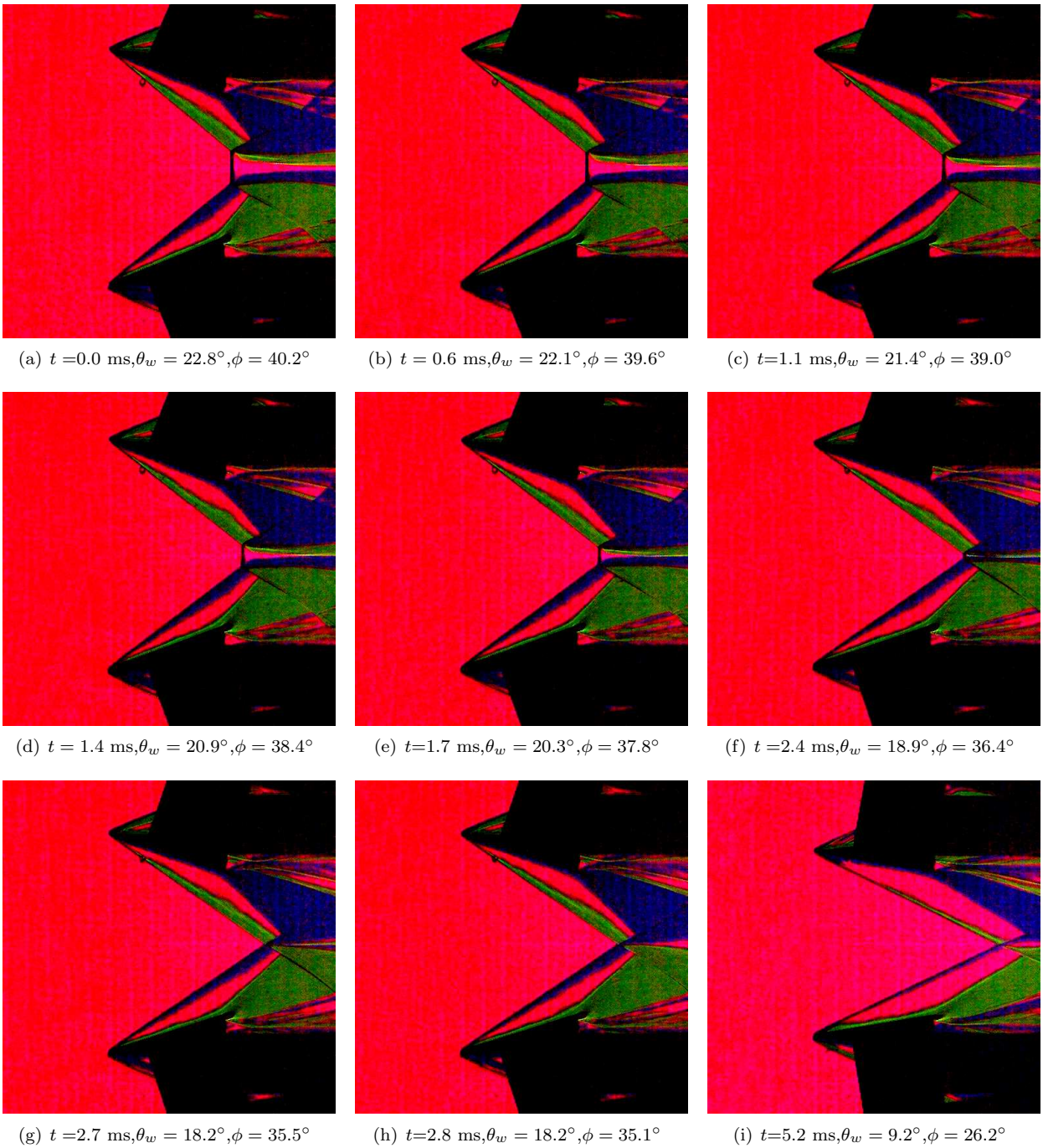
images. Measurements from the images are included in figures 7.3(a)- 7.3(d), i.e. time histories of wedge incidence, shock incidence, Mach stem height and the streamwise location of the reflection/triple point.

After tunnel startup, an initial, steady MR is set up just beyond the dual solution domain (figure 7.2(a)) after which time the wedge incidence was reduced rapidly. As θ_w decreases, the Mach stem moves downstream and the Mach stem height decreases (figures 7.2(b) - 7.2(f)) until transition to RR. In figure 7.2(h) the reflection pattern is clearly RR. The wedge rotation continues well after transition, but the flow field after transition is not analysed further here. The instantaneous rotation speed at the point of transition was approximately 2500 deg/s with $M_E = -0.008$, approximately 0.8% of the free stream acoustic speed. The tunnel conditions, measured wedge motion and initial shock incidence, ϕ_i, were used as inputs to the CFD simulation. Since the Euler equations do not model the flow deflection due to the wedge surface boundary layer, the initial wedge incidence, θ_{wi}, in the simulation was corrected to achieve the same ϕ_i in the experiment as discussed in chapter 4.

The experimental and computed Mach stem height variation with shock incidence angle is presented in figure 7.4. A linear fit to both data sets, only for $\phi \leq 38.0°$, is used to extrapolate ϕ_T at zero m/w. As indicated on the graph, the expected, initial difference in Mach stem height between the CFD and experiment is evident, though small at this initial condition (labelled m/w_{iCFD} and m/w_{iexp} respectively). As the wedge rotates there is a deviation from the steady case as indicated by "A" on figure 7.4. As the Mach stem height decreases, the unsteady CFD and experiment converge to $\phi_T \approx 35.5°$. The analytical transition condition was corrected for the speed of the triple point at transition and results are summarised in table 7.2. Transition was observed approximately 0.8° below ϕ_{NC} and there is close agreement on ϕ_T between the experiment and computation. Though the rotation speeds achieved here were not as large as in the RR → MR transition experiments, the dynamic effect of rapid wedge rotation on ϕ_T is still evident.

The Mach stem development from a simulation with the same free stream condition and ϕ_i, but with a larger and constant rotation speed about the wedge trailing edge at $M_E = -0.05$, is also plotted in figure 7.4. The deviation from the steady case is significant. In this instance transition to RR was predicted at $\phi_T \approx 32.7°$, 3.5° below ϕ_N and 4.5° below ϕ_{NC}.

The experiment at M = 2.96 yielded a similar result to the experiment at M = 3.26. Transition results

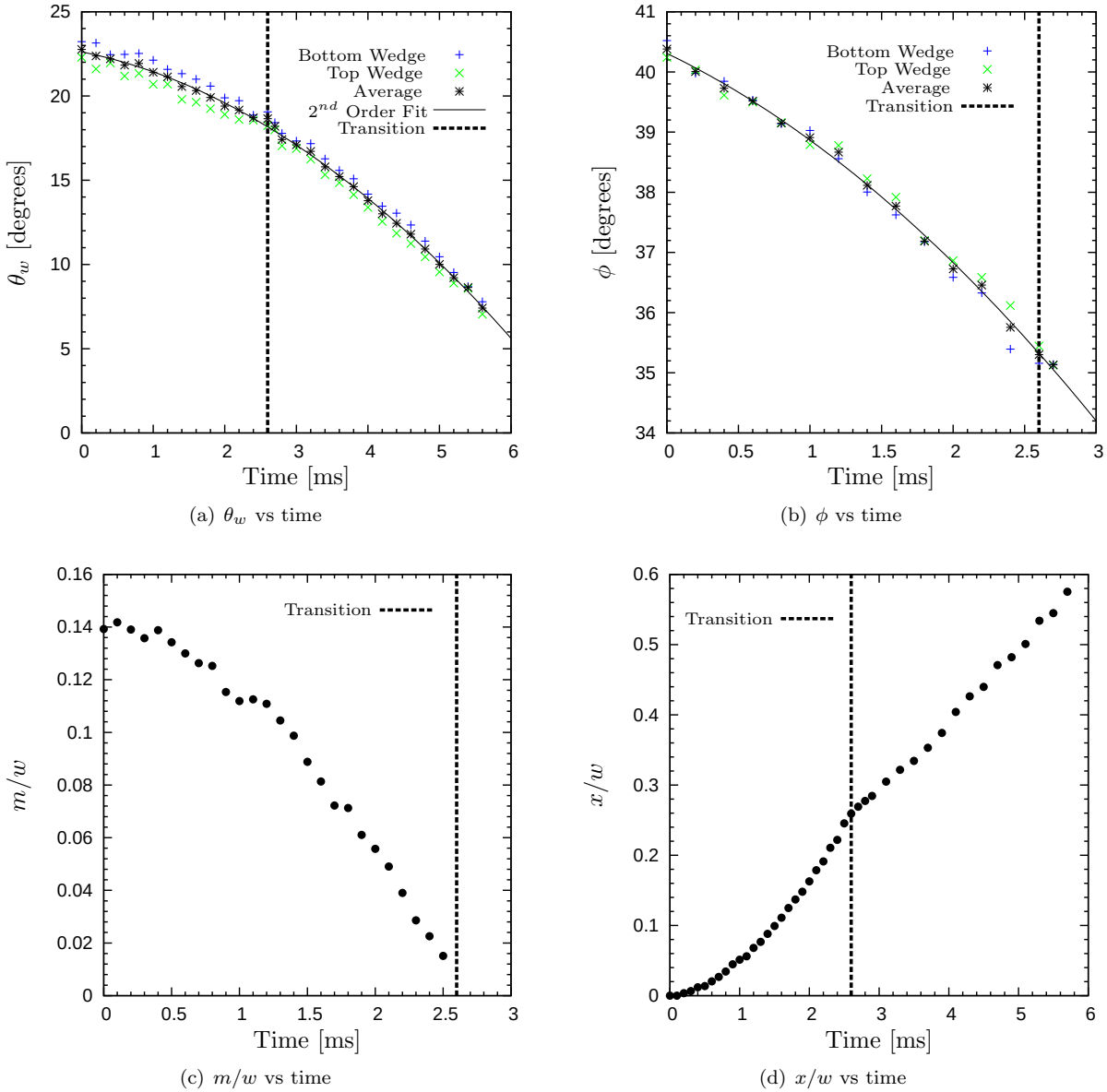


(a) t =0.0 ms,$\theta_w = 22.8°$,$\phi = 40.2°$ (b) t = 0.6 ms,$\theta_w = 22.1°$,$\phi = 39.6°$ (c) t=1.1 ms,$\theta_w = 21.4°$,$\phi = 39.0°$

(d) t = 1.4 ms,$\theta_w = 20.9°$,$\phi = 38.4°$ (e) t=1.7 ms,$\theta_w = 20.3°$,$\phi = 37.8°$ (f) t =2.4 ms,$\theta_w = 18.9°$,$\phi = 36.4°$

(g) t =2.7 ms,$\theta_w = 18.2°$,$\phi = 35.5°$ (h) t=2.8 ms,$\theta_w = 18.2°$,$\phi = 35.1°$ (i) t=5.2 ms,$\theta_w = 9.2°$,$\phi = 26.2°$

Figure 7.2: High-speed images from dynamic MR → RR experiment at $M = 3.26$



(a) θ_w vs time

(b) ϕ vs time

(c) m/w vs time

(d) x/w vs time

Figure 7.3: Measurements from the dynamic experiment at $M = 3.26$. The time of MR → RR transition is estimated from the images and is indicated on each graph with a broken line.

Table 7.2: Experimental and CFD results for steady and dynamic MR → RR transition at $M = 3.26$, $g/w \approx 0.6$.

Analytical steady von Neumann condition, ϕ_N	36.2°
Measured relative Mach number of reflection point at transition	- 0.03
Corrected analytical steady von Neumann condition, ϕ_{NC}	36.3°
Experiment : dynamic ϕ_T	35.5°
2D Euler CFD : steady state ϕ_T	36.2°
2D Euler CFD : dynamic ϕ_T	35.5°
Difference between dynamic ϕ_T and ϕ_{NC} (CFD and Experiment)	$\approx 0.8°$

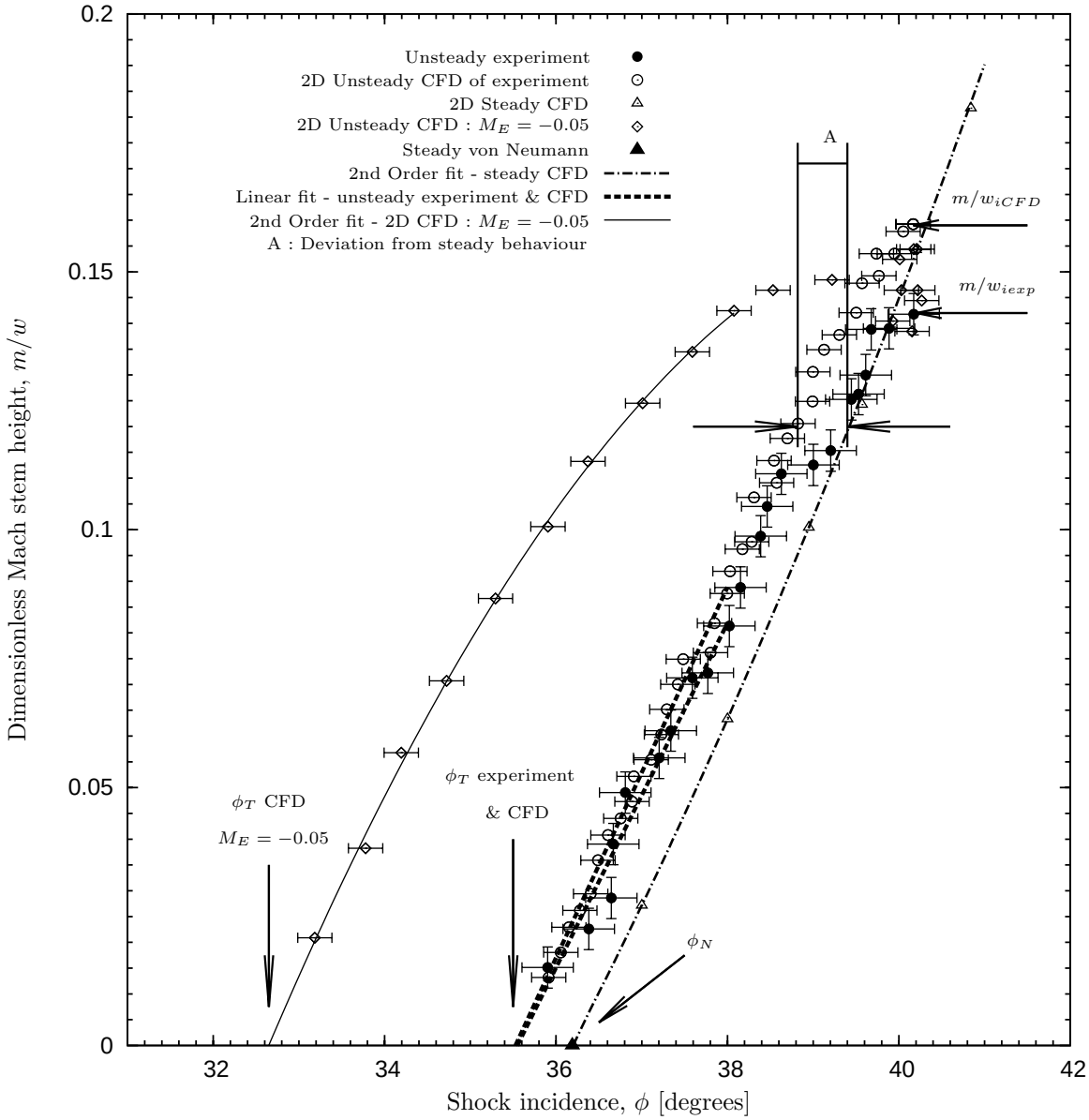


Figure 7.4: Mach stem development from experiment and CFD for dynamic MR → RR transition at $M = 3.26$, $g/w \approx 0.6$. The dashed and solid lines represent first and second-order fits respectively, only for $\phi \leq 38.0°$, to their respective data sets and are used to extrapolate ϕ_T at zero m/w. The offset from the steady data due to rapid rotation of the wedge is labelled "A".

Table 7.3: Experimental and CFD results for steady and dynamic MR → RR transition at $M = 2.96$, $g/w \approx 0.6$.

Analytical steady von Neumann condition, ϕ_N	37.6°
Measured relative Mach number of reflection point at transition	- 0.02
Corrected analytical steady von Neumann condition, ϕ_{NC}	37.6°
Experiment : dynamic ϕ_T	37.0°
2D Euler CFD : dynamic ϕ_T	36.8°
Difference between dynamic ϕ_T and ϕ_{NC} (CFD and Experiment)	$\approx 0.6 - 0.8°$

are summarised in table 7.3. Transition was observed approximately $0.6° - 0.8°$ below ϕ_{NC}. Once again, there is close agreement between the experiment and 2D Euler CFD result.

7.3 Parameter Investigation for Dynamic MR to RR Transition

Having established the necessary confidence in the Euler code to model the dynamic flow field of interest adequately for the purpose of this investigation, this section explores the sensitivity of ϕ_T as well as the dynamic flow field development to rotation speed and pivot point at $M = 1.93$ and 2.98 with CFD simulations. The sensitivity of ϕ_T to θ_{wi} is also investigated briefly. These free stream conditions are the same as those used in the parameter investigation for dynamic RR → MR transition in chapter 6.

When θ_w is decreased gradually from an initial, steady MR such that the flow field is approximately steady state at each point in time, the Mach stem decreases continuously with a decrease in θ_w until transition to RR. Transition to MR occurs at the detachment condition, with $\phi_T = \phi_D$, in the weak-reflection region and at the von Neumann condition, with $\phi_T = \phi_N$, in the strong-reflection region. MR → RR transition occurs when the triple point reaches the reflection plane, i.e. when the Mach stem height reduces to zero. It stands to reason that dynamic MR → RR transition is dependent on the initial Mach stem height and the vertical movement of the triple point (or Mach stem development).

For a given free stream condition, and wedge chord, the initial Mach stem height is dependent on ϕ_i and g/w or h/w. The effect of the initial Mach stem height will be investigated briefly, but the primary focus of this parameter investigation is to identify the dynamic effect of rapid rotation on the evolution of the Mach stem and hence transition to RR. This also includes the sensitivity of the flow field development to pivot point. Results for simulations at $M = 1.93$ and 2.98 are summarised in subsections 7.3.3 and 7.3.4. Due to the complex nature of the dynamic flow field under extreme rotation speeds, impulsive rotation about the wedge leading and trailing edges at $M = 1.93$ are analysed in some detail in subsections 7.3.1 and 7.3.2 to highlight particular, curious aspects of the flow field.

The theoretical transition angles are recalculated to take into account the decrease in local Mach number

at the triple point due to its streamwise movement. The corrected wedge and shock incidence at the detachment condition are labelled θ_{DC} and ϕ_{DC} respectively. The corrected wedge and shock incidence at the von Neumann condition are labelled θ_{NC} and ϕ_{NC} respectively. The speed of the reflection point at transition is dependent on the pivot point and hence θ_{DC} and ϕ_{DC} are also dependent on the pivot point. The abbreviations TE, LE and EXP will be appended to labels of quantities to indicate the rotation centre, viz. wedge trailing edge (TE), wedge leading edge (LE) and the model rotation centre in the experiment (EXP). For example the corrected ϕ_D for rotation about the trailing edge is ϕ_{DC_TE}. The deviation from the corrected theoretical transition condition (corrected detachment condition in this case) is labelled $\delta\theta_{WT}$ and $\delta\phi_T$.

7.3.1 Impulsive Rotation About the Wedge Leading Edge at $M = 1.93$

An initial, steady MR is set up at $\theta_{wi} = 13.4°$ in a $M = 1.93$ free stream with $h/w = 0.84$. The wedge is started impulsively and rotated about its leading edge with $M_E = -0.075$ until $\theta_w = 0.0°$. Computed pressure contours showing the development of the flow field are presented in figures 7.17 to 7.21 at the end of this chapter. Animations of the dynamic flow field are included on the accompanying data disc. The Mach stem evolution with respect to θ_w and ϕ is shown in figures 7.5 and 7.6. Four phases of the triple point movement are identified in figure 7.5. The steady state, 2D data computed with Fluent are superimposed.

Phase I : As the wedge rotates about its leading edge, away from the reflection plane, expansion waves are generated on the surface and propagate towards the triple point. Due to the rapid rotation speed, the wedge rotates approximately 1.9° before the surface expansion reaches the triple point. Up to this time the triple point is unaware of the wedge movement and the Mach stem height is approximately constant during phase I (see figures 7.17(a), 7.17(b) and 7.18(a)).

Phase II : When the expansion waves reach the triple point at $\theta_w \approx 11.5°$, the expansion has the effect of "sucking" the triple point away from the reflection plane and increasing the Mach stem height momentarily (see figures 7.18(b), 7.19(a) and 7.19(b)). This effect was first observed and discussed briefly by Felthun & Skews [12] for rapid, impulsive rotation about the wedge leading edge at $M = 3.0$. The Mach stem height increases until the end of phase II at $\theta \approx 8.5°$ (figure 7.19(b)).

Phase III : Between $\theta_w \approx 8.5°$ and 7.0°, there is very little change in Mach stem height.

Phase IV : The Mach stem height decreases until transition to RR at $\theta_{WT} = 1.7°$ (see figure 7.20). The wedge incidence at transition is estimated with a linear extrapolation of the data for $\theta_w \leq 4.5°$. At transition to RR, a shock is generated at the triple point, indicating a discontinuity in the flow conditions at the triple point as transition to RR occurs. As the shock propagates downstream the reflected wave incidence changes.

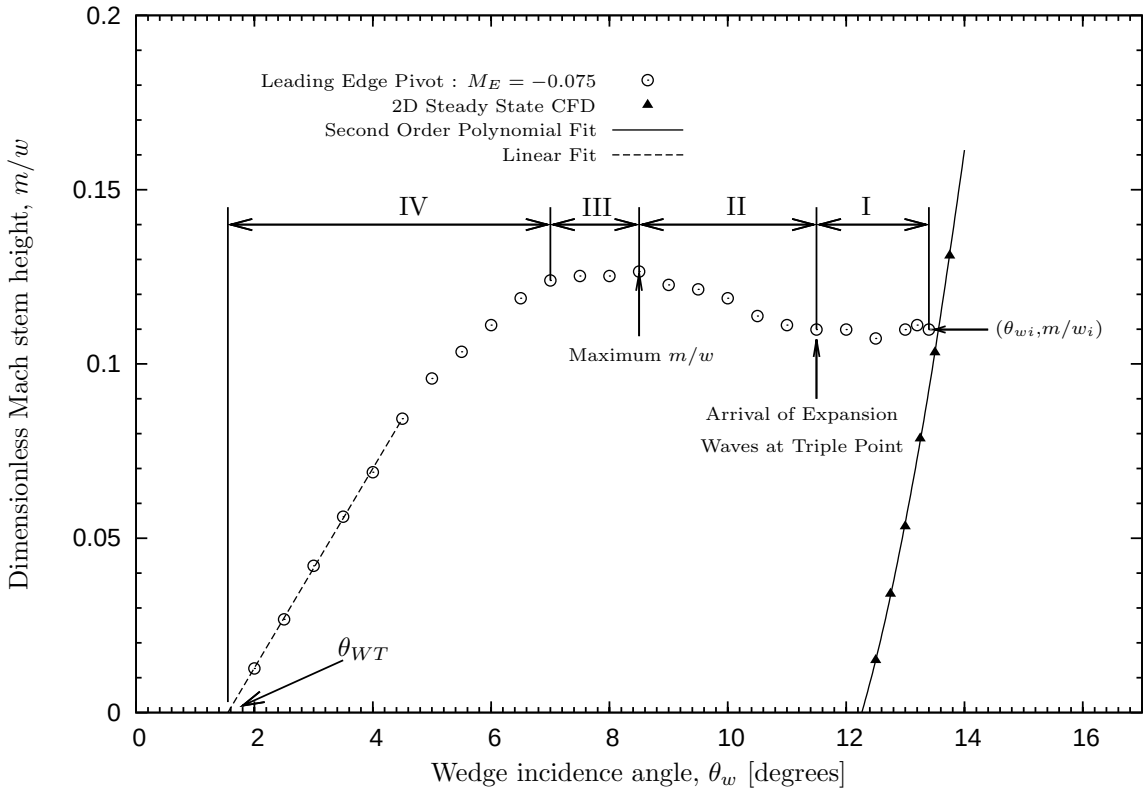


Figure 7.5: Computed variation of m/w with θ_w for impulsive rotation at $M_E = -0.075$. $M = 1.93$, $\theta_{wi} = 13.4°$, $h/w = 0.84$. The dashed line represents a linear fit of the data for $\theta_w \leq 4.5°$ and is used to estimate θ_{WT} at zero m/w for the rapidly rotating wedge. The solid line represents a second order fit of the steady data.

Consider the variation of m/w with ϕ in figure 7.6. The data points are connected with a dashed line to clarify the sequence of events. Results for the steady, 2D computation with Fluent are superimposed. The shock incidence and Mach stem height remain unchanged at $\phi = \phi_i = 45.1°$ and $m/w = m/w_i = 0.11$ in phase I. As the triple point moves away from the reflection plane, the suction has the effect of increasing the shock incidence to a maximum value of $\phi = 46.3°$ at the triple point. The point of maximum shock incidence does not coincide with the point of maximum Mach stem height. Before the maximum Mach stem height is achieved the shock incidence decreases and continues to do so until transition with $\phi_T \approx 39.2°$.

7.3.2 Impulsive Rotation About the Wedge Trailing Edge at $M = 1.93$

The steady, initial condition is set up at $\theta_{wi} = 13.4°$ in a $M = 1.93$ free stream (see figure 7.22(a)). The wedge is started impulsively and rotated at $M_E = -0.075$ about its trailing edge with $g/w = 0.6$. Figures 7.22 to 7.27 presented at the end of this chapter are selected images of pressure contours from the CFD solution between $\theta_{wi} = 13.4°$ and $\theta_w = 1.1°$. Animations of the computed flow field are included on the

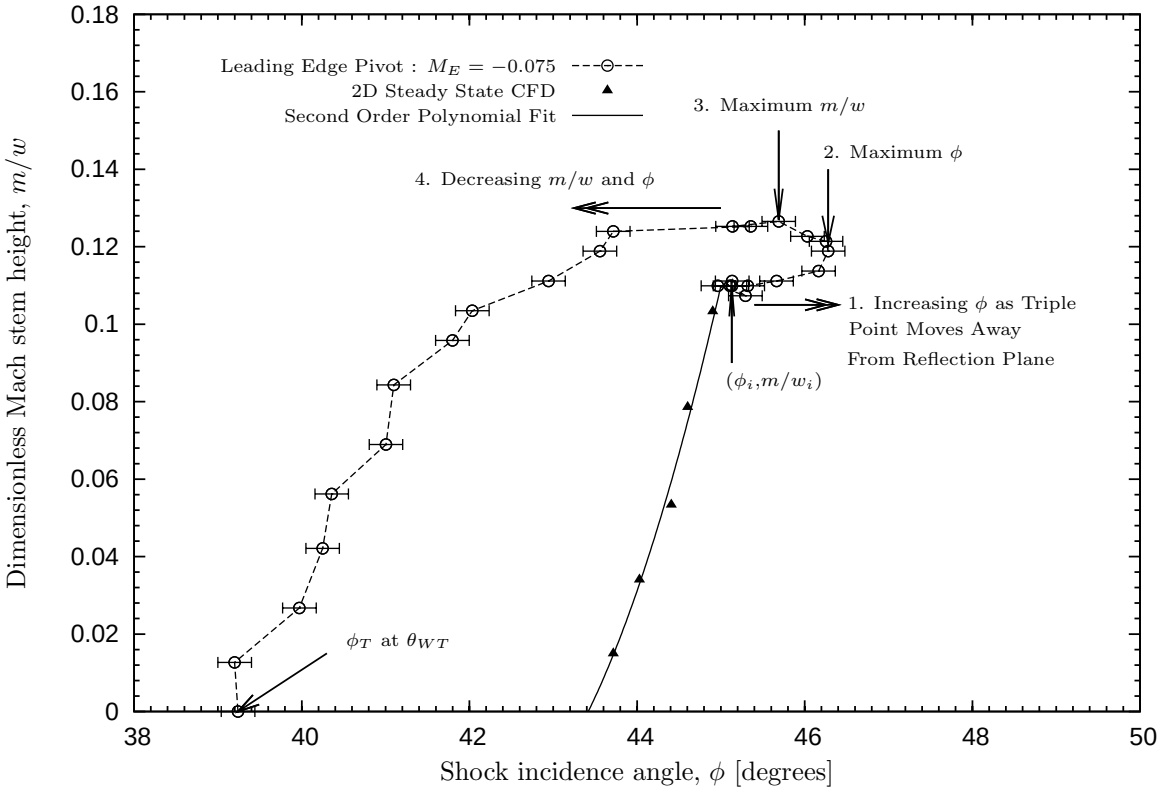


Figure 7.6: Computed variation of m/w with ϕ for impulsive rotation at $M_E = -0.075$. $M = 1.93$, $\theta_{wi} = 13.4°$, $h/w = 0.84$. The solid line represents a second order fit of the steady data. The data points from the unsteady simulation are connected with a dashed line to clarify the sequence of events.

accompanying data disc. The variation of m/w with θ_w and ϕ is presented in figures 7.7 and 7.8. Four phases of the triple point movement are identified in figure 7.7. The steady state, 2D data computed with Fluent are superimposed. There is a distinct difference in flow field development in comparison to the results for impulsive rotation about the wedge leading edge.

Phase I: The impulsive movement of the wedge tip generates a disturbance on the incident wave that propagates along the incident wave at a speed equal to the sum of the local acoustic speed and the local velocity component parallel to the incident wave. Figures 7.22(b), 7.23(a), 7.23(b) and 7.24(a) track the movement of the disturbance and downstream pressure wave until they reach the triple point. The red line corresponds to the planar incident wave at the initial condition and is shown to highlight the propagation of the disturbance on the incident wave. There cannot be any movement of the incident wave downstream of the disturbance. In phase I, the triple point is "unaware" of the movement of the wedge and the Mach stem height is constant until the disturbance reaches the triple point at $\theta_w \approx 11.6°$.

Phase II: The disturbance travels through the triple point and down the Mach stem, towards the reflection plane. As the disturbance passes through the triple point, the Mach stem height decreases rapidly, but only momentarily until $\theta_w = 9.5°$. By this time the disturbance has passed through the triple point. The pressure wave reflects from the reflection plane as seen in figure 7.24(b).

Phase III: Between $\theta_w = 9.5°$ and $7.5°$, the disturbance has already passed through the triple point and there is little further change in Mach stem height until the start of phase IV at $\theta_w = 7.5°$.

Phase IV: After the phase III, in which there was little movement of the triple point, the Mach stem height decreases until transition at $\theta_{WT} = 2.4°$ (see figures 7.26 and 7.27).

Consider the computed pressure contours in figure 7.24(b). The pressure contour between the incident and reflected waves that is closest to the triple point, is highlighted in a green dashed line. The intersection of the highlighted isobar with the incident wave indicates a discontinuity in curvature on the incident wave. The incident wave upstream of the discontinuity is curved and there is a pressure gradient along this segment of the incident wave. There is no pressure gradient along the planar segment of the incident wave, downstream of the discontinuity. As θ_w decreases the discontinuity moves towards the triple point and is evident from the movement of the pressure contours on the incident wave as seen in figures 7.25(a) and 7.25(b). By $\theta_w = 7.5°$ the incident wave is curved along its entire length. It appears that the start of phase IV in which the Mach stem height decreases, is co-incident with the arrival of the discontinuity on the incident wave at the triple point. A more detailed investigation is required to identify and quantify the mechanism(s) that marks the inception of phase IV. This lies beyond the scope of this thesis and is recommended for consideration in future work.

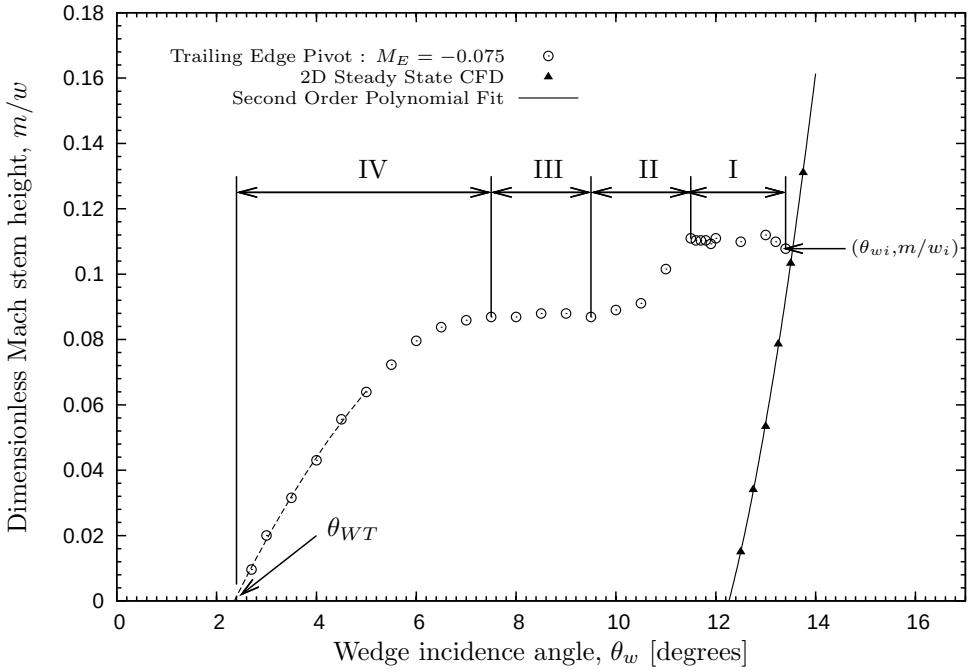


Figure 7.7: Computed variation of m/w with ϕ for impulsive rotation at $M_E = -0.075$. $M = 1.93$, $\theta_{wi} = 13.4°$, $g/w = 0.6$. The solid lines represent a second order fit of the steady and unsteady data. For the unsteady case, only data for $\theta_w \leq 5.0°$ is used to estimate θ_{WT}.

The wedge incidence at transition is extrapolated from a second order polynomial of the data for $\theta_w \leq 5.0°$. At transition to RR a shock is generated at the triple point. As it propagates downstream the reflected wave incidence changes and this indicates a discontinuity in the flow conditions in the vicinity of the reflection/triple point as transition to RR occurs.

Consider the variation of m/w with ϕ in figure 7.8. The data points are connected with a broken line to clarify the sequence of events. Results for the steady, 2D computation with Fluent are superimposed. The shock incidence remains constant until the arrival of the disturbance on the incident wave at the end of phase I. As the disturbance passes through the triple point there is a sudden decrease and increase of ϕ in phase II. In phase III, ϕ and m/w are constant. In phase IV, ϕ and m/w decrease until transition at $\phi_T = 37.9°$.

7.3.3 Parameter Investigation for Dynamic MR to RR Transition at $M = 1.93$

The variation of m/w with θ_w over a range of rotation speeds as well as the resultant θ_{WT} and ϕ_T is investigated with Euler CFD. Results are presented in figures 7.9, 7.10, 7.12(a) and 7.12(b) respectively. Figure 7.10 only includes results for $M_E = -0.01$ to avoid unnecessary clutter. Variation of m/w with ϕ and θ_w for $M_E = -0.075$ were already presented in figures 7.5 to 7.8. Table 7.4 summarises values for θ_T

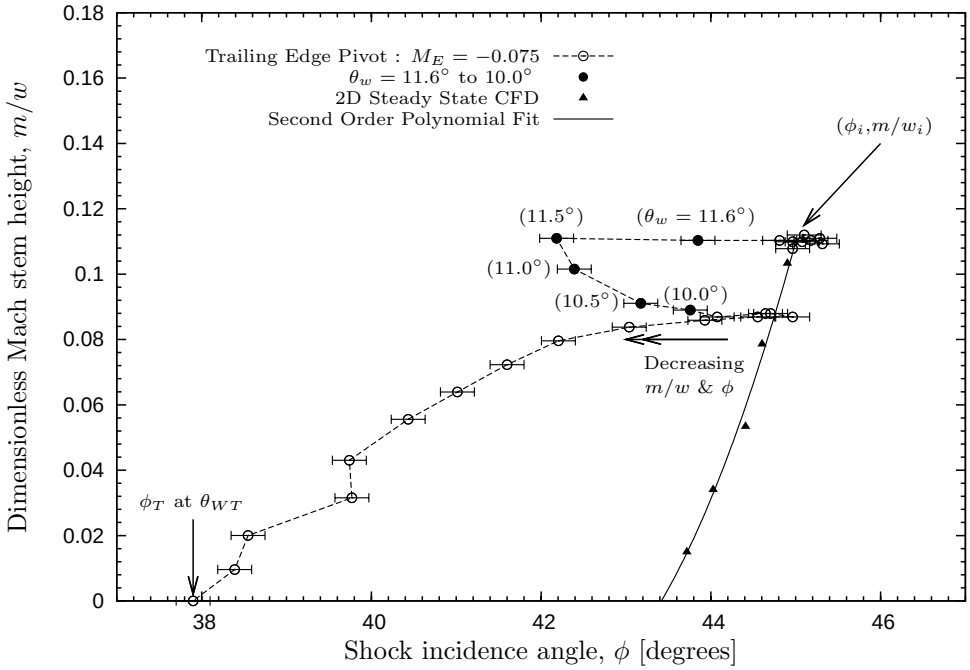


Figure 7.8: Computed variation of m/w with ϕ for impulsive rotation at $M_E = -0.075$. $M = 1.93$, $\theta_{wi} = 13.4°$, $g/w = 0.6$. The solid line represents a second order fit of the steady data. The data points from the unsteady simulation are connected with a dashed line to clarify the sequence of events.

and ϕ_T.

Consider the variation of m/w with θ_w and ϕ in figures 7.9 (for $M_E = -0.01$, -0.05 and -0.1) and 7.10 (for $M_E = -0.01$ only). The dynamic effect of rapid rotation on the Mach stem development for $M_E = -0.075$ presented in subsections 7.3.1 and 7.3.2 are not visible at $M_E = -0.01$. It would appear that at this smaller rotation speed, the rotation centre makes little difference to the transient Mach stem development or to the values of θ_{WT} and ϕ_T (see also figures 7.12(a) and 7.12(b)).

Also, consider the results for $M_E = -0.1$ in figure 7.9. While the Mach stem development is consistent with the observations made at $M_E = -0.075$, the impulsive start and rapid rotation result in a curious scenario in which MR is maintained even at $\theta_w = 0.0°$. Selected pressure contours from the flow solution for rapid rotation about the leading edge are presented in figure 7.11. The wedge is started impulsively at $\theta_{wi} = 13.4°$ and stopped at $\theta_w = 0.0°$. At $\theta_w = 0.0°$, the wave system detaches from the wedge tip and proceeds to wash downstream. The Mach stem on the residual wave reflection is clearly visible in figure 7.11(c). Figures 7.11(d), 7.11(e) and 7.11(f) are magnified views in the vicinity of the reflection plane showing the transition of the residual reflection from MR to RR as the wave system washes downstream.

For the range of rotation speeds investigated, $\delta\theta_{WT}$ and $\delta\phi_T$ increased with an increase in rotation speed. For the range of rotation speeds investigated, $1.2° \leq \delta\theta_{T_TE} \leq 7.1°$ and $1.0° \leq \delta\theta_{T_LE} \leq 6.2°$. The

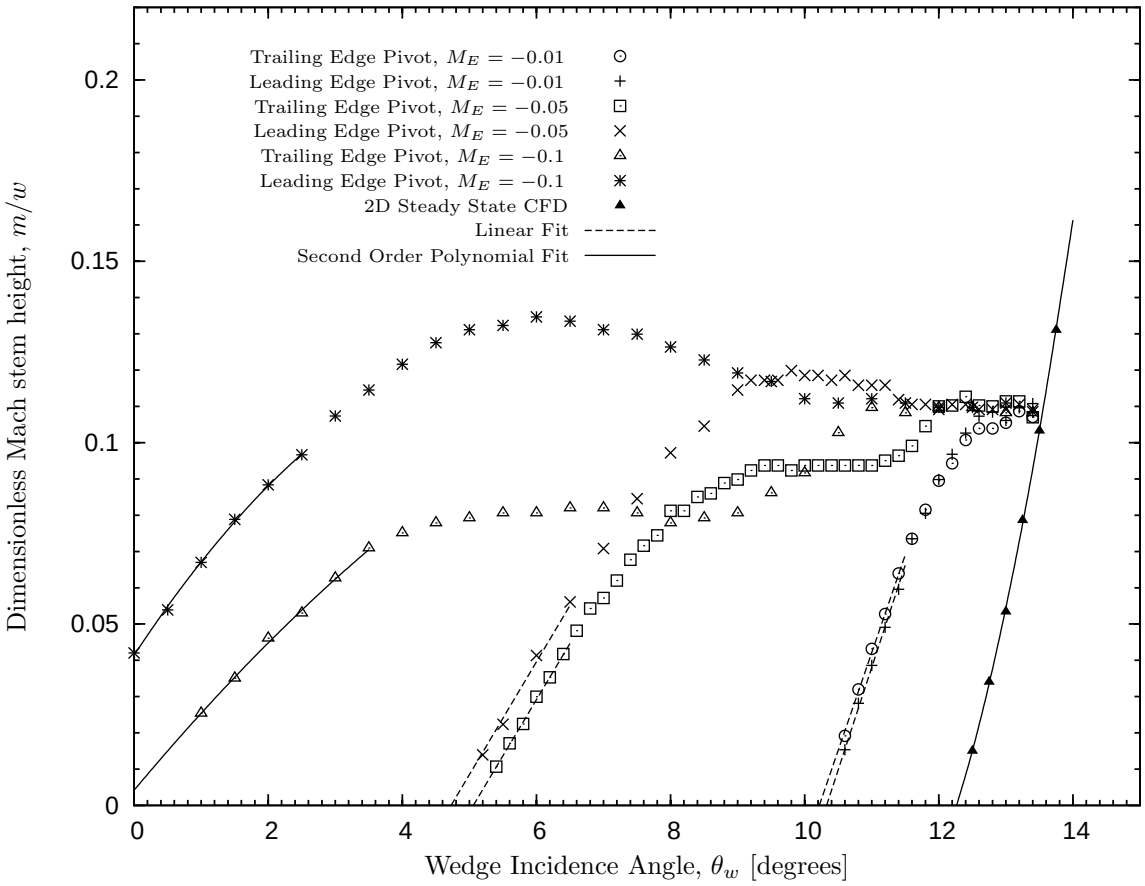


Figure 7.9: Computed variation of m/w with θ_w for rapid, impulsive rotation. $M = 1.93$, $\theta_{wi} = 13.4°$, $h/w = 0.84$ (for rotation about the leading edge), $g/w = 0.6$ (for rotation about the trailing edge). Dashed lines represent linear fits used to estimate θ_{WT} for $M_E = -0.01$ and -0.05. Solid lines are second-order polynomial fits used to estimate θ_{WT} for $M_E = -0.1$ and the steady state case.

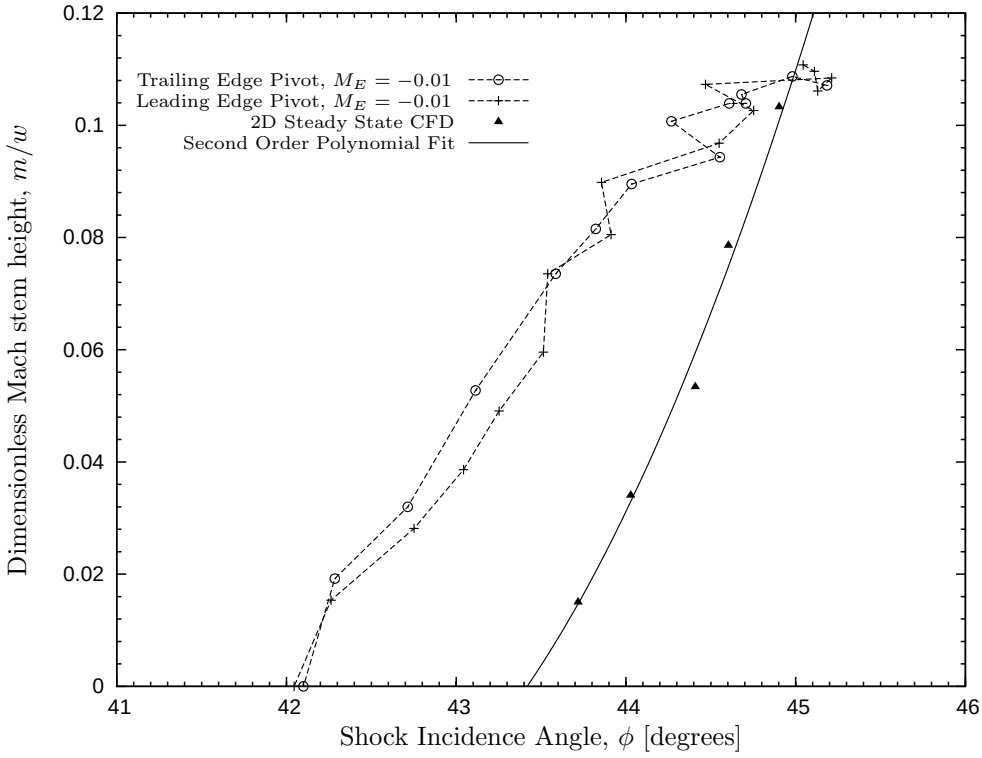
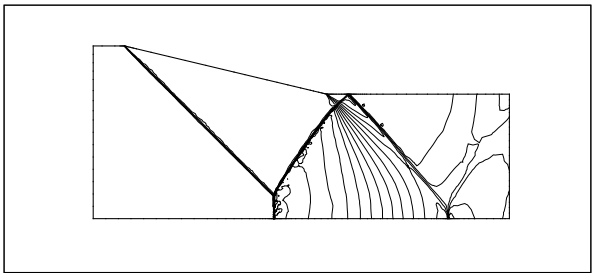
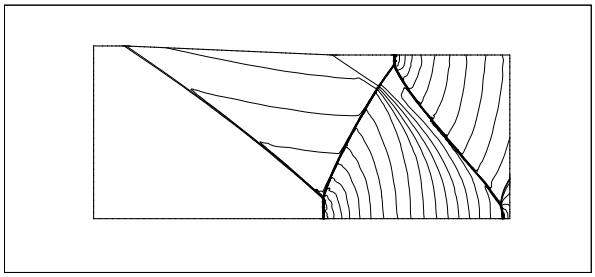


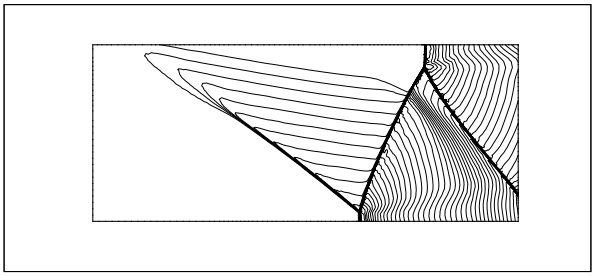
Figure 7.10: Computed variation of m/w with ϕ for rapid, impulsive rotation. $M = 1.93$, $\theta_{wi} = 13.4°$, $h/w = 0.84$ (for rotation about the leading edge), $g/w = 0.6$ (for rotation about the trailing edge). The solid line is a second-order polynomial fit used to estimate θ_{WT} for the steady state case. The dashed line joins the data points in each data set to aid visualisation. ϕ_T was measured from the flow solution at θ_{WT} in each case.



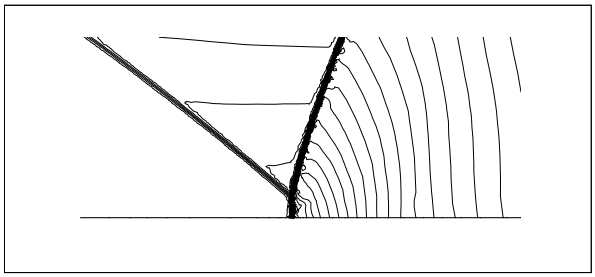
(a) $t = 0.0s$, $\theta_{wi} = 13.4°$



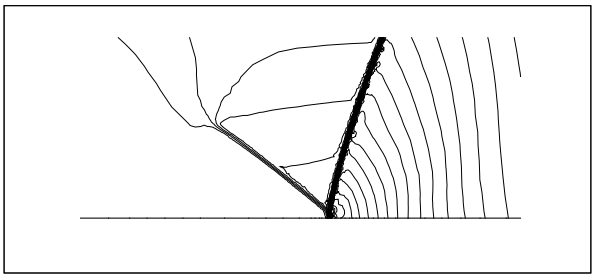
(b) $t = 10.6\mu s$, $\theta_w = 2.5°$



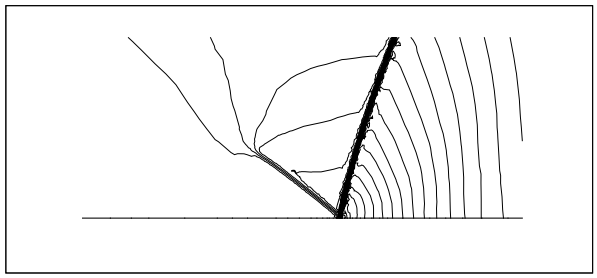
(c) $t = 23.8\mu s$, $\theta_w = 0.0°$



(d) Magnified view of residual wave reflection in the vicinity of the reflection point at $t = 50.2\mu s$ while $\theta_w = 0.0°$.



(e) Magnified view of residual wave reflection in the vicinity of the reflection point at $t = 71.4\mu s$ while $\theta_w = 0.0°$.



(f) Magnified view of residual wave reflection in the vicinity of the reflection point showing transition to RR at $t = 76.7\mu s$ while $\theta_w = 0.0°$.

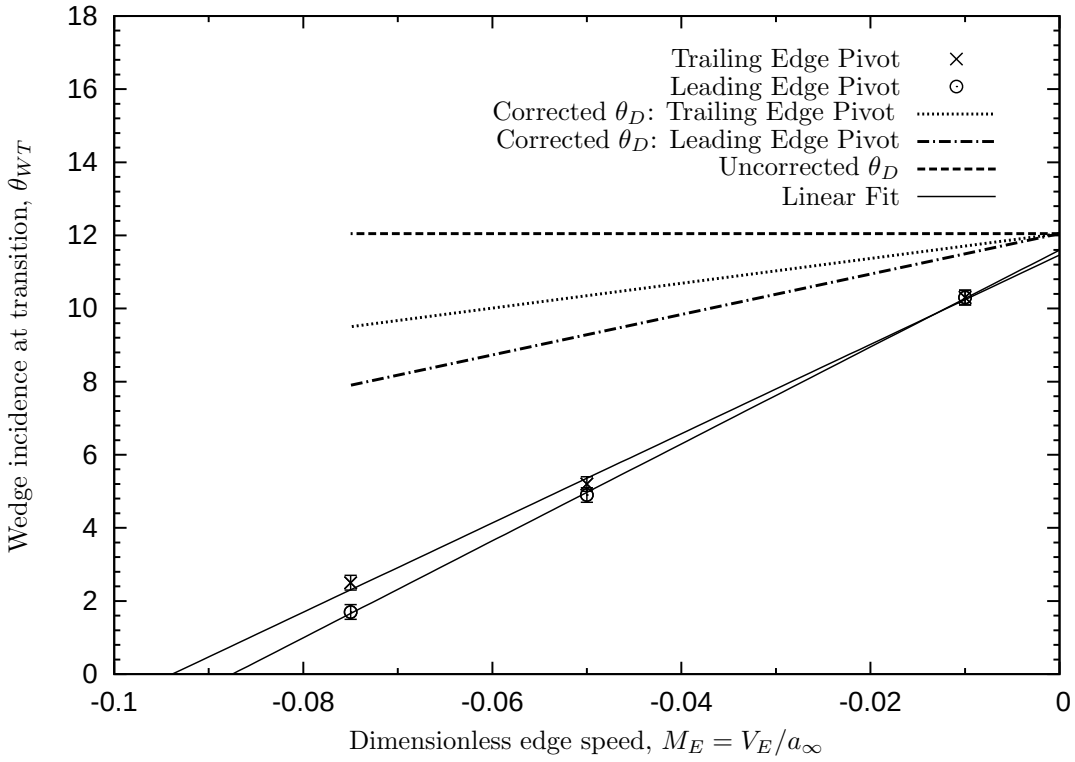
Figure 7.11: Computed pressure contours for impulsive rotation at $M_E = -0.1$. $M = 1.93$, $\theta_{wi} = 13.4°$, $h/w = 0.84$.

corresponding deviation of ϕ_T from ϕ_{DC} ranges as follows: $1.5° \leq \delta\phi_{T_TE} \leq 7.4°$ and $1.7° \leq \delta\phi_{T_LE} \leq 7.9°$. In contrast, the maximum deviation observed at $M_E = +0.1$ for RR $\rightarrow$ MR transition was in the order of $\delta\phi_T = 1.6°$, significantly smaller than the maximum values observed here.

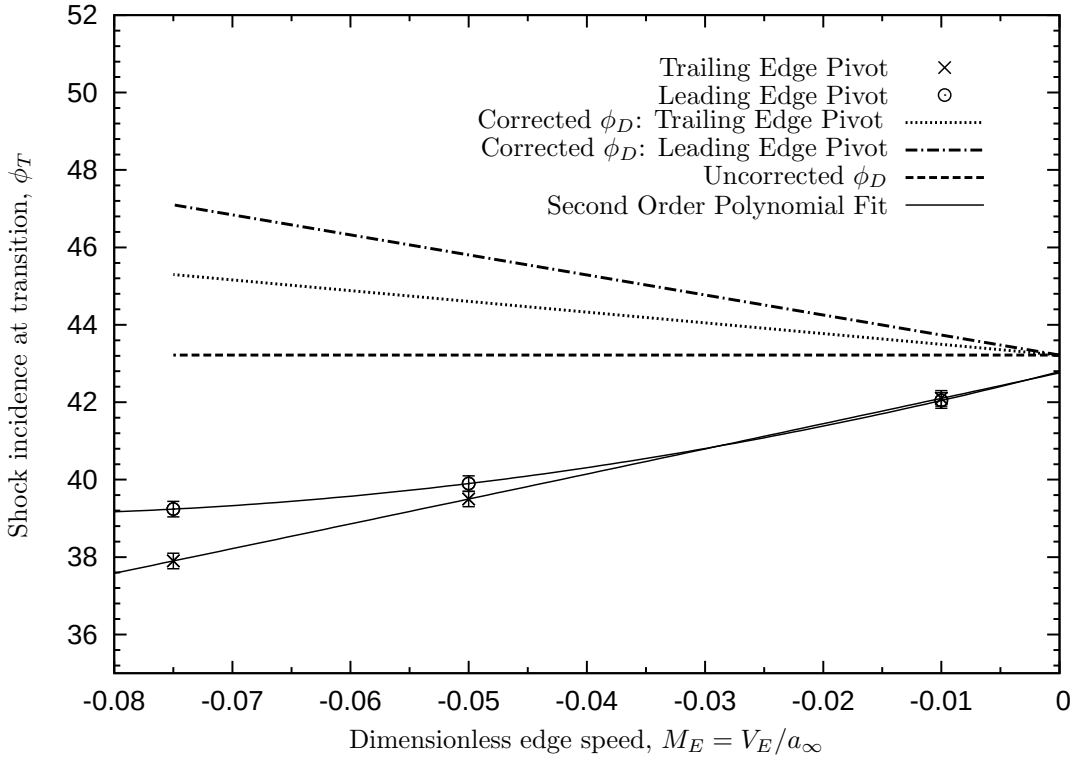
7.3.4 Parameter Investigation for Dynamic MR to RR Transition at $M = 2.98$

The variation of m/w with θ_w at $M_E = -0.01$, -0.05 and -0.1 as well as the resultant θ_{WT} and ϕ_T was also investigated at $M = 2.98$. Results are presented in figures 7.14, 7.13(a) and 7.13(b) respectively. Table 7.5 summarises values for θ_T and ϕ_T.

Consider the variation of m/w with θ_w in figure 7.14. In general, the trends are similar to the results at



(a) θ_{WT} vs. M_E at $M = 1.93$



(b) ϕ_T vs. M_E at $M = 1.93$

Figure 7.12: θ_{WT} and ϕ_T vs. M_E at $M = 1.93$

Table 7.4: Wedge and shock incidence at transition : M 1.93, $\theta_{wi} = 13.4°$

M_E	-0.01	-0.05	-0.075
θ_{WT_TE}	10.3	5.2	2.4
ϕ_{T_TE}	42.1	39.5	37.9
θ_{WT_LE}	10.3	4.9	1.7
ϕ_{T_LE}	42.0	39.9	39.2

Table 7.5: Wedge and shock incidence at transition : $M = 2.98$, $\theta_{wi} = 24.5°$

M_E	-0.01	-0.05	-0.1
θ_{WT_TE}	18.2	12.7	7.1
ϕ_{T_TE}	36.3	32.5	29.0
θ_{WT_LE}	18.3	12.6	5.7
ϕ_{T_LE}	36.3	32.8	30.2

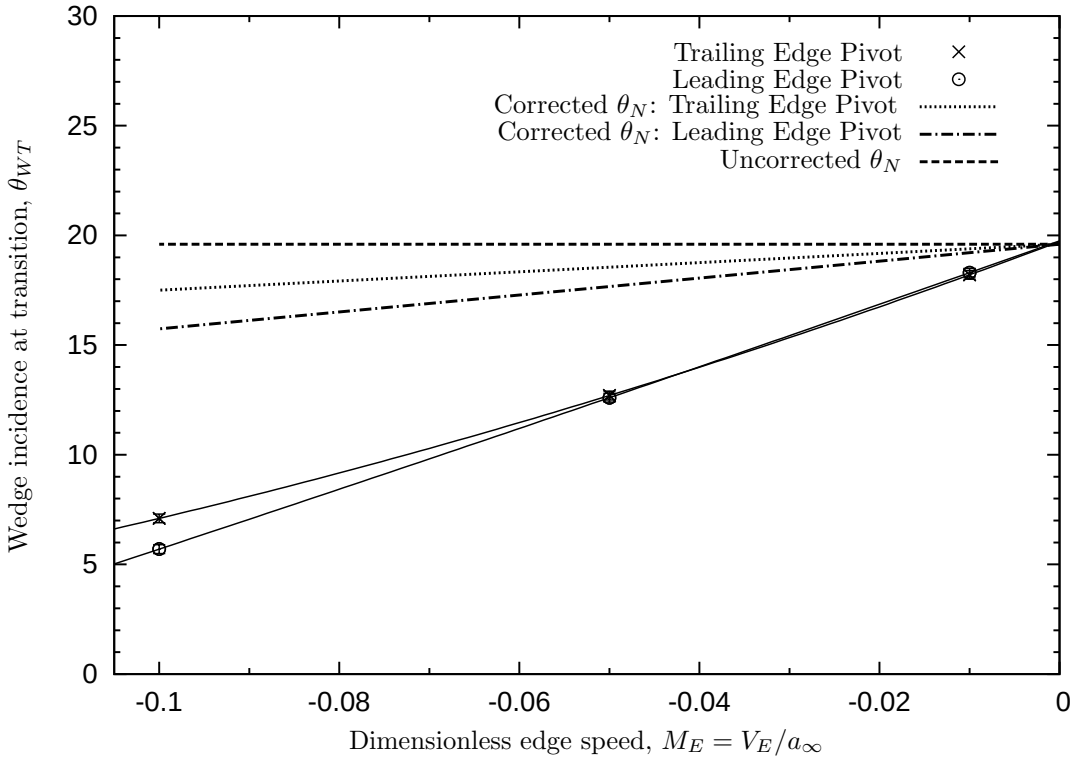
$M = 1.93$. However, a small, but perhaps significant difference, is noted at $M_E = -0.1$ for rotation about the wedge trailing edge (open triangular symbols in figure 7.14). After phase II in which the Mach stem height decreases, there is a small but observable increase in Mach stem height whereas the Mach stem height is approximately constant in phase III in figure 7.7. This is also noted at $M_E = -0.05$ for rotation about the wedge trailing edge (open square symbols in figure 7.14).

For the range of rotation speeds investigated, $\delta\theta_{WT}$ and $\delta\phi_T$ increased with an increase in rotation speed. For the range of rotation speeds investigated, $1.2° \leq \delta\theta_{T_TE} \leq 10.4°$ and $1.1° \leq \delta\theta_{T_LE} \leq 10.0°$. The corresponding deviation of ϕ_T from ϕ_{DC} ranges as follows: $1.5° \leq \delta\phi_{T_TE} \leq 10.9°$ and $1.5° \leq \delta\phi_{T_LE} \leq 10.9°$.

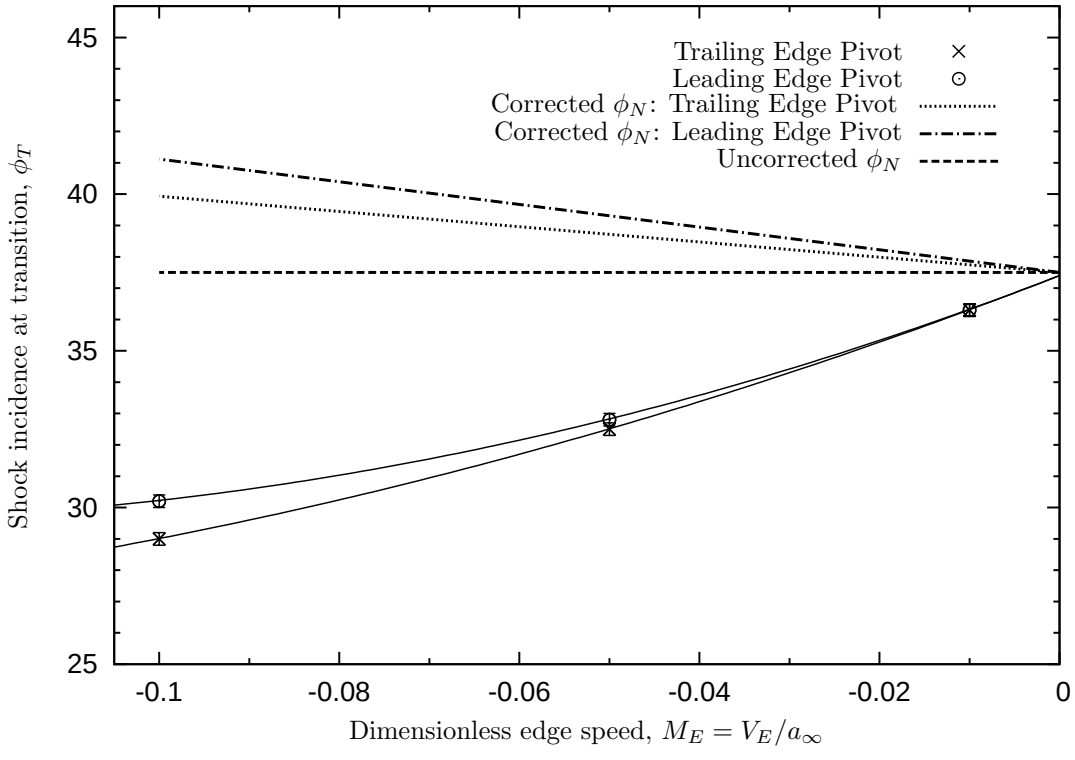
The effect of initial incidence and rotation centre were investigated very briefly. Results are summarised in table 7.6. Results in rows 2 and 3 are compared to to results in row 1. Consider the result in row 2 which shows the sensitivity of transition to changing the pivot point from the trailing edge to the model pivot point in the experiment. $\delta\theta$ increases by approximately 1.5° and $\delta\phi$ reduces by approximately 1.5°. This difference is likely to be smaller at a smaller rotation rate. Consider the result in row 3 which shows the sensitivity of transition to reducing the initial incidence. The change in $\delta\theta$ is very small and $\delta\phi$ reduces by approximately 1.8°. Due to the complex nature of the dynamic case, it is not possible to generalise the result from two numerical experiments. However, they do prove that MR $\rightarrow$ RR transition is sensitive to rotation centre and initial condition.

7.4 Thoughts on Three-dimensional Effects

The work of Ivanov et al. [24] on steady, 3D shock wave reflection was presented earlier in chapter 4. Their findings show, for a given geometry and free stream condition, that the 2D Mach stem height is always



(a) θ_{WT} vs. M_E at $M = 2.98$



(b) ϕ_T vs. M_E at $M = 2.98$

Figure 7.13: θ_{WT} and ϕ_T vs. M_E at $M = 2.98$

Table 7.6: Sensitivity of $\delta\theta_{WT}$ and $\delta\phi_T$ to pivot point and θ_{wi} for $M_E = -0.1$ at $M = 2.98$

Case Description	$\delta\theta_{WT}$	$\delta\phi_T$
$\theta_{wi} = 24.5°$, Trailing edge pivot	10.4	10.9
$\theta_{wi} = 24.5°$, Model pivot in experiment	12.0	9.4
$\theta_{wi} = 23.5°$, Trailing edge pivot	10.2	9.1

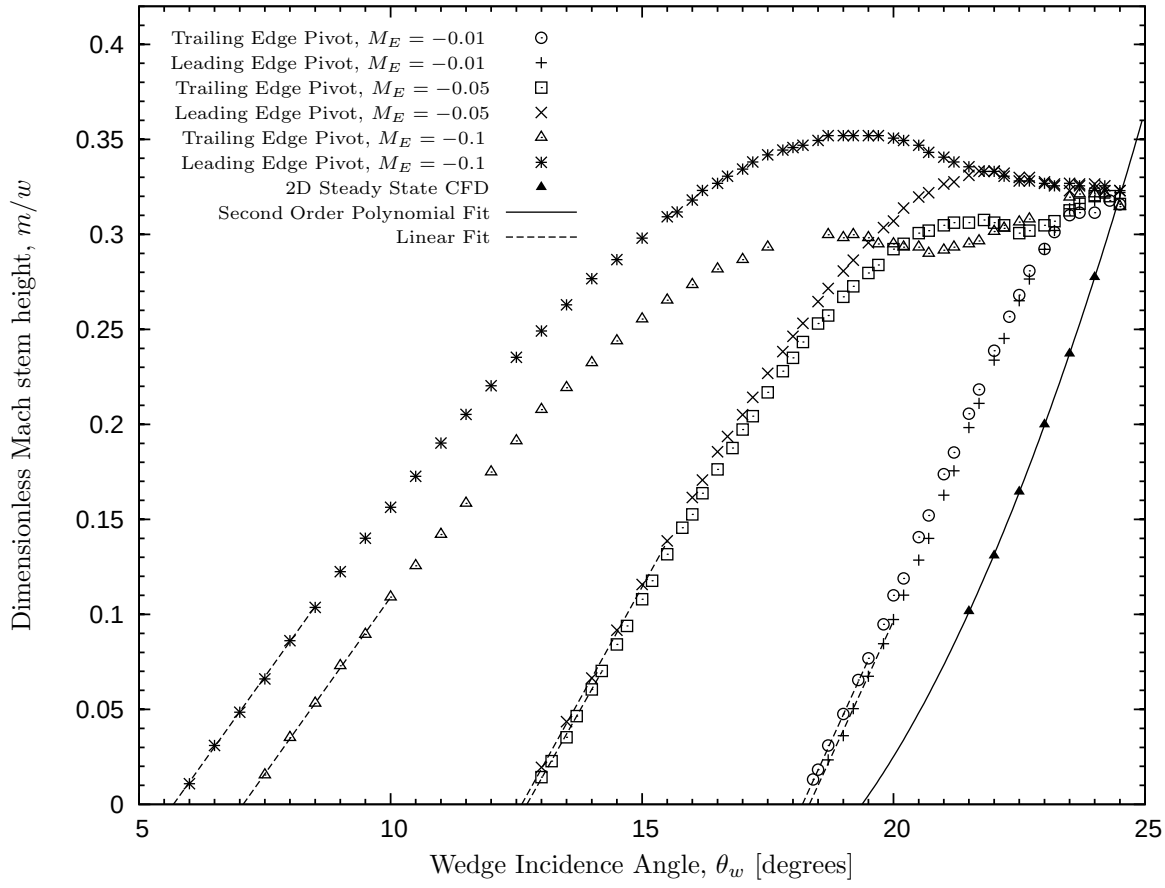


Figure 7.14: Computed variation of Mach stem height with θ_w for rapid, impulsive rotation. $M = 2.98$, $\theta_{wi} = 24.5°$, $h/w = 1.01$ (for rotation about the leading edge), $g/w = 0.6$ (for rotation about the trailing edge). Dashed lines represent linear fits used to estimate θ_{WT} for $M_E = -0.01$, -0.05 and -0.01. Solid lines are second-order polynomial fits used to compute θ_{WT} for the steady state case.

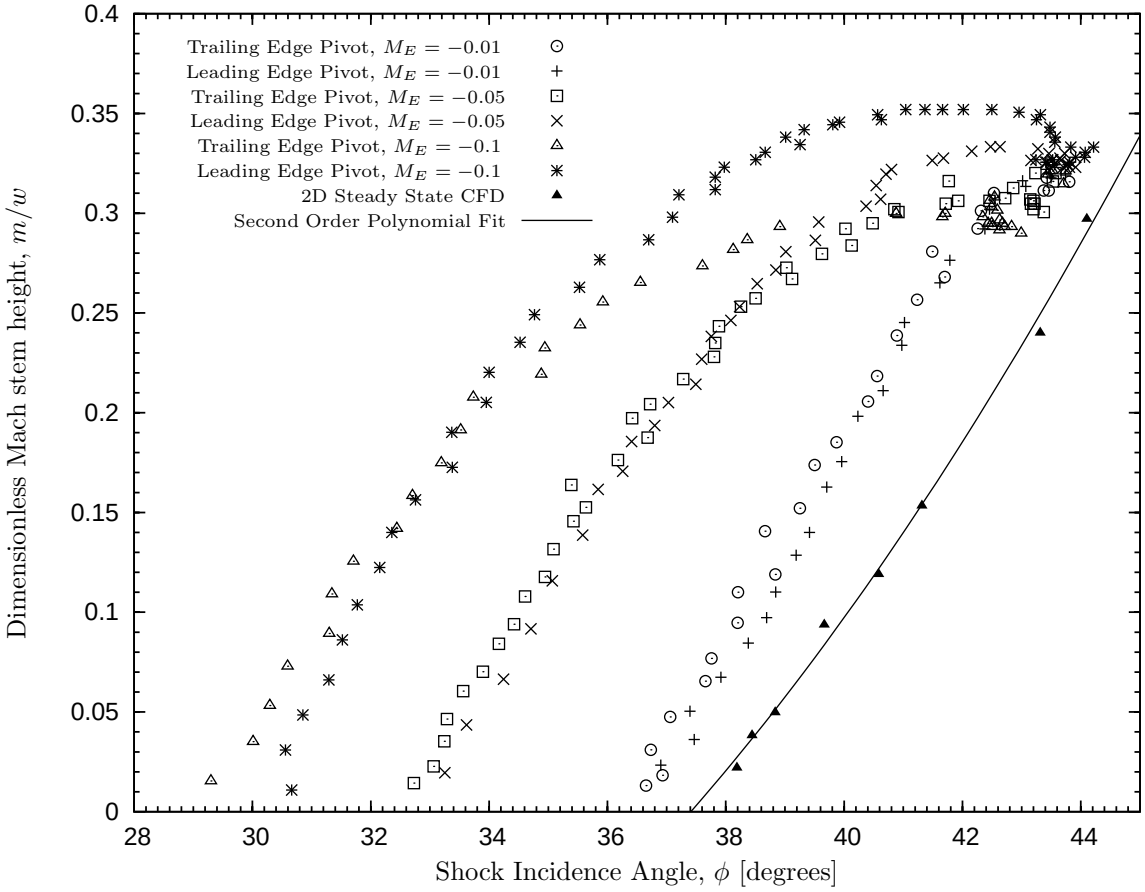


Figure 7.15: Computed variation of Mach stem height with ϕ for rapid, impulsive rotation. $M = 2.98$, $\theta_{wi} = 24.5°$, $h/w = 1.01$ (for rotation about the leading edge), $g/w = 0.6$ (for rotation about the trailing edge). The solid line is a second-order polynomial fit to compute ϕ_T for the steady state case. ϕ_T is measured at θ_{WT}.

larger than that set up with a finite aspect ratio wedge. For MR, the flow downstream of the Mach stem is subsonic and the reflection pattern in the vertical plane of symmetry is always influenced by 3D spanwise effects. In the limit, as the wedge aspect ratio approaches infinity, the 3D effects vanish and the reflection in the vertical plane of symmetry is 2D. Though there is a difference in Mach stem height between the 2D and finite aspect ratio wedges, ϕ_T is the same, provided the wedge aspect ratio is sufficiently large (see Skews [39]).

In the dynamic experiment presented earlier in this chapter, the difference in initial Mach stem height between the wind tunnel experiment and the 2D CFD result was evident. As ϕ decreased with decreasing θ_w, the experimental and 2D CFD result (see figure 7.4) converged to similar values of ϕ_T as observed in the steady case of Ivanov et al. [24].

In this experiment, transition to RR occurred approximately 2.6 ms after the wedge motion commenced. Given the free stream conditions at $M = 3.26$ and $T_O = 302.0K$, the local acoustic speed behind the Mach stem at the initial condition is approximately 341 m/s. Given the wedge semi-span of 85 mm, information of any disturbance can traverse the semi-span approximately 10 times in 2.6 ms. The time taken for any acoustic signal to traverse the semi-span is significantly smaller than the time taken to complete the wedge motion. This leads to the question of the sensitivity of ϕ_T should the time taken for information to traverse the semi-span be much larger than the time taken to rotate the wedge to the point of transition. This may be achieved by increasing the wedge span. This will have practical implications for experiments and computations, but if implemented successfully may delay transition to RR in comparison to the 2D case due to the delayed arrival of spanwise information at the triple point. It implies that increasing the wedge aspect ratio in the dynamic case may result in a deviation from the 2D result for ϕ_T. In the steady case, there is no difference in ϕ_T between the 2D and 3D case beyond some critical wedge aspect ratio. In the dynamic case, a difference in ϕ_T between the 2D and 3D case may be observed and may be found to increase for increasing wedge aspect ratios beyond a critical wedge aspect ratio. It may also be possible to delay the 3D transition with respect to the 2D transition by increasing the wedge rotation speed. While the time to complete the wedge motion will decrease, it is possible that, due to the dynamic effects highlighted in this chapter, the wedge reaches zero incidence before transition occurs.

Consider the 3D reflection pattern in figure 7.16 published by Ivanov et al. [24]. The reflection in the vertical plane of symmetry is MR. In the spanwise direction the reflection changes from MR to RR and back to MR. This highlights the possibility of the intermediate RR acting as a filter that prevents information from the wedge corner from reaching the reflection in the vertical plane of symmetry. The range of scenarios that may be possible is ideally investigated with computational fluid dynamics. However, this requires a

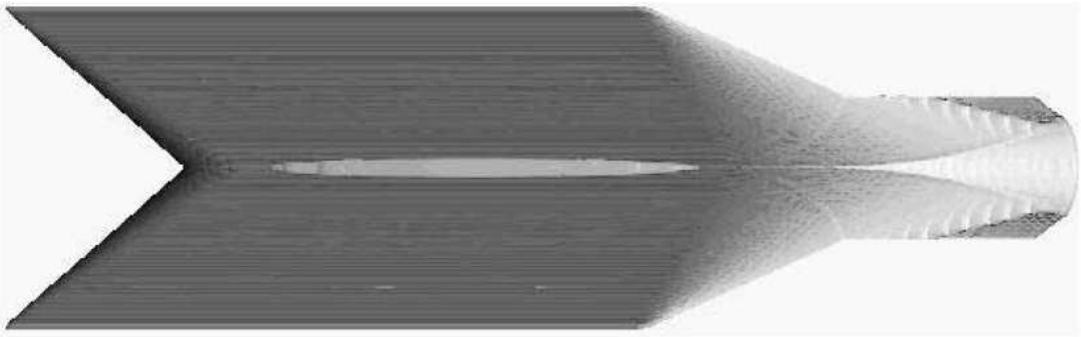


Figure 7.16: Steady, 3D reflection pattern computed with an Euler code by Ivanov et al. [24]. $M = 4.0$, $\phi = 35.5°$, $b/w = 3.75$, $g/w = 0.3$.

3D moving mesh capability with the necessary grid refinement algorithms for accurate and efficient shock capture. This is recommended for future work.

7.5 Conclusion

Experiments were completed in the CSIR supersonic wind tunnel to investigate dynamic MR → RR transition at $M = 3.26$ and 2.96. The experiments at $M = 3.26$ and 2.96 were completed successfully and provided sufficient data to validate the CFD code. The measured motion and the initial shock incidence were used to mimic the experiment with a 2D Euler CFD code. The expected difference between the initial Mach stem heights in the experiment and the CFD solution was observed. However, there was close agreement in ϕ_T between experiment and CFD. This provided sufficient confidence in the ability of the CFD code to model the dynamic case of interest and to extend its application to other scenarios beyond the current experiments.

CFD was used to further investigate the sensitivity of transition to rotation speed, initial incidence and rotation centre in the strong and weak-reflection ranges. The flow downstream of the Mach stem is subsonic and is influenced by any interaction or disturbance that appears in this subsonic region. Due to impulsive wedge start and rapid wedge rotation, there are very marked dynamic effects on the variation of Mach stem height with wedge incidence and the deviation from the steady transition conditions is significant. MR → RR transition depends on the initial condition and the transient variation of Mach stem height with wedge incidence. In chapter 5, on dynamic RR → MR transition, the maximum computed deviation from ϕ_{DC} at $M_E = +0.1$ was in the order of $\delta\phi_T = 1.6°$. For the reverse transition, the maximum computed deviations from the steady, theoretical transition values are significantly larger.

$M = 1.93$: For the range of rotation speeds investigated, $\delta\theta_{WT}$ and $\delta\phi_T$ increased with an increase in rotation speed. For the range of rotation speeds investigated, $1.2° \leq \delta\theta_{T_TE} \leq 7.1°$ and $1.0° \leq \delta\theta_{T_LE} \leq 6.2°$.

The corresponding deviation of ϕ_T from ϕ_{DC} ranges as follows: $1.5° \leq \delta\phi_{T_TE} \leq 7.4°$ and $1.7° \leq \delta\phi_{T_LE} \leq 7.9°$.

$M = 2.98$: For the range of rotation speeds investigated, $\delta\theta_{WT}$ and $\delta\phi_T$ increased with an increase in rotation speed. For the range of rotation speeds investigated, $1.2° \leq \delta\theta_{T_TE} \leq 10.4°$ and $1.1° \leq \delta\theta_{T_LE} \leq 10.0°$. The corresponding deviation of ϕ_T from ϕ_{DC} ranges as follows: $1.5° \leq \delta\phi_{T_TE} \leq 10.9°$ and $1.5° \leq \delta\phi_{T_LE} \leq 10.9°$.

The sensitivity of ϕ_T to changing the rotation point from the trailing edge to the model pivot point was investigated briefly at $M = 2.98$ with $M_E = -0.1$. θ_T increased by 1.5° and ϕ_T reduced by 1.5°, a significant variation.

The effect of initial incidence was also investigated briefly at $M = 2.98$ at $M_E = -0.1$. By reducing θ_{wi} from 24.5° to 23.5° $\delta\phi_T$ decreases by approximately 1.8°, also a marked sensitivity.

The flow field development for impulsive rotation about the wedge trailing and leading edges at $M = 1.93$ for $M_E = -0.075$ was analysed in some detail. The flow field development is very sensitive to the rotation centre, more especially at large rotation rates. Four phases of the Mach stem development were identified in both cases.

Rotation about the wedge leading edge at $M = 1.93$ *for* $M_E = -0.075$: The Mach stem height remains constant until the expansion wave arrives at the triple point. This is followed by an increase in Mach stem height. After the maximum Mach stem height is reached there is little change in Mach stem height for a small period after which time the Mach stem height decreases until transition to RR.

Rotation about the wedge trailing edge at $M = 1.93$ *for* $M_E = -0.075$: The impulsive start of the wedge generates a disturbance on the incident wave. The disturbance propagates down the incident wave and propagates through the triple point and down the Mach stem towards the reflection plane. The Mach stem height is constant until the arrival of the disturbance on the incident wave. The disturbance causes a sudden, but momentary decrease in Mach stem height. Subsequently, there is little change in the Mach stem height for a period of time, before the Mach stem height decreases until transition to RR. In contrast, at $M = 2.98$, the Mach stem height increases slightly in phase III.

It was demonstrated that MR can be maintained until zero wedge incidence with a sufficiently large rotation rate ($M_E = -0.1$ at $M = 1.93$). At small rotation speeds ($M_E = -0.01$), Mach stem development and ϕ_T exhibit little sensitivity to rotation centre.

There was good agreement in ϕ_T between the 3D experiment and the 2D CFD result. It is possible, for a given rotation speed, that the results deviate beyond some critical value of wedge aspect ratio due to the delay in arrival of spanwise information to the reflection pattern in the wedge vertical plane of symmetry. If true, it would mark a fundamental difference between the steady and dynamic cases. In the steady case, the 3D and 2D values for ϕ_T converge above a critical wedge aspect ratio. In the dynamic case, the 3D and 2D

values for ϕ_T may diverge above a critical wedge aspect ratio. Intermediate RR in the spanwise direction may also influence the propagation of spanwise information to the wedge vertical plane of symmetry and this may also influence ϕ_T.

7.6 Recommendations for Future Work

The following items were raised during the course of this work. Though they lie beyond the scope of this work, they are highlighted for consideration in future work.

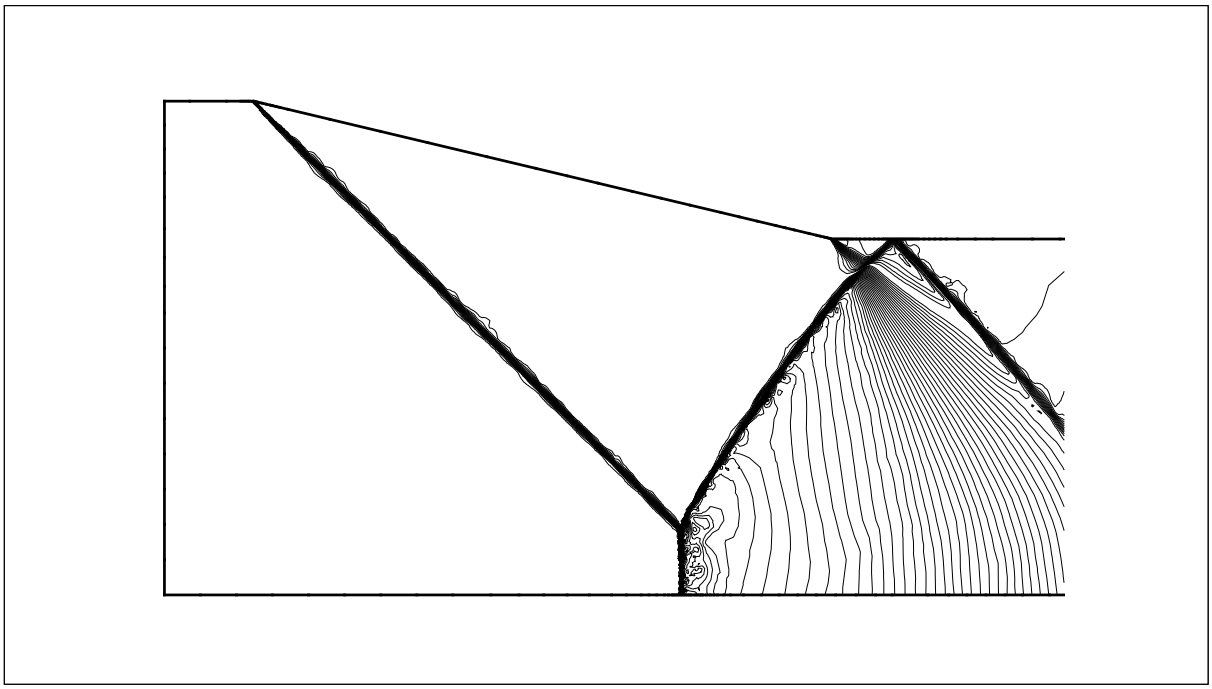
1. A detailed investigation to identify and quantify the mechanism(s) in phases III and IV of the Mach stem development at $M = 1.93$ and $M = 2.98$.

2. Development of an appropriate 3D flow solver for the investigation of dynamic, three-dimensional effects on MR $\rightarrow$ RR transition. The issues of mesh movement, solver accuracy, flow field resolution and solver speed are pertinent for consideration here.

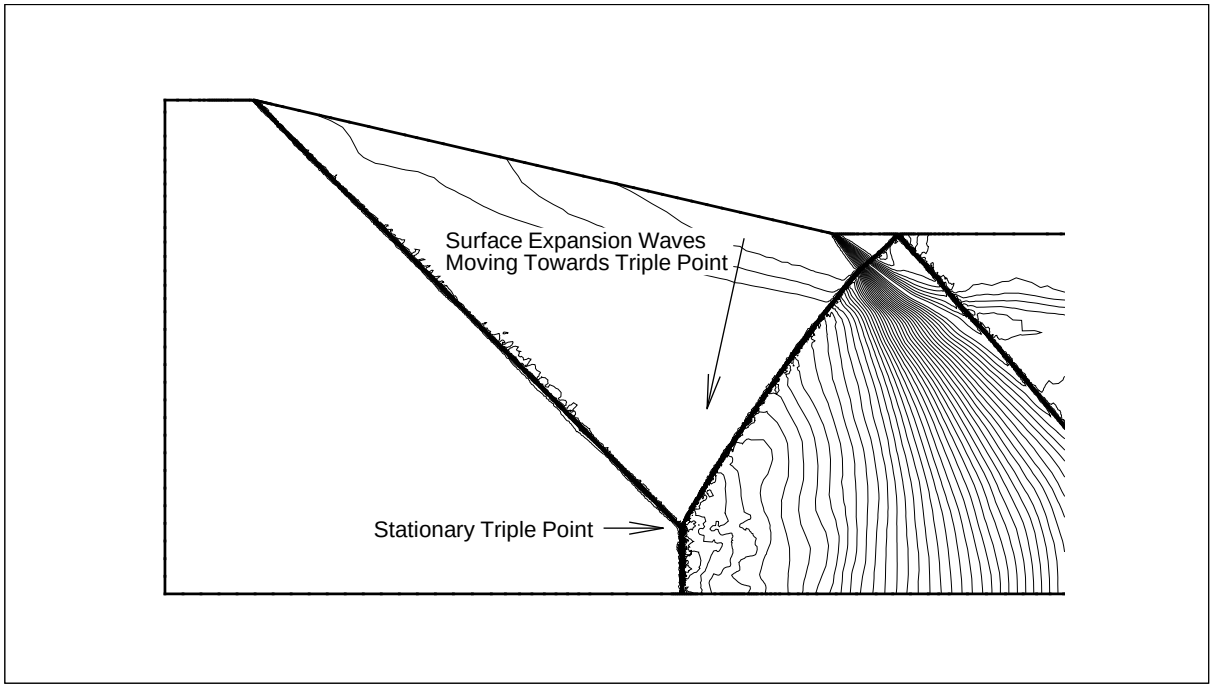
3. Investigation of the effect of increasing wedge aspect ratio on ϕ_T with respect to the 2D result.

4. Investigation of the effect of increasing the rotation speed of a finite aspect ratio wedge on ϕ_T with respect to the 2D result.

5. Investigation of the effect of intermediate spanwise RR patterns to the propagation of spanwise information and its effect on ϕ_T.

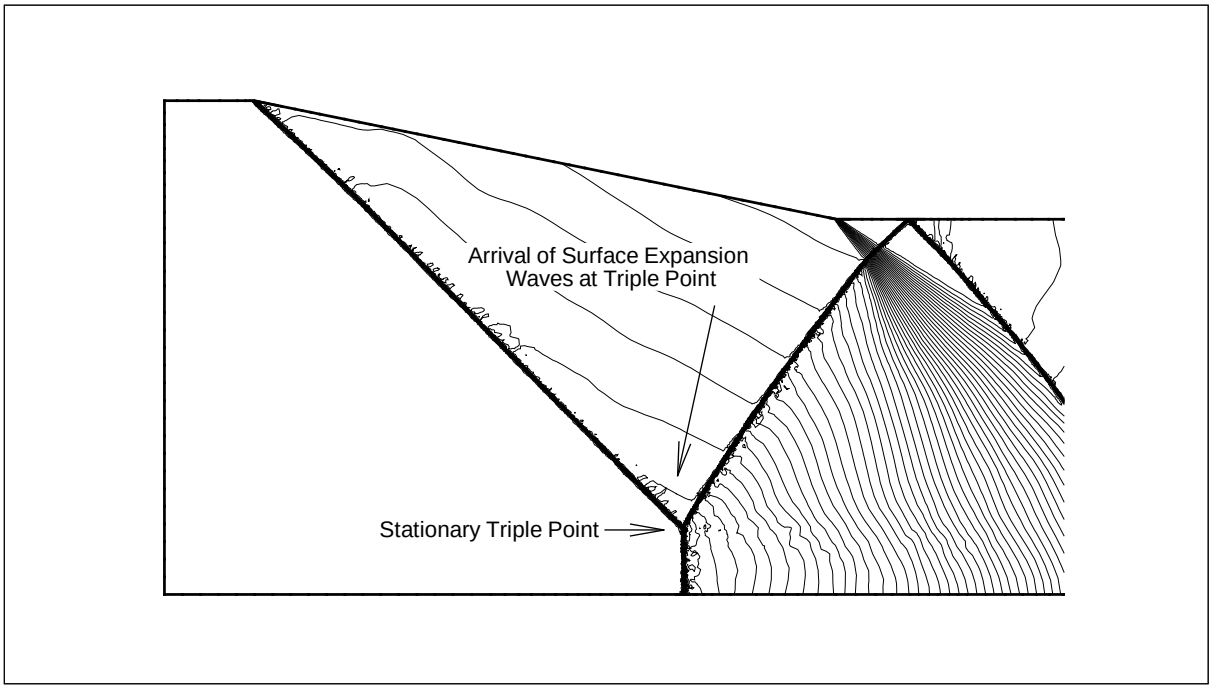


(a) The initial, steady MR at $\theta_{wi} = 13.4°$, $t = 0.0$ s

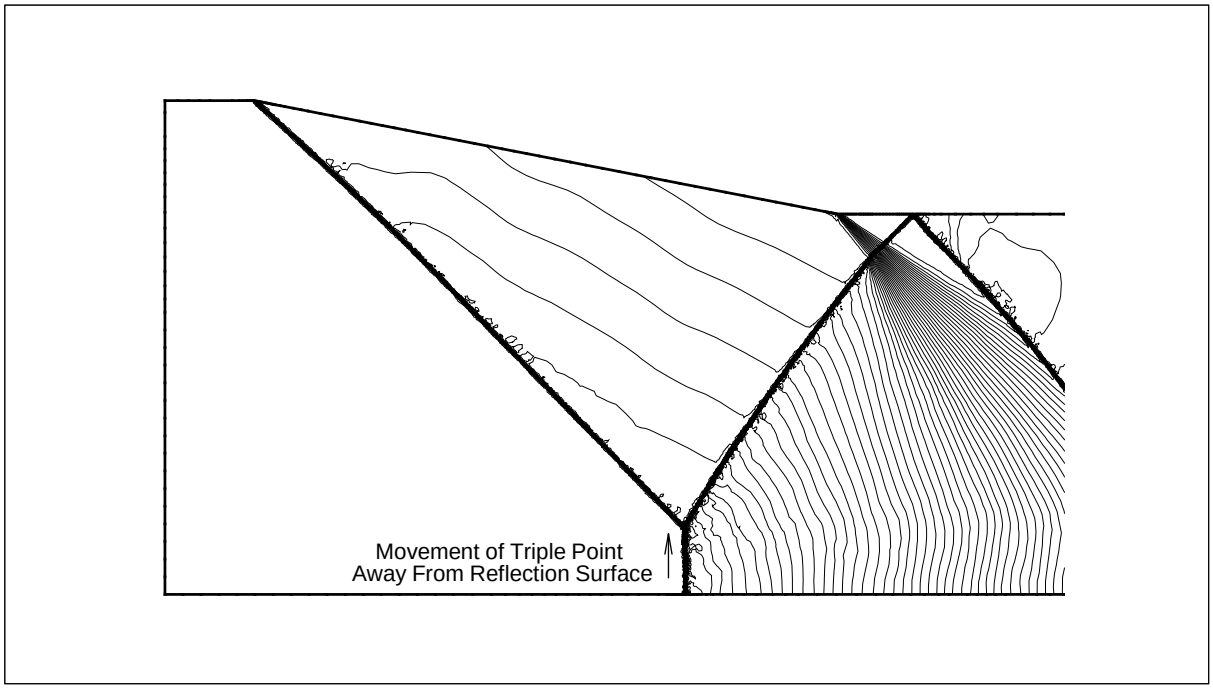


(b) The flow field at $\theta_w = 13.0°$, $t = 14.1\mu s$. The expansion waves from the wedge surface move toward the triple point. At this time the flow in the vicinity of the triple point is "unaware" of the movement of the wedge and the triple point is stationary.

Figure 7.17: Computed pressure contours at (a) $\theta_{wi} = 13.4°$ and (b) $\theta_w = 13.0°$ for impulsive rotation about the wedge leading edge at $M_E = -0.075$. $M = 1.93$, $\theta_{wi} = 13.4°$, $h/w = 0.84$.

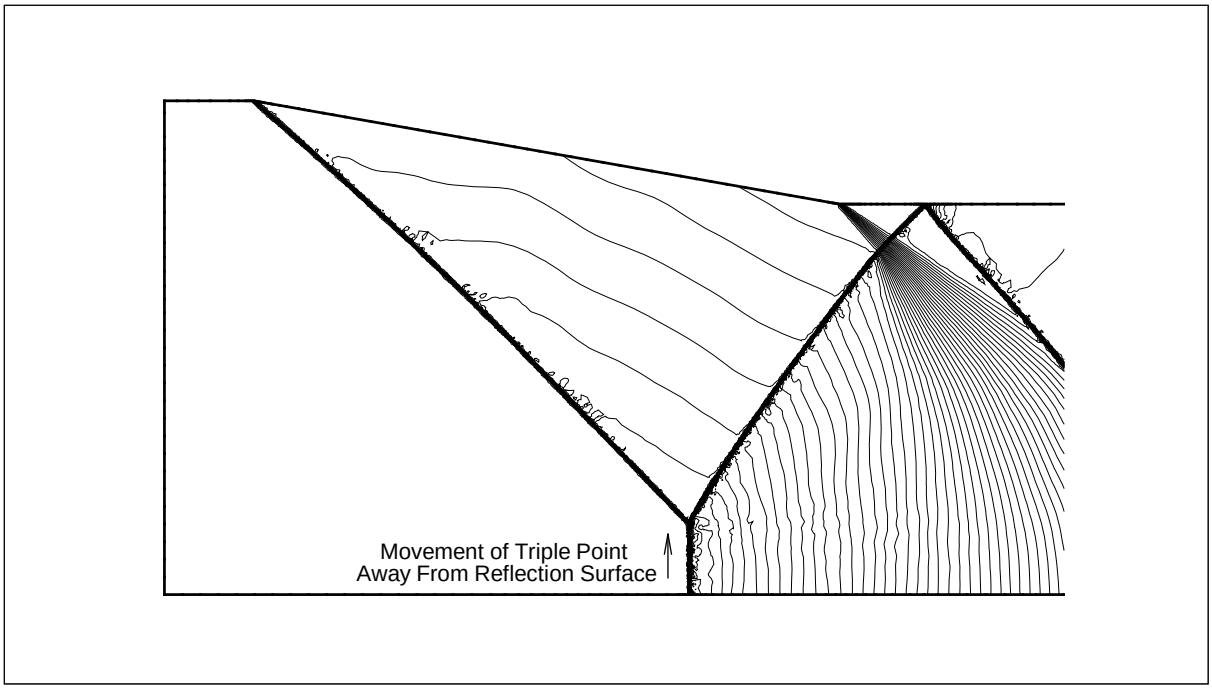


(a) The expansion waves from the wedge surface arrive at the triple point at $\theta_w \approx 11.5°$ at $t = 67\mu s$. Up to this time there has been no movement of the triple point.

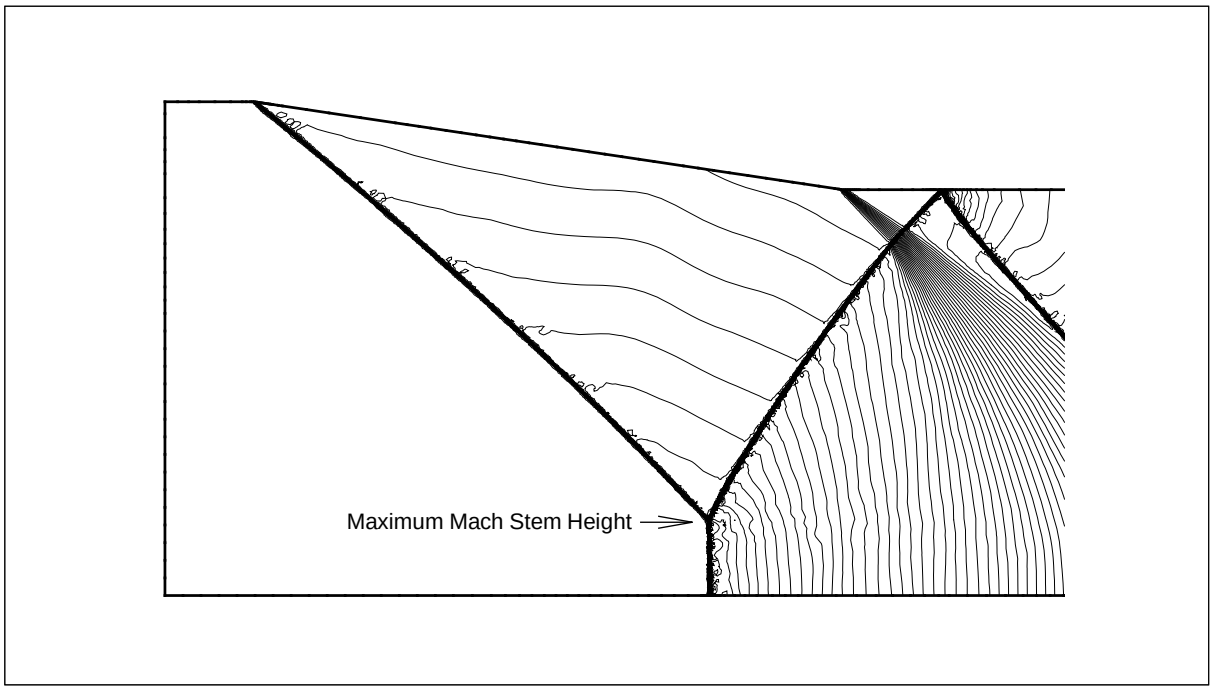


(b) $\theta_w = 11.0°$, $t = 84.6\mu s$. The first movement of the triple point is observed after the surface expansion waves reach the triple point. The expansion waves "suck" the triple point away from the reflection surface. This increase in Mach stem was also reported on briefly by Felthun and Skews [12] for rotation about the wedge leading edge in a $M = 3.0$ free stream.

Figure 7.18: Computed pressure contours at (a) $\theta_w = 11.5°$ and (b) $\theta_w = 11.0°$ for impulsive rotation about the wedge leading edge at $M_E = -0.075$. $M = 1.93$, $\theta_{wi} = 13.4°$, $h/w = 0.84$.

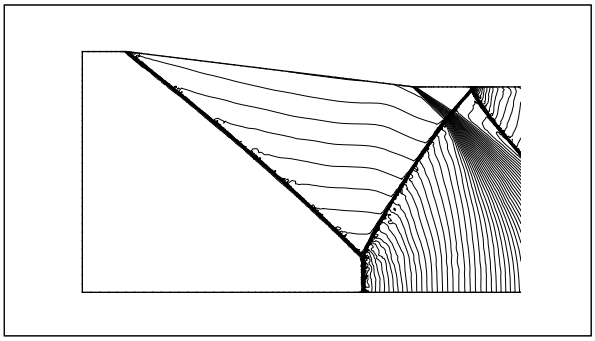


(a) The Mach stem height continues to increase at $\theta_w = 10.0°$, $t = 119.9\mu s$

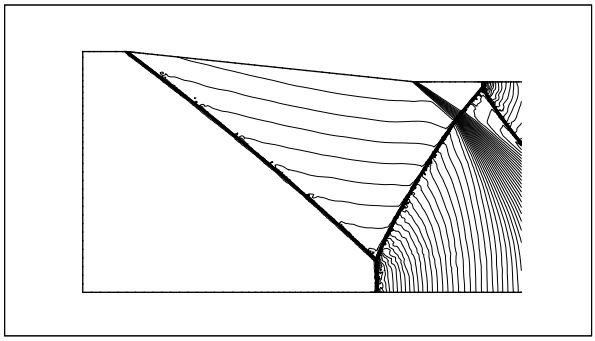


(b) The Mach stem height reaches a maximum value at $\theta_w = 8.5°$, $t = 172.8\mu s$.

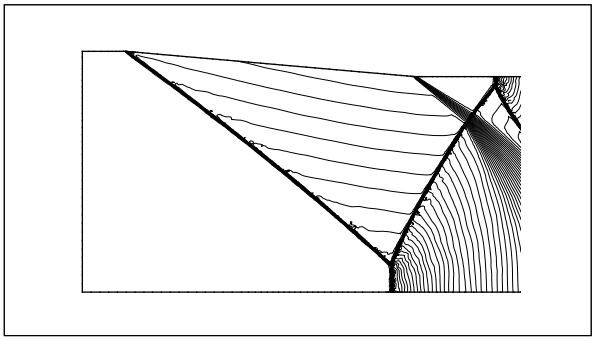
Figure 7.19: Computed pressure contours at (a) $\theta_w = 10.0°$ and (b) $\theta_w = 8.5°$ for impulsive rotation about the wedge leading edge at $M_E = -0.075$. $M = 1.93$, $\theta_{wi} = 13.4°$, $h/w = 0.84$.



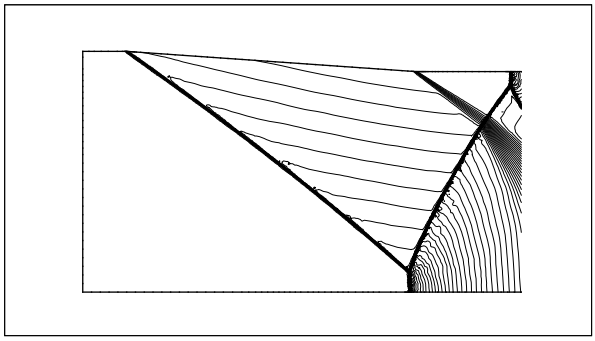
(a) $\theta_w = 7.0°$, $t = 225.6\mu s$



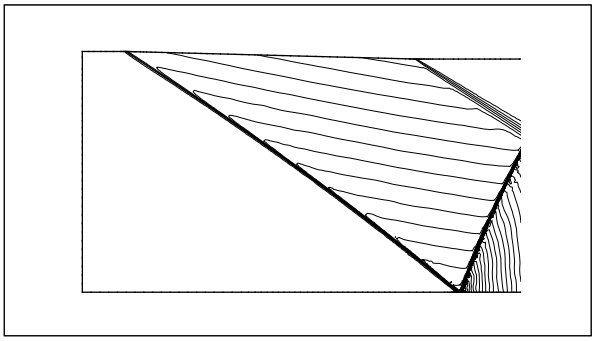
(b) $\theta_w = 6.0°$, $t = 260.9\mu s$.



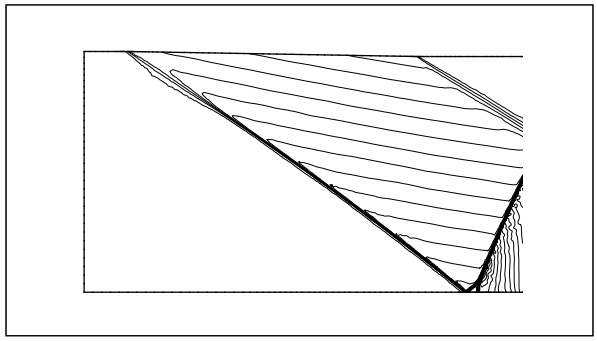
(c) $\theta_w = 5.0°$, $t = 296.2\mu s$.



(d) $\theta_w = 4.0°$, $t = 331.4\mu s$.

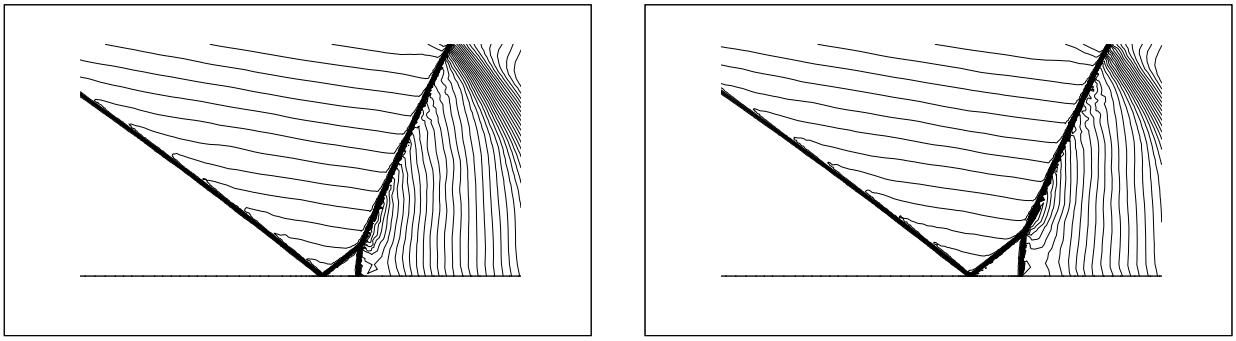


(e) $\theta_w = 1.5°$, $t = 419.6\mu s$.



(f) $\theta_w = 1.0°$, $t = 437.2\mu s$.

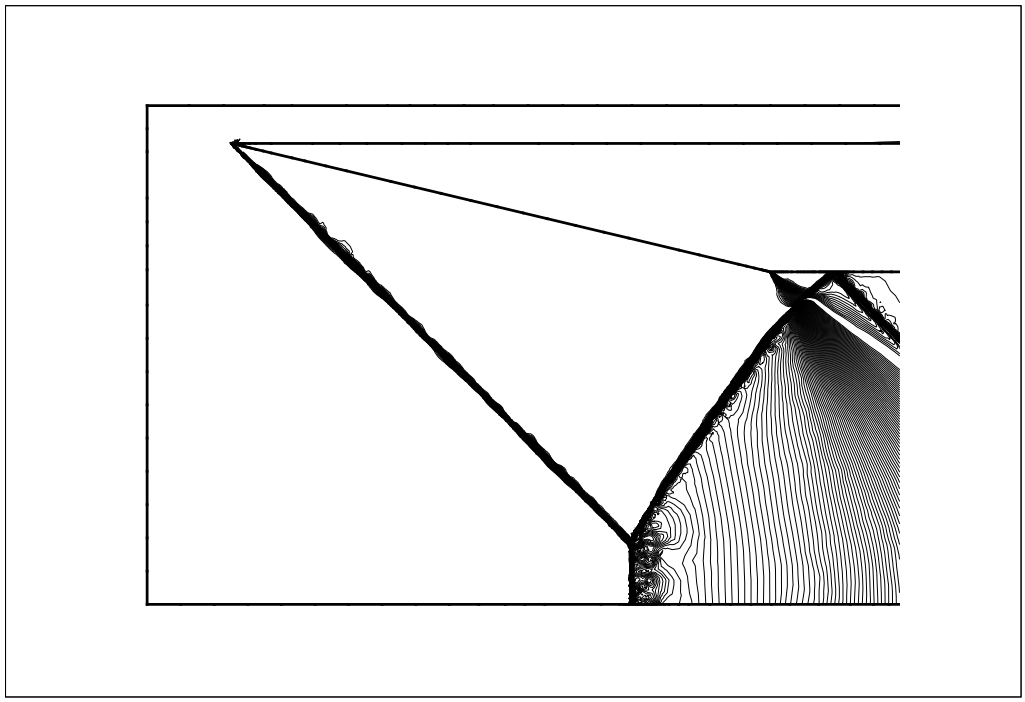
Figure 7.20: Computed pressure contours showing decreasing Mach stem height between $\theta_w = 7.0°$ and $\theta_w = 1.0°$ for impulsive rotation about the wedge leading edge at $M_E = -0.075$. $M = 1.93$, $\theta_{wi} = 13.4°$, $h/w = 0.84$.



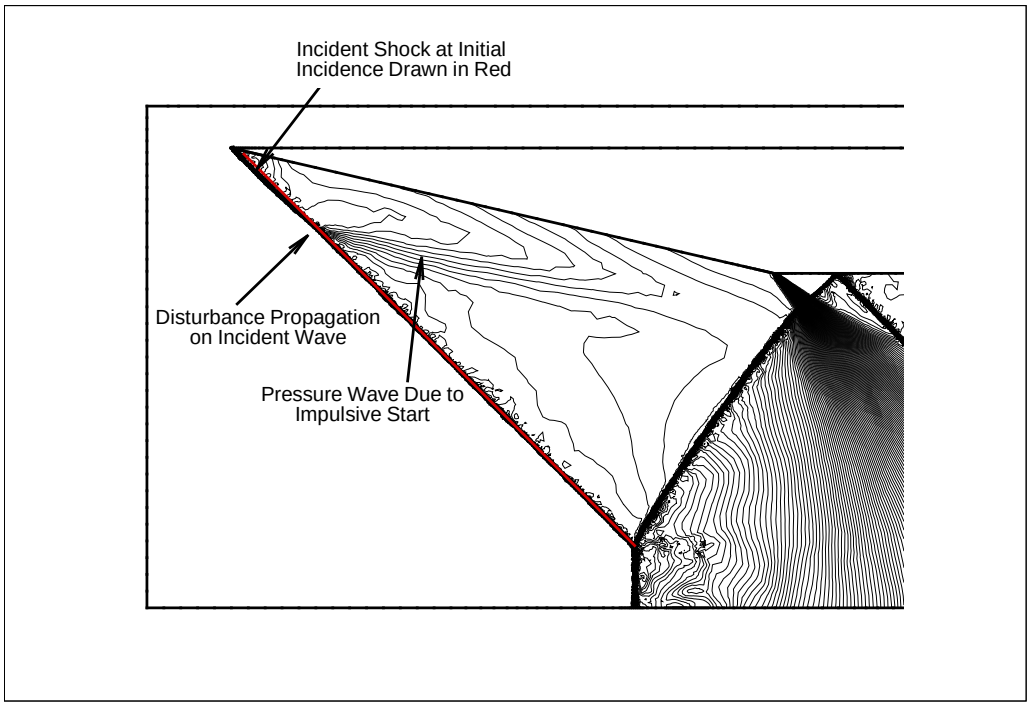
(a) $\theta_w = 0.5°$, $t = 454.8\mu s$

(b) $\theta_w = 0.1°$, $t = 468.9\mu s$.

Figure 7.21: Development of flow field in the vicinity of the reflection point after transition to RR between (a) $\theta_w = 0.5°$ and (b) $\theta_w = 0.1°$ for impulsive rotation about the wedge leading edge at $M_E = -0.075$. $M = 1.93$, $\theta_{wi} = 13.4°$, $h/w = 0.84$.

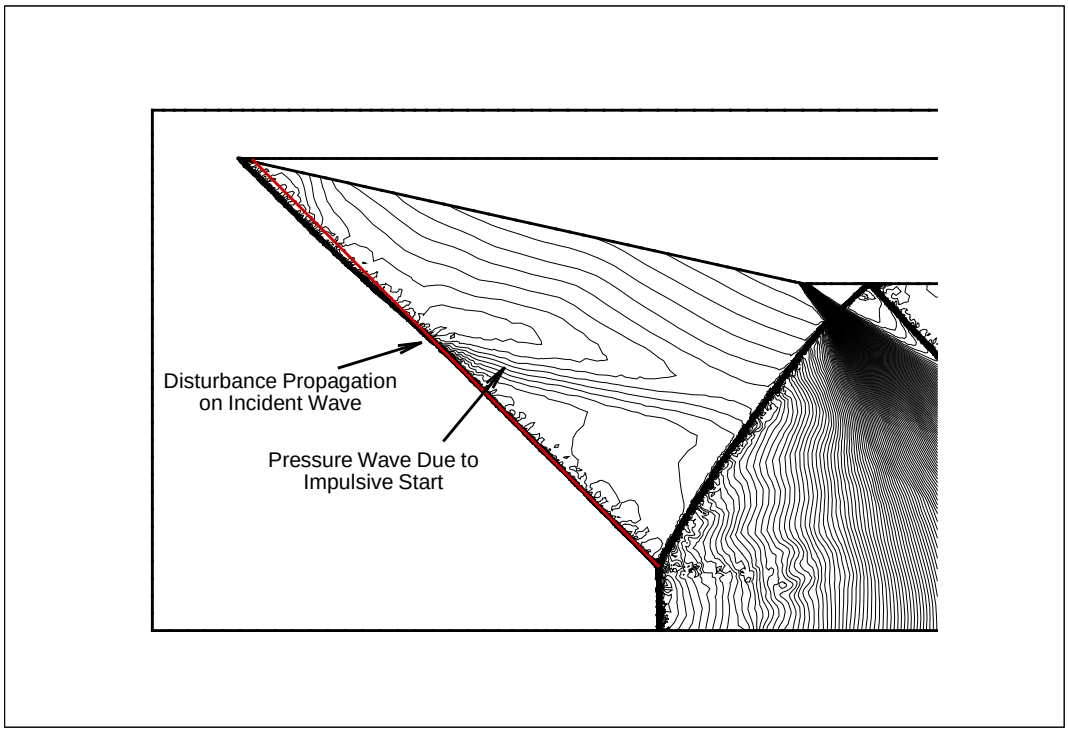


(a) The initial, steady MR at $\theta_{wi} = 13.4°$, $t = 0.0$ s

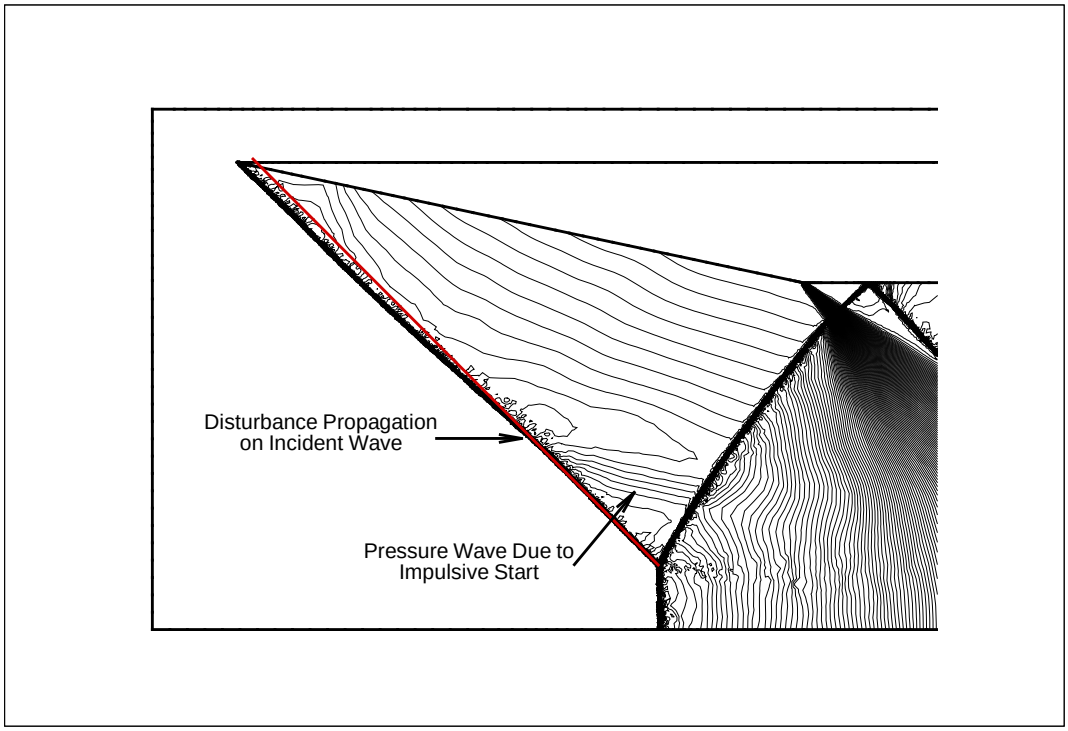


(b) $\theta_w = 13.0°$, $t = 14.1\mu s$. The impulsive movement of the wedge tip generates a disturbance that propagates down the length of the incident wave. The resultant pressure wave between the incident wave and the wedge surface is indicated. At the same time compression waves are generated at the wedge surface. The solid red line indicates the position of the incident wave at the initial condition.

Figure 7.22: Computed pressure contours at (a) $\theta_{wi} = 13.4°$ and (b) $\theta_w = 13.0°$ for impulsive rotation about the wedge trailing edge at $M_E = -0.075$. $M = 1.93$, $\theta_{wi} = 13.4°$, $g/w = 0.6$.

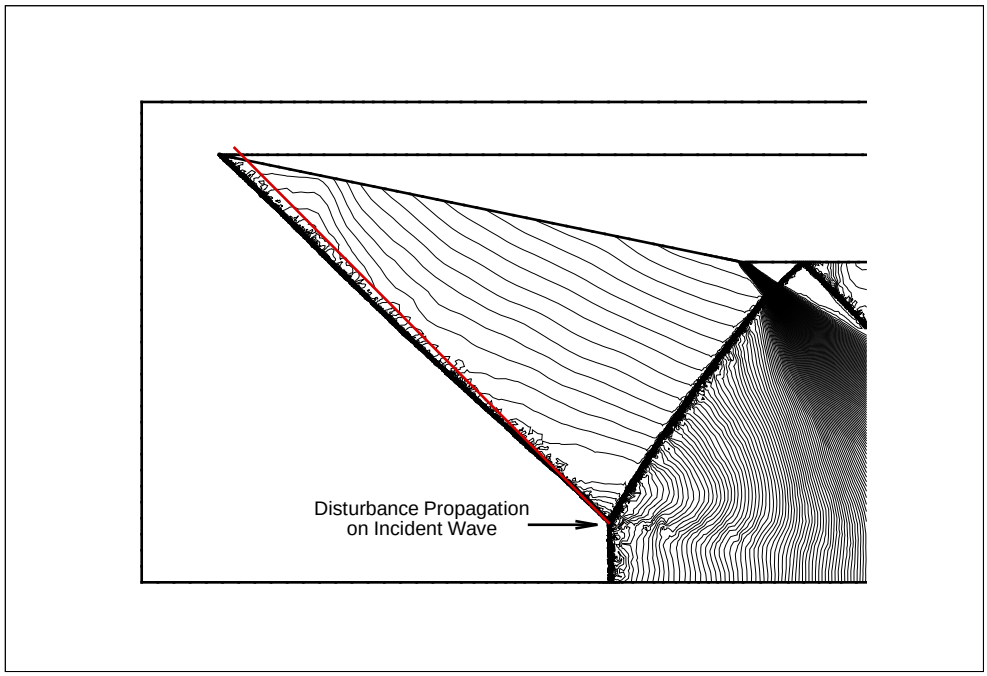


(a) $\theta_w = 12.5°$, $t = 31.7\mu s$.

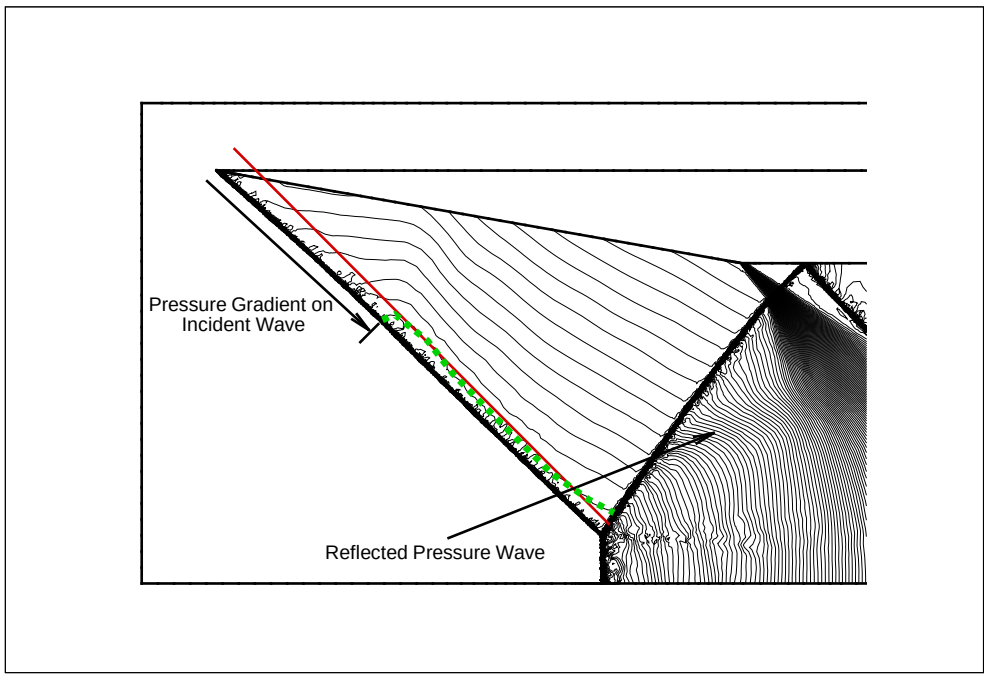


(b) $\theta_w = 12.0°$, $t = 49.4\mu s$

Figure 7.23: Computed pressure contours at (a) $\theta_w = 12.5°$ and (b) $\theta_w = 12.0°$ for impulsive rotation about the wedge trailing edge at $M_E = -0.075$. $M = 1.93$, $\theta_{wi} = 13.4°$, $g/w = 0.6$. The disturbance propagates down the length of the incident wave and the compression waves from the wedge surface continue propagating away from the surface. The solid red line indicates the position of the incident wave at the initial condition.

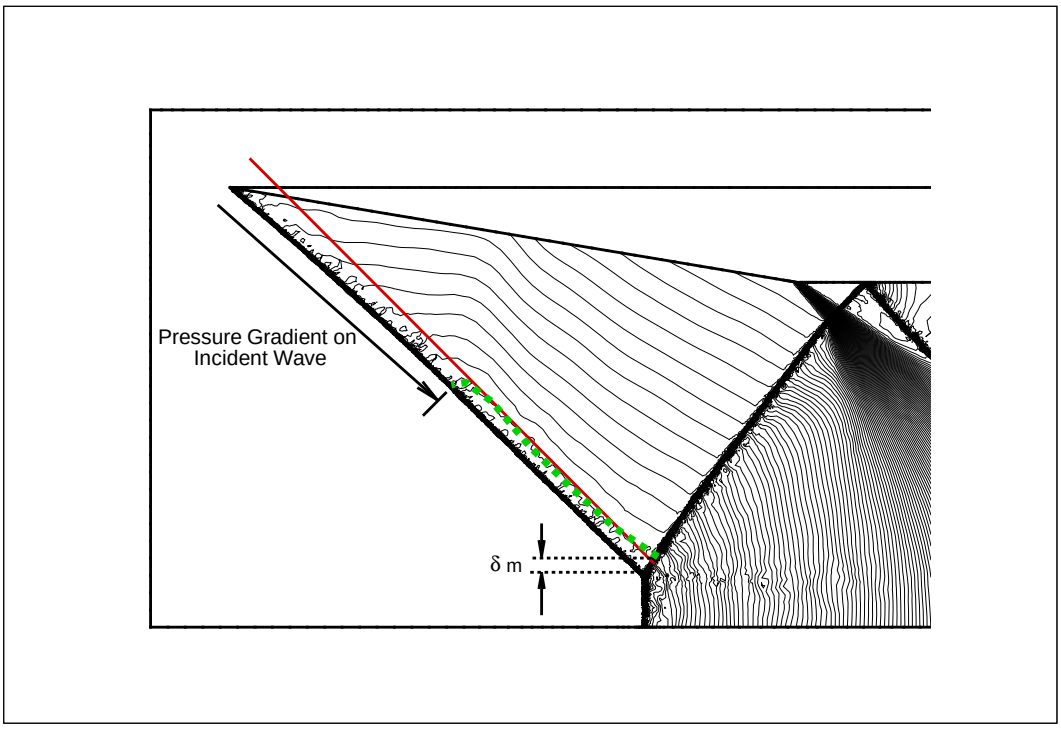


(a) The disturbance on the incident wave reaches the triple point at $\theta_w = 11.6°$, $t = 63.5\mu s$.

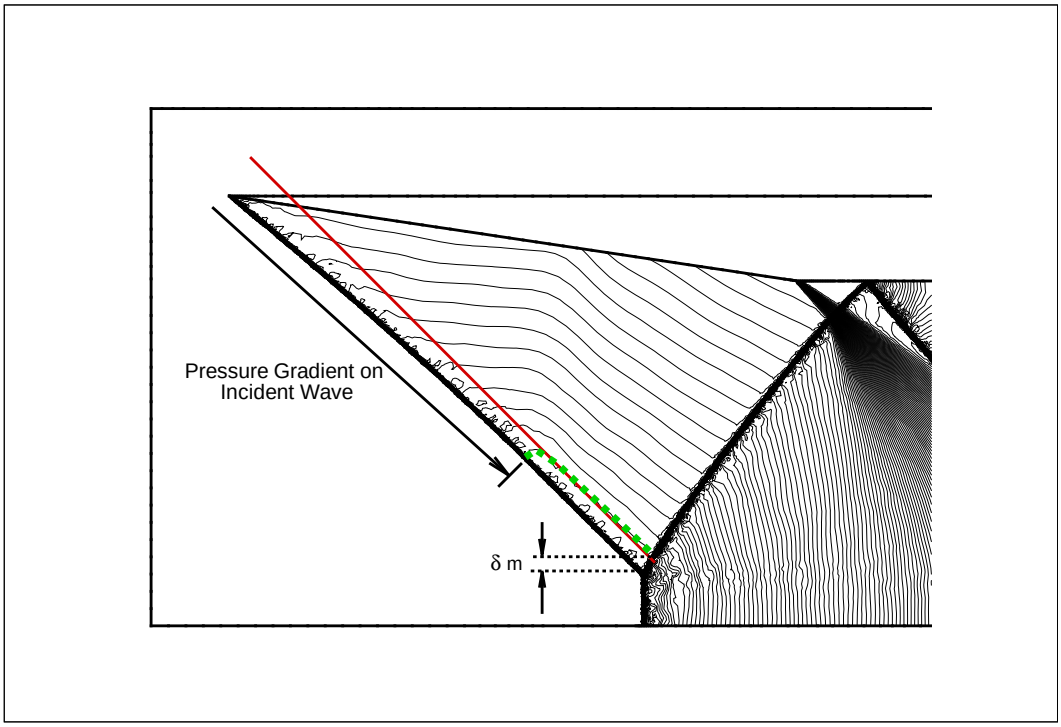


(b) Computed flow field at $\theta_w = 10.0°$, $t = 119.9\mu s$. As the disturbance passes through the triple point there is a rapid and momentary decrease in Mach stem height. The pressure wave generated on the incident wave by the impulsive start reflects from the reflection plane. The intersection of the isobar highlighted in green with the incident wave indicates the location of the discontinuity in curvature on the incident wave. The segment upstream of the discontinuity is curved and a pressure gradient is evident over this segment of the incident wave. The segment downstream of the discontinuity is planar and there is no pressure gradient over this segment.

Figure 7.24: Computed pressure contours at (a) $\theta_w = 11.6°$ and (b) $\theta_w = 10.0°$ for impulsive rotation about the wedge trailing edge at $M_E = -0.075$. $M = 1.93$, $\theta_{wi} = 13.4°$, $g/w = 0.6$. The solid red line indicates the position of the incident wave at the initial condition.

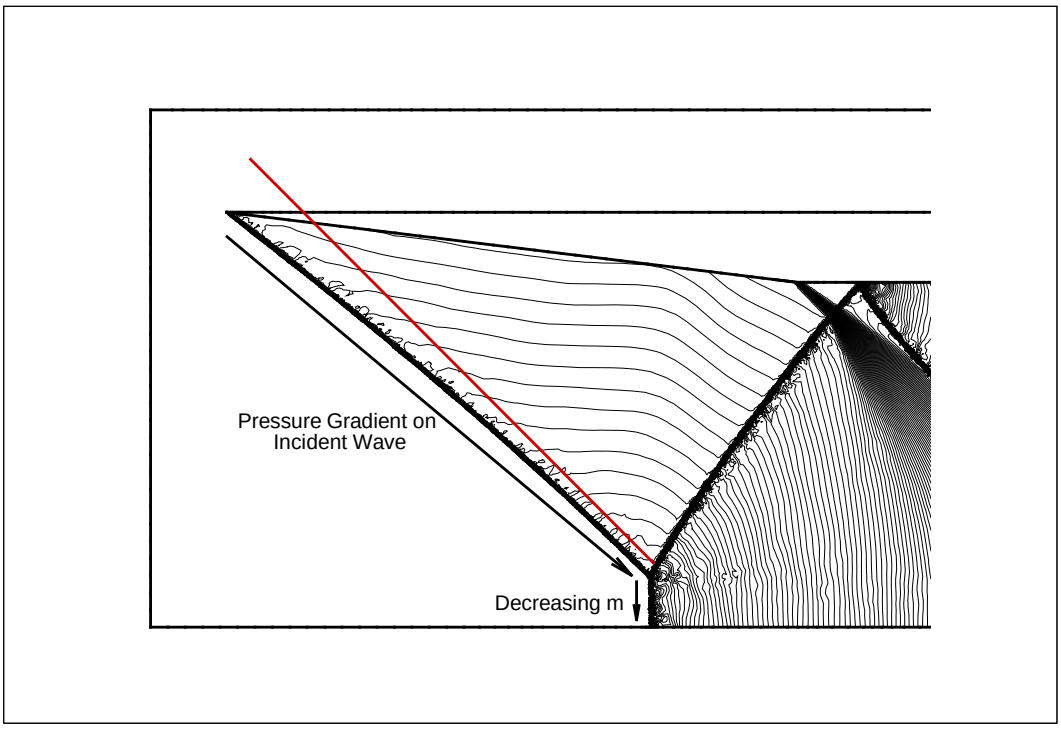


(a) $\theta_w = 9.5°$, $t = 137.5\mu s$

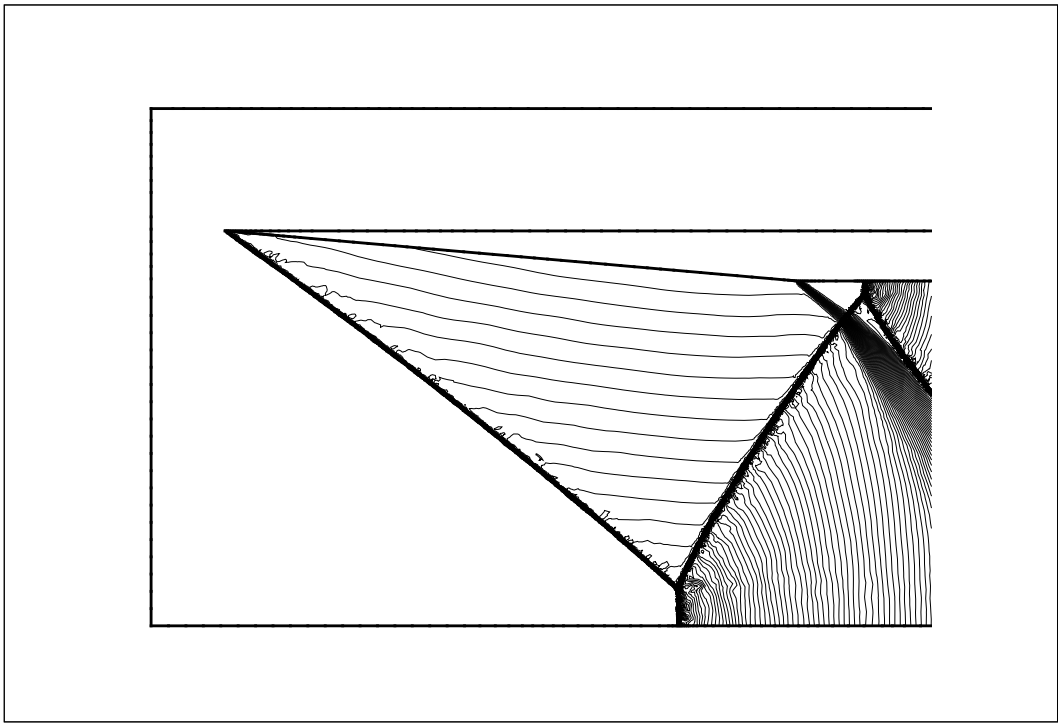


(b) $\theta_w = 8.5°$, $t = 172.8\mu s$

Figure 7.25: Computed pressure contours at (a) $\theta_w = 9.5°$ and (b) $\theta_w = 8.5°$ for impulsive rotation about the wedge trailing edge at $M_E = -0.075$. $M = 1.93$, $\theta_{wi} = 13.4°$, $g/w = 0.6$. Between $\theta_w = 9.5°$ and $7.5°$ the Mach stem height is constant at approximately δm below the initial Mach stem height. The discontinuity on the incident wave continues to move towards the triple point. The solid red line indicates the position of the incident wave at the initial condition.

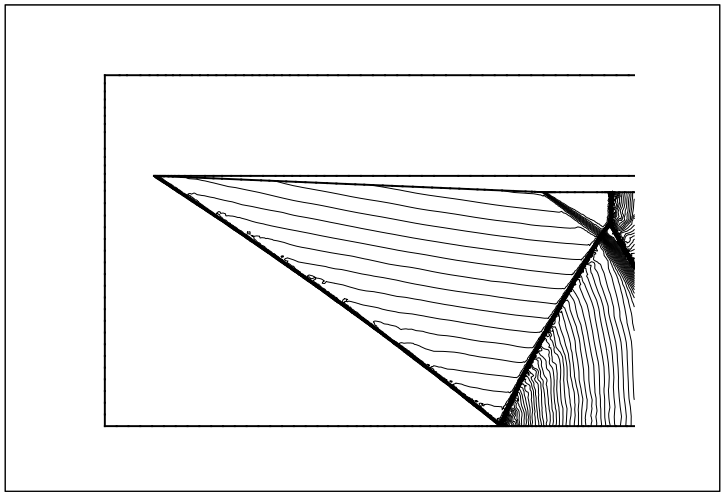


(a) $\theta_w = 7.0°$, $t = 225.6\mu s$

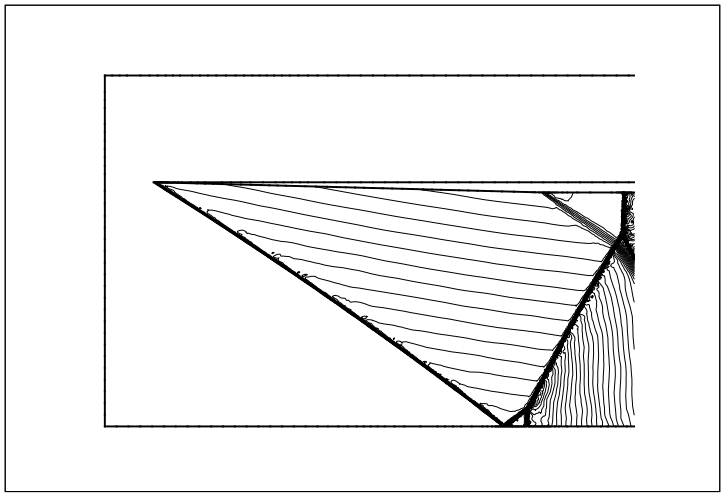


(b) $\theta_w = 5.0°$, $t = 296.2\mu s$

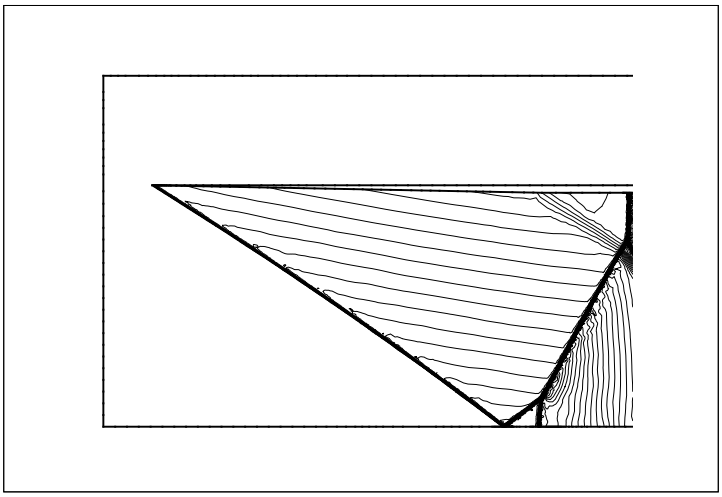
Figure 7.26: Computed pressure contours at (a) $\theta_w = 7.0°$ and (b) $\theta_w = 5.0°$ for impulsive rotation about the wedge trailing edge at $M_E = -0.075$. $M = 1.93$, $\theta_{wi} = 13.4°$, $g/w = 0.6$. The discontinuity on the incident wave has reached the triple point and the incident wave is curved along its entire length. The Mach stem height decreases until transition to RR. The solid red line indicates the position of the incident wave at the initial condition.



(a) $\theta_w = 2.4°$, $t = 387.8\mu s$



(b) $\theta_w = 1.5°$, $t = 419.6\mu s$



(c) $\theta_w = 1.1°$, $t = 433.7\mu s$

Figure 7.27: Computed pressure contours at (a) $\theta_{WT} = 2.4°$, (b) $\theta_w = 1.5°$ and (c) $\theta_w = 1.1°$ for impulsive rotation about the wedge trailing edge at $M_E = -0.075$. $M = 1.93$, $\theta_{wi} = 13.4°$, $g/w = 0.6$.

Chapter 8

Conclusions and Recommendations for Future Work

8.1 Conclusions

There have been numerous studies on the steady state transition criteria between regular reflection (RR) and Mach reflection (MR) of shock waves for a stationary, two-dimensional (2D) wedge in a steady supersonic flow, since the original shock wave reflection research by Ernst Mach in 1878. The steady, 2D transition criteria between RR and MR are well established. There has been little done to consider the dynamic effect of rapid wedge rotation on RR $\leftrightarrow$ MR transition.

This thesis presents the results of an investigation of the effect of rapid wedge rotation on transition between 2D regular and Mach reflection in the weak and strong-reflection ranges, with experiment and computational fluid dynamics. A novel facility was designed to rotate a pair of large aspect ratio wedges in a 450 mm $\times$ 450 mm supersonic wind tunnel at wedge rotation speeds up to 11000 deg/s resulting in wedge tip speeds approximately 3.3 % of the free stream acoustic speed. Steady state, baseline experiments in which the wedges were rotated very gradually were also completed. A schlieren system and optical measurement system was developed. High-speed images and measurements were presented for the steady and dynamic experiments. Numerical solution of the inviscid governing flow equations was used to model the steady case and to mimic the experimental motion in the dynamic experiments. Most steady state simulations were completed with Fluent V 12.0 and all dynamic simulations were done with an in-house, 2D Euler Code.

Steady state, baseline experiments were completed in the weak and strong-reflection ranges and transition measurements were compared to 2D steady state, theoretical values and Euler computations. There was close agreement between theoretical, computational and experimental transition for the steady case, with the following exception. Due to the levels of free stream noise in the supersonic wind tunnel, incidence-induced

hysteresis was not observed in the strong-reflection region and transition occurred at the von Neumann condition for increasing and decreasing incidence. In the ideal case, RR → MR transition occurs at the detachment condition and the reverse transition occurs at the von Neumann condition. Therefore, there is discrepancy between steady theory/CFD and experiment for RR → MR transition in the strong-reflection range only, which is consistent with observations in other facilities with sufficient levels of free stream noise.

8.1.1 Summary of Results for Dynamic RR to MR Transition

Rapid wedge rotation generated a measurable dynamic effect on RR → MR transition. The first experimental evidence of 2D RR → MR reflection transition beyond the steady detachment condition in the weak and strong-reflection ranges was presented (see figure 8.1). In the dynamic experiments and computations of the experiments at $M = 1.93$ and 2.98, RR persisted approximately $0.9° - 1.3°$ beyond the corrected detachment condition. In all instances, there was good agreement between experiment and CFD, including dynamic RR → MR transition in the strong-reflection region. The agreement between the dynamic experiment, in which small perturbations are always present in the free stream, and the dynamic CFD, in which the free stream is without perturbations, implies that RR → MR transition in the strong-reflection region becomes insensitive to free stream noise above a certain critical rotation speed.

Due to the close agreement between CFD and experiment, Euler CFD was also applied to scenarios beyond the limits of the current facility to explore the influence of variables in the parameter space. Over the range of free stream conditions and rotation speeds investigated, the deviation from the corrected, steady, theoretical shock incidence at transition, $\delta\phi_T$, ranged between 0.4° at $M_E = +0.01$ and 1.6° at $M_E = +0.1$. For a given rotation centre and free stream condition, there was little dependence of transition on initial incidence, for the values of initial incidence tested.

CFD was also used to investigate the dynamic transition mechanism over a limited number of simulations. For dynamic RR → MR transition, a distinction is drawn between the sonic, length scale and detachment conditions. The point at which the flow downstream of the reflection point goes sonic is not necessarily the point at which the wedge length scale, from the wedge trailing edge expansion, is communicated to the reflection point. There is evidence to support that the RR → MR transition criteria for the rapidly rotating wedge is neither the sonic or length scale conditions, but rather the condition at which the reflected wave can no longer satisfy the boundary condition at the reflection point. Dynamic simulations showed that RR could be maintained for some time with a length scale present at the reflection point. It is possible that RR is maintained as long as the reflected wave is able to turn the incoming flow parallel to the reflection plane. Other simulations showed that transition to MR was possible without the wedge length scale being

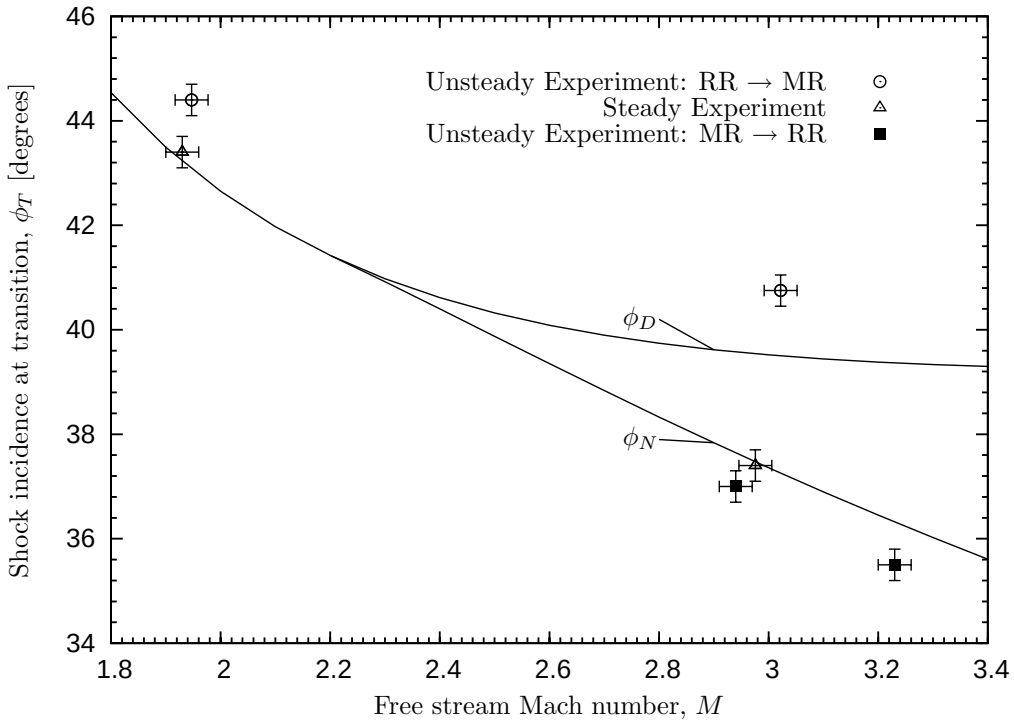


Figure 8.1: Measured ϕ_T from experiments compared to analytical steady transition criteria

communicated to the reflection point, perhaps due to the failure of RR to maintain the boundary condition at the reflection point.

Pressure traces through the reflection point show that rapid rotation increases the maximum achievable pressure rise through the reflection point of a RR in comparison to the steady case. As in the steady case, transition to MR in the strong-reflection region, is accompanied by a rapid decrease in pressure rise through the reflection/triple point. Due to the similarity in trend between the steady and dynamic cases, steady state shock polars may be useful in identifying the critical trend that highlights the point of transition in the dynamic case.

8.1.2 Summary of Results for Dynamic MR to RR Transition

Rapid wedge rotation generated a measurable effect on MR → RR transition. The first experimental evidence of 2D MR → RR transition below the steady von Neumann condition is presented (see figure 8.1). In experiments and computations for dynamic MR → RR transition at $M = 3.26$, transition was delayed approximately 0.8° below the corrected von Neumann condition. Once again, there was good agreement between experiment and CFD of the experiment. CFD was used to further investigate the sensitivity of

transition to rotation speed, initial incidence and rotation centre in the strong and weak-reflection ranges. Due to impulsive wedge start and rapid wedge rotation, there are very marked dynamic effects on the variation of Mach stem height with wedge incidence and the deviation from the steady transition conditions is significant. MR $\rightarrow$ RR transition depends on the initial condition and the transient variation of Mach stem height with wedge incidence. For the range of rotation speeds investigated at $M = 1.93$ and 2.98, $\delta\phi_T$ ranged from 1.2° at $M_E = -0.01$ to 10.9° at $M_E = -0.1$. It was demonstrated that MR can be maintained until zero wedge incidence with a sufficiently large rotation rate (for example $M_E = -0.1$ at $M = 1.93$). For the range of simulations completed, the dependence of transition to initial incidence and rotation centre is marked, especially at larger rotation speeds, e.g. $M_E = -0.1$.

Some ideas on three-dimensional (3D) effects were presented. For this particular experimental setup there was good agreement on transition angle between 2D CFD and 3D experiment. It is possible, for a given rapid rotation speed, that they deviate beyond some critical wedge aspect ratio due to the delay in arrival of spanwise information to the reflection pattern in the wedge vertical plane of symmetry. If true, it would mark a significant deviation from the steady case, i.e. in the steady case, there is no difference in transition between the 2D and 3D case beyond a critical wedge aspect ratio. In the dynamic MR $\rightarrow$ RR case, a difference in transition may be observed between the 2D and 3D case beyond a critical wedge aspect ratio, and this may increase for increasing wedge aspect ratios.

8.2 Recommendations for Future Work

The recommendations for future work summarised in chapters 6 and 7 are listed here:

8.2.1 Dynamic RR to MR Transition

1. Determination of the minimum critical wedge rotation speed required such that transition is independent of free stream perturbations in the CSIR facility. This could be followed by a more general, but detailed investigation into the relationship between free stream noise and the minimum critical wedge rotation speed required to achieve RR $\rightarrow$ MR transition that is independent of the level of free stream noise and this could be applied to any facility.

2. An investigation to quantify the effect of rapid wedge rotation on the incident wave curvature and pressure gradient along the incident wave.

3. A detailed investigation into the "detachment" condition for the dynamic case.

4. Execution of the dynamic experiments at $M = 4.0$ in which the dual solution domain is larger. At $M = 4.0$ the difference between ϕ_D and ϕ_N is 5.8°.

5. Execution of the experiment described by Hornung [17]. Establish an initial, steady, RR below the dual solution domain, preferably at $M = 4.0$. Rotate the wedges rapidly and terminate the motion just below the detachment condition. The development of the reflection pattern would be of primary interest. The challenge, from an experimental perspective, lies in the termination of the wedge motion at the desired condition in a way that does not introduce vibration that influences transition or the development of the reflection pattern.

6. Investigation of the curious negative second gradient for Mach stem development against ϕ with $M_E = +0.01$ at $M = 2.98$.

7. The rig developed here may be applied to various interesting experimental studies, e.g. the effect of acceleration of finite aspect ratio wings in a steady, supersonic free stream on the unsteady evolution of the wing wake structure.

8.2.2 Dynamic MR to RR Transition

1. A detailed investigation to identify and quantify the mechanism(s) in phases III and IV of the Mach stem development at $M = 1.93$ and $M = 2.98$.

2. Development of an appropriate 3D flow solver for the investigation of dynamic, three-dimensional effects on MR $\rightarrow$ RR transition. The issues of mesh movement, solver accuracy, flow field resolution and solver speed are pertinent for consideration here.

3. Investigation of the effect of increasing wedge aspect ratio on ϕ_T with respect to the 2D result.

4. Investigation of the effect of increasing the rotation speed of a finite aspect ratio wedge on ϕ_T with respect to the 2D result.

5. Investigation of the effect of intermediate spanwise RR patterns to the propagation of spanwise information and its effect on ϕ_T.

Appendix A

Data Acquisition of Freestream Conditions

A.1 Mach Number Measurement

The test section Mach number is calculated from:

$$M = \left[\left\{ \left(\frac{P_O}{p} \right)^{\frac{\gamma-1}{\gamma}} - 1 \right\} \left\{ \frac{2}{\gamma - 1} \right\} \right]^{\frac{1}{2}} \tag{A.1}$$

For isentropic flow, the stagnation pressure between the settling chamber and the test section is constant. Stagnation pressure is measured with a stagnation pressure probe in the settling chamber and test section static pressure is measured from a static pressure port in the test section wall. Stagnation and static pressure measurements are relative to atmosphere. A dedicated atmospheric pressure transducer is used to measure the atmospheric pressure. The following sections document the calibration of the stagnation, static and atmospheric pressure transducers.

A.1.1 Pressure Transducer Calibration

A calibrated Druck Digital Pressure Indicator 605 (See Figure A.1) was used to calibrate all pressure transducers, viz. stagnation, static and atmospheric pressure transducers. The technical specifications of the calibration standard are tabulated in Table A.1. All pressure transducers were calibrated by applying a known pressure from the DPI605 and recording the voltage output on the National Instruments data acquisition system. The transducer output voltage was recorded when a stable pressure reference was established on the DPI605.

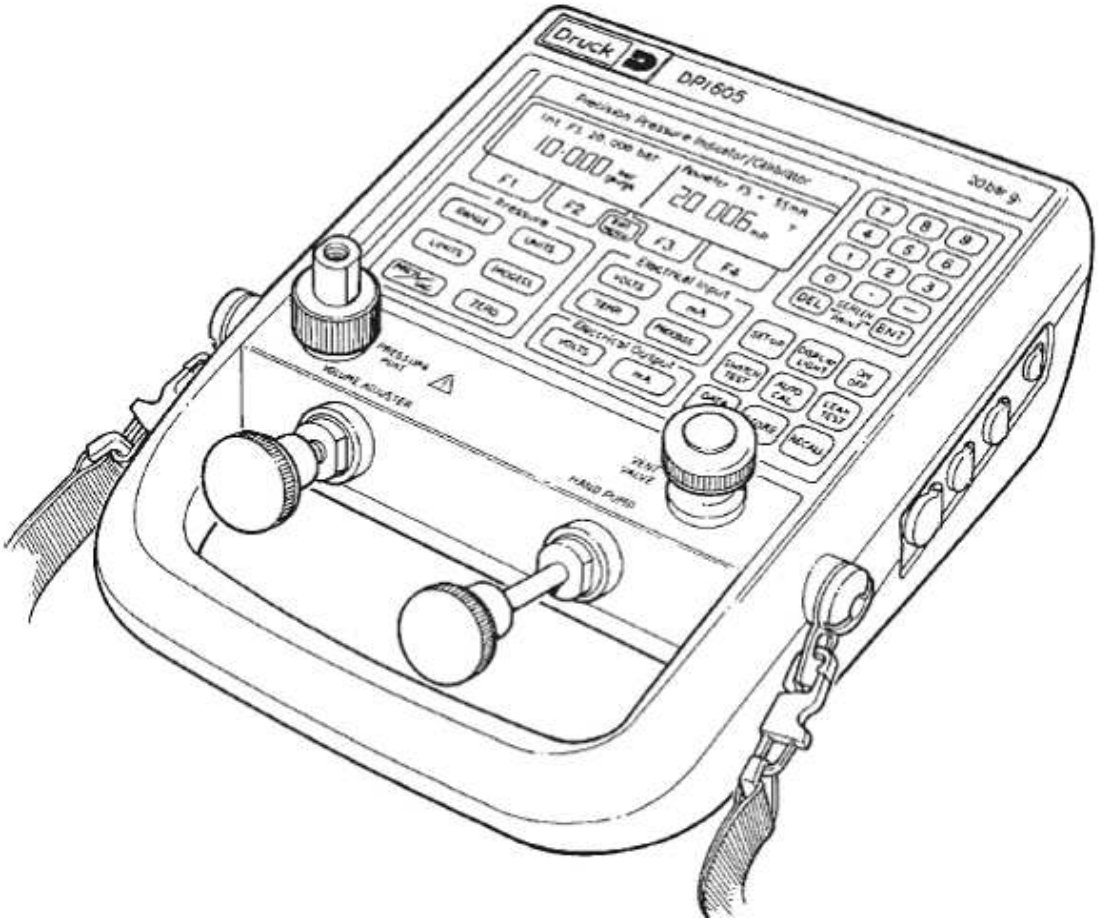


Figure A.1: Druck Digital Pressure Indicator 605

Table A.1: Technical specifications of the Druck DPI605

Item	**Details**
Instrument Name	Druck DPI 605
Calibration Date	10 September 2009
Calibration Authority	Unique Metrology
Calibration Certificate Number	0909P2536-1
Serial Number	1140/93-4
Measurement Uncertainty (0 - 10 bar)	±0.0022bar
Measurement Uncertainty (10 - 20 bar)	±0.0032bar
Maximum Correction (12 bar)	-0.00309 bar
Pressure range	0 - 20 bar

Table A.2: Pressure Transducer Specifications

Transducer	TP-HI	TP-LO	Static Press.	Atmospheric Press.
Instrument Name	Schaevitz	Schaevitz	Schaevitz	Vaisala PTB101B
Serial Number	124151	41024	131546	X1250006
Input Range	0-200 PSI Gauge	0-3.5 Bar Abs.	0 - 20 PSI Gauge	100 - 1060 hPa
Excitation	5.0 V DC	5.0 V DC	5.0 V DC	10 - 30 V DC
Output Range	-0.35 mV to 25 mV	0 to 25 mV	-0.2 to 25 mV	0 - 2.5 V
Calibration Date	22/10/2009	22/10/2009	22/10/2009	22/10/2009

Table A.3: Total pressure transducer calibration: High Range

Applied Pressure (kPa)	Data Acquisition Reading (mV)
0	-0.2828
255.38	4.4075
541.8	9.6516
811.14	14.5623
1102.56	19.8493
650.6	11.6464
295.26	5.1474
103.96	1.6407
0.002	-0.2821

A.1.2 Pressure Transducer Specfication and Calibration Results

Stagnation pressure measurement in the settling chamber is performed with two transducers. One is dedicated to measurement between 0 - 3.5 bar absolute (TP-LO) and the other between 3.5 bar absolute to 200 PSI guage (TP-HI). Table A.2 includes the specifications of all the pressure transducers. Table A.7 summarises the regression statistics from the calibration process. A comparison of calibration coefficients for all pressure transducers in the CSIR HSWT indicate a negligible variation since March 2008.

The values of pressure applied with the DPI 605 per transducer is tabulated in Tables A.3 - A.6. Figure A.2 includes the results of the calibration and the linear fit of the data.

Table A.4: Total pressure transducer calibration: Low Range

Applied Pressure (kPa)	Data Acquisition Reading (mV)
0	6.9255
119.51	15.3477
179.42	19.5724
239.38	23.787
180.5	19.6694
111.32	14.7932
0	6.9308

Table A.5: Static pressure transducer calibration

Applied Pressure (kPa)	Data Acquisition Reading (mV)
-0.012	-0.1134
32.11	5.579
59.95	10.5233
89.97	15.8801
129.98	23.0047
110	19.4671
50.03	8.8049
-0.012	-0.0819
-65.97	-11.741

Table A.6: Atmospheric pressure transducer calibration

Applied Pressure (kPa)	Data Acquisition Reading (mV)
87.167	-1.48
84.03	-1.3079
86.01	-1.4165
88.04	-1.528
90.003	-1.6353
87.16	-1.4798

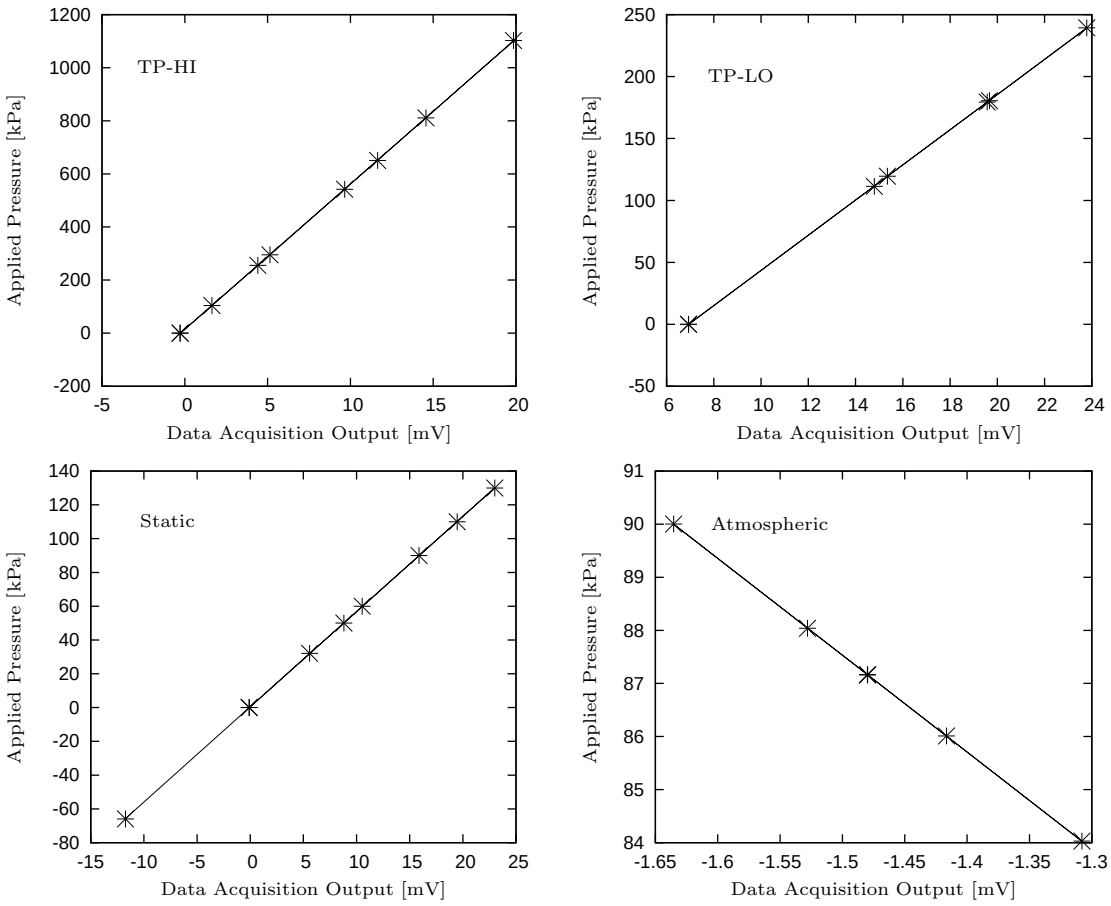


Figure A.2: Calibration and regression for pressure transducers

Table A.7: Summary of pressure transducer regression statistics

Transducer	**TP-HI**	**TP-LO**	**Static Press.**	**Atmospheric Press.**
R Squared	0.999992757	0.999996514	0.999992675	0.999998269
Standard Error [Pa]	1106.03	187.28	177.92	2.94
Slope, m [Pa/mV]	54733.607	14190.514	5635.744	-18239.333
Δm[Pa/mV]	55.678	11.849	5.765	11.999
Intercept, c [Pa]	14406.451	-98374.822	454.327	60172.917
Δc[Pa]	551.686	194.507	74.863	17.734

A.1.3 Mach Number Calculation and Uncertainty Analysis

The uncertainty estimation method documented by Kirkup [29] is implemented. The ratio of total and static pressure as a function of free stream Mach number for an isentropic flow may be expressed as:

$$\frac{P_O}{p} = \left(1 + \frac{\gamma - 1}{2} M^2\right)^{\frac{\gamma}{\gamma - 1}} \tag{A.2}$$

Given the stagnation and static pressures the Mach number is given by:

$$M = \left[\left(\frac{P_O}{p}\right)^{\frac{\gamma - 1}{\gamma}} - 1\right]^{\frac{1}{2}} \tag{A.3}$$

In the CSIR supersonic tunnel, the stagnation and static pressure transducers are used as guage pressure transducers. The gauge reading is added to an accurate atmospheric measurement to obtain an absolute measurement. Therefore:

$$P_{O,absolute} = P_{O,gauge} + p_{atmosphere} \tag{A.4}$$

and

$$p_{absolute} = p_{gauge} + p_{atmosphere} \tag{A.5}$$

Since the stagnation and static pressure gauges are used as gauge pressure transducers only the gradient, m, of the linear fit through the transducer calibration data is necessary. The gauge pressure (stagnation and static) may be calculated from the data acquisition readings from:

$$P_{O,gauge} = (mV \times m_{P_O}) \tag{A.6}$$

and

$$p_{gauge} = (mV \times m_p) \tag{A.7}$$

The atmospheric pressure is calculated in a similar manner, with the exception that the y intercept,c, of the linear fit through the tranducer calibration data is also used, i.e.:

$$p_{atmosphere} = (mV \times m_{atmosphere}) + c_{atmosphere} \tag{A.8}$$

Substituting equations A.6 - A.8 into equations A.4 and A.5 produces:

$$P_{O,absolute} = [(mV \times m_{P_O})] + [(mV \times m_{atmosphere}) + c_{atmosphere}] \tag{A.9}$$

and

$$p_{absolute} = [(mV \times m_p)] + [(mV \times m_{atmosphere}) + c_{atmosphere}] \tag{A.10}$$

Substituting equation A.9 and A.10 into A.3 yields Mach number from the static and stagnation pressure measurements:

$$M = \left[\left(\frac{[(mV \times m_{P_O})] + [(mV \times m_{atmosphere}) + c_{atmosphere}]}{[(mV \times m_p)] + [(mV \times m_{atmosphere}) + c_{atmosphere}]} \right)^{\frac{\gamma-1}{\gamma}} - 1 \right]^{\frac{1}{2}} \tag{A.11}$$

From the calibration of the various pressure transducers, the uncertainty in the slope and intercept from a least squares fit of the calibration data are denoted as Δm and Δc respectively. If

$$P_{O,gauge} \mid_{max} = (mV \times (m_{P_O} + \Delta m_{P_O})) \tag{A.12}$$

$$P_{O,gauge} \mid_{min} = (mV \times (m_{P_O} - \Delta m_{P_O})) \tag{A.13}$$

$$p_{gauge} \mid_{max} = (mV \times (m_p + \Delta m_p)) \tag{A.14}$$

$$p_{gauge} \mid_{min} = (mV \times (m_p - \Delta m_p)) \tag{A.15}$$

$$p_{atmosphere}\,|_{max} = ((mV \times m_{atmosphere} + \Delta m_{atmosphere})) + (c_{atmosphere} + \Delta c_{atmosphere}) \tag{A.16}$$

$$p_{atmosphere}\,|_{min} = ((mV \times m_{atmosphere} - \Delta m_{atmosphere})) + (c_{atmosphere} - \Delta c_{atmosphere}) \tag{A.17}$$

The uncertainty may then be used to determine the range of absolute stagnation and static pressures (taking into account the uncertainty in the slope and intercept of the transducer calibrations).

$$\begin{aligned} P_{O,absolute}\,|_{max} &= P_{O,gauge}\,|_{max} + p_{atmosphere}\,|_{max} \\ &= (mV \times (m_{P_O} + \Delta m_{P_O})) + ((mV \times m_{atmosphere} + \Delta m_{atmosphere})) \\ &\quad + (c_{atmosphere} + \Delta c_{atmosphere}) \end{aligned} \tag{A.18}$$

$$\begin{aligned} P_{O,absolute}\,|_{min} &= P_{O,gauge}\,|_{min} + p_{atmosphere}\,|_{max} \\ &= (mV \times (m_{P_O} - \Delta m_{P_O})) + ((mV \times m_{atmosphere} - \Delta m_{atmosphere})) \\ &\quad + (c_{atmosphere} - \Delta c_{atmosphere}) \end{aligned} \tag{A.19}$$

$$\begin{aligned} p_{absolute}\,|_{max} &= p_{gauge}\,|_{max} + p_{atmosphere}\,|_{max} \\ &= (mV \times (m_p + \Delta m_p)) + ((mV \times m_{atmosphere} + \Delta m_{atmosphere})) \\ &= + (c_{atmosphere} + \Delta c_{atmosphere}) \end{aligned} \tag{A.20}$$

$$\begin{aligned} p_{absolute}\,|_{min} &= p_{gauge}\,|_{min} + p_{atmosphere}\,|_{min} \\ &= (mV \times (m_p - \Delta m_p)) + ((mV \times m_{atmosphere} - \Delta m_{atmosphere})) \\ &= + (c_{atmosphere} - \Delta c_{atmosphere}) \end{aligned} \tag{A.21}$$

When substituted into equation A.3 the uncertainty in Mach number only arising from the uncertainties in the slope and intercepts of the first order curve fit to the transducer calibration data may be calculated. Static and stagnation pressure readings are offset such that they give guage pressure readings. The offset is calculated from the first 500 data points before the tunnel start for which the guage pressure readings for the static and stagnation tranducers must give an average of 0 Pa. Due to inherent noise in the data acquisition system these corrections also have a minimum and maximum value which contribute to the overall uncertainty of the derived Mach number. These must also be taken into account (Δp_η and $\Delta P_{O,\eta}$). Sample values from actual data acquisitions during tests were used to calculate the uncertainties at 3 different nozzle settings. Take into account the transducer linear regression statistics in A.7 and the fact that TP-LO is only used from 0 - 3.5 bar absolute pressure, the uncertainties are calculated as follows:

Uncertainty calculation at a M 2.0 nozzle setting:

$$
\begin{aligned}
p_{atmosphere,mV} &= -1.422V \\
p_{atmosphere} &= (-1.422V \times -18239.333Pa/V) + 60172.917Pa = 86111.820Pa \\
p_{atmosphere}\,|_{max} &= (-1.422V \times (-18239.333Pa/V + 11.999Pa/V)) + (60172.917Pa + 17.734Pa) \\
&= 86146.618Pa \\
p_{atmosphere}\,|_{min} &= (-1.422V \times (-18239.333Pa/V - 11.999Pa/V)) + (60172.917Pa - 17.734Pa) \\
&= 86077.023Pa
\end{aligned}
$$

Taking $\Delta p_\eta = -847.371$Pa, $\Delta p_\eta\,|_{max} = -941.862$Pa, $\Delta p_\eta\,|_{min} = -737.110$Pa and $\Delta P_{O,\eta} = 97139.294$Pa, $\Delta P_{O,\eta}\,|_{max} = 97187.384$Pa and $\Delta P_{O,\eta}\,|_{min} = 97079.110$Pa, the following corrected gauge pressure measurements are:

$$
\begin{aligned}
P_{O,gauge,mV} &= 17.149mV \\
P_{O,gauge} &= (-17.149mV \times 14190.51Pa/V) - \Delta P_{O,\eta} = 146208.081Pa \\
P_{O,gauge}\,|_{min} &= (-17.149mV \times 14190.51Pa/V) - \Delta P_{O,\eta}\,|_{min} = 145956.791Pa \\
P_{O,gauge}\,|_{max} &= (-17.149mV \times 14190.51Pa/V) - \Delta P_{O,\eta}\,|_{max} = 146471.463Pa \\
P_{O,absolute} &= 146208.081Pa + 86111.820Pa = 232319.901Pa \\
P_{O,absolute}\,|_{min} &= 145956.791Pa + 86077.023Pa = 232033.814Pa \\
P_{O,absolute}\,|_{max} &= 146471.463Pa + 86146.618Pa = 232618.081Pa
\end{aligned}
$$

$$
\begin{aligned}
p_{gauge,mV} &= -9.497mV \\
p_{gauge} &= (-9.497mV \times 5635.744Pa/V) - \Delta P_{O,\eta} = -52674.869Pa \\
p_{gauge}\,|_{min} &= (-9.497mV \times 5635.744Pa/V) - \Delta P_{O,\eta}\,|_{min} = -52839.881Pa \\
p_{gauge}\,|_{max} &= (-17.149mV \times 14190.51Pa/V) - \Delta P_{O,\eta}\,|_{max} = -52525.628Pa \\
p_{absolute} &= -52674.869Pa + 86111.820Pa = 33436.951Pa \\
p_{absolute}\,|_{min} &= -52839.881Pa + 86077.023Pa = 33237.142Pa \\
p_{absolute}\,|_{max} &= -52525.628Pa + 86146.618Pa = 33620.990Pa
\end{aligned}
$$

The derived Mach number is calculated as follows:

$$
\begin{aligned}
M &= \left[\left(\frac{P_{O,absolute}}{p_{absolute}}\right)^{\frac{\gamma-1}{\gamma}} - 1\right]^{\frac{1}{2}} \\
&= \left[\left(\frac{232319.901Pa}{33436.951Pa}\right)^{\frac{\gamma-1}{\gamma}} - 1\right]^{\frac{1}{2}} \\
&= 1.923
\end{aligned}
$$

Substituting the extreme values of stagnation and static pressures the minimum and maximum derived

Table A.8: CSIR tunnel test section calibration

Nozzle Setting	ΔM $\mid_{\text{Trans.Calib.}}$	$2\sigma \mid_{TestSect.Calib.}$	ΔM $\mid_{\text{Total}}$	**Correction Factor**
2.0	0.004	0.002	0.006	1.0029
3.0	0.01	0.008	0.011	1.0198
3.3	0.013	0.013	0.026	1.000818

Mach numbers may be calculated. In the above sample they are:

$$\begin{aligned} M \mid_{min} &= 1.919 \\ M \mid_{max} &= 1.927 \\ 2 \times \Delta M &= M \mid_{max} - M \mid_{min} \\ &= 0.007 \\ \Delta M &= 0.004 \end{aligned}$$

The Mach number and its uncertainty from the pressure transducer calibration at this particular data point is expressed as M1.923 ± 0.004. This uncertainty is the uncertainty in the Mach number measurement due to pressure transducer calibration process. The uncertainty for the remaining nozzle settings are included in table A.8. The uncertainty in the Mach number from test section calibration must also be taken into account. The test section calibration done by the CSIR in 2006 correlates the Mach number derived from the static pressure measurement on the wall with the Mach number in the test section. The uncertainties of the test section calibration and the correction factors for each nozzle setting is included in table A.8. A sum of the uncertainties from the test section calibration and the pressure transducer calibrations will provide an estimate of the total uncertainty in the Mach number in the test section.

In view of the results in table A.8, a value of ΔM $\mid_{\text{Total}} = 0.03$ is assumed across the range of test conditions. Continuing with the example, application of the correction factor and the test section calibration uncertainty results in :

$$\begin{aligned} M \mid_{corrected} &= 1.923 \times 1.0029 = 1.929 \\ \Delta M \mid_{Total} &= \pm 0.03 \\ M &= 1.929 \pm 0.03 \end{aligned}$$

A.2 Test Section Acoustic Speed Measurement

Given that

$$\frac{T_O}{T} = 1 + \frac{\gamma - 1}{2} M^2 \tag{A.22}$$

for isentropic flows and that the total temperature is constant between the settling chamber and the test section, the static temperature and acoustic speed in the test section may be calculated from the test section Mach number and a total temperature measurement in the settling chamber as follows :

$$T = \frac{T_O}{1 + \frac{\gamma-1}{2} M^2} \tag{A.23}$$

$$a = \sqrt{\gamma R T} = \sqrt{\gamma R \frac{T_O}{1 + \frac{\gamma-1}{2} M^2}} \tag{A.24}$$

A.2.1 Stagnation Temperature Probe and Transducer Specification

The total temperature probe discussed in Chapter 3 is repeated at this point in figure A.3. The probe consists of a PT100 Resistance Temperature Detector (RTD) sensor housed in a machined stainless steel shroud. The PT100 Platinum RTD was customised for these tests to increase exposure of the sensor to the settling chamber flow to increase the rate of heat transfer for the short duration test. PT100's generally have a second order response to temperature through its entire range and the response between 0 and 50°C is approximately linear. The PT100 has a dedicated current source that supplies the transducer with the necessary excitation to produce a DC voltage output. When connected to the power supply, the PT100 generates a 10V DC signal at 50°C and a 0V DC signal at 0°C. The tranducer response for the range $-200 \rightarrow 349$°C was supplied by WIKA Instruments (figure A.4). A linear fit to the response in the expected operational range ($0 \rightarrow 50$°C is also provided. As can be seen from the regression the response is approximately linear in this range.

In the range $0 \rightarrow 50$°C the maximum deviation of the predicted temperature (from the slope of a linear regression) to the calibrated temperature is approximately 0.06°C. This is negligible in comparison to the uncertainty from the measurement technique. For example, consider the sample measurement at Mach 3.0 presented earlier and repeated in figure A.5, the uncertainty in the measurement is estimated at 0.5 K.

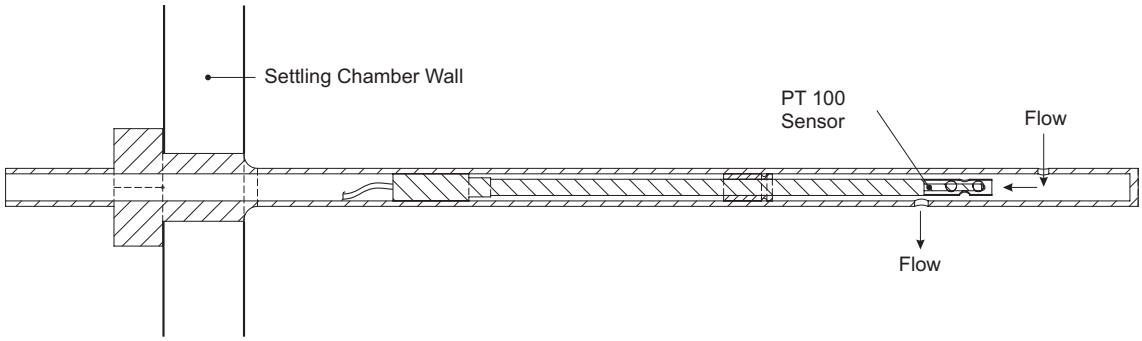


Figure A.3: Schematic of stagnation temperature probe in settling chamber

A.2.2 Acoustic Speed Calculation and Uncertainty Analysis

The uncertainty in Mach number and stagnation temperature may be used to determine the range of acoustic speed values bounded by a_{min} and a_{max}.

$$a\mid_{max} = \sqrt{\gamma R \frac{T_O\mid_{max}}{1+\frac{\gamma-1}{2}M^2\mid_{min}}} \tag{A.25}$$

$$a\mid_{min} = \sqrt{\gamma R \frac{T_O\mid_{min}}{1+\frac{\gamma-1}{2}M^2\mid_{max}}} \tag{A.26}$$

For the sample measurement in figure A.5, in which $M = 3.0 \pm 0.03$ and $T_O = 29.0°C \pm 0.5$:

$$\begin{aligned} a\mid_{max} &= \sqrt{1.4 \times 287.06 \times \frac{(29.0+0.5+273.15)}{1+\frac{\gamma-1}{2}(3.0-0.03)^2}} \\ &= 209.8 m.s^{-1} \\ a\mid_{min} &= \sqrt{1.4 \times 287.06 \times \frac{(29.0-0.5+273.15)}{1+\frac{\gamma-1}{2}(3.0+0.03)^2}} \\ &= 206.7 m.s^{-1} \end{aligned}$$

Given that

$$\begin{aligned} a &= \sqrt{1.4 \times 287.06 \times \frac{(29.0+273.15)}{1+\frac{\gamma-1}{2}(3.0)^2}} \\ &= 207.9 m.s^{-1} \end{aligned}$$

the uncertainty band is approximately $a\mid_{max} - a\mid_{min} = 3.0 m.s^{-1}$, approximately $3.0/207.9 = 1.5\% \approx \pm 0.75\%$

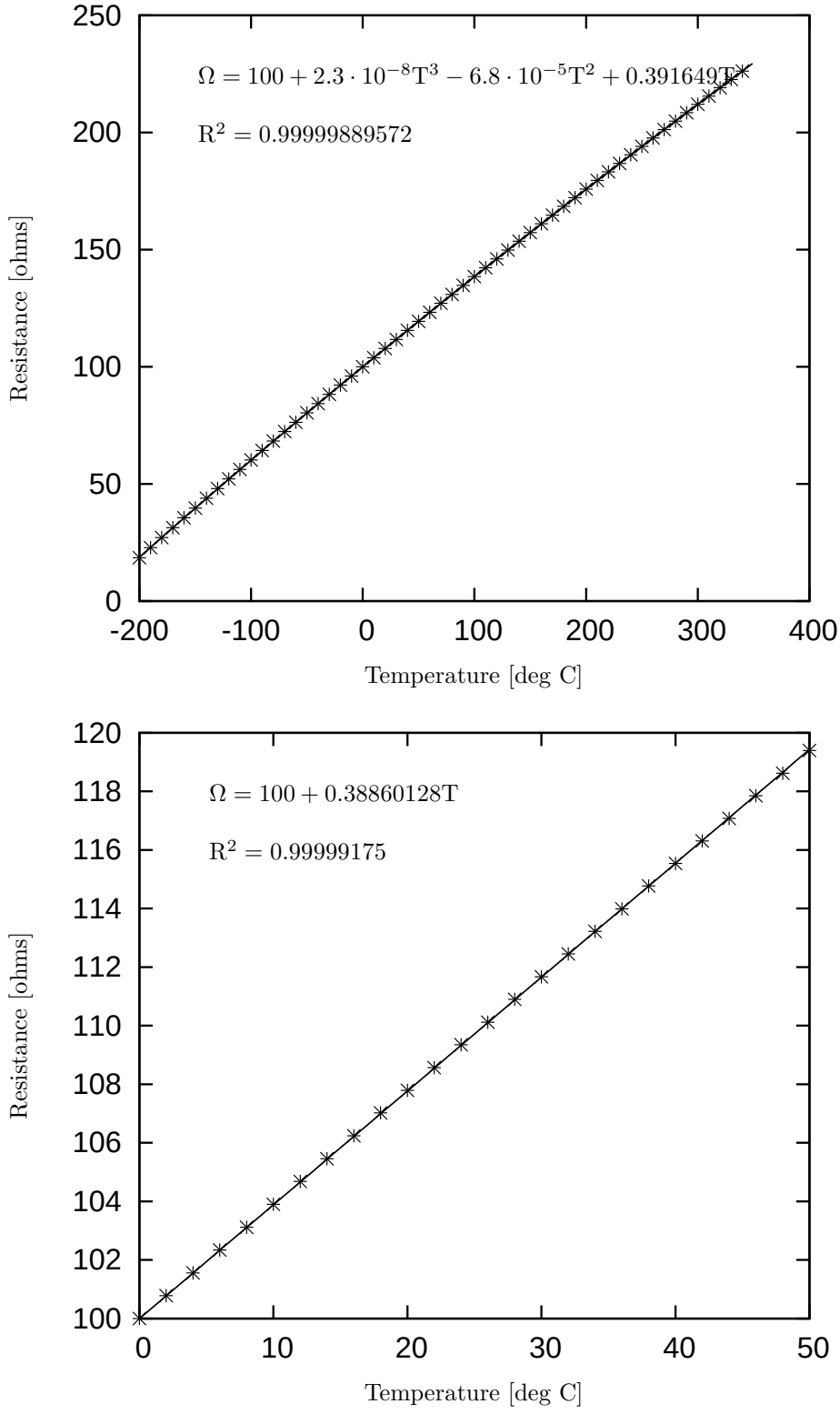


Figure A.4: Transducer response supplied by WIKA Instruments

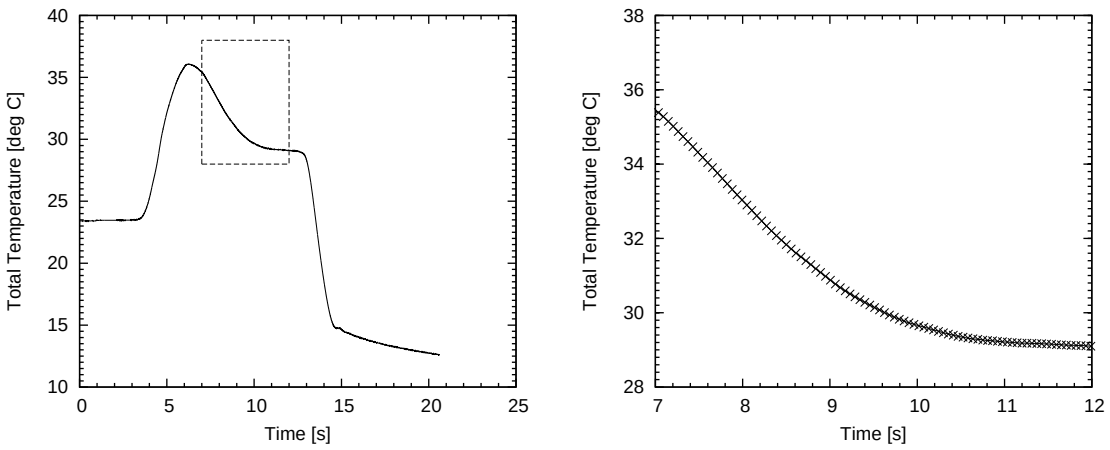


Figure A.5: Sample total temperature probe measurement (magnified view of select data range on the right hand side)

of the nominal value of acoustic speed. Since $M_E = V_E/a_\infty$, the contribution to the uncertainty in dimensionless edge speed is also approximately $\pm 0.75\%$.

A.3 National Instruments Data Acquisition System

Figure A.6 illustrates the 24 channel National Instruments data acquisition system architecture for the CSIR supersonic wind tunnel facility. Transducer signals may be logged from the pc during the tests. Excitation is supplied from the SCXI-1520 cards. The tranducers interface with the signal conditioning unit through the National Instruments 1314 custom terminal block. The SCXI-1520 cards, in addition to providing transducer excitation, set channel gains and signal noise filtering. The SCXI-1520 interfaces to a PCI based 6052e Analog to Digital Data acquisition card. The operator interfaces with the data acquisition system through a Labview software interface for configuration setup and data logging.

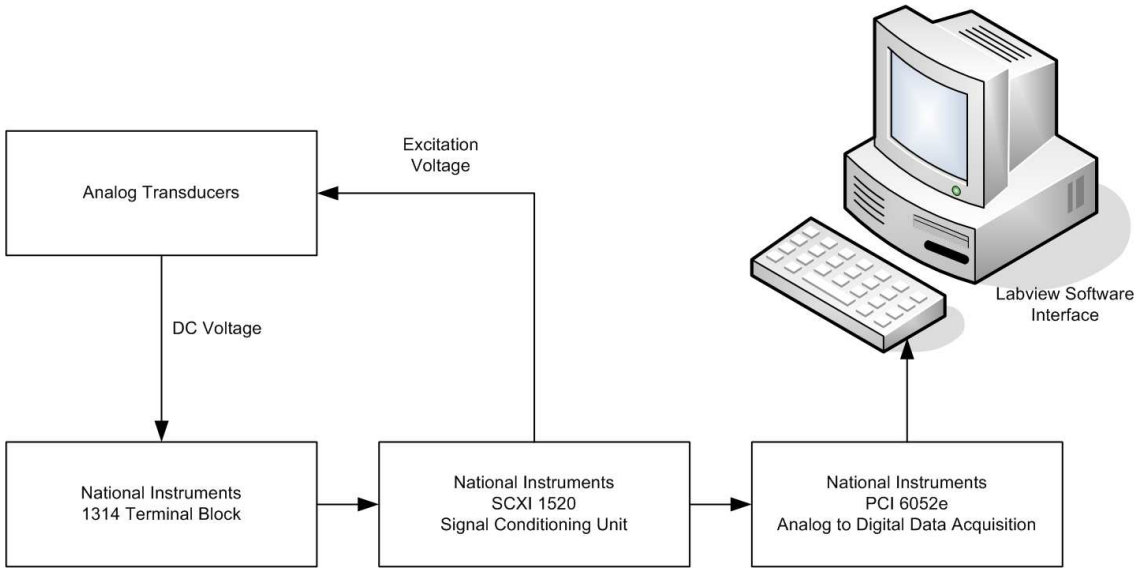


Figure A.6: Data Acquisition Architecture

Appendix B

Schlieren System, High-Speed Imaging and Optics

B.1 Schlieren System Specification

A standard z-type schlieren system was designed and developed specifically for the dynamic tests [[**?**],[37]]. Optical parameters of the system are documented in Table B.1 below. At the required 10000 fps only the central 512 x 512 pixels of the Photron Ultima APX-RS CCD chip are active. The schlieren system was optimised to focus the schlieren image onto this central section of the imaging chip.

B.1.1 Optical Alignment

Alignment of the schlieren system was done in accordance with the guidelines documented by Settles [37]. All elements were levelled with the ground with a bubble level. All centre points of the elements of the schlieren system were arranged at approximately the same height above the ground to ensure co-incidence with the system optical axis. Alignment was performed with the assistance of a precision manufactured laser pointer as shown in Figure B.2. The laser pointer was mounted on a machined collar on the front end of the light source and provided an excellent visible marker to locate the system optical axis. The first mirror directed the laser light from the light source through the test section glass. As each surface of the two glass windows are not perfectly parallel to each other, each surface reflects a small amount of light back to the source. The four reflected images of the laser point on the windows were kept in sharp focus in the plane of the light source origin (perpendicular to the optical axis). This ensured that the light source was located at the focal point of the first mirror. The four reflections of the light source were also arranged about the optical axis as symmetrical as possible. This ensured that the first mirror directed the light source image perpendicular to the test section. A collimator was also designed to assist the alignment of the system and

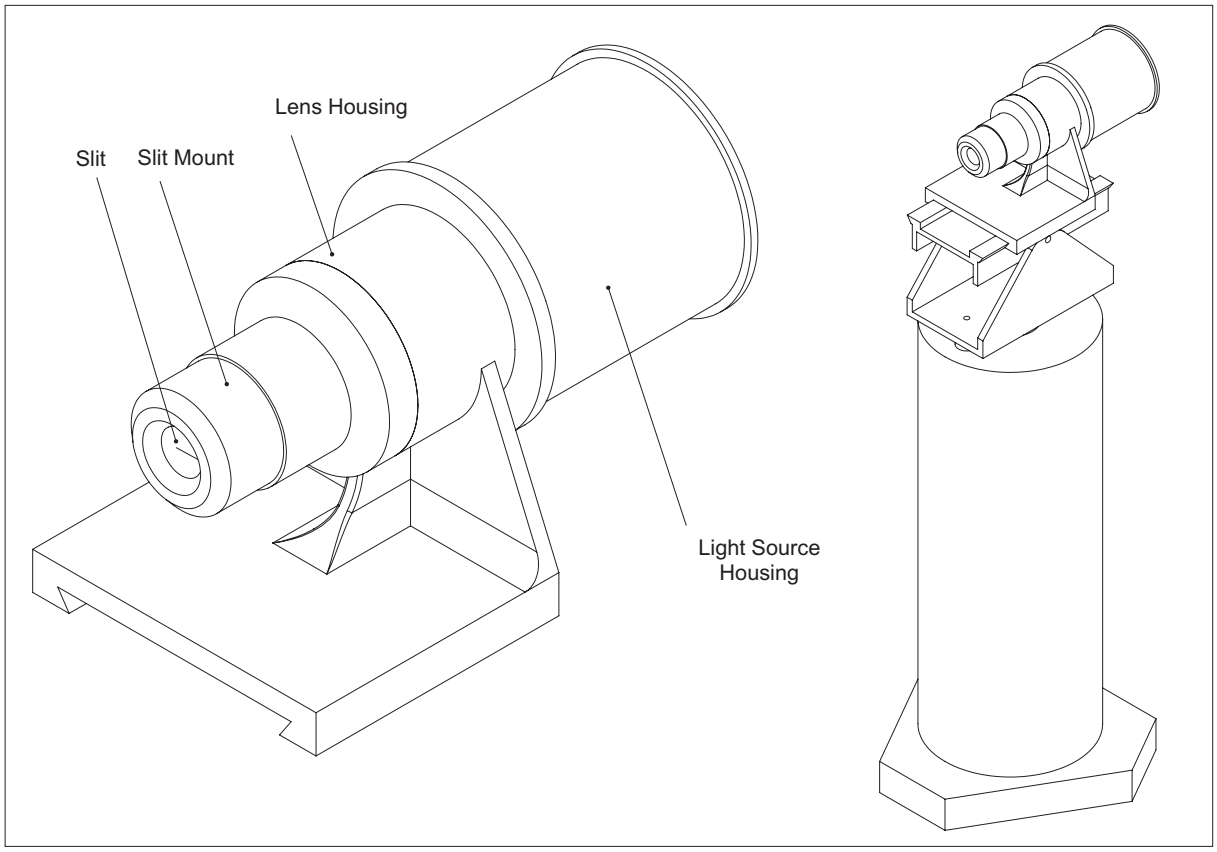


Figure B.1: Schlieren system light source

was installed at the location of the cut-off and imaging lens (Figure B.3). The collimator has an entry hole for the incoming laser light. If the incoming light is co-incident with the optical axis and the collimator is arranged perfectly about the axis, the incoming laser light goes through the centre of the collimator entrance and can be seen on the reflection in the middle of the body. The second mirror and stand mount for the schlieren cut-off and imaging lens were adjusted to achieve a perfectly collimated beam.

B.2 Technical Specifications of High Speed Camera

Technical high speed camera specifications are listed in table B.2.

B.3 Inclinometer Specification and Calibration

A Wyler bubble inclinometer and Pro3600 digital inclinometer were used for angular measurements. The Wyler bubble inclinometer was calibrated by the National Metrology Institute of South Africa (NMISA) and used as a secondary standard to check the calibration of the Pro3600 digital inclinometer.

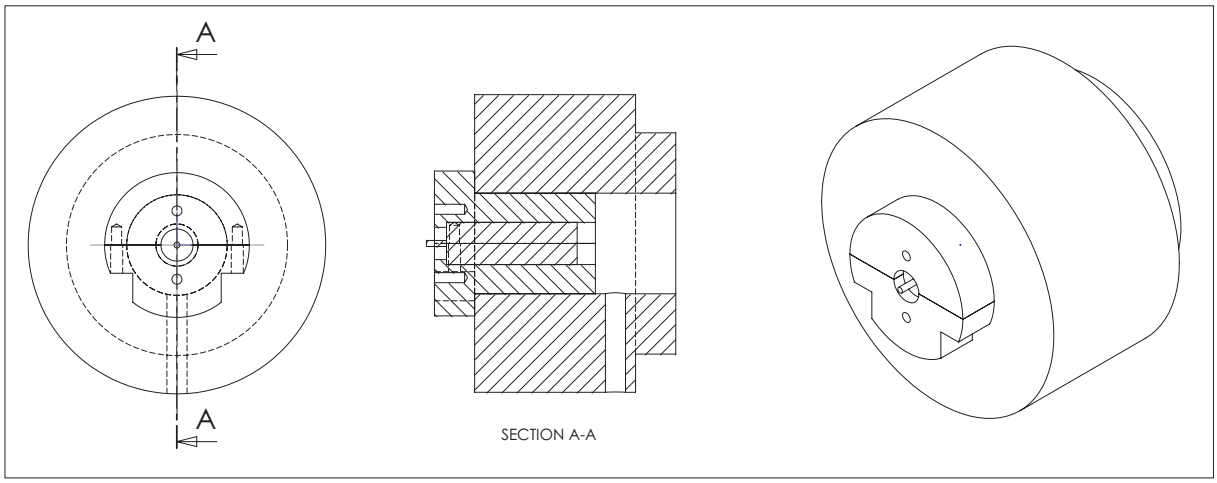


Figure B.2: Machined collar for laser pointer to replace slit mount on schlieren light source for system alignment

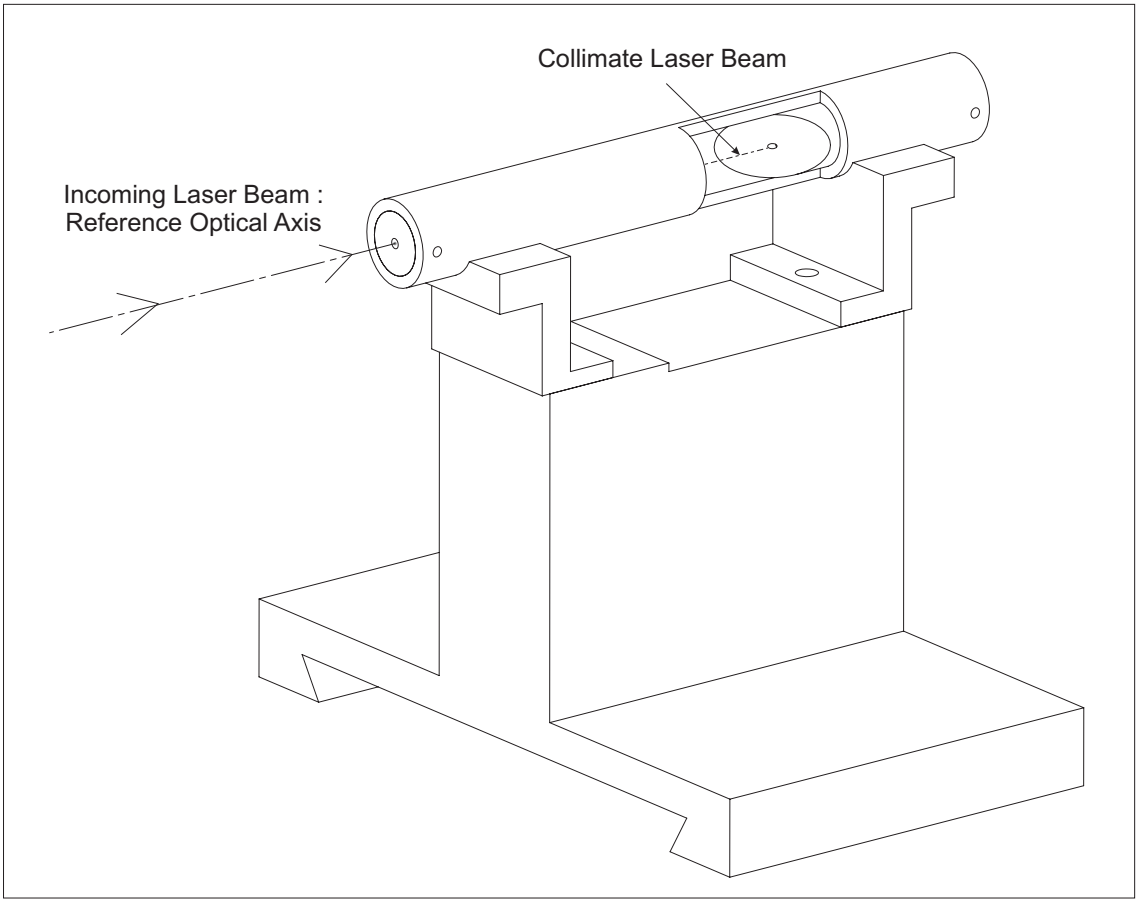


Figure B.3: Custom collimator for adjustment of second mirror

Table B.1: Optical parameters of schlieren system

Item	Description
Image sensor size at 10000 fps	8.7 mm x 8.7 mm
Parabolic Mirror Diameter	6 inch = 152.4 mm
Focal length	f/8 mirrors → 1219.2 mm
Distance from Second Mirror to Test Article	4000.00 mm
Distance from First Mirror to Test Article	4000.00 mm
Imaging Lens Focal Length	100.00 mm
Imaging Lens Specification	Edmund Optics Achromatic Lens with MgF_2 coating
Approximate Size of Object Field	100 mm
Distance from knife edge to lens	130.8 mm
Distance from lens to image sensor	80.14 mm

Table B.2: Technical specifications of high speed camera

Item	Description
Manufacturer	Photron
Model	Photron Ultima APX-RS
Maximum Image resolution up to 3000 fps	1024 x 1024
Image resolution at 10000 fps	512 x 512
Memory	8 GB
Record time at 10000 fps	2.5 seconds
Maximum Images recorded at 10000 fps	24576
Sensor	10 bit CMOS
Pixel size	17μm
Shutter speed	16.7 ms to 2μs

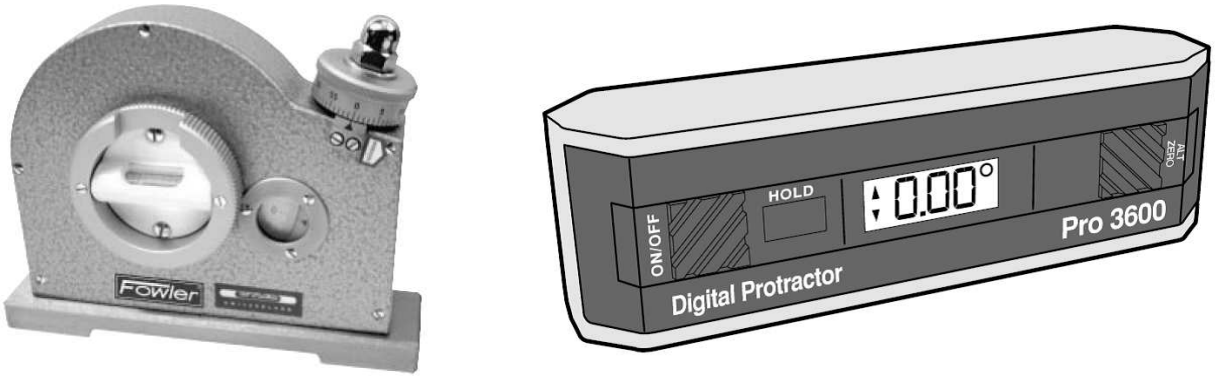


Figure B.4: Wyler and Pro3600 Inclinometers

Table B.3: Technical specifications of the Wyler Bubble Inclinometer

Item	**Details**
Instrument Name	Wyler Bubble Inclinometer
Calibration Date	4 August 2009
Calibration Authority	NMISA
Calibration Certificate Number	DM \ DIM − 3229
Serial Number	80/150
Measurement Uncertainty	0.017°

Table B.4: Calibration check of Pro3600 digital Protractor

Data Point Number	**Wyler Inclinometer** [°]	**Digital Protractor** [°]	**Error**
1	-5.03	-5.09	-0.06
2	0.05	0.04	0.01
3	2.55	2.49	0.06
4	5.08	4.99	0.09
5	10.17	10.10	0.07
6	15.03	14.90	0.13
7	20.18	20.10	0.08
8	25.45	25.40	0.05

The bubble inclinometer has a resolution of 1 minute and was calibrated in 10 degree intervals from $0 \pm 180°$. The magnitude of the error against the calibration standard was 0 minutes for most of the angles tested and approximately 1 minute (0.017°) between $70\text{to}180°$ and $-80\text{to} - 180°$. The magnitude of the error was also 1 minute at $-10\text{and} - 20°$. The Pro3600 digital protractor was checked against the Wyler inclinometer and since the inclinometer(s) were to be used for angular measurements below 25°, the bubble inclinometer served as an excellent secondary calibration standard. Most of the angular measurements during test setup were measured with the Pro3600 digital inclinometer primarily for its ease of use. For this reason a calibration check against a reliable secondary standard was necessary.

The magnitude of the maximum error in the digital inclinometer reading in the range of interest is approximately 0.13°.

B.4 Routine for co-ordination calculation in GNU Octave

The following short script was used to transform image pixel co-ordinates to spatial co-ordinates using a known calibration grid. The pixel co-ordinates of the imaged calibration grid were used to calculate the location of any point of interest.

xpixel = [Ordered array of pixel location of points on calibration grid in x direction]

ypixel = [Ordered array of pixel location of points on calibration grid in y direction]

xmap = [Ordered array of x-ordinates of calibration grid]

ymap = [Ordered array of y-ordinates of calibration grid]

Pointxpixel = [Ordered array containing pixel location of point of interest (x direction)]

Pointypixel = [Ordered array containing pixel location of point of interest (y direction)]

Pointx = griddata(xpixel,ypixel,xmap,Pointxpixel,Pointypixel,"linear")

Pointy = griddata(xpixel,ypixel,ymap,Pointxpixel,Pointypixel,"linear")

Comment : Pointxpixel and Pointypixel are the pixel co-ordinates of the point of interest. Pointx and Pointy are the required spatial co-ordinates of the pixel of interest.

Appendix C

Rig Design Calculations

This chapter documents important calculations to size the servo-driven and spring-driven actuators. The rig operator interface for both actuators is presented. Select photographs of the rig and its components are also included. The rationale for the selection of the maximum model cross sectional area is also discussed briefly.

C.1 Maximum Rig Cross Sectional Area

There is an upper limit on the model frontal cross sectional area that will permit the establishment of the required tunnel free stream conditions and is a function of free stream Mach number. A Naval Ordnance report [43] documents experimental data that compares the maximum model frontal cross sectional area for a few simple geometries (a 60° cone, a 30° and a solid circular disk) against the maximum theoretical area calculated from the one-dimensional isentropic relations. The data is reproduced here and the frontal cross sectional area of the experimental rig described in Chapter 3 is included. The model cross sectional area is labelled, A_m, and the tunnel cross sectional area is labelled, A_t. The data published in the report [43] shows a significant deviation from the ideal case and must be considered when undertaking model design for supersonic testing. The design limit was specified at $A_m/A_t \approx 0.045$ in an attempt to avoid tunnel blockage as experienced with the first version of the rig (presented in Chapter 3). This was adequate to establish the required free stream conditions.

C.2 Motor Sizing for Servo-driven Actuator for Steady State Experiments

The force required to actuate the wedges with a servo-motor in the steady state, baseline experiments is calculated at the condition that the wave system disgorges and is detached from the wedge surface. Only the

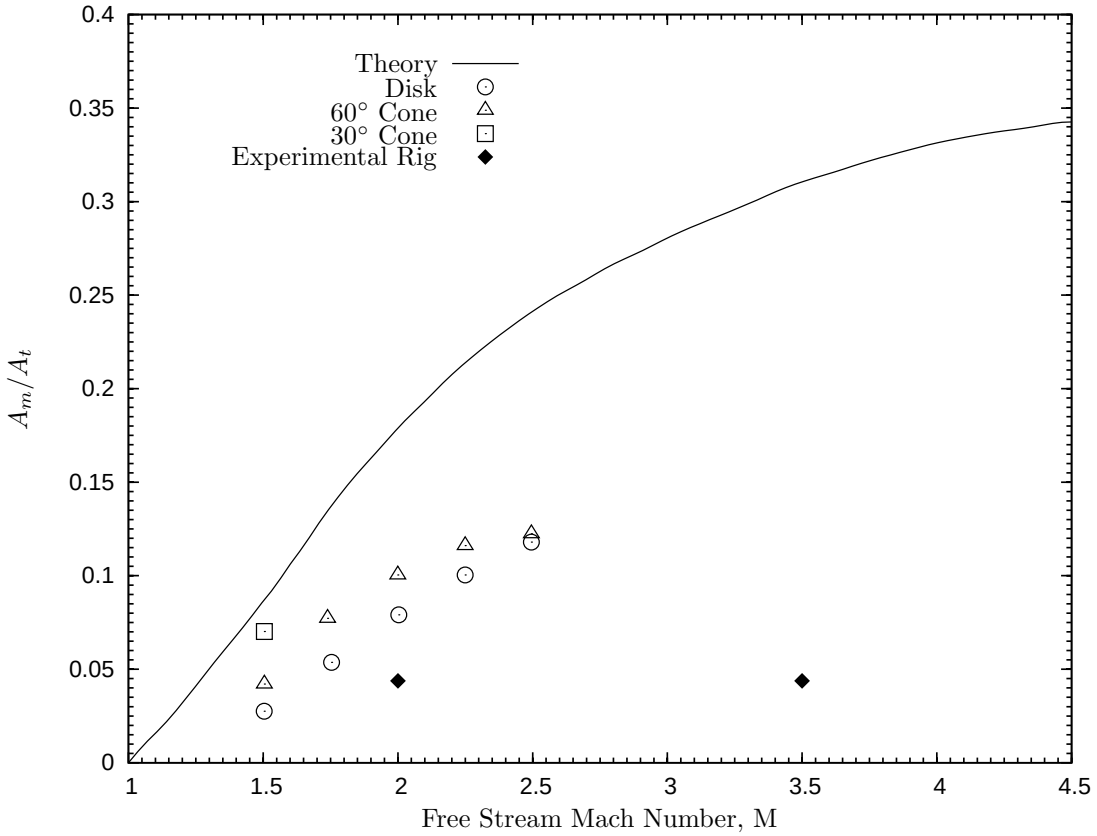


Figure C.1: Data used to determine the maximum permissable model cross sectional area extracted from a US Naval Ordnance Report [43].

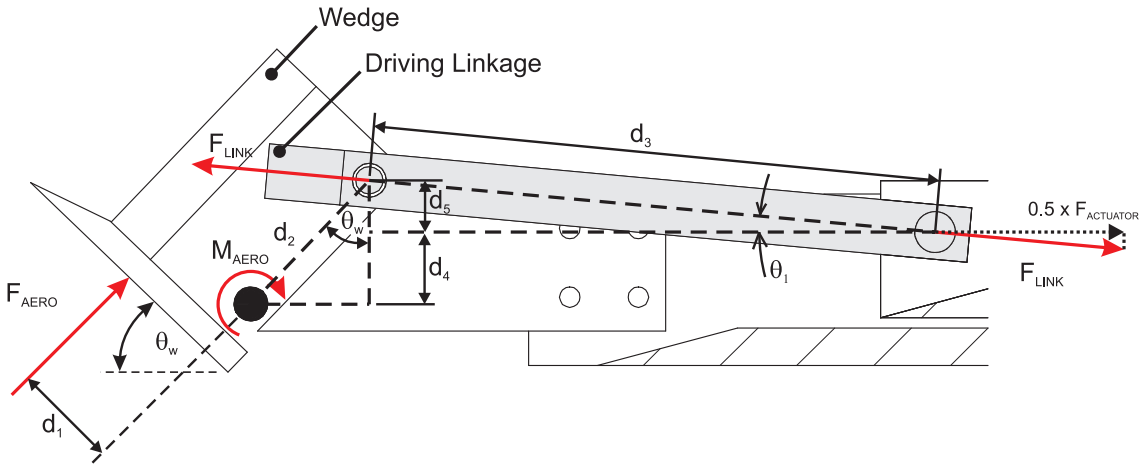


Figure C.2: Schematic showing derivation of actuator force

aerodynamic force perpendicular to the wedge surface is included in the estimation. The component parallel to the surface is not included in the calculation. As will be demonstrated later in this section, its inclusion reduces the force required to actuate the wedges. The approach adopted here is a conservative one. Figure C.2 illustrates the geometry and forces on a single wedge. The pressure rise through a normal shock is used to estimate the static pressure, P, at the wedge surface. The design free stream condition is at $M = 3.5$ with P_O= 787 kPa. Equation A.2 from Appendix A yields $P_O/P_\infty = 76.27$, where P_∞ is the free stream static pressure. The static pressure rise across a normal shock at M=3.5 is $P/P_\infty = 14.125$ and

$$\begin{aligned} P &= \frac{P}{P_\infty} \times \frac{P_\infty}{P_O} \times P_O \\ &= 14.125 \times \frac{1}{76.27} \times 787kPa \\ &= 145746kPa \end{aligned}$$

The resultant force, F_{AERO}, on a single wedge with surface area, A, is

$$\begin{aligned} F_{AERO} &= P \times A \\ &= 145746kPa \times 40mm \times 170mm \\ &= 991N \end{aligned}$$

The moment generated by F_{AERO} about the wedge centre of rotation is

$$M_{AERO} = F_{AERO} \times d_1 \tag{C.1}$$

The force required to balance M_AERO at the end of the driving linkage is F_{LINK} and the total actuator force for both wedges is $F_{ACTUATOR}$. Given the geometry in figure C.2 and that

$$M_{AERO} = F_{LINK} \times d_2 \tag{C.2}$$

the actuator force is related to the normal force on the wedge surface as follows:

$$F_{AERO} \times d_1 = \frac{0.5 \times F_{ACTUATOR}}{\cos\theta_1} \times d_2$$

and

$$F_{ACTUATOR} = 2F_{AERO}\cos\theta_1 \frac{d_1}{d_2} \tag{C.3}$$

for both wedges. The wedge incidence angle, θ_w, and the θ_1 are related as follows:

$$d_3 sin\theta_1 = d_2 cos\theta_w - d_4$$

Therefore

$$sin\theta_1 = \frac{(d_2 cos\theta_w - d_4)}{d_3} \tag{C.4}$$

Given the values for $d_1 = 16.5mm$, $d_2 = 25mm$, $d_3 = 83mm$, $d_4 = 10.5mm$, θ_w and $F_{AERO} = 991N$, the value for θ_1 and $F_{ACTUATOR}$ can be determined. Consider the maximum value of θ_w beyond which the incident wave detaches from the leading edge of the wedge. At $M = 3.5$, $\theta_w = 34.07°$ and $\theta_1 = 7.1°$, $F_{ACTUATOR} \approx 1298N$. If one considers figure C.2, the aerodynamic force component parallel to the wedge surface will produce an anti-clockwise moment about the wedge centre of rotation, hence reducing the actuator force required. Shigley [38] documents the mechanics of power screws. The motor torque, T, required to balance $F_{ACTUATOR}$, with a lead screw of diameter, d_m, and thread pitch, l, is

$$T = \frac{F d_m}{2}\left(\frac{l + \pi\mu d_m}{\pi d_m - \mu l}\right) \tag{C.5}$$

where μ is the coefficient of friction. Figure C.3 illustrates the lead screw arrangement used in the serov-driven actuator. The lead screw turns in a ball bearing arrangement and μ is very small. A value $\mu = 0.1$ is assumed. With $d_m = 8mm$ and $l = 2.5mm$, the required motor torque is $T = 1.05$ N.m. A motor and

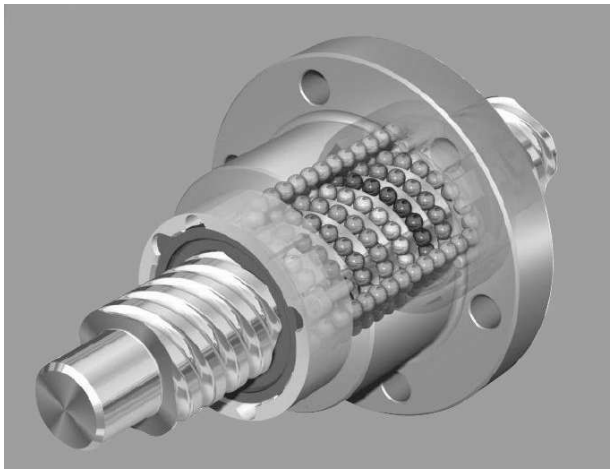


Figure C.3: Lead screw and bearing assembly to convert rotational motion of the DC servo motor to horizontal motion of the actuator required to pitch the wedges. The image is taken from the Rexroth Bosch Group product catalogue on precision ball screw assemblies.

Table C.1: Technical specifications for DC servo motor

Supplier	Faulhaber, Minimotor SA
Motor Description	DC micromotor series 3557
Motor Model No.	3557K-024CR 4.3G60
Power Supply	24V DC
Maximum Torque	50 mN.m
Rotational Speed	5000 RPM
Gearbox Description	Planetary Gearhead Series 30/1
Gearbox Model No.	30/1 S 43:1
Gear Reduction Ratio	43:1
Maximum Continuous Torque	4.5 N.m with steel gears

gearbox combination from Faulhaber Minimotor SA (Switzerland) capable of delivering 4.5 N.m of torque was used (see table C.1 with a lead screw and bearing assembly from Rexroth of the Bosch Group (see table C.2).

Table C.2: Technical specifications for the lead screw and bearing arrangement

Supplier	Rexroth, Bosch Group
Lead Screw Specification	Precision-rolled screw SN-R, Diameter = 8mm, Pitch = 2.5 mm
Bearing Description	Ball screw with flanged single nut
Bearing Model No.	$8 \times 2,5\text{R} \times 1,588 - 3$

C.3 Component Sizing for Spring-Based Actuator for Dynamic Tests

The following conceptual design calculations are applicable for $M_\infty = 2.0$. Assume $T_{O\infty} = 300.0$K and $P_{O\infty} = 250.0 \times 10^3$Pa. The specific heats ratio for air is $\gamma = 1.4$. Also assume a wedge chord of c = 40.0mm and a universal gas constant, R = 287.0J.kg^{-1}.K^{-1}. Free stream static temperature is calculated by:

$$T_\infty = T_{O\infty}\left(1 + \frac{\gamma - 1}{2}M_\infty^2\right) = 166.67K \tag{C.6}$$

The free stream acoustic velocity is given by:

$$a_\infty = (\gamma R T_\infty) = 258.8 m.s^{-1} \tag{C.7}$$

Given that θ' is the wedge pitch rate expressed in radians per second (rad.s^{-1}):

$$M_E = \frac{V_E}{a_\infty} = \frac{c\theta'}{a_\infty} \tag{C.8}$$

Then for $M_E = 0.1$

$$\theta' = 647.02 rad.s^{-1} = 37071.26°.s^{-1} \tag{C.9}$$

and $V_E = 25.88$m.s^{-1}

For $M_E = 0.01$, $\theta' = 64.7$rad.s^{-1} $= 3707.13°$.s^{-1} and $V_E = 2.59$m.s^{-1}.

Assuming a total pitch scan of $\Delta\theta = 25.0°$. Total time to pitch $\Delta\theta$ is given by:

$$\Delta t = \frac{\Delta\theta}{\theta'} \tag{C.10}$$

$\Delta t = 0.67 \times 10^{-3}$sec for $M_E = 0.1$ and $\Delta t = 6.7 \times 10^{-3}$sec for $M_E = 0.01$

The second order ordinary differential equation governing the response of an undamped spring mass system was used to estimate the required spring stiffness. Assume that m is the mass being accelerated and k is the spring stiffness, then

$$m\frac{dx^2}{dt^2} + kx = 0 \tag{C.11}$$

The solution of equation C.11 is given by

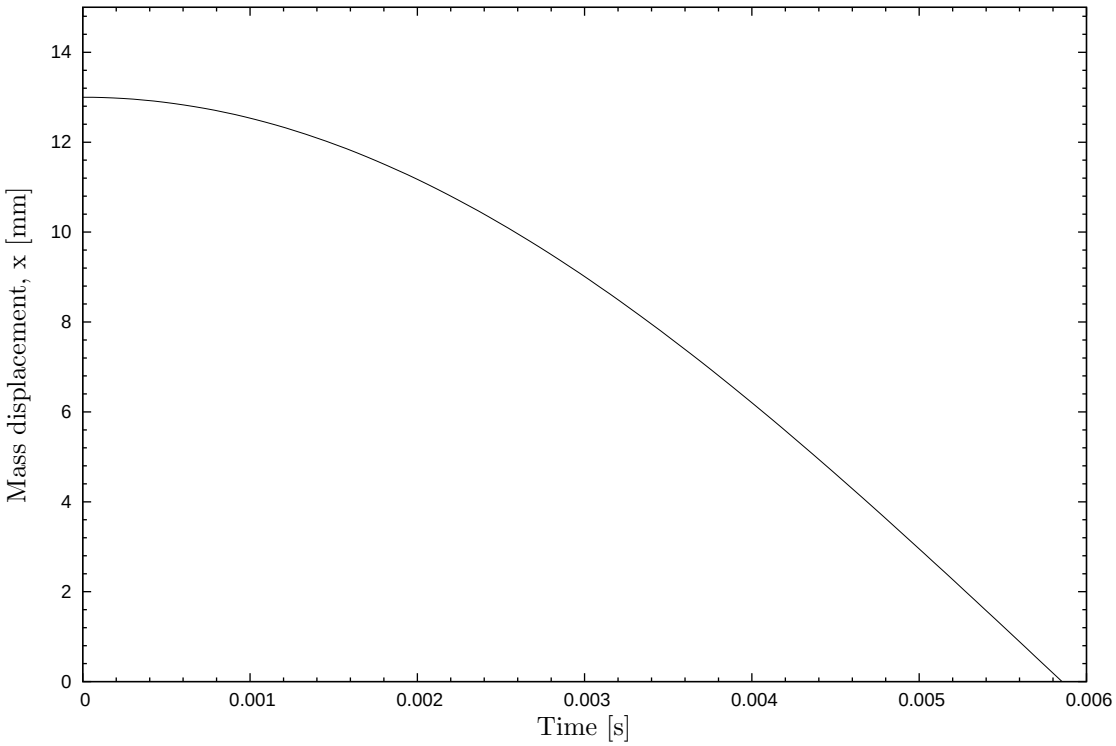


Figure C.4: Solution of the one dimensional ordinary differential equation for the spring mass system with $m = 1.0$ kg, $k = 72 \times 10^3$ N/m, $x_o = 13.0$ mm and zero initial speed

$$x = x_o \cos(\omega_n t) + \frac{dx}{dt} \frac{\sin(\omega_n t)}{\omega_n} \tag{C.12}$$

where ω_n is the natural frequency of the system and is given by :

$$\omega_n = \sqrt{\frac{k}{m}} \tag{C.13}$$

Assume an initial displacement, $x_o = 13.0$ mm, which is the linear travel of the actuator required to achieve 25.0° pitch and m = 1.0 kg, which is the approximate mass of the system connected to the actuator. Assume zero initial velocity, i.e.

$$\frac{dx}{dt} \mid_{t=0} = 0 \tag{C.14}$$

The solution of x with a spring stiffness of $k = 72 \times 10^3$ N/m is plotted in figure C.4. The solution shows that it is feasible to achieve the required motion in the required time.

The stiffness of a helical spring in compression is approximated by the following equation ([38]):

Table C.3: Technical specifications for safety pin solenoid

Supplier	BLP, Suffolk, England
Specification	Series 124 Tubular Solenoid
Description	Pull type tubular solenoid
Model No.	124 420 610 620
Power Supply	12 V DC
Approximate Stroke	10 mm
Approximate Pulling Force	50 N

Table C.4: Technical specifications for release actuator

Supplier	Phoenix Mecano
Description	Electric Cylinder
Model No.	M10/BGR 010
Power Supply	24 V DC
Total Stroke	40 mm
Travel Speed	4 mm/s
Actuator Force	200 N

$$k = \frac{Gd^4}{8nD^3} \tag{C.15}$$

where G is the shear modulus of elasticity, d is the wire diameter, D is the mean coil diameter and n is the number of turns on the spring. Using two springs in series requires each to have a stiffness, $k \approx 40000$ N/m each. The spring diameter, D (excluding the wire thickness), takes into account the space available normal to the streamwise direction. A value of D=16.2mm was selected. With G = 76.9 GPa for steel, d = 3.8 mm, D =16.2 mm and $k \approx 40000$ N/m, n = 11.5 turns. Two springs, installed in series, with these mechanical properties are sufficient to achieve the required motion. Two springs with an uncompressed length, L = 93mm, were manufactured for the dynamic actuator. The free length takes into account the space available within the actuator volume.

The operation of the latch mechanism was discussed in detail in Chapter 3 and may be consulted on the description of the design. The actuator has a safety pin that prevents the latch from releasing the spring load on tunnel startup. The safety pin is actuated by a solenoid. Solenoid technical specifications of are included in table C.3. Once, the solenoid is energised and the safety pin is disengaged, the latch is opened to release the spring load. The lever that opens the latch is actuated by a release actuator. The actuator is also a commercial off-the-shelf item and is essentially a linear motion electrical cylinder. It has a 200 N load capacity which is sufficient to open the latch. Specification are summarised in figure C.4.

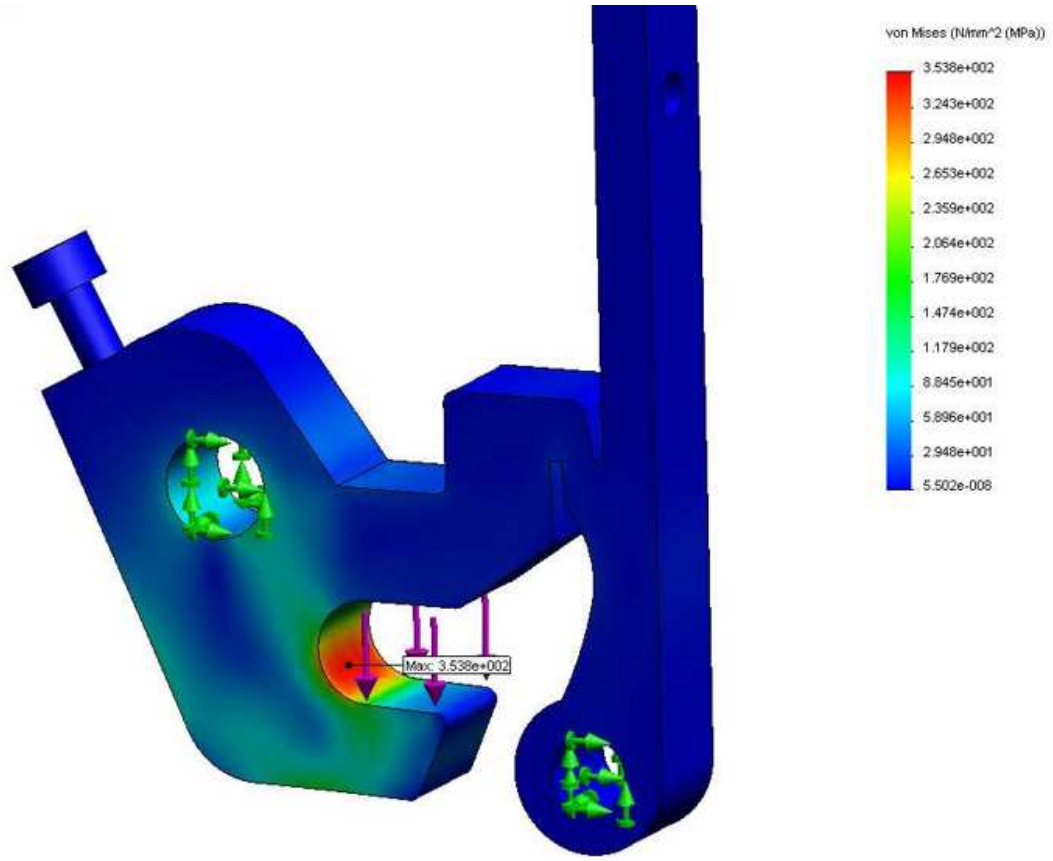


Figure C.5: Contours showing the distribution of computed stress in the latch and release pillar. The region of maximum stress at approximately 354 MPa is indicated. The FEM analysis was performed by Ryan Raath at the CSIR, Pretoria.

C.4 Finite Element Analysis for Latch Design

Due to the large loads involved in loading the spring, care was taken to apply the necessary safety factors and a finite element analysis of the latch was performed with *SolidWorksExpress*. The distribution of computed stress in the latch and release pillar is shown in figure C.5. The maximum stress with a 2000 N spring load is approximately 354 MPa. The latch and release pillar were manufactured with 174-Ph Stainless steel, heat treated at 900° C. In the hardened condition it has a maximum yield strength of approximately 1170 MPa and a maximum ultimate strength of 1300 MPa, which provides an adequate safety factor (3.3 on yield strength and 3.6 on ultimate strength).

C.5 Description of the Rig Operator Interface

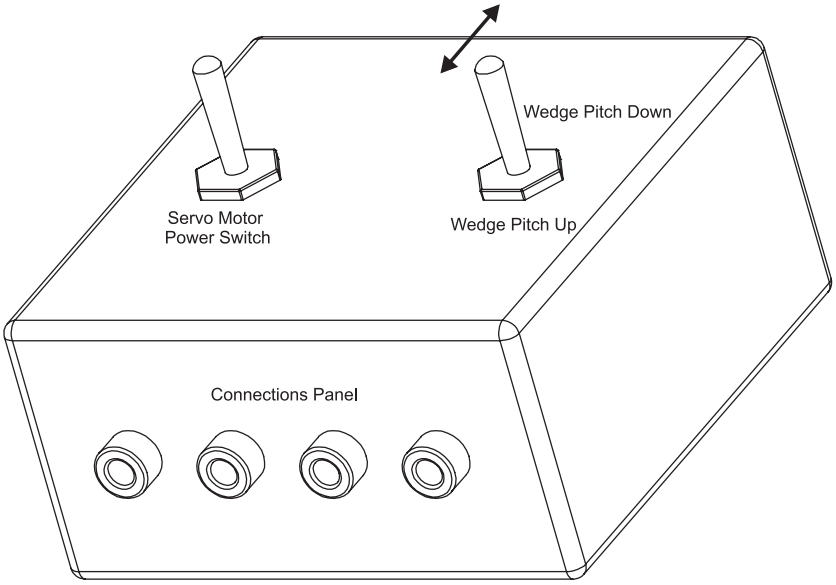
A control and electrical connections interface was built for the servo and spring-driven actuators as illustrated in figure C.6 and C.8. This enables the remote operation of either actuator from the control room.

The interface for the servo-driven actuator consists of a switch to power the motor and a double throw double pole switch to rotate the motor clockwise or anti-clockwise. The rotation is translated to linear motion of the actuator through the bearing assembly discussed earlier in this chapter. The servo circuit diagram is presented in figure C.7.

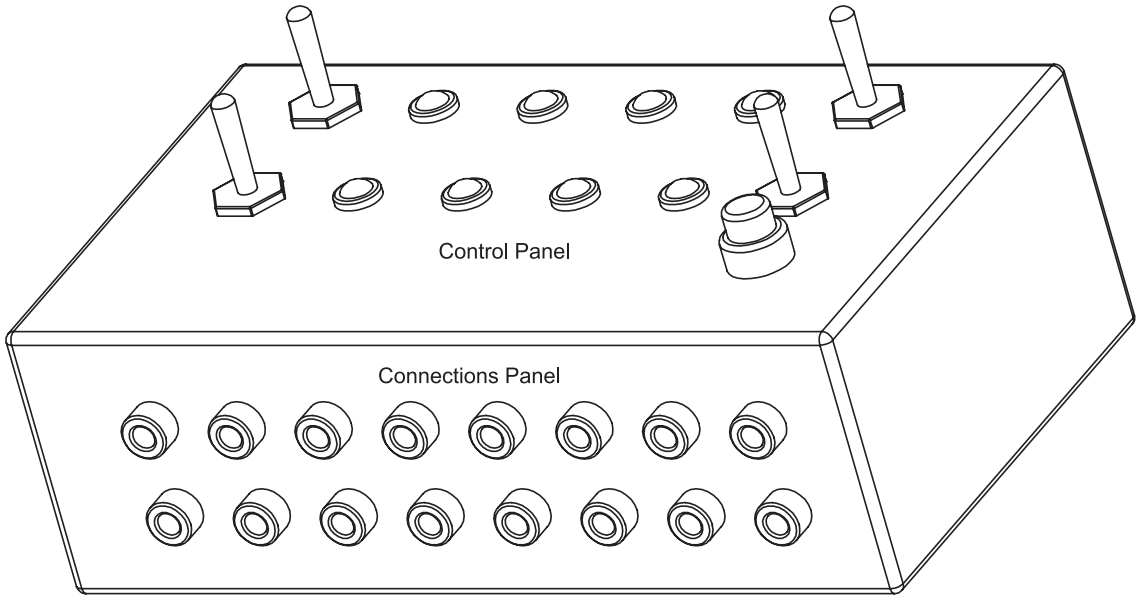
The interface for the spring-driven actuator controls the operation of the safety pin and the latch release actuator. Indicator lights on the interface indicate the status of the safety pin and the release actuator during a test. After tunnel startup, the solenoid is energised and the safety pin is disengaged. When the pin is disengaged the indicator LED is illuminated and the rig operator may proceed to open the latch with the release actuator. Once the latch is released an indicator light on the panel signals the camera operator to trigger the image capture. As the camera is running in "centre" mode it stores images before and after the trigger is activated. The circuit diagram for the solenoid and the release actuator are presented in figures C.9 and C.10.

C.6 Photographs of Rig

A detailed description of the rig design and operation was presented in Chapter 3 with detailed accompanying schematics. Photographs of the rig and its components are presented in figures C.11-C.16.



(a) Control and electrical connections interface for servo-driven actuator



(b) Control and electrical connections interface for spring-driven actuator

Figure C.6: Control and electrical connections interface for actuators

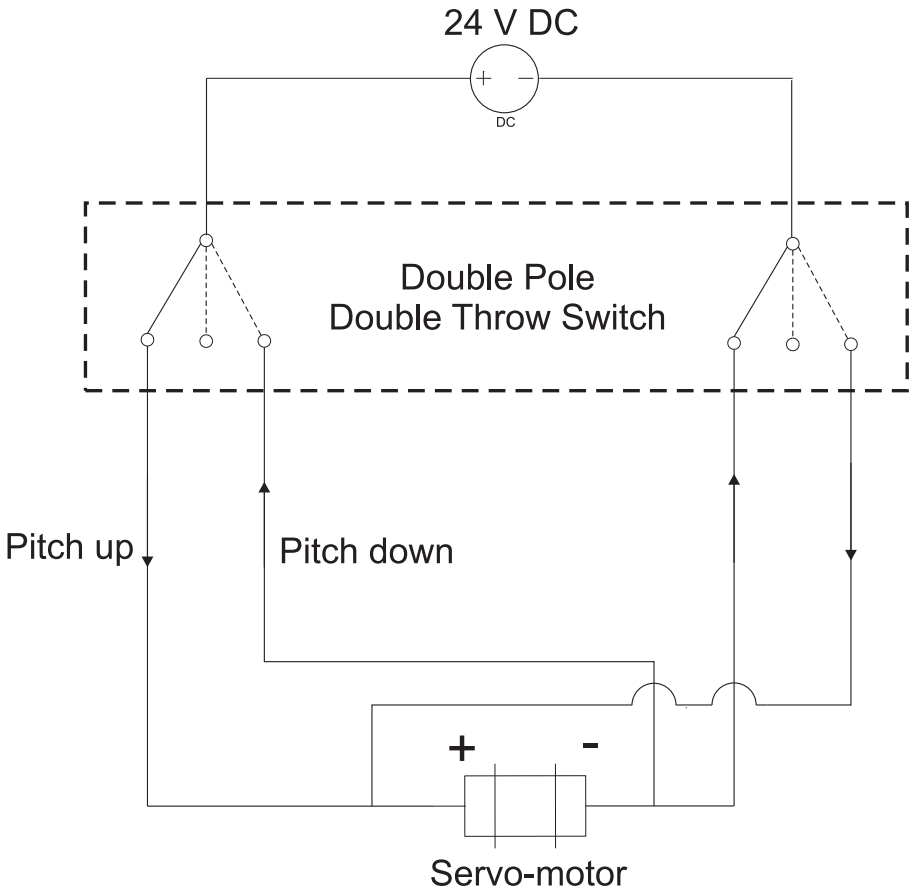
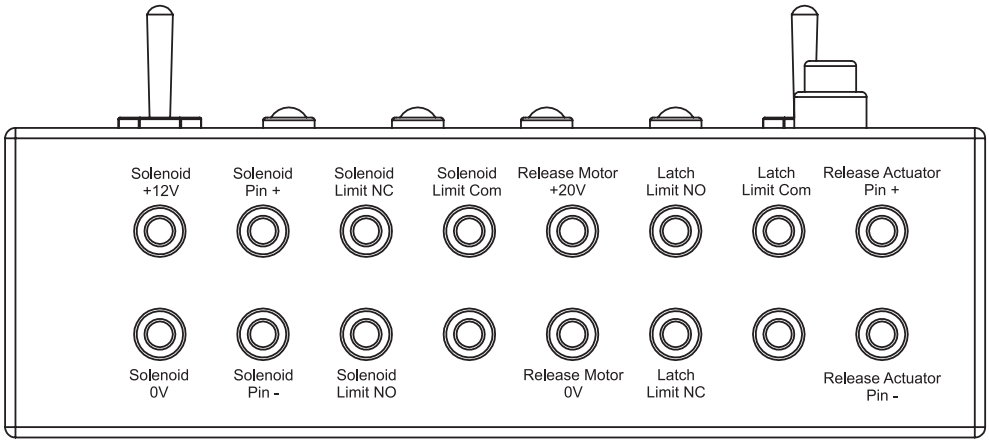
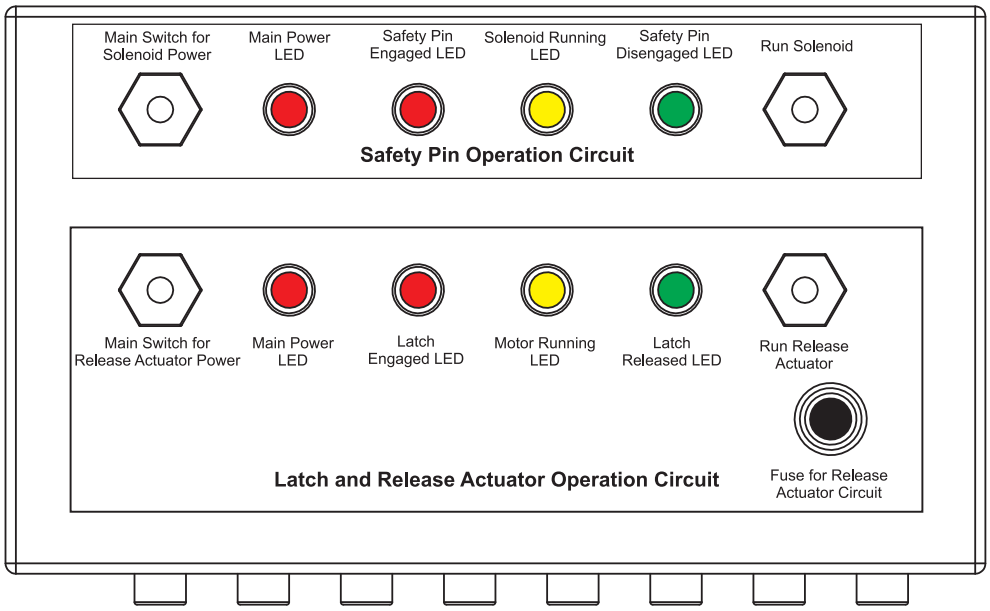


Figure C.7: Electrical circuit for operation of servo-motor showing current direction for wedge pitch up and pitch down



(a) Front view showing operation panel for operation of the safety pin and release actuator



(b) Top view showing electrical connections panel for dynamic actuator

Figure C.8: (a) Front and (b) top views of control interface for spring-driven actuator

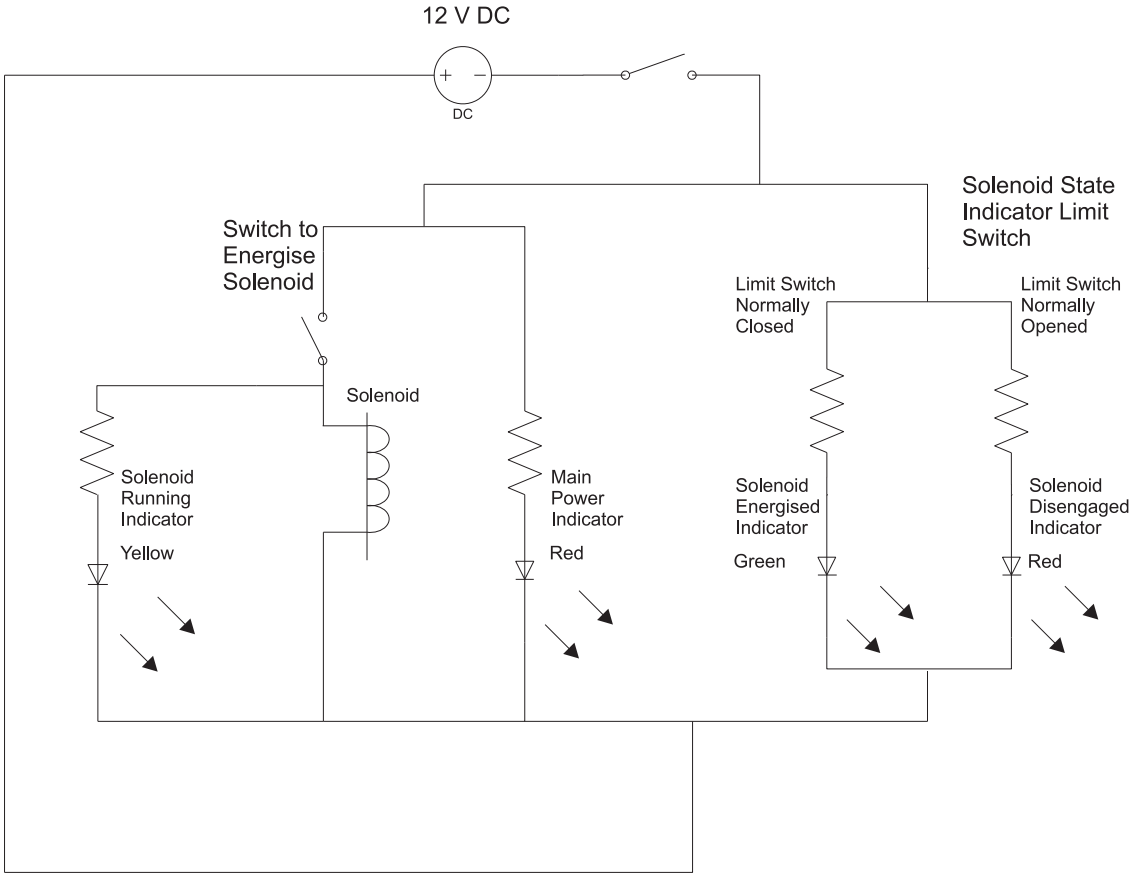


Figure C.9: Solenoid circuit for the operation of the safety pin in the spring-driven actuator

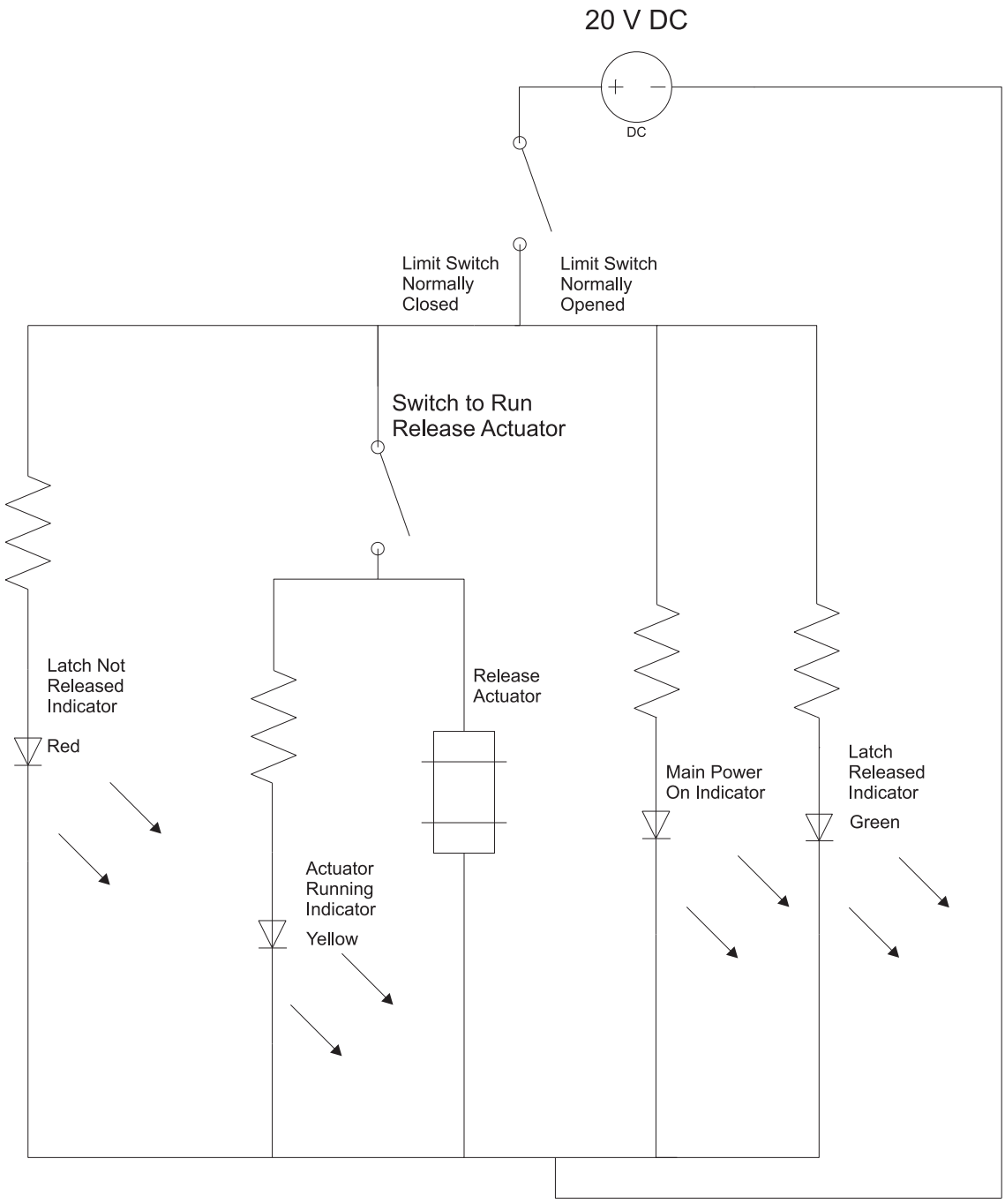
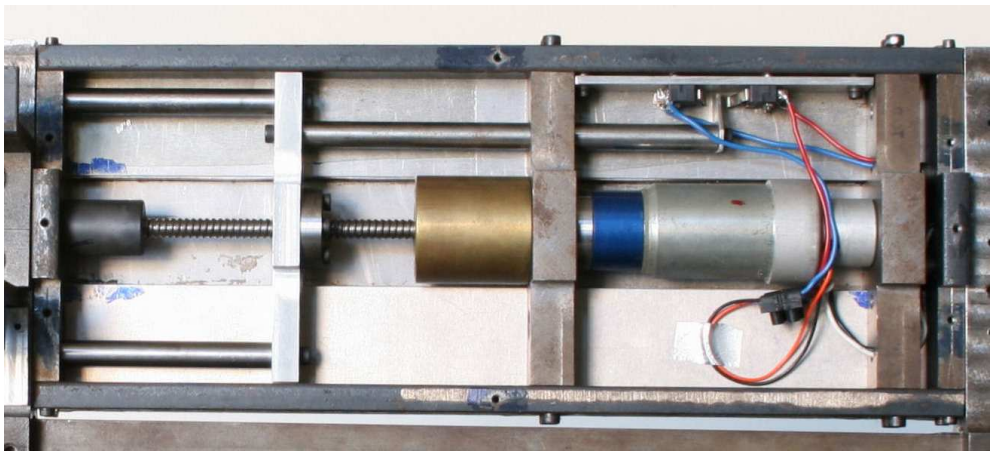
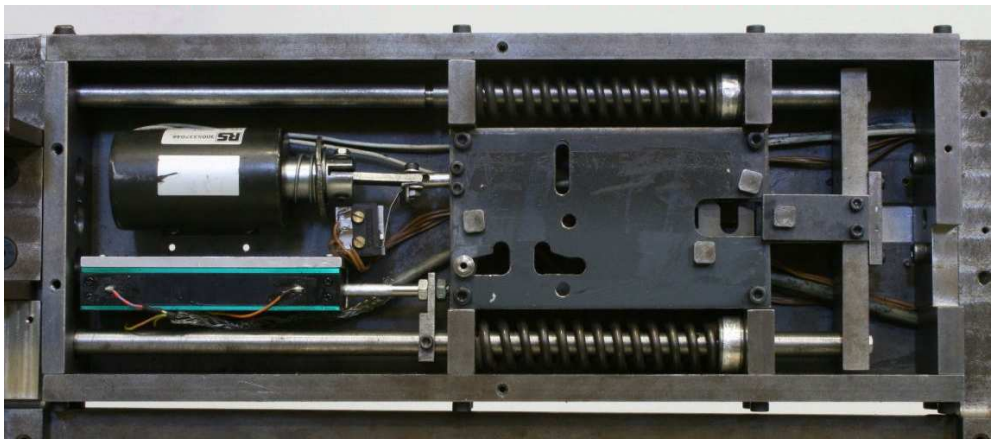


Figure C.10: Latch release circuit diagram for the spring-driven actuator



(a) Servo-driven actuator used for steady state baseline experiments



(b) Spring-driven actuator used for dynamic experiments without the latch release actuator installed

Figure C.11: Actuators for (a) steady state, baseline experiments and (b) dynamic experiments



Figure C.12: Rig used for dynamic shock wave reflection experiments. Cover plates are installed and the release actuator has been removed.

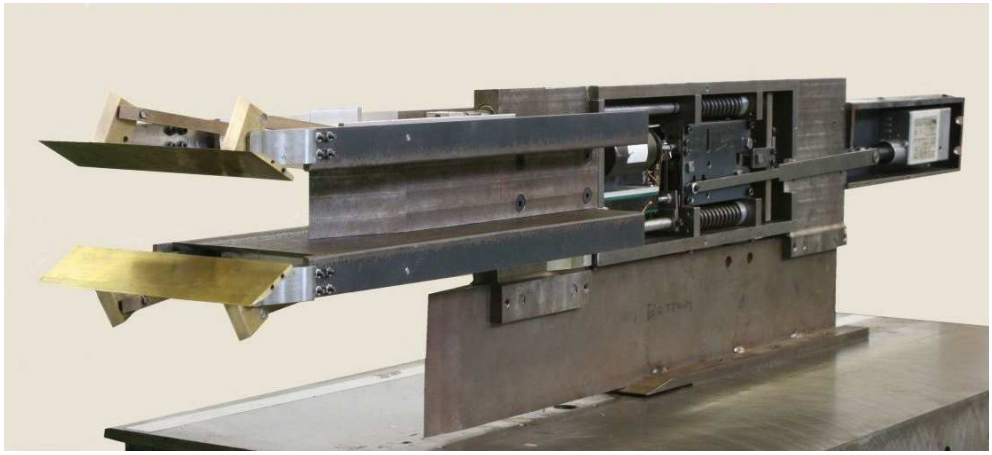


Figure C.13: Rig with cover plates removed and release actuator installed. The actuator is assembled to execute the dynamic RR → MR transition experiment.

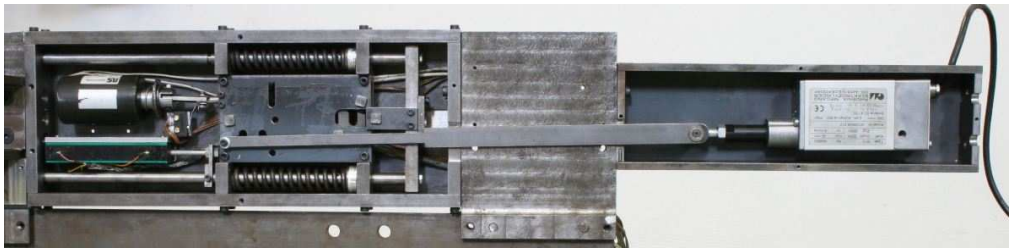


Figure C.14: Closeup view of the spring-driven actuator with the release actuator installed. The actuator is assembled to execute the dynamic RR → MR transition experiment.

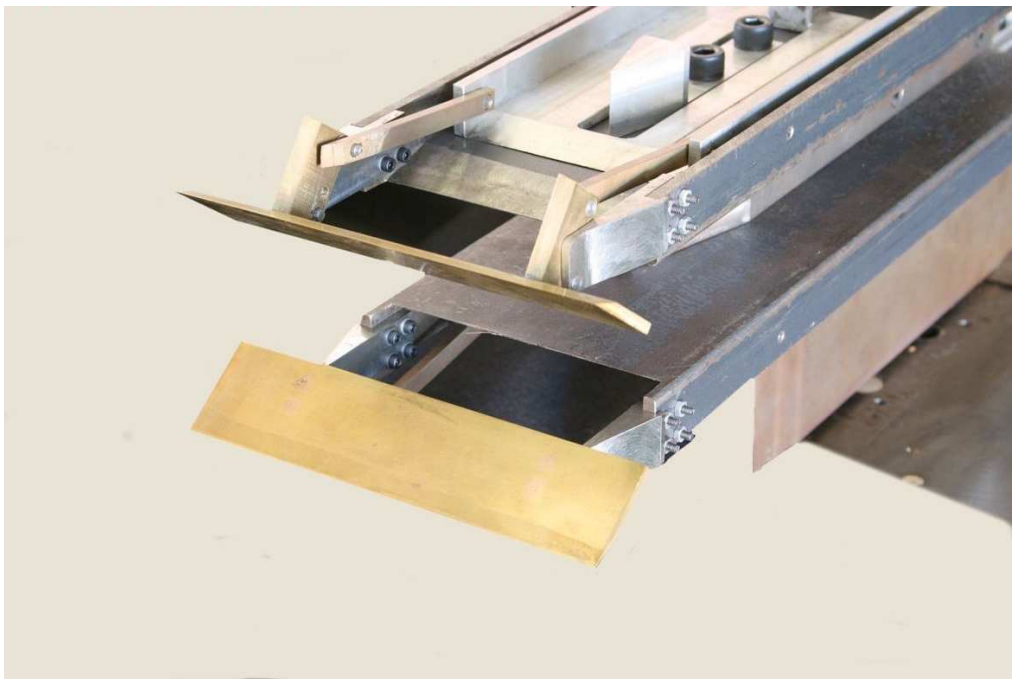


Figure C.15: Closeup view of wedges



Figure C.16: Stream wise view of the rig installed in tunnel test section

References

[1] D J Azevedo and C S Liu. Engineering approach to the prediction of shock patterns in bounded high-speed flows. *AIAA J.*, 31(1):83–90, 1993.

[2] G Ben-Dor. Hysteresis phenomena in shock wave reflections in steady flows. In *Proceedings 22nd International Symposium on Shock Waves*. Society for Shock Wave Research Imperial College, 1999.

[3] G Ben-Dor. *Shock Wave Reflection Phenomena*. Springer, second edition, 2007.

[4] G Ben-Dor, M Ivanov, EI Vasilev, and T Elperin. Hysteresis processes in the regular reflection $\leftrightarrow$ mach reflection transition in steady flows. *Progress in Aerospace Sciences*, 38, 2002.

[5] C J Chapman. *High Speed Flow*. Cambridge University Press, first edition, 2000.

[6] A Chpoun and G Ben-Dor. Numerical confirmation of the hysteresis phenomenon in the regular to mach reflection transition in steady flows. *Shock Waves*, 5:199–203, 1995.

[7] A Chpoun, D Passerel, H Li, and G Ben-Dor. Reconsideration of oblique shock wave reflections in steady flows. part 1. experimental investigation. *J. Fluid Mech.*, 301:19–35, 1995.

[8] Eastman Kodak Company. *Schlieren Photography*. Eastman Kodak, first edition, 1960.

[9] R Courant and K O Friedrichs. *Supersonic Flow and Shock Waves*. Interscience Publishers Ltd., first edition, 1948.

[10] C Farhat, C Degand, B Koobus, and M Lesoinne. Torsional springs for two-dimensional dynamic unstructured fluid meshes. *Comput. Methods Appl. Mech. Engrg.*, 163:231–245, 1998.

[11] L T Felthun. *The Modelling of Compressible Euler Flows with Moving Boundaries*. PhD thesis, University of the Witwatersrand, 2002.

[12] L T Felthun and B W Skews. Dynamic shock wave reflection. *AIAA J.*, 42(8):1633–1639, 2004.

[13] V M Fomin, H G Hornung, M S Ivanov, A M Kharitonov, G P Klemenkov, A N Kudryavtsev, and A A Pavlov. The study of regular and mach reflection of shockw aves in different wind tunnels. In *Proceedings of the 12th International Mach Reflection Symposium*, 1996.

[14] L F Henderson and A Lozzi. Experiments on transition of mach reflection. *J. Fluid Mech.*, 68:139–155, 1975.

[15] L F Henderson and A Lozzi. Further experiments on transition to mach reflexion. *J. Fluid Mech.*, 94:541–559, 1979.

[16] H G Hornung. Regular and mach reflection of shock waves. *Annual Review of Fluid Mechanics*, 18:33–58, 1986.

[17] H G Hornung. On the stability of steady-flow regular and mach reflection. *Shock Waves*, 7:123–125, 1997.

[18] H G Hornung, H Oertel, and R J Sandeman. Transition to mach reflection of shock-waves in steady and pseudo-steady flow with and without relaxation. *J. Fluid Mech.*, 90:541–560, 1979.

[19] H G Hornung and M L Robinson. Transition from regular to mach reflection of shock waves. part 2. the steady flow criterion. *J. Fluid Mech.*, 123:155–164, 1982.

[20] H G Hornung and N Sudani. Stability and analogy of shock wave reflection in steady flow. *Shock Waves*, 8:367–374, 1998.

[21] M S Ivanov, S F Gimelshein, and A E Beylich. Hysteresis effect in stationary reflection of shock-waves. *Phys. Fluids*, 7:685–687, 1995.

[22] M S Ivanov, A N Kudryavtsev, S B Nikiforov, D V Khotyanovsky, and A A Pavlov. Experiments on shock wave reflection transition and hysteresis in low-noise wind tunnel. *Phys. Fluids*, 15:1807, 2003.

[23] M S Ivanov, G N Markelov, A N Kudryatsev, and S F Gimelshein. Numerical analysis of shock wave reflection transition in steady flows. *AIAA J.*, 36(11):2079–2086, 1998.

[24] M S Ivanov, D Vandromme, V M Fomin, A N Kudryavtsev, A Hadjadj, and D V Khotyanovsky. Transition between regular and mach reflection of shock waves: new numerical and experimental results. *Shock Waves*, 11):199–207, 2001.

[25] M S Ivanov, D Zeitoun, J Vuillon, S F Gimelshein, and G N Markelov. Investigation of the hysteresis phenomena in steady shock reflection using kinetic and continuum methods. *Shock Waves*, 5(6):341–346, 1996.

[26] J D Anderson Jr. *Fundamentals of Aerodynamics*. McGraw Hill Book Company, first edition, 1984.

[27] D V Khotyanovsky, A N Kudryavtsev, G Ben-Dor, and M S Ivanov. Strong regular reflection of steady shock waves. In *Proceedings 23rd International Symposium on Shock Waves*, 2001.

[28] D V Khotyanovsky, A N Kudryavtsev, and M S Ivanov. Numerical study of transition between steady regular and mach reflection caused by free-stream perturbations. In *Proceedings 22nd International Symposium on Shock Waves*. Society for Shock Wave Research Imperial College, 1999.

[29] L Kirkup. *Experimental Methods: An Introduction to the Analysis and Presentation of Data*. Wiley, first edition, 1996.

[30] A N Kudryavtsev, D V Khotyanovsky, M S Ivanov, A Hadjadj, and D Vandromme. Numerical investigations of transition between regular and mach reflections caused by free-stream disturbances. *Shock Waves*, 12):157–165, 2002.

[31] H Li and G Ben-Dor. Application of the principle of minimum entropy production to shock wave reflections. i. steady flows. 80(4):2027–2037, 1996.

[32] H Li, A Chpoun, and G Ben-Dor. Analytical and experimental investigations of the reflection of asymmetric shock waves in steady flows. *J. Fluid Mech.*, 390:25–43, 1999.

[33] M S Liou. A sequal to ausm:ausm+. *J. Comput. Phys.*, 129:364–382, 1996.

[34] G N Markelov, I V Pivkin, and M S Ivanov. Impulsive wedge rotation effects on transition from regular to mach reflection. In *Proceedings of the 22nd International Sumposium on Shock Waves*, 1999.

[35] C A Mouton and H G Hornung. Mach stem height and growth rate predictions. *AIAA J.*, 45:1977, 2007.

[36] C A Mouton and H G Hornung. Experiments on the mechanism of inducing transition between regular and mach reflection. *Phys. Fluids*, 20:126103–1, 2008.

[37] G S Settles. *Schlieren and Shadowgraph Techniques:Visualising Phenomena in Transparent Media*. Springer, first edition, 2001.

[38] J E Shigley. *Mechanical Engineering Design*. McGraw Hill Book Company, first edition, 1986.

[39] B W Skews. Aspect ratio effects in wind tunnel studies of shock wave reflection transition. *Shock Waves*, 7:373–383, 1997.

[40] B W Skews. Three dimensional effects in wind tunnel studies of shock wave reflection. *J. Fluid Mech.*, 407:85–104, 2000.

[41] N Sudani and H G Hornung. Stability and analogy of shock wave reflection in steady flow. *Shock Waves*, 8:367–374, 1998.

[42] N Sudani, M Sato, T Karasawa, J Noda, A Tate, and M Watanabe. Irregular effects on the transition from regular to mach reflection of shock waves in wind tunnel flows. *J. Fluid Mech.*, 459:167–185, 2002.

[43] R J Volluz. *Naval Ordnance Report 1488 Volume 6 Section 20 : Wind Tunnel Instrumentation.* United States Naval Ordnance, first edition, 1985.

[44] John von Neumann. Oblique reflection of shocks. Technical report, Bureau of Ordnance, 1943.

[45] J Vuillon, D Zeitoun, and G Ben-Dor. Reconsideration of oblique shock wave reflection in steady flows. part 2. numerical investigation. *J. Fluid Mech.*, 301:37–50, 1995.

[46] M J Zukrow and J D Hoffman. *Gas Dynamics Volume 1.* John Wiley and Sons, first edition, 1976.